

21

# Vortex-Induced Vibrations of Structural Members in Natural Winds

by

Chen-Yang Fei

S.M., Ocean Engineering, M.I.T. (1991)

B.Sc. Naval Architecture and Ocean Engineering, Shanghai Jiao  
Tong University (1988)

Submitted to the Department of Ocean Engineering  
in partial fulfillment of the requirements for the degree of

Doctor of Philosophy in Ocean Engineering

at the

MASSACHUSETTS INSTITUTE OF TECHNOLOGY

February 1995

© Massachusetts Institute of Technology 1995. All rights reserved.

Author .....  .....

Department of Ocean Engineering


January 20, 1995

Certified by .....  .....

Professor J. Kim Vandiver

Professor of Ocean Engineering

Thesis Supervisor

Accepted by .....  .....

Professor A. Douglas Carmichael

Chairman, Departmental Graduate Committee

**Barker Eng**

FEB 11 1995

# Vortex-Induced Vibrations of Structural Members in Natural Winds

by  
Chen-Yang Fei

Submitted to the Department of Ocean Engineering  
on January 20, 1995, in partial fulfillment of the  
requirements for the degree of  
Doctor of Philosophy in Ocean Engineering

## Abstract

Vibrations of structural members induced by natural winds have been the source of fatigue damage to offshore platforms during fabrication and transportation and to flarebooms during in-service conditions. To design fatigue-resistant structural members based on steady-state vibrations at a constant windspeed is not acceptable since steady-state vibrations would lead to excessively conservative predictions.

This thesis provides analytical and empirical models to predict fatigue damage of structural members induced by natural winds. Results of wind tunnel experiments on a 1.903 inch diameter flexible cylinder indicate that unsteady fluctuations in the mean windspeed typically prevent vortex-excited vibrations from reaching steady-state amplitudes. A time domain model is proposed, where the transient vibrations of a flexible cylinder induced by unsteady winds are simulated in the time domain by an equivalent single degree of freedom (SDOF) oscillator. This SDOF oscillator has the properties of the responding resonant mode of the cylinder. After the dependence of steady-state response on the windspeed is determined, the excitation force on the oscillator is modeled as the steady-state sinusoidal excitation corresponding to the input windspeed sequence. The resultant transient vibrations of the flexible cylinder are found by a convolution of the derived excitation force and the impulse response function of the SDOF oscillator. The predictions by the time domain model agree well with the wind tunnel measurements.

To predict fatigue damage of a flexible cylinder induced by natural winds, a probabilistic model is proposed. After analyzing relevant wind statistics and structural parameters, this probabilistic model identifies three fatigue damage discount factors. The first factor accounts for the fluctuations of the instantaneous windspeed around the mean, and can be determined by the probability density function (PDF) of the instantaneous windspeed and the critical velocity of the structural member ( $V_{crit}$ ). The second factor accounts for the finite rise time of the structural response, and is predicted in terms of the ratio of the expected duration of a visit by the windspeed to the critical velocity interval to the rise time of the structural response. The third factor accounts for the over-estimation of fatigue damage caused by discretizing the PDF of the mean windspeed into rather broad bins. The real fatigue damage with

natural winds is equal to the fatigue damage with steady-state conditions, multiplied by these three discount factors. The probabilistic model is verified against the time domain model using high sampling rate real windspeed data.

Desirable wind statistics which determine the duration of a visit by the wind-speed to the critical velocity interval are analyzed from high sampling rate raw wind data measured at a typical maritime site. A design methodology for fatigue resistant structural members excited by natural winds is proposed based on the probabilistic model. The design methodology is illustrated through examples.

Thesis Supervisor: Professor J. Kim Vandiver

Title: Professor of Ocean Engineering

Dedicated to my parents,  
whose bounties are as boundless as sea.

## Acknowledgements

I would like to express my deepest gratitude to my thesis advisor Professor J. Kim Vandiver, for his insightful guidance and warm-hearted encouragement during my graduate study at M.I.T.. He taught me how to solve practical engineering problems from a practitioner's perspective. For his generous financial support without which it would have been impossible to fulfill my childhood M.I.T. dream.

I would like to thank Dr. Brad Campbell of Exxon Production Research Company for providing me with the opportunity to work on the wind engineering research project, from which this thesis is motivated, during his chairmanship of the API Technical Advisory Committee on Vortex-induced Vibrations. I would also like to thank him for providing valuable expertise as well as wind measurements and computer programs. I would also like to thank the American Petroleum Institute and a joint industry consortium with the participants from Amoco, British Petroleum, Chevron, Conoco, Exxon Production Research, Mobil, Petrobras and Shell Development Company, for sponsoring the research project upon which this thesis is based. I would also like to thank my thesis committee members, Professors Michael Triantafyllou and John Lienhard, and Dr. Brad Campbell, for their constructive criticism. Professor Daniele Veneziano of the Civil and Environmental Engineering Department at M.I.T., for being my thesis Reader as well as for insightful discussions during the infant stages of developing probabilistic models.

As to the real wind data, I would like to express my gratitude to the participants in the Statoil Joint Industry Project on Maritime Turbulent Wind Field Measurements and Models, for releasing the wind database specifically for the purpose of developing improved design guidelines. Special thanks to Daniel Rudge of Shell U.K. Exploration and Production, for his long-term interest and for his support of the project and for his efforts to provide access to the wind data.

I would also like to thank Stephen Nicholls, a former fellow graduate student, for his ingenious fabrication skills and assistance with wind-tunnel experiments. My gratitude is extended to my basketball buddies, office mates in room 5-007 and friends in the Ashdown House and in the local area, for their friendship which made my study at M.I.T. bearable and fun. Rama Rao V.N., for relaxing and humorous conversations on the civilizations of China and India. Tian-Shu Pan of Harvard University, for his rich humor and wonderful companionship which made my final year in Cambridge memorable.

# Contents

<b>1</b>	<b>Introduction</b>	<b>14</b>
1.1	Vortex-induced vibrations . . . . .	14
1.2	Vibrations induced by natural winds . . . . .	17
1.3	A preview of the chapters that follow . . . . .	18
<b>2</b>	<b>Experimental Studies</b>	<b>20</b>
2.1	Review . . . . .	20
2.2	Model descriptions . . . . .	22
2.3	Instrumentation . . . . .	22
2.3.1	Wind tunnel . . . . .	23
2.3.2	Turbulence-generating grids . . . . .	23
2.3.3	Strain gauges . . . . .	24
2.3.4	Hot wire anemometers . . . . .	24
2.3.5	Data acquisition . . . . .	25
2.4	Turbulence measurements . . . . .	28
2.4.1	Power spectral density functions of longitudinal turbulence components . . . . .	29
2.4.2	Turbulence length scales . . . . .	30
2.4.3	Turbulence intensity . . . . .	31
2.5	Model response at different turbulence levels . . . . .	33
2.5.1	Results of steady state tests . . . . .	35
2.5.2	Results of transient tests . . . . .	45
2.6	Summary of test results . . . . .	46
<b>3</b>	<b>Time Domain VIV Prediction Model</b>	<b>51</b>
3.1	Overview . . . . .	51
3.2	Mathematical basis of the VIV prediction model . . . . .	52
3.2.1	Derivation of equivalent excitation force . . . . .	52
3.2.2	Prediction of transient vibrations of a flexible cylinder . . . . .	56
3.2.3	Assessment of fatigue damage . . . . .	59
3.3	Implementation of the prediction procedure . . . . .	62
3.4	Examples . . . . .	65
3.4.1	Case one: predictions <i>v.s.</i> wind tunnel measurements . . . . .	67
3.4.2	Case two: effect of different steady-state response functions . . . . .	68
3.4.3	Case three: effect of downsampling the wind speed . . . . .	71

3.4.4	Case four: effect of using mean windspeed . . . . .	75
3.5	Summary . . . . .	77
<b>4</b>	<b>Probabilistic Models for VIV Predictions</b>	<b>83</b>
4.1	Motivation . . . . .	83
4.2	Analysis of time scales . . . . .	84
4.2.1	Duration of a visit by the wind speed to an interval $[a, b]$ . . . . .	84
4.2.2	Rise time of structural response . . . . .	91
4.3	Introduction of a Gaussian windspeed approximation . . . . .	91
4.4	Development of probabilistic prediction methodology . . . . .	96
4.4.1	Predicting $\gamma_0$ , the fatigue damage discount factor due to instantaneous fluctuations of windspeed . . . . .	97
4.4.2	Predicting $\gamma_1$ , the fatigue damage discount factor due to structural response rise time . . . . .	104
4.5	Examples . . . . .	110
4.5.1	Implementing the probabilistic model . . . . .	110
4.5.2	Using the probabilistic model based on wind statistics from raw wind data . . . . .	116
4.6	Verification of probabilistic prediction methodology using high sampling rate real wind data . . . . .	118
4.6.1	Verifying $\gamma_0$ . . . . .	119
4.6.2	Verifying $\gamma_1$ . . . . .	121
4.6.3	Verifying the predictions based on longer-term wind data . . . . .	124
4.7	Summary . . . . .	125
<b>5</b>	<b>Effects of Discretizing the PDF of Mean Windspeeds</b>	<b>127</b>
5.1	Fatigue damage of a structural member when the mean windspeed is a random variable . . . . .	127
5.2	The scatter diagram of the mean windspeed and the effect of finite bin sizes . . . . .	127
5.2.1	Approximating $E[\gamma]$ . . . . .	130
5.2.2	A model for $\gamma_{bin}$ . . . . .	133
5.3	Summary . . . . .	140
<b>6</b>	<b>Characteristics of Natural Winds</b>	<b>141</b>
6.1	Review of existing knowledge on natural winds . . . . .	141
6.1.1	Hourly average windspeed . . . . .	142
6.1.2	Turbulence . . . . .	144
6.1.3	Wind directionality effects . . . . .	147
6.2	Estimating desirable wind statistics from raw windspeed data . . . . .	148
6.2.1	The wind database . . . . .	149
6.2.2	$p_U(u)$ . . . . .	149
6.2.3	$T_u$ . . . . .	149
6.2.4	$\sigma_{\dot{U}}$ . . . . .	151
6.3	Summary . . . . .	152

<b>7</b>	<b>The Design of Fatigue Resistant Structural Members Excited by Natural Winds</b>	<b>153</b>
7.1	Design procedure . . . . .	153
7.2	Examples . . . . .	160
7.2.1	A worked example to illustrate the design procedure . . . . .	160
7.2.2	The effect of different values of turbulence intensity . . . . .	165
7.2.3	The effect of different values of $\sigma_{\dot{V}}$ . . . . .	166
7.2.4	The effect of different values of $V_{crit}$ . . . . .	167
7.3	Summary . . . . .	168
<b>8</b>	<b>Conclusions and Recommendations</b>	<b>171</b>
8.1	Conclusions . . . . .	171
8.2	Recommendations . . . . .	172
8.2.1	Wind directionality . . . . .	172
8.2.2	Dependence of $\sigma_{\dot{V}}$ on $\bar{V}$ . . . . .	173
<b>A</b>	<b>State Equations and Input-Output Models for a Linear System</b>	<b>174</b>
A.1	State equations and analytical solutions . . . . .	174
A.2	Input-output relationship for a linear system . . . . .	177
A.3	An example . . . . .	178



# List of Figures

1-1	The dependence of Strouhal number on Reynolds number relationship for circular cylinders, from Blevins (1990) . . . . .	15
1-2	The maximum cross-flow displacement range, $2Y_{EFF,MAX}$ (twice the maximum cross-flow displacement amplitude), as a function of the response parameter $S_G$ , from Griffin (1985) . . . . .	16
2-1	Configuration of the model . . . . .	23
2-2	Hot wire set-up, from Nicholls (1993) . . . . .	26
2-3	Hot wire calibration curve . . . . .	27
2-4	Geometries of grids . . . . .	29
2-5	Power spectral density function of longitudinal turbulence, case zero (empty tunnel) . . . . .	30
2-6	Power spectral density function of longitudinal turbulence, case one . . . . .	31
2-7	Power spectral density function of longitudinal turbulence, case two . . . . .	32
2-8	Power spectral density function of longitudinal turbulence, case three . . . . .	33
2-9	Steady state r.m.s. vibration amplitude at mid-span of the test tube as a function of reduced velocity, case 0 (empty tunnel) . . . . .	36
2-10	Steady state r.m.s. vibration amplitude at mid-span of the test tube as a function of reduced velocity, case 1 (turbulence intensity 9.9%) . . . . .	37
2-11	Steady state r.m.s. vibration amplitude at mid-span of the test tube as a function of reduced velocity, case 2 (turbulence intensity 7.5%) . . . . .	38
2-12	Steady state r.m.s. vibration amplitude at mid-span of the test tube as a function of reduced velocity, case 3 (turbulence intensity 7.7%) . . . . .	39
2-13	Test 28 (empty tunnel): power spectral density functions of the measured cross-flow vibration amplitudes at three different reduced velocities. . . . .	40
2-14	Test 29 (turbulence intensity 9.9%): power spectral density functions of the measured cross-flow vibration amplitudes at three different reduced velocities. . . . .	41
2-15	Test 32 (turbulence intensity 7.5%): power spectral density functions of the measured cross-flow vibration amplitudes at three different reduced velocities. . . . .	42
2-16	Test 37 (turbulence intensity 7.7%): power spectral density functions of the measured cross-flow vibration amplitudes at three different reduced velocities. . . . .	43

2-17	Test 28 (case 0, empty tunnel): power spectral density functions of the wake velocity in the longitudinal direction at three different reduced velocities. . . . .	44
2-18	Test 29 (case 1, turbulence intensity 9.9%): power spectral density functions of the wake velocity in the longitudinal direction at three different reduced velocities. . . . .	45
2-19	Test 32 (case 2, turbulence intensity 7.5%): power spectral density functions of the wake velocity in the longitudinal direction at three different reduced velocities. . . . .	46
2-20	Test 37 (case 3, turbulence intensity 7.7%): power spectral density functions of the wake velocity in the longitudinal direction at three different reduced velocities. . . . .	47
2-21	Peak magnitudes of averaged wake coherence functions <i>vs.</i> turbulence intensities, Cases 0, 1, 2, 3. . . . .	48
2-22	Time trace of the wind speed. Test 31 (case one, turbulence intensity 9.9%) . . . . .	49
2-23	Time trace of the cross-flow transient motion. Test 31 (case one, turbulence intensity 9.9%) . . . . .	50
3-1	A generic $S - N$ curve . . . . .	59
3-2	Variation of the r.m.s. lift force coefficient with Reynolds number, from Rudge & Fei (1991) . . . . .	63
3-3	Steady-state response function, proposed by Fei & Vandiver . . . . .	65
3-4	Time trace of the measured windspeed in metric units . . . . .	66
3-5	Time trace of the measured windspeed expressed in terms of reduced velocities . . . . .	68
3-6	Time trace of the predicted excitation force acting on the SDOF oscillator, in newtons per unit mass . . . . .	69
3-7	Time trace of the predicted transient vibrations at the mid-span of the cylinder, in diameters, from the proposed method . . . . .	70
3-8	Envelope of the predicted and the measured transient vibration amplitudes at the mid-span of the cylinder, in diameters . . . . .	71
3-9	Comparison of the predicted and the measured transient vibration envelopes. Steady-state response function proposed by <b>DnV</b> is used for prediction. . . . .	72
3-10	Comparison of the predicted and the measured transient vibration envelopes. Steady-state response function proposed by <b>BS 8100</b> is used for prediction. . . . .	73
3-11	Comparison of the predicted and the measured transient vibration envelopes. Steady-state response function proposed by <b>ESDU 85038/Brown &amp; Root</b> is used for prediction. . . . .	74
3-12	Comparison of the predicted and the measured transient vibration envelopes. Steady-state response function proposed by <b>Fei &amp; Vandiver</b> is used for prediction. . . . .	75

3-13	Time traces of the original wind speed (sampling frequency of 512 Hertz) and the downsampled wind speed (sampling frequency of 0.1 Hertz) . . . . .	76
3-14	Time traces of the envelopes of the measured transient vibrations (sampling frequency of 512 Hertz) and the predicted transient vibrations (sampling frequency of 0.1 Hertz) . . . . .	77
3-15	Time traces of the original wind speed (sampling frequency of 512 Hertz) and the downsampled wind speed (sampling frequency of 0.025 Hertz) . . . . .	78
3-16	Time traces of the envelopes of the measured transient vibrations (sampling frequency of 512 Hertz) and the predicted transient vibrations (sampling frequency of 0.025 Hertz) . . . . .	79
3-17	Time traces of the original wind speed sequence(sampling frequency of 512 Hertz) and the mean wind speed sequence . . . . .	80
3-18	Time traces of the envelopes of the measured transient vibrations (sampling frequency of 512 Hertz) and the predicted transient vibrations corresponding to the mean wind speed sequence . . . . .	81
4-1	Duration of a visit by the wind speed to an interval $[a, b]$ . . . . .	85
4-2	Durations of stay above and below a fixed threshold $y$ . . . . .	86
4-3	Variation of average numerical and Gaussian durations with critical velocities, from the 12 windspeed records in group 1 with large turbulence (17%) . . . . .	94
4-4	Variation of average numerical and Gaussian durations with critical velocities, from the 3 windspeed records in group 1 with small turbulence (8%) . . . . .	95
4-5	Values of $\gamma_0$ as functions of mean wind speed $\bar{V}$ and the critical wind speed of the structural member $V_{crit}$ for Gaussianly-distributed wind-speed and the turbulence intensity of 10%. . . . .	102
4-6	Variation of $\gamma_0$ as functions of $\frac{\bar{V}}{V_{crit}}$ at different turbulence intensity levels. . . . .	103
4-7	Variation of $\gamma_1$ with $r$ , the ratio of the mean duration of a visit to structural response rise time . . . . .	109
4-8	Variation of $\frac{\gamma_0}{(\gamma_0)_{max}}$ and $\frac{\gamma_1}{(\gamma_1)_{max}}$ with $\frac{\bar{V}}{V_{crit}}$ . . . . .	110
4-9	Time trace of the windspeed from transpacific tow, from Campbell (1992) . . . . .	117
4-10	Variation of $\gamma_0$ with the ratio of the mean windspeed to the critical velocity of the member . . . . .	122
4-11	Variation of $\gamma_1$ with the ratio of the mean duration to the rise time . . . . .	124
4-12	Values of $\gamma$ as a function of $\frac{\bar{V}}{V_{crit}}$ based on the time domain model and the probabilistic model. slope of $S - N$ curve = 3.74. Reduced velocity range is from 3.8 to 7.7 . . . . .	125
5-1	PDF of mean windspeed . . . . .	128
5-2	A scatter diagram of mean windspeed . . . . .	129
5-3	Variation of $\gamma$ with mean windspeeds . . . . .	131
5-4	Variation of $\gamma_{bin}$ with bin sizes, from a numerical example . . . . .	132

5-5	Variation of $\gamma_{bin}$ with bin sizes at turbulence intensity = 10%, numerical solution <i>v.s.</i> model prediction. $m = 3.74$ . . . . .	137
5-6	Variations of $\gamma_{bin}$ with $\frac{\Delta \bar{U}}{V_{crit}}$ at $T_u = 10\%$ for different values of structural damping. $m = 3.74$ . . . . .	139
6-1	Variation of $T_u$ with $\bar{U}$ at three different elevations. from high sampling rate raw windspeed data . . . . .	150
6-2	Variation of $\sigma_{\bar{U}}$ with $\bar{U}$ at three different elevations. from high sampling rate raw windspeed data . . . . .	151
7-1	Variation of the r.m.s. lift force coefficient with Reynolds number. from Rudge & Fei (1991) . . . . .	155
7-2	Variation of $(\gamma_0)_{max}$ with turbulence intensities at three different values of the slope of $S - N$ curves . . . . .	158
7-3	Variation of $\mathcal{T} [s]$ with $V_{crit}$ and turbulence intensity at $\sigma_{\bar{U}} = 1.0 [m \cdot s^{-1}]$	159
7-4	Variation of $(\gamma_1)_{max}$ with $r_{max}$ for three different $S - N$ curves . . . . .	160
7-5	Contour plot of $\gamma_{bin}$ as functions of velocity bin size and turbulence intensity. slope of $S - N$ curve ( $m$ ) = 3.00 . . . . .	161
7-6	Contour plot of $\gamma_{bin}$ as functions of velocity bin size and turbulence intensity. slope of $S - N$ curve ( $m$ ) = 3.74 . . . . .	162
7-7	Contour plot of $\gamma_{bin}$ as functions of velocity bin size and turbulence intensity. slope of $S - N$ curve ( $m$ ) = 4.38 . . . . .	163
7-8	Scatter diagram of the long-term hourly mean windspeed . . . . .	164
A-1	A generic continuous-time system . . . . .	175

# List of Tables

2.1	Grid geometries . . . . .	28
2.2	Summary of turbulence characteristics at the model plane for cases 0, 1, 2 and 3. . . . .	32
2.3	A summary of measured structural damping ratios, $K_s$ values, measured peak cross-flow r.m.s. vibration amplitudes and their corresponding reduced velocity values from different tests. . . . .	34
3.1	Values of $F_i$ for different boundary conditions, from Rudge & Fei (1991)	81
3.2	Values of $\gamma_i$ for different boundary conditions, from Rudge & Fei (1991)	81
3.3	Prediction of the maximum vibration amplitude . . . . .	82
4.1	Summary of a worked example of the proposed probabilistic model . . . . .	115
4.2	Results of the predictions from both time domain VIV mode <sup>1</sup> and the probabilistic model . . . . .	117
5.1	Values of $\mathcal{F}_m$ at different values of turbulence and the exponent of the $S - N$ curve . . . . .	138
7.1	Values of $\gamma_i$ and $F_i$ for different boundary conditions . . . . .	154
7.2	Step by step implementation of the design procedure . . . . .	169
7.3	Variation of fatigue damage discount factor with turbulence intensity	170
7.4	Variation of fatigue damage discount factor with $\sigma_V$ . . . . .	170

# Chapter 1

## Introduction

### 1.1 Vortex-induced vibrations

The flow around a circular cylinder is a classical problem in fluid mechanics. At very low Reynolds numbers (less than 5), the flow around the cylinder remains unseparated. As the Reynolds number is increased to 15, two attached vortices appear in the wake behind the cylinder, and grow in size with Reynolds numbers. As the Reynolds number is increased to 40, the wake becomes unstable to small disturbances. The boundary layers on either side of the cylinder separate. Vortices shed alternatively from either side of the cylinder and move downstream, generating a periodic asymmetric flow, which is known as a vortex street.

In the subcritical Reynolds number range ( $300 < Re < 1.5 \times 10^5$ ), the transition to turbulence begins to occur further downstream in the vortex street, then moves progressively forward to the near body as the Reynolds number is increased. The vortex street becomes fully turbulent when the transition to turbulence occurs prior to rolling up into vortices. In the transitional Reynolds number range ( $1.5 \times 10^5 < Re < 3.5 \times 10^6$ ), the transition to turbulence occurs in the laminar boundary layers. Turbulent mixing causes the separation point to move downstream along the surface of the body. The wake becomes narrower and disorganized. The vortex street disappears. Regular vortex shedding resumes with fully-established turbulent boundary layers in the supercritical Reynolds number range ( $Re > 3.5 \times 10^6$ ).

The frequency of vortex shedding is related to the flow velocity, the diameter of the cylinder and a dimensionless constant known as Strouhal number:

$$f_s = \frac{S_t V}{D} \quad (1.1)$$

where  $f_s$  [ $s^{-1}$ ] is the vortex shedding frequency,  $V$  [ $m \cdot s^{-1}$ ] is the free stream flow velocity approaching the cylinder,  $D$  [m] is the diameter of the cylinder, and  $S_t$  is the Strouhal number. The Strouhal number of a stationary circular cylinder in a subsonic flow is a function of Reynolds number and, to a lesser extent, surface roughness

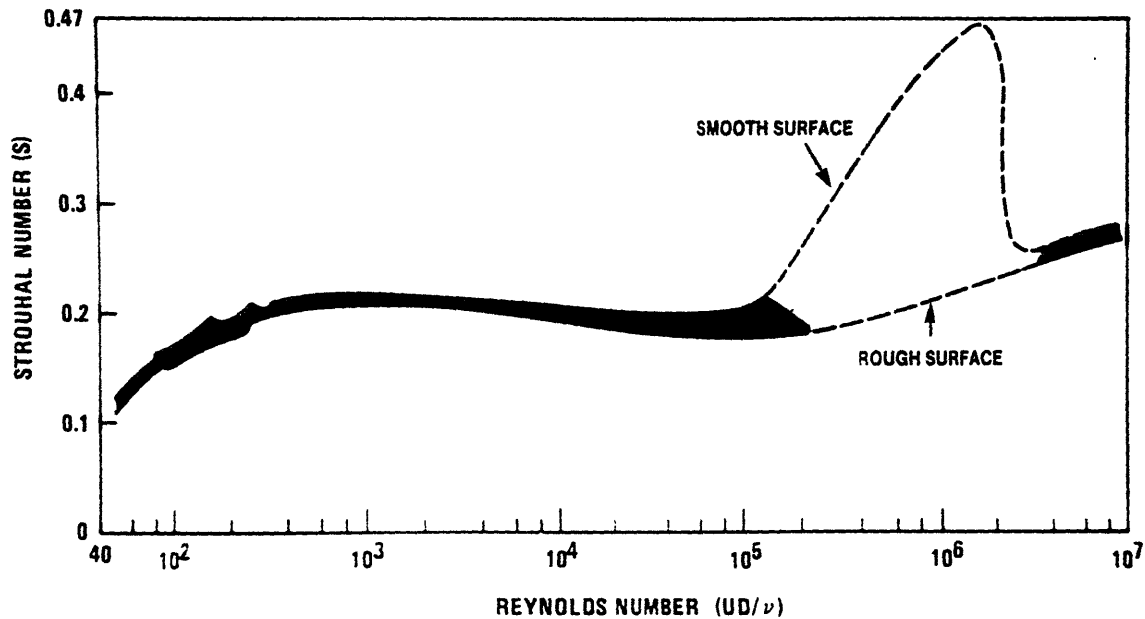


Figure 1-1: The dependence of Strouhal number on Reynolds number relationship for circular cylinders, from Blevins (1990)

and free stream turbulence (in the transitional Reynolds number range), as shown in Figure 1-1.

The alternate shedding of vortices in the near wake causes fluctuating velocities and pressures in the vicinity of the cylinder, which in turn cause oscillating lift and drag forces on the cylinder. The oscillating lift forces are predominant, and if the cylinder is free to move, it responds to the oscillating lift and vibrates in a direction transverse to the ambient flow. These vibrations are referred to as “vortex-induced vibrations”.

As the flow velocity is increased or decreased so that the frequency of the vortex shedding approaches the natural frequency of the cylinder, the vortex shedding frequency suddenly locks onto the structure frequency. The resultant vibrations occur at or nearly at the natural frequency of the structure. The motion of the cylinder is referred to as “locked-in”. Lock-in is characterized by some significant changes in the aeroelastic mechanism driving the structure, most notably a large increase in the correlation length of vortices, and hence a large increase in the correlated force along the structure. However, this mechanism is self-limiting, with maximum amplitudes of the order of 1 to 1.5 diameters.

Lock-in sustains over a range of flow velocities, but the vibration amplitude varies

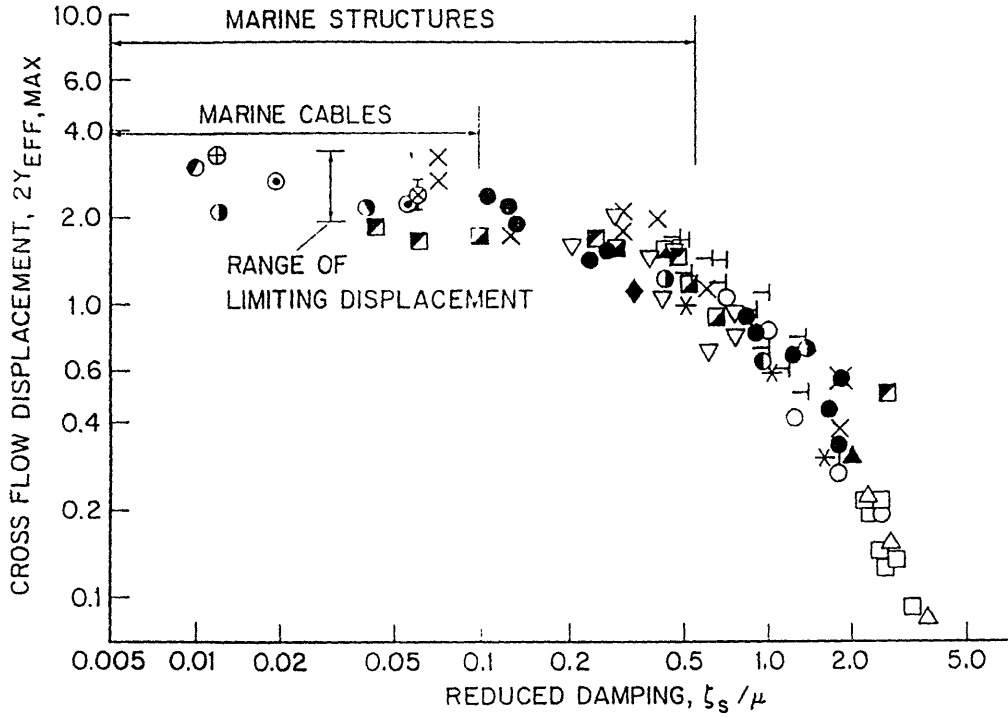


Figure 1-2: The maximum cross-flow displacement range,  $2Y_{EFF,MAX}$  (twice the maximum cross-flow displacement amplitude), as a function of the response parameter  $S_G$ , from Griffin (1985)

with the flow velocity. Figure 1-2, originally presented by Griffin and Ramberg (1982) and subsequently amended [14] to incorporate the latest work, shows the general trend of the maximum cross-flow amplitude of a circular cylindrical section in water as a function of the response parameter ( $S_G$ ).<sup>1</sup> The experimental data depicted encompasses a wide range of single cylinders of various configurations and Reynolds numbers from 300 to  $10^6$ .

The critical velocity ( $V_{crit}$ ) is defined as the velocity at which the maximum vibration amplitude occurs. Using the same terminology, the range of flow velocities at which lock-in occurs is referred to as the critical velocity interval ( $[a, b]$ ). The critical velocity interval is often established based on empirical observations.

<sup>1</sup>The response parameter ( $S_G$ ) is defined as

$$S_G = 2\pi S_f^2 K_s \quad (1.2)$$

where  $K_s = \frac{2m_e \delta}{\rho_f D^2}$  is known as the reduced damping [5], or the stability parameter [10].  $m_e$  is the effective mass per unit length of the structure.  $\delta$  is the logarithmic decrement of structural damping,  $\rho_f$  is the mass density of the fluid.



## 1.2 Vibrations induced by natural winds

Structural members of offshore platforms exposed in natural winds may vibrate as a result of vortex shedding. Since both speed and direction of natural winds vary with time in a random fashion, strong vibrations are seen to occur at random time intervals separated intermittently by weak or no vibrations. Vibrations start to develop when the windspeed stays in the critical velocity interval of the member, and start to decay as soon as the windspeed moves out of the critical velocity interval.

Transient vibrations of structural members induced by natural winds have direct impact on their fatigue lives. Random fluctuations of natural windspeed considerably reduce the frequency of occurrence of the critical wind velocity. Consequently, the amplitudes of transient vibrations are smaller than the amplitudes of steady-state vibrations at the critical velocity. This seems to explain why practical experience [16] has revealed that current VIV prediction methods based on the mean windspeed *over-predict* the response, and, predict structural failures *too* frequently.

While the reduction of fatigue damage (or increase in fatigue life) of wind sensitive structures in natural winds is favorable in design's perspective, vibrations induced by natural winds could still be destructive. Natural wind-induced vibration of structural members has resulted in fatigue damage to offshore platforms during fabrication and transportation, and flarebooms during in-service conditions [16]. It is important to accurately predict vibrations and the resulting fatigue damage caused by natural winds, to avoid potential disasters.

Predicting fatigue damage of a structural member in natural winds is difficult due to aerodynamic and structural reasons. Random fluctuation of the natural wind often does not allow the instantaneous windspeed to stay within the critical velocity interval of the member for very long, allowing lock-in to develop to its fullest extent. On the other hand, even under ideal wind conditions, a structural member needs a finite amount of time to build-up large response. This finite amount of time, known as the rise time, depends on the natural frequency as well as structural damping. Large-amplitude vibrations seem to be possible only when the duration of a visit by the windspeed to the critical velocity interval is longer than the rise time of the structural response.

This thesis is intended to study vibrations of a flexible cylinder induced by natural winds and their impact on the design of fatigue-resistant structural members. Results of wind tunnel experiments on a 1.903 inch diameter flexible cylinder indicate that unsteady fluctuations in the mean windspeed typically prevent vortex-excited vibrations from reaching steady-state amplitudes. A time domain model is proposed, where the transient vibrations of a flexible cylinder induced by unsteady winds are simulated by an equivalent single degree of freedom (SDOF) oscillator. This SDOF oscillator has the properties of the responding resonant mode of the cylinder. The excitation force on the oscillator is modeled as that which would exist at steady-state

vibration levels for each sequential value of windspeed. The resultant transient vibrations of the flexible cylinder are a convolution between the time varying excitation force and the impulse response function of the SDOF oscillator. The predictions by the time domain model agree well with the wind tunnel measurements.

To predict fatigue damage of a flexible cylinder induced by natural winds, a probabilistic model is proposed. After analyzing relevant wind statistics and structural parameters, this probabilistic model identifies three fatigue damage discount factors. The first factor accounts for the fluctuations of the instantaneous windspeed around the mean, and can be determined by the probability density function (PDF) of the instantaneous windspeed and the critical velocity of the structural member ( $V_{crit}$ ). The second factor accounts for the finite rise time of the structural response, and is predicted in terms of the ratio of the expected duration of a visit by the windspeed to the critical velocity interval to the rise time of the structural response. The third factor accounts for the over-estimation of fatigue damage caused by discretizing the PDF of the mean windspeeds into rather broad bins. The real fatigue damage with natural winds is equal to the fatigue damage with steady-state conditions, multiplied by these three discount factors. The probabilistic model is verified against the time domain model using high sampling rate real windspeed data.

Desirable wind statistics which determine the duration of a visit by the windspeed to the critical velocity interval are analyzed from high sampling rate windspeed data measured at a typical maritime site. A design methodology for fatigue resistant structural members excited by random winds is proposed based on the probabilistic model. The design methodology is illustrated through examples.

### 1.3 A preview of the chapters that follow

This thesis has eight chapters. The introductory material presented thus far comprises the first chapter. The contents of each of the following chapters are briefly summarized below.

Chapter Two contains extensive descriptions of wind tunnel experiments on a 1.903 inch diameter carbon-fiber tube. These include a brief review of experimental results by different authors, model descriptions, instrumentation of the wind tunnel, turbulence-generating grids, strain gauges, hot-wire anemometers, data acquisition systems, turbulence measurements, and test results at different turbulence levels.

Chapter Three proposes a time domain algorithm for predicting vortex-induced vibrations of structural members in unsteady winds. Procedures to implement the time domain model are presented and illustrated by an example, where predictions are compared with the wind tunnel measurements. Results using steady-state response functions proposed by different authors are compared. The effect of downsampling

the windspeed sequence and the effect of using the mean windspeed on VIV predictions are illustrated through examples.

Chapter Four proposes a probabilistic model for predicting fatigue damage of structural members induced by random winds. Time scales which determine VIV in natural winds are analyzed. Two fatigue damage discount factors are identified to account for the effects of random fluctuations of the instantaneous windspeed and the finite rise time of structural response. Examples to illustrate the use of the proposed probabilistic model are presented in a designer's perspective. Predictions by both the probabilistic model and the time domain model proposed in Chapter Three are compared using high sampling rate real windspeed data.

Chapter Five studies the effect of discretizing the PDF of the mean windspeeds on fatigue damage estimation. The third fatigue damage discount factor is derived to account for the over-estimation of fatigue damage caused by discretizing the PDF of the mean windspeeds into rather broad bins. This factor is modeled as a function of turbulence level and the ratio of the bin size to the critical velocity for various S-N curves.

Chapter Six studies the characteristics of natural winds. Existing knowledge on natural winds are summarized. A typical maritime wind database which contains 0.85 Hertz sampling frequency windspeed measurements is introduced. Wind statistics which determine the duration of a visit into an interval are derived directly from the raw wind data.

Chapter Seven proposes a design methodology for fatigue resistant structural members excited by natural winds, based on the probabilistic model developed in Chapter Four and Chapter Five. The wind statistics that have been developed based on real maritime wind data are recommended as the input to the probabilistic model. The implementation of the proposed design methodology is presented in terms of formulae and figures.

Chapter Eight presents conclusions of the thesis and recommendations to future work which could improve the performance of the proposed probabilistic model and the design methodology.

# Chapter 2

## Experimental Studies

### 2.1 Review

Current design guidelines for preventing structures from vortex-induced fatigue damage often predict consistently high dynamic response [30] for offshore structural members. One of the reasons of the apparent over-prediction is due to negligence of the free stream turbulence effect. Free stream turbulence is generated in the atmospheric boundary layer when wind blows past the surface of the earth. A number of investigators have studied the effects of free stream turbulence on vortex shedding and dynamic forces on stationary and rigid circular cylinders in wind tunnels over the years. Following is a brief summary of the major findings on this subject:

#### Surry

Surry [36] measured pressure correlations along the span of a rigid circular cylinder at subcritical Reynolds numbers (approximately 40,000). High intensity (greater than 10%) large scale (from 0.36 to 4.4 cylinder diameters) free stream turbulence was generated by biplanar grids. He concluded that turbulence broadens the bandwidth of vortex shedding but does not disrupt the vortex shedding phenomenon.

#### Novak and Tanaka

Novak and Tanaka [25] measured the pressure correlations on both a stationary and a driven cylinder in smooth and turbulent flows (generated by a coarse grid) at subcritical Reynolds numbers. They concluded that turbulence produces significant broadening of the power spectrum of pressure and shortening of the spanwise correlation length. Vibration increases the correlation length dramatically, particularly in smooth flow. A motion with an amplitude of 0.1 diameters increased the correlation length from 3.5 diameters to 43 diameters in smooth flow and from 2.4 diameters to 10.4 diameters in turbulent flow (turbulence intensity 11%).

## Howell and Novak

Howell and Novak [17] measured pressure correlations and response on freely vibrating and driven cylinders in turbulent flows at subcritical Reynolds numbers. Two types of turbulent flows were used: grid generated homogeneous turbulence and turbulent boundary layers. They confirmed the conclusions made by Novak and Tanaka [25]. In addition, they calculated the r.m.s. lift coefficient as a function of amplitude up to 0.1 diameters from the pressure measurements in both smooth and turbulent flows. A motion of 0.075 diameters resulted in an r.m.s. lift coefficient of 0.42 in smooth flow and 0.15 in turbulent flows (turbulence intensity 11%).

## Cheung and Melbourne

Cheung and Melbourne [8] obtained the lift force coefficient, drag coefficient and Strouhal number from pressure measurements on stationary cylinders for different levels of turbulence intensity (up to 9.1%) at critical and supercritical Reynolds numbers up to  $10^6$ . Their data showed that mean drag force, fluctuating drag and lift force decrease at higher turbulence at subcritical Reynolds and increase with turbulence in the supercritical regime. All of the above results were to provide quantitative understanding of free stream turbulence effects on the vortex shedding phenomenon with rigid cylinders. The results cannot be unduly extended to the case of flexible cylinders without further justification.

Our experiment was intended to investigate the effect of free stream turbulence on dynamic response of a flexible circular cylinder due to wind-induced vortex shedding at subcritical Reynolds numbers. The cylinder was made of carbon fiber, and had a diameter of 1.903 inches with pinned-pinned supports. The Reynolds number at the critical velocity was 26,000. Bi-planar grids were used to produce homogeneous turbulence fields with longitudinal scales ranging from 1.8 to 6.2 inches (or 0.95 to 3.25 diameters) and with longitudinal intensities up to 9.9%.

Measurements of steady state vibration magnitudes at different wind speeds indicated that turbulence intensity up to 9.9% did not drastically reduce the peak vibration magnitude at critical velocity, but reduce the hysteresis effect as turbulence intensity increases. Helical strakes that were wrapped around the cylinder were very effective in suppressing VIV response. Low-frequency variation in mean wind speed typically prevented the VIV response from reaching steady state, thus reducing its fatigue damage.

In the following sections, model descriptions, instrumentation, turbulence measurements, test results and a summary are presented, respectively.

## 2.2 Model descriptions

The model was mounted vertically in the test section of the tunnel. One end of the model was attached at the base to the load measuring balance while the other end was attached at the top to an existing mounting rail through mounting plates.

The flexible model was designed to have pinned-pinned supports to achieve a mode shape more representative of the real structural members. The pinned boundary conditions were achieved using carbon fiber membrane flexures in the latest tests. These flexures allowed for thermal expansion of the wind tunnel test section as well as cylinder vibration in both “in-line” and “cross-flow” directions while contributing very little to the model’s structural damping.

The model was made of carbon fiber because of its ability to withstand high cyclic stresses, its low material damping, and the ability to tolerate high tunnel temperatures up to  $160^{\circ}F$ .

The material and sectional properties of the cylinder were:

- Total length ( $L$ ) = 2.0955 [m] or 82.5 [in]
- Outside diameter ( $D$ ) = 0.0483 [m] or 1.903 [in]
- Wall thickness ( $t$ ) = 0.0023 [m] or 0.089 [in]
- Mass density ( $\rho_m$ ) = 1597.674 [kg·m<sup>-3</sup>] or 3.100 [slug·ft<sup>-3</sup>]
- Natural frequency (first mode  $f_1$ ) = 32.375 [s<sup>-1</sup>]
- Structural damping ratio in air ( $\zeta$ ) = 0.12% to 0.16%
- Young’s modulus ( $E$ ) =  $7.7 \times 10^6$  [psi] or  $5.3 \times 10^4$  [MPa].

Figure 2-1 shows the configuration of the model as described. More detailed descriptions of the model as well as its design evolutions can be found in Rudge et. al [30], [31] and Nicholls [26].

## 2.3 Instrumentation

Instrumentations include wind tunnel, turbulence-generating grids, strain gauges, hot wire anemometers and data acquisition. Each is described in details as follows.

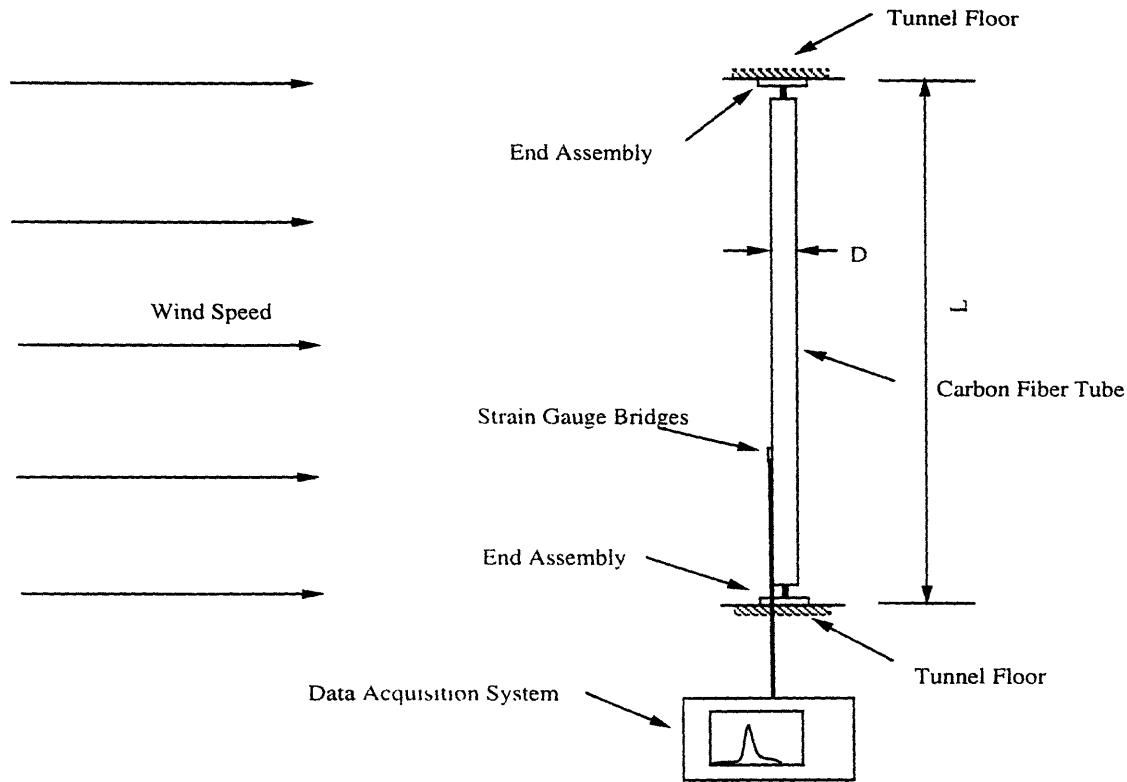


Figure 2-1: Configuration of the model

### 2.3.1 Wind tunnel

The testing program was undertaken in M.I.T.'s Wright Brothers Wind Tunnel. The tunnel is of the pressurized, closed circuit type with an elliptical test section 10 feet in width, 7.5 feet in height and 15 feet in length. A variable pitch propeller is driven by a motor, and can be rotated at different rpm, which gives the tunnel an airspeed capability of up to 140 miles per hour at atmospheric pressure. The model was located at the downstream end of the tunnel test section in order to maximize the allowable distance between the model and the turbulence-generating grid.

### 2.3.2 Turbulence-generating grids

Turbulence with the desired properties (turbulence intensity and length scales) can be generated by placing grids in the air flow. Grids were constructed as square biplanar lattices of wooden boards or bars. This biplanar screen, consisting of bars, served as a two dimensional array of jets to mix up the flow field as the flow passed through the screen, and creating turbulence.

The turbulence characteristics behind grids has been studied extensively in the past. It has been found that immediately behind the grid, the flow is highly inhomogeneous with a strong memory of the particular grid geometry. The flow becomes more

homogeneous and the turbulence intensity decreases with downstream distance. Typically the flow approaches homogeneity between about five and ten mesh lengths, and approaches isotropy after about twenty mesh lengths [35]. While turbulence intensity decreases rapidly downstream, turbulence integral length scales increase slowly due to the dissipation of high frequency turbulence components. It has also been found that the turbulence intensity obeys the following power law beyond twenty mesh lengths, when the turbulence becomes isotropic [4].

$$T_u = \frac{u'}{\bar{U}} = 1.12\left(\frac{x}{b}\right)^{-5/7} \quad (2.1)$$

where  $T_u$  is the turbulence intensity,  $\bar{U}$  is the mean velocity in longitudinal direction.  $u'$  is the root mean squared (r.m.s.) value of fluctuating velocity in longitudinal direction.  $x$  is the distance between the grid and the measuring spot.  $b$  is the bar width of the grid.

### 2.3.3 Strain gauges

Strain gauges were used to measure deflections of the model. Strain gauge bridges were mounted, on the cross-flow and in-line axes, at approximately the lower quarter point of the model. This ensured that both first and second mode response could be identified.

Static calibrations of the strain gauges were made after the model was installed in the wind tunnel [26]. The final calibration constant between the deflection of the model at its mid-span in diameters and the measured strain gauge output in volts was corrected to account for the sinusoidal mode shape [30].

### 2.3.4 Hot wire anemometers

Hot wire anemometers were used to measure the streamwise fluctuating velocities in the free stream and in the wake of the model while it was vibrating. The hot wire anemometers employed were single wire U-probes and were operated in the constant temperature mode.

In measuring the free stream turbulence, two DISA hot wire U-probes, both installed on probe supports, were used to measure the longitudinal component of velocity fluctuations (perpendicular to the test tube) at the model plane. The two wire and support assemblies were placed perpendicular to the model plane, parallel to the centerline of the wind tunnel. Both U-probes were connected to the data acquisition system through cables on the probe supports. One of the U-probes was placed stationary at about a quarter height away from the ceiling of the wind tunnel; while the other U-probe was placed originally at slightly lower than the stationary one,



and could be moved vertically downward by a traversing mechanism. The traversing mechanism was controlled by a motor, and was capable of moving the probe vertically, thus covering about one half the height of the test section in the center of the tunnel. Figure 2-2 shows the set-up of the hot wires.

In measuring the wake coherence, a pair of DISA hot wire U-probes were placed in the wake of the tube, each 1 diameter off the centerline of the tube and 3 diameters behind the axis of the tube. One probe was held stationary, while the other probe was capable of moving downward parallel to the axis of the tube to a maximum distance of half the length of the tube from the stationary one, through a motor controlled traversing mechanism. This traversal of the hot wires allowed us to examine the lateral coherence between the velocity fluctuations in the wake and thus the coherence of vortex shedding in the spanwise direction of the flexible model.

In calibrating each hot wire, the wind velocity was increased incrementally. At each wind velocity, both the wind speed reading from a pitot probe and the voltage reading from the hot wire circuit were recorded. After about twenty such wind velocity increments, the collected data points were used to fit a fourth order polynomial. This polynomial is then the calibration curve of this particular hot wire, which determines the corresponding wind speed from the voltage reading of this hot wire. Figure 2-3 shows a typical hot wire calibration curve. See Nicholls [26] for the details of the hot wire calibrations.

### 2.3.5 Data acquisition

Data acquisition was handled by a Tektronix 2630 Fourier Analyzer, which was controlled by a portable 386 Personal Computer. This four channel device first passes the input signal through a low-pass anti-aliasing filter, with a flat bandpass ranging from 0 to 20 kHz. This filtered signal is then digitally sampled at 51.2 kHz, using a sampling factor of 2.56. Lower bandwidths were achieved by digital filtering and decimation. A data file typically contained data from the four channels, and was stored on the hard disk of the PC.

Typical sampling parameters were:

- frequency bandwidth, 100 or 200 Hz.
- frame size, 1024, 2048 or 4096.
- number of averages, 10, 16 or 40.

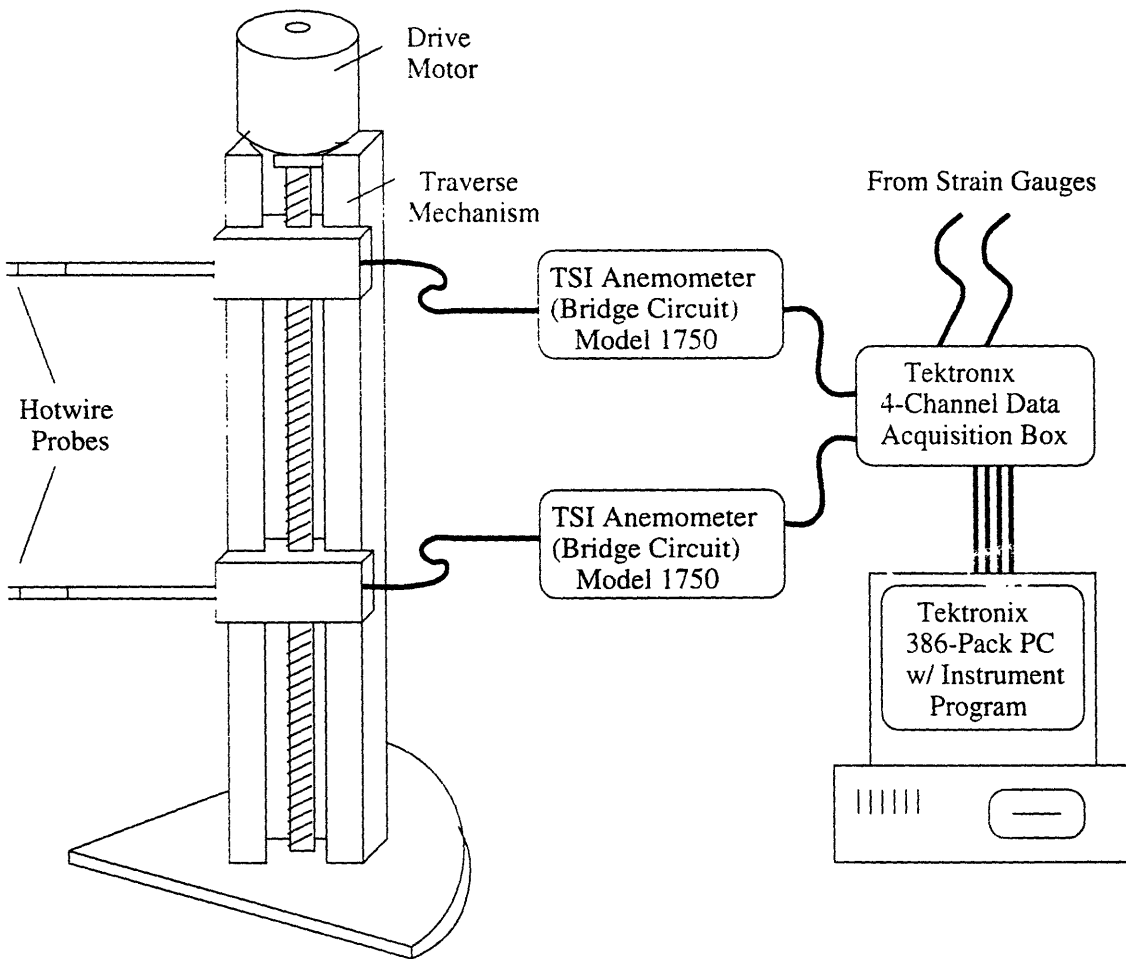


Figure 2-2: Hot wire set-up. from Nicholls (1993)

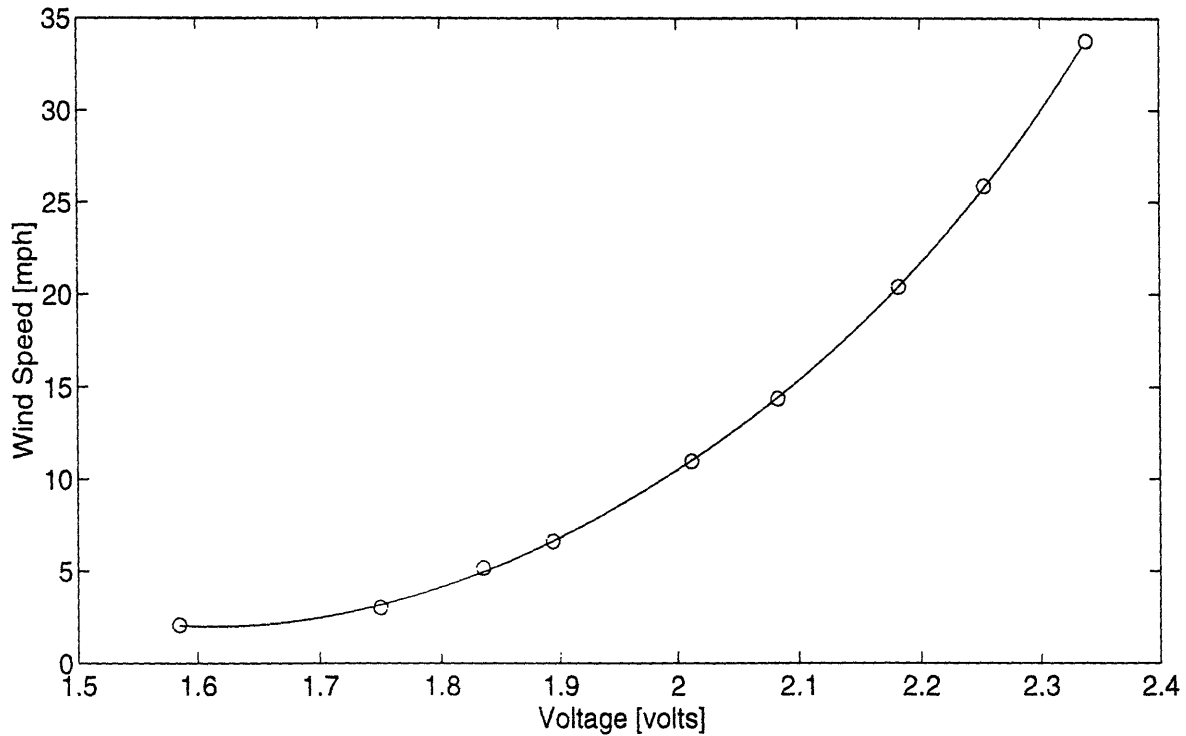


Figure 2-3: Hot wire calibration curve

In measuring the free stream turbulence, the following information were contained in a single data file:

- time traces of the last data frame taken, for channels 1 and 2, the inputs from the two hot wire U-probes.
- averaged power spectral density functions and auto-correlation functions for channels 1 and 2, computed by the Instrument Program built in the Fourier Analyzer.
- cross-correlation functions, cross spectra and coherence functions between channels 1 and 2, computed by the Instrument Program.

In measuring the response of the tube and the wake coherence, the following information were contained in a single data file:

- time traces of the last data frame taken, for channels 1 and 2, the inputs from the in-line and the cross-flow strain gauges.

- averaged power spectral density functions for channels 1 and 2. computed by the Instrument Program.
- time traces of the last data frame taken, for channels 3 and 4. the inputs from the two hot wire U-Probes deployed in the wake of the model.
- averaged power spectral density functions for channels 3 and 4. computed by the Instrument Program.
- wake coherence functions between channel 3 and channel 4. computed by the Instrument Program.

## 2.4 Turbulence measurements

In our tests, turbulence with different intensities and length scales was generated in the wind tunnel through installation of one of the two bi-planar grids upstream of the model. These two grids were originally designed and used by Lazar and Durgin [20], to investigate the distortion limitations on the frequency response of stagnation pressure taps in grid-generated isotropic turbulence. The two grids are geometrically similar, thus having the same solidity ratio <sup>1</sup>, but different sizes. Geometries of the grids are defined by two parameters,  $b$  and  $M$ .  $b$  is the bar width, and  $M$  is the mesh size, which is the spacing between the centers of successive bars. The values of  $b$  and  $M$  of the two grids are defined in Table 2.1. Geometries of the two grids are shown in Figure 2-4.

Grid Number	Bar Width ( $b$ ) (inches)	Mesh Size ( $M$ ) (inches)	Solidity Ratio
A	0.75	4.5	0.306
B	3.0	18.0	0.306

Table 2.1: Grid geometries

Four flow fields were measured: two cases (case one and case two) with grid A, one case (case three) with grid B and one case (case zero) with no grid. In case one and case two, grid A is placed at 30 and 45 inches respectively, upstream of the test plane where the test tube was located. In case three, grid B was placed at 15 feet (10 mesh sizes) upstream of the model plane. For each case, turbulence characteristics at the model, including power spectral density functions, turbulence length scales and intensities, were measured.

---

<sup>1</sup>ratio of the obstructed area of screen to the total area of the screen.

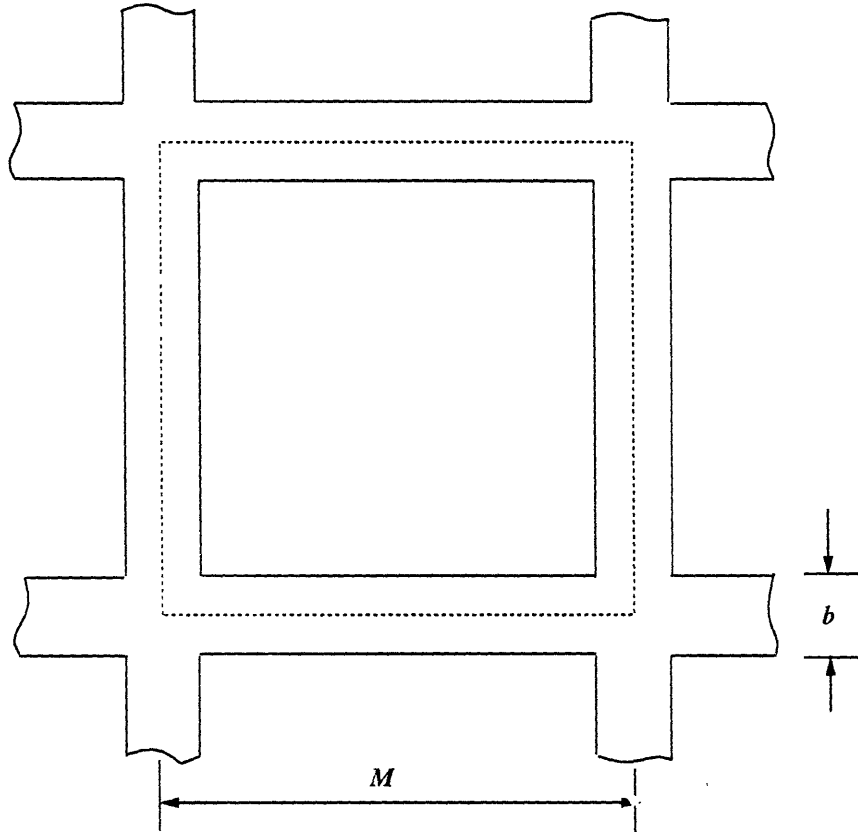


Figure 2-4: Geometries of grids

### 2.4.1 Power spectral density functions of longitudinal turbulence components

For each case, the mean wind speed was set at the critical velocity of the model where the maximum steady state vibration amplitude was observed. Time histories of fluctuating velocity in the longitudinal direction were recorded in the plane of the model at four (case zero), nine (case one), and eleven (case two and case three) lateral positions respectively. Averaged power spectral density functions at each lateral position were computed by the Instrument Program. The spectral data was then presented in the form  $S_{uu}/\sigma_u^2$ , where  $S_{uu}(f)$  is the calculated power spectral density function at frequency  $f$ , and  $\sigma_u^2$  is the variance of the spectrum.

These normalized power spectral density functions were averaged across lateral positions in the model plane to form a mean normalized power spectral density function for each case. For case zero, where no grids were present, the mean normalized spectral function was merely a noise spectrum. For case one, case two and case three, the mean normalized spectral functions were found to fit reasonably well by the von-Karman spectrum model [35], which is given by:

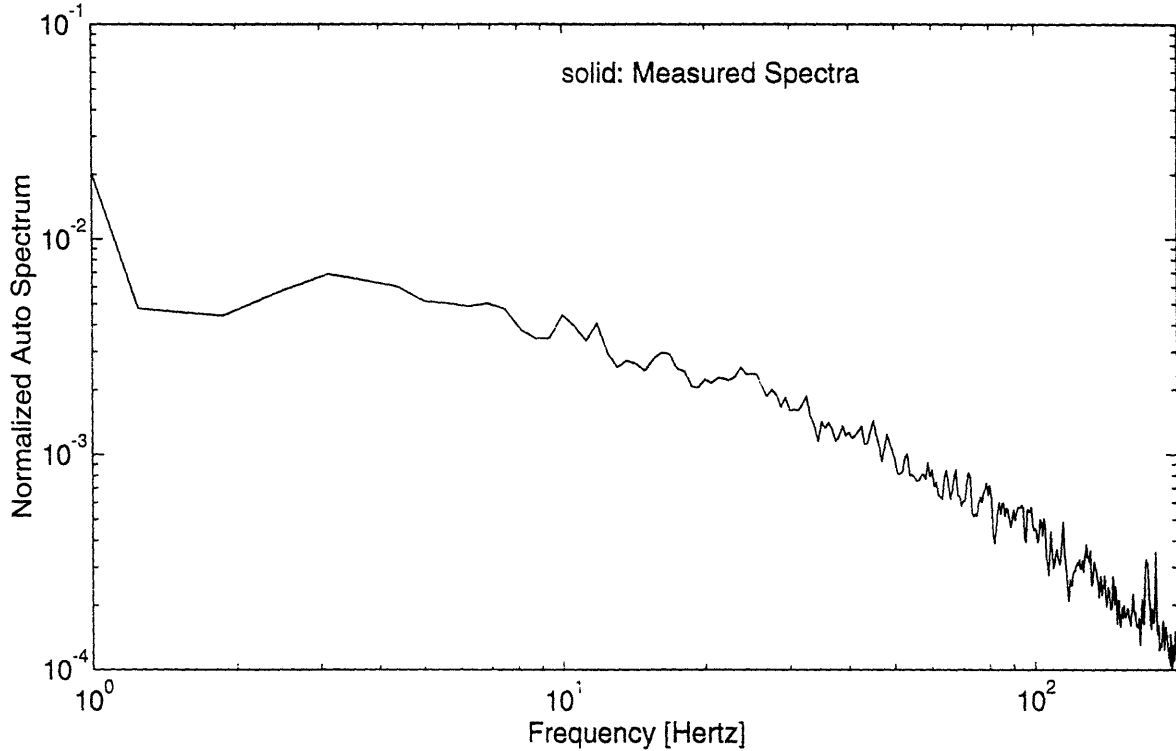


Figure 2-5: Power spectral density function of longitudinal turbulence, case zero (empty tunnel)

$$\frac{S_{uu}(f)}{\sigma_u^2} = \frac{4L_u}{\bar{U}} \frac{1}{\left[1 + \left(1.339 \frac{2\pi f L_u}{\bar{U}}\right)^2\right]^{5/6}} \quad (2.2)$$

where  $L_u$  [m] is the turbulence length scale in longitudinal direction.  $\bar{U}$  is the mean velocity in longitudinal direction.  $f$  [s<sup>-1</sup>] is the frequency.

The mean normalized power spectral density functions for each of the four cases are shown in figures 2-5, 2-6, 2-7 and 2-8 respectively.

## 2.4.2 Turbulence length scales

For case one, case two and case three, the longitudinal turbulence length scale was determined as the value which enabled the Von-Karman spectrum model to best fit the calculated mean power spectral density function. For case zero (empty tunnel), the measured noise spectrum did not fit well to Von-Karman spectrum model for any reasonable value of longitudinal turbulence length scales. Therefore, the longitudinal turbulence length scale was not calculated for that case. Table 2.2 shows a summary of turbulence length scales in longitudinal direction for all cases 1, 2 and 3. As expected, turbulence length scales grow as distance increases due to the dissipation of

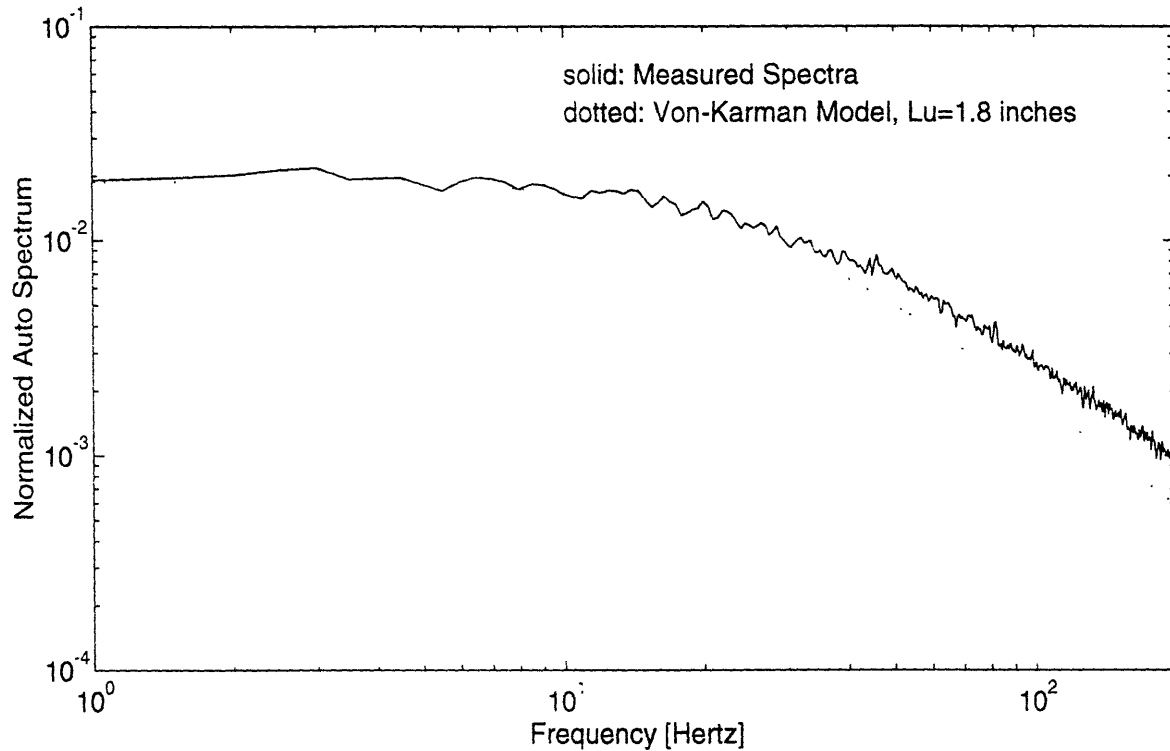


Figure 2-6: Power spectral density function of longitudinal turbulence, case one

high frequency turbulence components.

### 2.4.3 Turbulence intensity

Turbulence intensity is defined as the ratio of the r.m.s. velocity fluctuation to the mean velocity.

$$T_u = \frac{u'}{\bar{U}} \quad (2.3)$$

where  $T_u$  is the turbulence intensity,  $\bar{U}$  [ $\text{m}\cdot\text{s}^{-1}$ ] is the mean velocity in longitudinal direction.  $u'$  is the r.m.s. fluctuating velocity in longitudinal direction. Due to limited test section length in the wind tunnel, the turbulence was not truly homogeneous at the test plane. Subsequently, turbulence intensity varied along the axis of the model. Turbulence intensity at the model was estimated as the average of local turbulence intensities that were measured at different lateral stations across the model plane.

$$\bar{T}_u = \frac{\sum_{i=1}^{n_s} (T_u)_i}{n_s} \quad (2.4)$$

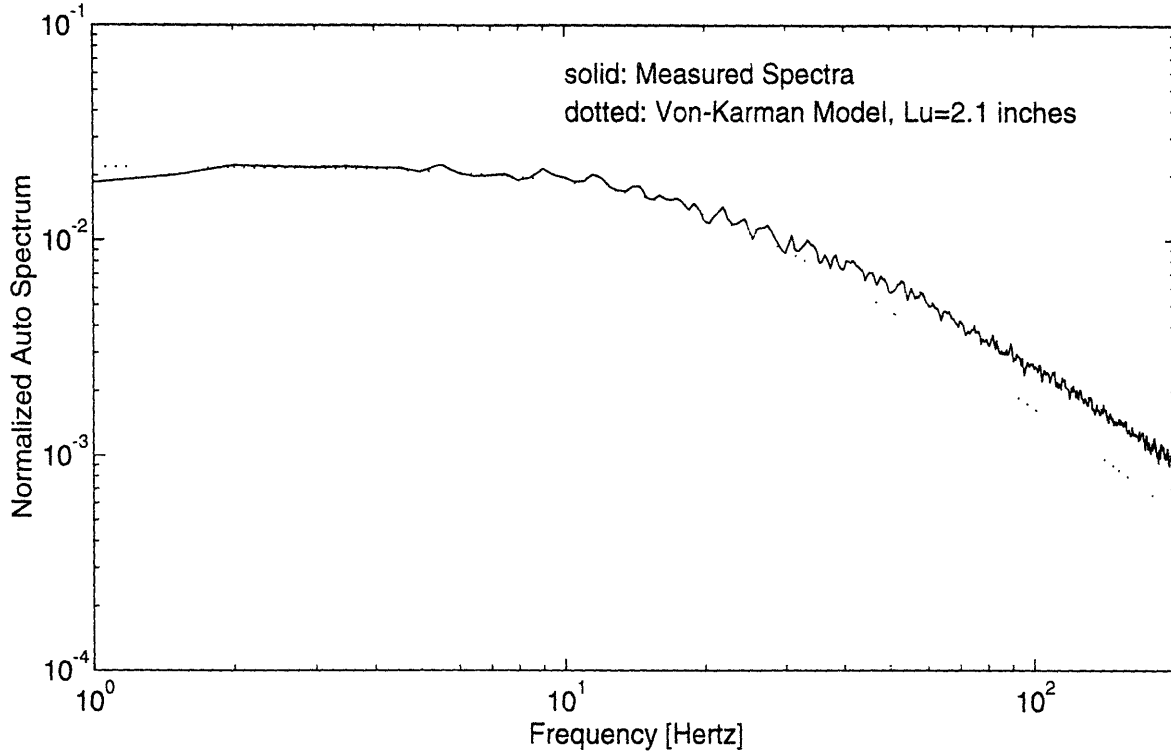


Figure 2-7: Power spectral density function of longitudinal turbulence, case two

where  $\bar{T}_u$  is the mean turbulence intensity along the axis of the model.  $n_s$  is the number of stations where turbulence was measured along the axis of the model,  $n_s$  varies from 4 to 11, depending on each case.  $(T_u)_i$  is the local turbulence intensity at station  $i$  along the axis of the model, and can be calculated by Equation 2.3.

Turbulence inhomogeneity at the model for each case can be evaluated by  $\frac{\max\|(T_u)_i - \bar{T}_u\|}{\bar{T}_u}$ , the maximum relative percentage deviation of local turbulence intensity compared to its spatially-averaged value. Both the mean turbulence intensities and the percent turbulence inhomogeneity for each case are summarized in Table 2.2.

Case Number	Grid Number	$x$ (inches)	$\bar{T}_u$	$\frac{\max\ (T_u)_i - \bar{T}_u\ }{\bar{T}_u}$	$L_u$ (inches)
0			1.3%	3%	
1	A	30	9.9%	8%	1.8
2	A	45	7.5%	12%	2.1
3	B	180	7.7%	4%	6.2

Table 2.2: Summary of turbulence characteristics at the model plane for cases 0, 1, 2 and 3.



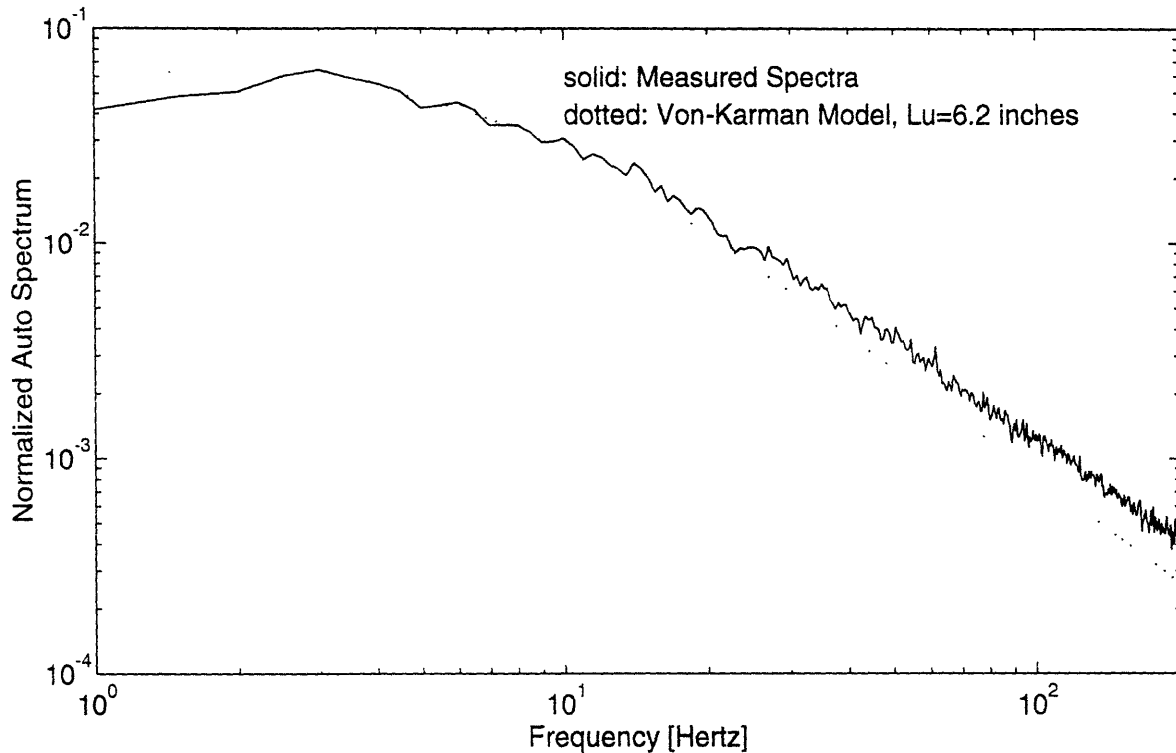


Figure 2-8: Power spectral density function of longitudinal turbulence, case three

## 2.5 Model response at different turbulence levels

13 different tests were conducted on the model in the wind tunnel during the spring of 1993. For each of the 13 tests, the test tube was located at about 15 feet from the entrance of the tunnel test section. A pair of strain gauges were installed on the surface of the tube, to infer instantaneous displacements at the mid-span of the tube.

Each of the 13 tests belongs to one of the four turbulence cases that were defined earlier. In addition, each test is either a steady state test or a transient test. In the steady state test, the wind speed was held at a constant value, and the corresponding steady state vibration amplitude of the model was recorded. In the transient test, the wind speed changed continuously in time, and the corresponding transient displacement response was measured.

Each of the steady state tests was conducted by increasing the mean velocity in the wind tunnel monotonically, passing through the range of speeds at which the tube responded primarily at its first mode: followed by decreasing the mean velocity monotonically back to its starting value. At each speed, the instantaneous strain gauge output at both in-flow and cross-flow directions were recorded, so that the instantaneous motion of the tube at the mid-span could be inferred: the instantaneous velocity fluctuations in the longitudinal direction in the wake at different locations along the tube were recorded through the hot wire outputs: power spectral density

functions of the tube transient motion and of the velocity fluctuations in longitudinal direction in the wake, as well as coherence functions between the two hot wires were also calculated.

Case Number	Test Number	Test Type	$\zeta_s$ (% Critical)	$K_s$	$(\eta_{rms})_{max}$ (% Diameter)	$V_r$ at $(\eta_{rms})_{rms}$
Case 0	Test 28	Steady	0.12	2.9	30	6.7
	Test 35 <sup>+</sup>	Steady	0.15	3.6	15	6.3
	Test 36 <sup>-</sup>	Steady	0.15	3.6	14	6.2
	Test 14*	Steady	0.24	5.8	31	6.4
Case 1	Test 29	Steady	0.13	3.2	28	6.2
	Test 30	Transient	0.14	3.4	31	6.0
	Test 31	Transient	0.13	3.2	34	6.2
Case 2	Test 32	Steady	0.13	3.2	24	6.2
	Test 33	Transient	0.15	3.6	30	6.4
	Test 34	Transient	0.15	3.6	30	6.3
Case 3	Test 37	Steady	0.14	3.4	25	6.7
	Test 38	Steady	0.16	3.9	19	6.4
	Test 39	Transient	0.13	3.2	30	6.4
	Test 40	Transient	0.13	3.2	30	6.6

*Note:* + denotes that the surface of the model was wrapped helically by a wire with a diameter of  $\frac{5}{32}$  inches. The helical spacing is 16 inches per wrap.  
 - denotes that the surface of the model was wrapped helically by a wire with a diameter of  $\frac{1}{4}$  inches. The helical spacing is 16 inches per wrap.  
 \* denotes that the test was conducted in the summer of 1992.

Table 2.3: A summary of measured structural damping ratios,  $K_s$  values, measured peak cross-flow r.m.s. vibration amplitudes and their corresponding reduced velocity values from different tests.

For each of the transient tests, the wind speed was varied continuously through manually-controlled adjustments of the pitch angle of the tunnel fan. The wind speed was sampled at 512 Hertz, and was recorded continuously for 246 seconds by the Spectral Analyzer. The corresponding in-line and cross-flow transient motion was also recorded simultaneously by the Spectral Analyzer. The total recorded length of both wind speed and transient motion was 246 seconds.

The results of the structural damping measurements, taken prior to, or on completion of, each test is summarized in Table 2.3. The peak vibration magnitude and the corresponding reduced velocity value for each test are also listed in the same table. Structural damping ratios were found by the log-decrement method of square root of the total response energy, total response energy being found by taking the sum of the squares of the in-line and the cross-flow response decay time histories.

## 2.5.1 Results of steady state tests

Steady state tests were conducted for each of the four turbulence cases. The results of steady state tests at different turbulence levels are presented in the following forms:

- r.m.s. vibration amplitudes *vs.* wind speeds.
- averaged power spectral density functions of vibration amplitudes at different wind speeds.
- averaged power spectral density functions of wake velocity in the longitudinal direction at different wind speeds.
- averaged wake coherence functions at peak vibration magnitudes.
- The effects of helical strakes on suppressing steady state vibration magnitudes.

### R.M.S. vibration amplitudes *vs.* wind speeds

Figures 2-9, 2-10, 2-11 and 2-12 show the steady state r.m.s. vibration amplitudes at the mid-span of the test tube as functions of windspeeds expressed in terms of reduced velocities for case 0, case 1, case 2 and case 3 respectively. Each case consists of a forward pass and a backward pass. The forward pass starts at a small wind speed where the tube did not respond. The wind speed increased monotonically, and the steady state responses were measured at progressively higher wind speeds, until at a wind speed where no considerable response of the model was observed. In the backward pass, the wind speed decreased from the last wind speed recorded in the forward pass, and the steady state responses were measured at lower wind speeds.

Test 28 (case 0, empty tunnel) was intended to test the performance of the flexure end assembly [26] that was designed for the test tube in the summer of 1992. Figure 2-9 shows the complete forward pass of Test 28, and the complete forward and backward passes of Test 14 that were conducted in the summer of 1992, shortly after the end assembly was designed. The peak magnitude measurements from the two tests are remarkably similar, thus demonstrating the reliability of the newly designed end assembly. Test 28 was also intended to be the benchmark results to compare against cases with grid turbulence. The peak measured r.m.s. vibration amplitude was about 30% of a diameter.

In Test 29 and Test 32, grid A was placed at 30 and 45 inches upstream of the model plane respectively. Figures 2-10 and 2-11 show the response measurements for

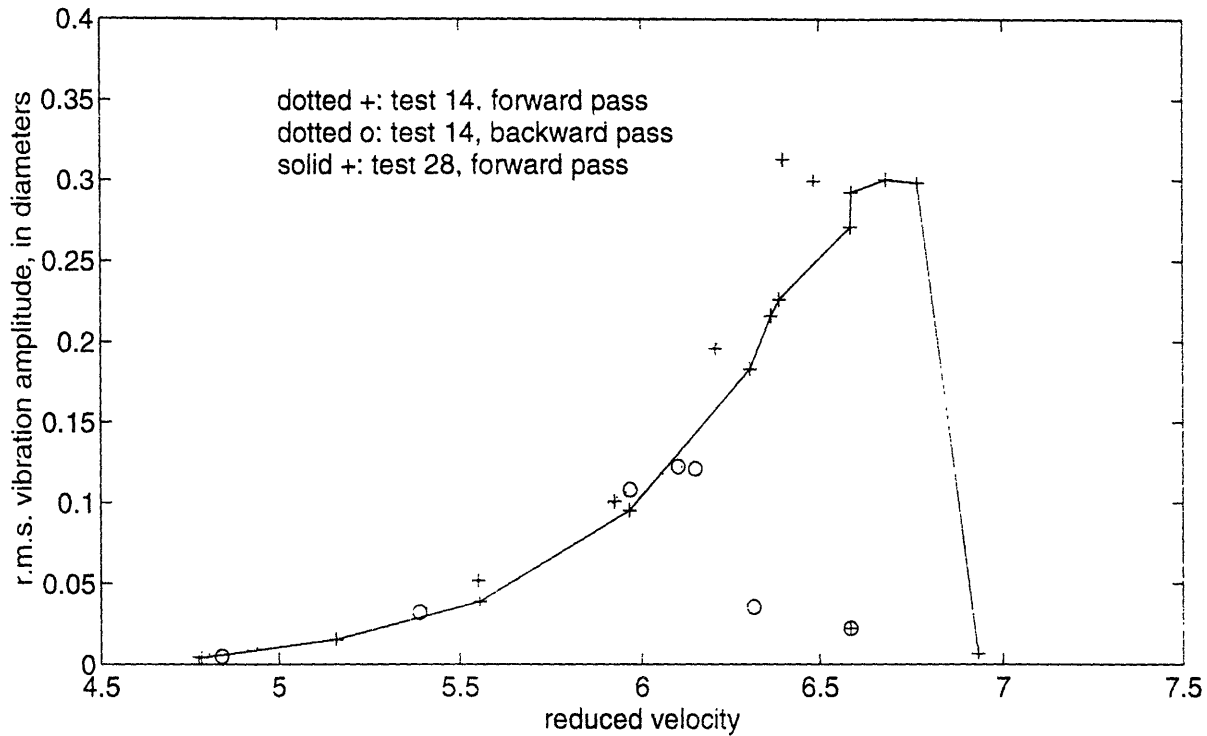


Figure 2-9: Steady state r.m.s. vibration amplitude at mid-span of the test tube as a function of reduced velocity, case 0 (empty tunnel)

Test 29 and Test 32. In the presence of grid turbulence, the peak magnitudes of the model were 0.28 diameters (Test 29, 9.9% turbulence intensity) and 0.26 diameters (Test 32, 7.5% turbulence intensity), as compared with 0.3 diameters (Test 28, no grid). Although the peak response magnitude was achieved in the forward pass for both Test 29 and Test 32, as it was for Test 28, the difference in peak magnitudes between the forward path and backward path was not as apparent in both Test 29 and 30 as it was in Test 28. The degree of hysteresis effect is reduced in the presence of grid turbulence.

In Test 37 and Test 38, grid B was placed 15 feet upstream of the test plane. Figure 2-12 shows the complete forward and backward passes for both tests. This Figure seems to tell a similar story as the previous two figures did: the peak response magnitude was 0.25 diameters for Test 37 and 0.19 diameters for Test 38<sup>2</sup>; Hysteresis effect was apparent in the response *vs.* windspeed for both tests, especially for Test 37, but not as severe as that for Test 28, where no grid was present.

<sup>2</sup>Sizable drop of peak vibration magnitude for Test 38, where the test conditions were the same as those for Test 37, was caused by a slight increase of structural damping from 0.14% to 0.16%.

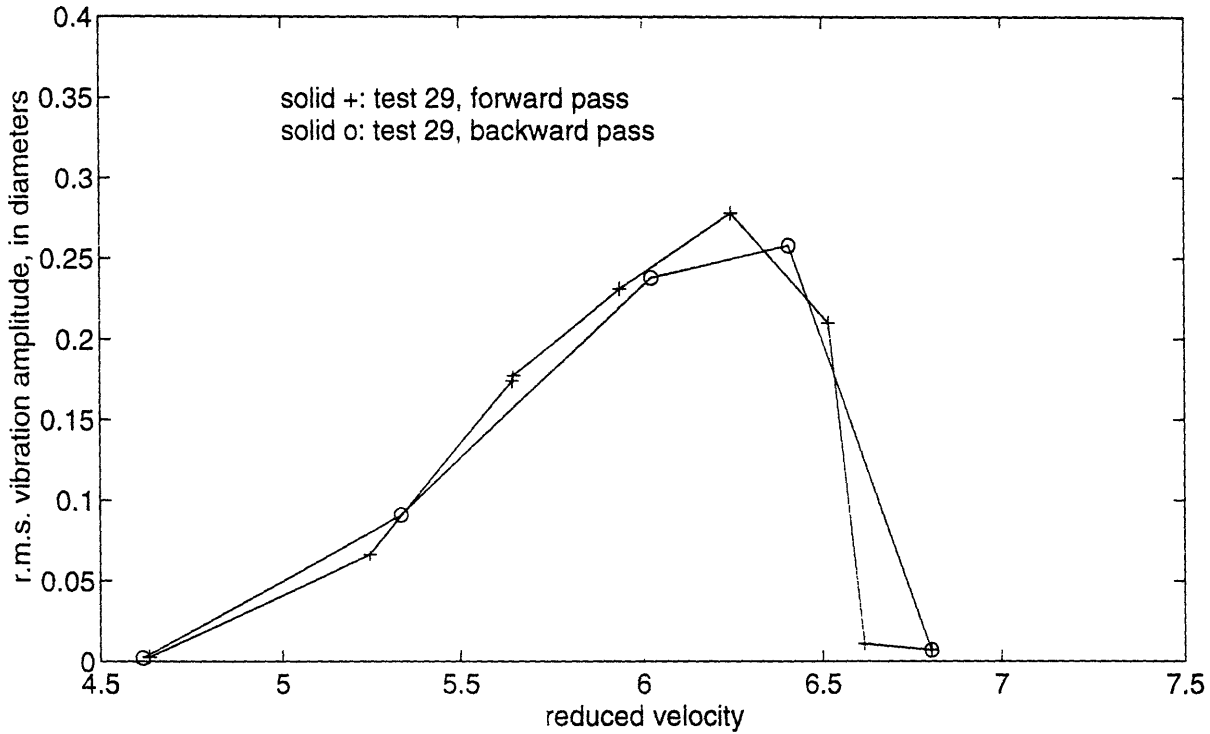


Figure 2-10: Steady state r.m.s. vibration amplitude at mid-span of the test tube as a function of reduced velocity, case 1 (turbulence intensity 9.9%)

**Power spectral density functions of vibration amplitudes at different wind-speeds**

Figures 2-13, 2-14, 2-15 and 2-16 show the power spectral density functions of the cross-flow vibration amplitudes at three different reduced velocities for Test 28 (case 0, empty tunnel), Test 29 (case 1, turbulence intensity 9.9%), Test 32 (case 2, turbulence intensity 7.5%) and Test 37 (case 3, turbulence intensity 7.7%) respectively. The values of the three different reduced velocities for each case were chosen as less than the critical reduced velocity, close to the critical reduced velocity and greater than the critical reduced velocity.

Figure 2-13 shows the power spectral density functions of the cross-flow vibration response for Test 28 (case zero, empty tunnel) at the reduced velocities of 4.8, 6.7 and 6.9 respectively. In this test, there was no grid upstream of the test plane. For each of the three response spectra at different reduced velocities, major peaks at about 32 Hertz and 130 Hertz which correspond to the first mode and the second mode of transverse vibrations of the model respectively, are clearly visible, but the magnitude and the bandwidth of the peaks are drastically different. At the reduced velocity of 4.8, the corresponding wind speed is smaller than the critical velocity of the model. Two adjacent spectrum peaks are visible near 32 Hertz. The first peak is located at 28.375 Hertz, and it is the dominant vortex-shedding frequency at the

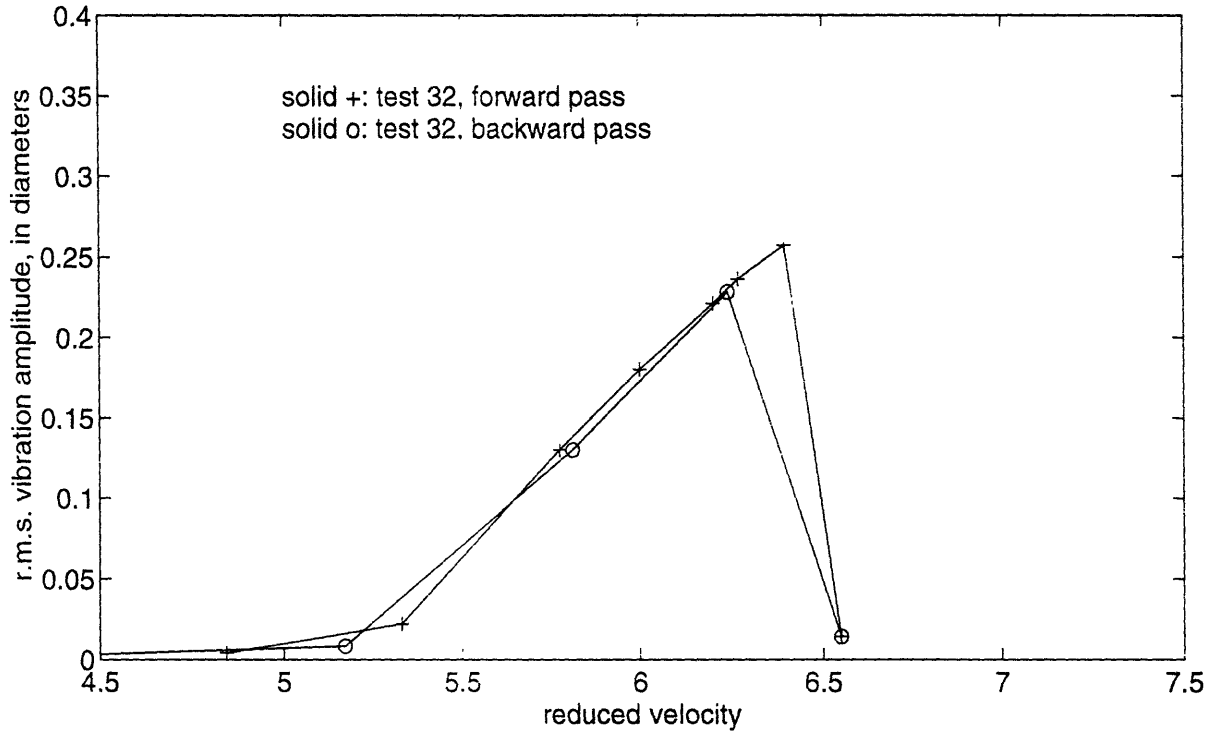


Figure 2-11: Steady state r.m.s. vibration amplitude at mid-span of the test tube as a function of reduced velocity, case 2 (turbulence intensity 7.5%)

location of strain gauges, with the Strouhal number of 0.18. The second is located at 32.375 Hertz, and it is the first mode natural frequency of the model. Vibrations at the second mode and at higher harmonics of the vortex-shedding frequency are also present, but never as dominant as vibrations in the neighborhood of the first mode and the vortex-shedding frequency. This is a typical non-lockin response spectrum.

As the wind speed increased to the value where the corresponding reduced velocity was 6.7, the response spectrum tells a different story. In stead of dual peaks near the natural frequency of the model, there is only one spectrum peak at 32.375 Hertz. Compared to the corresponding peak in Figure 2-13(a), the single peak in (b) at 32.375 Hertz is 4 orders of magnitude greater, and the band-width is much narrower. The peak at the 129.375 Hertz resonance is also visible, but about 4 orders of magnitude smaller than the peak at the first mode. This is a typical lock-in response spectrum, when the vortex-shedding is controlled by single-mode dominated vibrations.

As the wind speed further advanced to a value where the corresponding reduced velocity was 6.9, the response spectrum was very similar to that at the reduced velocity of 4.8, with the exception that in this case, the vortex-shedding frequency is located at 41 Hertz. It shows that as the wind speed further increases, the synchro-

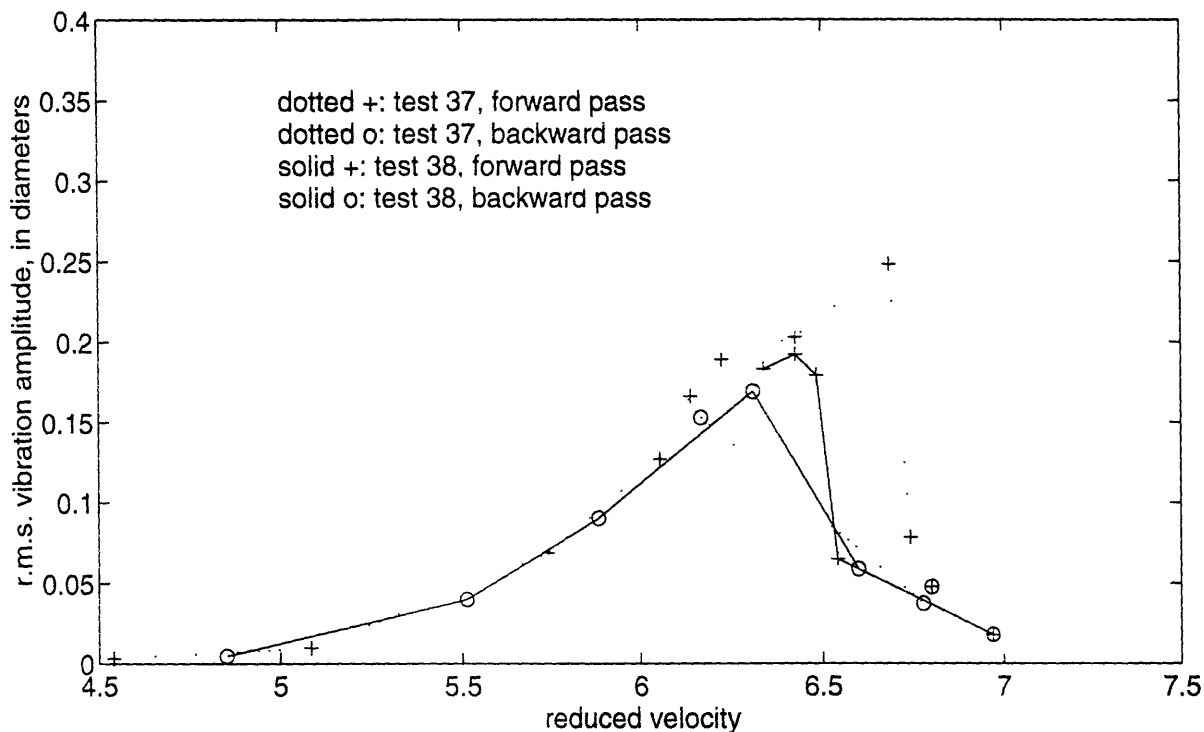


Figure 2-12: Steady state r.m.s. vibration amplitude at mid-span of the test tube as a function of reduced velocity, case 3 (turbulence intensity 7.7%)

nization between the vortex-shedding and the response of the model broke down.

Figure 2-14 shows the power spectral density function of the cross-flow vibration response for Test 29 (case 1, turbulence intensity 9.9%) at the reduced velocities of 4.6, 6.2 and 6.8 respectively. In this test, Grid A was installed at 30 inches upstream of the model plane, which in effect generated 9.9% turbulence at the model. The response spectra before lock-in, at lock-in and after lock-in were not noticeably different from those in Figure 2-13, thus suggesting that free-stream turbulence up to about 10% does not have appreciable effect on the VIV response spectrum. Figures 2-15 and 2-16 reveal the same conclusions for the results of Test 32 (case 2) and Test 37 (case 3). In Test 32, Grid A was installed at 45 inches upstream of the model plane, effectively generating 7.5% turbulence at the model plane. In test 37, Grid B was installed at 15 feet (180 inches) upstream of the model, effectively generating 7.7% turbulence at the model.

### Power spectral density functions of wake velocity in the longitudinal direction

Time traces of wake velocity in the longitudinal direction were measured simultaneously with the vibration response. Averaged power spectral density functions (aver-

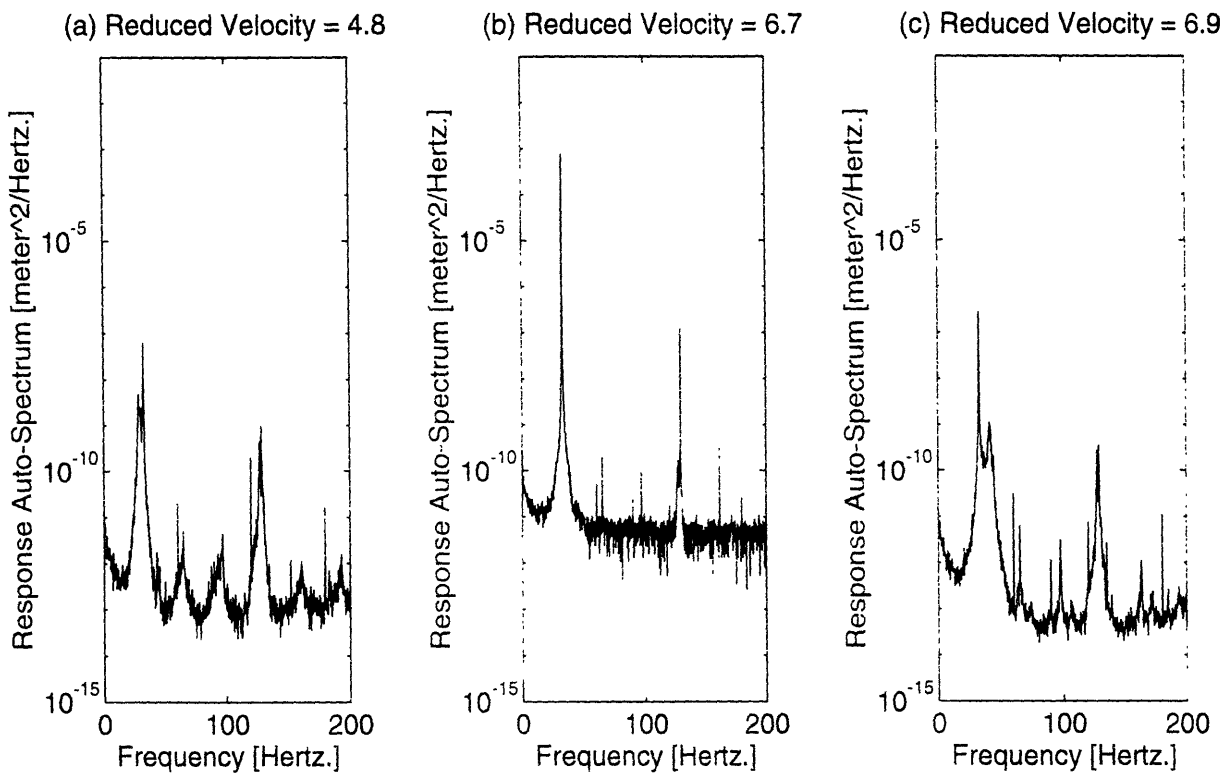


Figure 2-13: Test 28 (empty tunnel): power spectral density functions of the measured cross-flow vibration amplitudes at three different reduced velocities.

age in frequency domain over 16 frames) were calculated. The results indicate that free-stream turbulence affects the wake velocity spectrum differently than it does the corresponding VIV response spectrum.

Figure 2-17 shows the averaged power spectral density functions of the wake velocity fluctuations in the longitudinal direction behind the model which corresponds to each of the three response power spectral density functions shown in Figure 2-13. The wake velocity fluctuations in the longitudinal direction were measured by a stationary hot wire U-probe. This stationary U-probe was installed longitudinally in the wake of the model at about 3 diameters behind the axis of the model and vertically about a quarter height of the tunnel from the ceiling. In this case (case 0), no grid was installed.

As the wind speed increased to a reduced velocity of 4.8, where the wind speed is less than the critical wind speed of the model, a narrow spectrum peak at 30.25 Hertz. is clearly visible. This is the dominant vortex-shedding frequency at the stationary probe with the Strouhal number of 0.19. Notice that this local shedding frequency is slightly different from the local shedding frequency at the strain gauges shown in Figure 2-13, revealing the inhomogeneity of the flow across the test section. The wake field seems to be dominated by the local vortex-shedding frequency. Higher



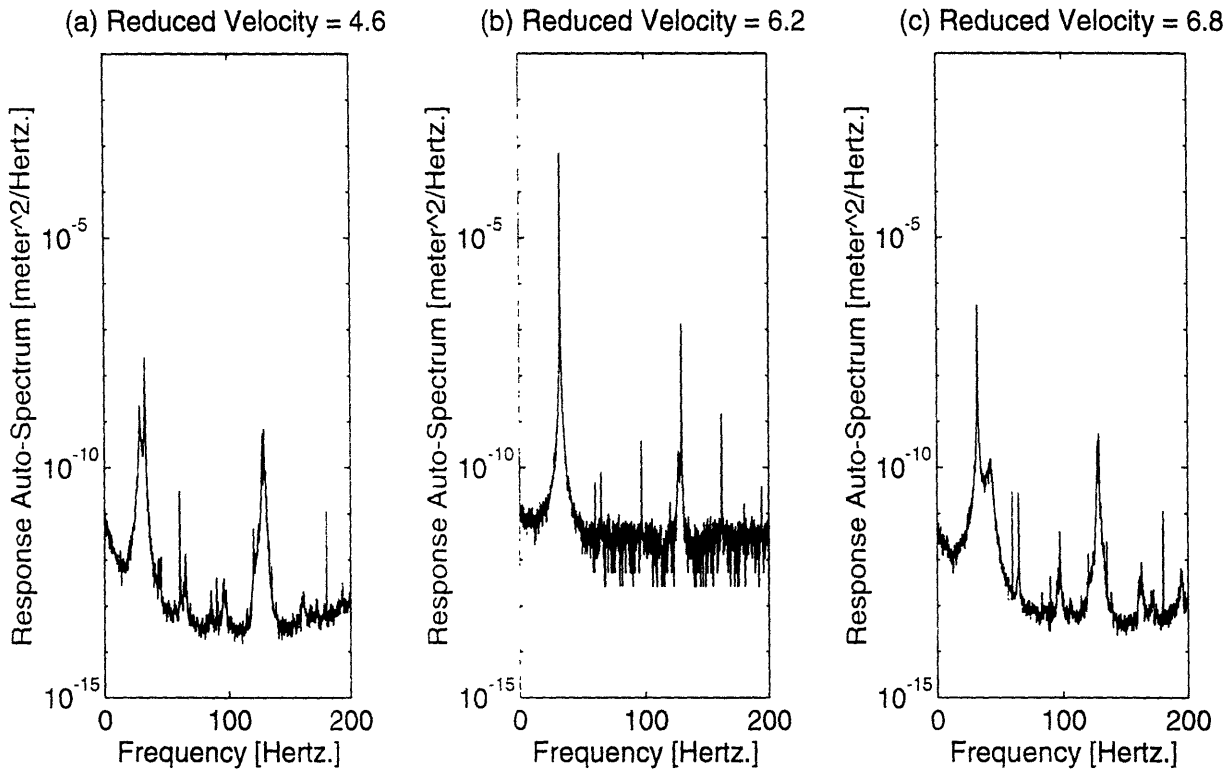


Figure 2-14: Test 29 (turbulence intensity 9.9%): power spectral density functions of the measured cross-flow vibration amplitudes at three different reduced velocities.

harmonics, except the second harmonic, are hardly recognizable.

As the wind speed increased to a reduced velocity of 6.7, a quite different spectrum was observed. The spectrum peak moves forward to 32.375 Hertz. This is the lock-in phenomenon that we previously observed from the response auto-spectrum shown in Figure 2-13. From the wake spectrum, we observe that the local vortex-shedding is totally controlled by the motion: The wake band-width is very narrow: higher order harmonics of the Strouhal frequency (up to 4th) are also narrow-banded and clearly visible.

As the wind speed further increased to a reduced velocity of 6.9, the wake-motion synchronization collapsed. The spectrum is very similar to that at the reduced velocity of 4.8, with the exception that the spectrum peak has moved to 44 Hertz. That frequency is the new dominant vortex-shedding frequency at the stationary probe, with the strouhal number of 0.20. The band-width is considerably broader than the wake auto-spectrum at lock-in.

Figures 2-18 shows the corresponding power spectral density functions of wake velocity fluctuations in the longitudinal direction to each of the three response power spectral density functions shown in Figure 2-14. In this case (case 1), grid A was in-

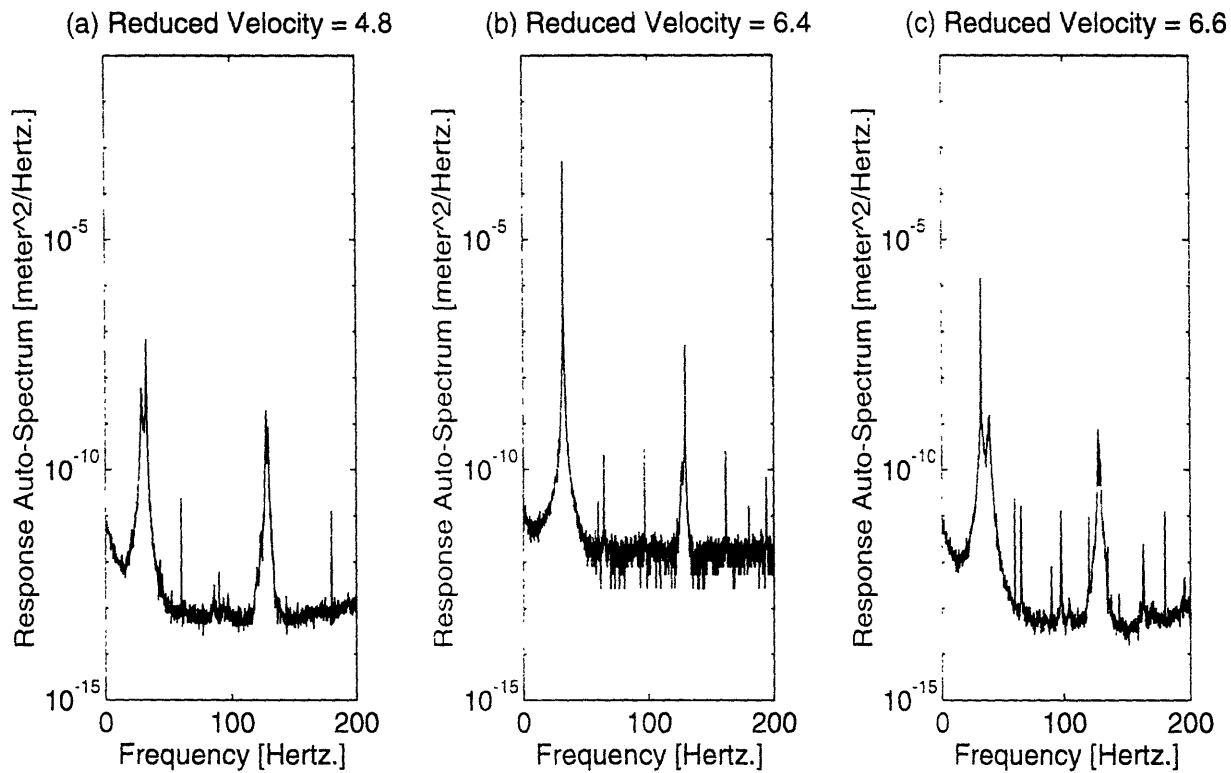


Figure 2-15: Test 32 (turbulence intensity 7.5%): power spectral density functions of the measured cross-flow vibration amplitudes at three different reduced velocities.

stalled at 30 inches upstream of the model, thus generating 9.9% turbulence intensity at the model plane.

Noticeable differences in the wake spectrum between Figure 2-18 and Figure 2-17 suggest that free-stream turbulence may have the following effects on vortex-shedding processes in the wake of a flexible member:

- free-stream turbulence reduces the energy in the wake at higher order harmonics of the shedding frequency.
- free-stream turbulence tends to broaden the band-width of the Strouhal peak in the wake spectrum.

The above observations were further supported by Figures 2-19 and 2-20, where the wake spectra at different reduced velocities for Test 32 and Test 37 were shown. In Test 32, grid A was placed at 45 inches upstream of the model plane, thus generating 7.5% turbulence intensity at the model plane. In Test 37, grid B was placed at 15 feet upstream of the model, thus generating 7.7% turbulence intensity at the model plane.

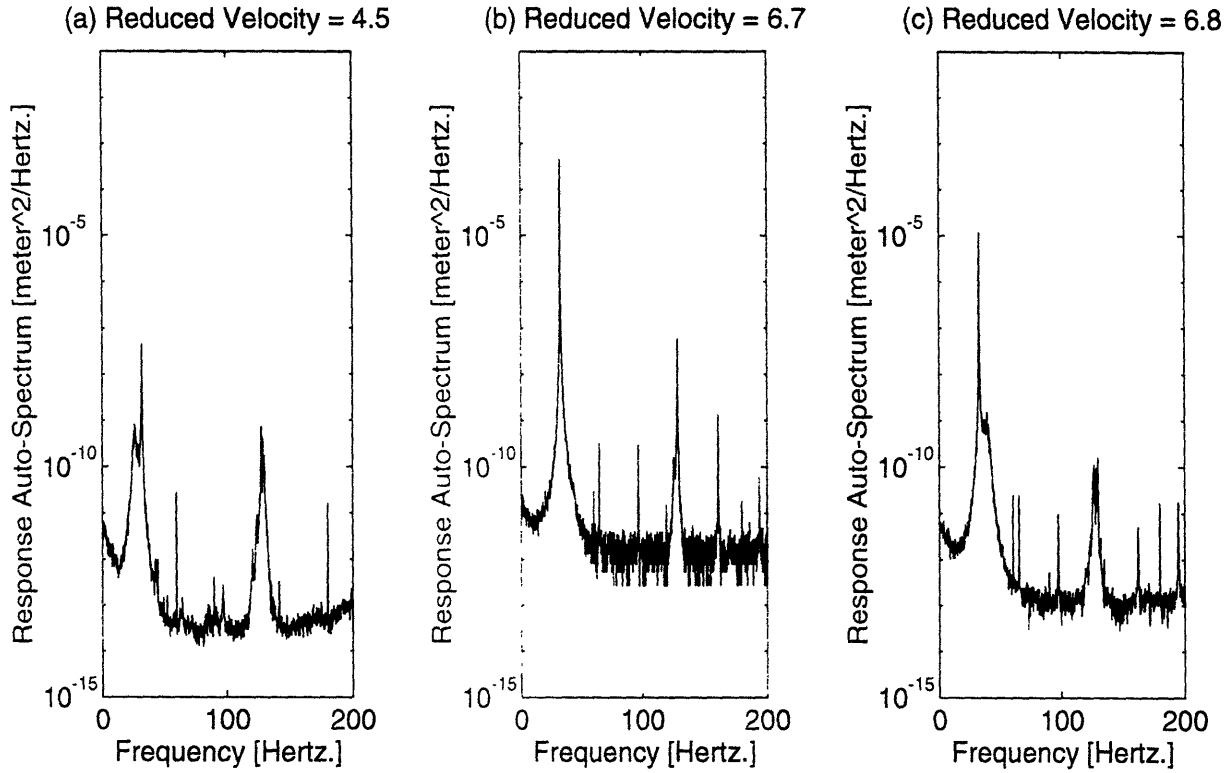


Figure 2-16: Test 37 (turbulence intensity 7.7%): power spectral density functions of the measured cross-flow vibration amplitudes at three different reduced velocities.

### Wake coherence functions

The wake coherence function between two different locations is defined as follows:

$$\gamma^2(f) = \frac{\|S_{u_1u_2}(f)\|^2}{\sqrt{S_{u_1u_1}(f)S_{u_2u_2}(f)}} \quad (2.5)$$

where  $S_{u_1u_1}(f)$  and  $S_{u_2u_2}(f)$  are the power spectral density functions of the fluctuating velocity in the longitudinal direction at locations 1 and 2.  $S_{u_1u_2}(f)$  is the cross-spectrum of the fluctuating velocity in longitudinal direction between locations 1 and 2.  $\gamma^2(f)$  is the coherence function between locations 1 and 2. The magnitude of  $\gamma^2(f)$  varies between 0 and 1.

At the maximum steady state response of each case, the wake coherence function was calculated by the Spectrum Analyzer from the time traces of the two hot wire U-probes. The two hot wire probes were installed at about 3 diameters behind the axis of the model. One probe was located at about a quarter height of the test section from the tunnel ceiling. The other probe was located at 40.25 inches downward from the stationary probe, so that the distance between the two probes was approximately half of the total length of the model.

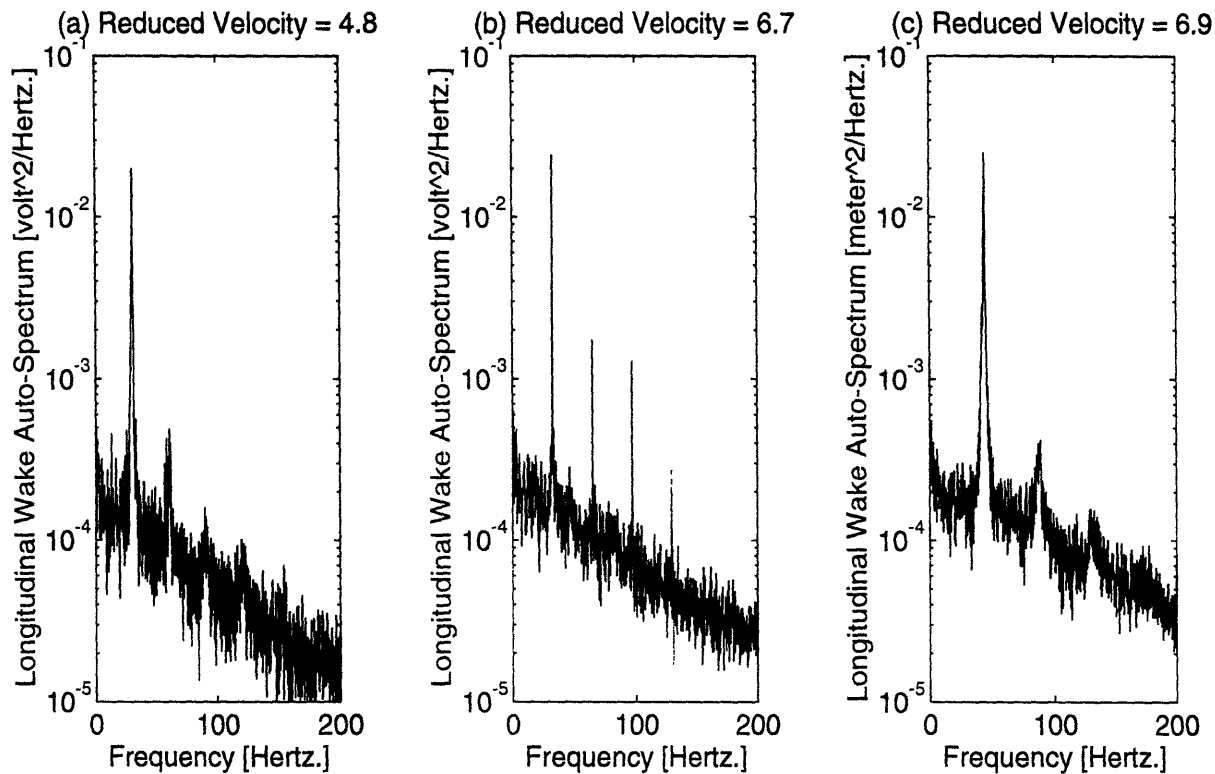


Figure 2-17: Test 28 (case 0; empty tunnel): power spectral density functions of the wake velocity in the longitudinal direction at three different reduced velocities.

Figure 2-21 shows the peak magnitudes at lock-in of the averaged wake coherence functions as a function of measured turbulence intensities for cases 0, 1, 2 and 3. The averaged wake coherence functions are the arithmetic average of wake coherence functions in the frequency domain over 16 data frames. The peak magnitudes of coherence functions seem to decrease a little in the presence of free-stream turbulence, but the wake is still highly correlated over half of the total length of the model (21.15 diameters).

### Effects of helical strakes on suppressing VIV response

In Test 35 and Test 36, the effects of helical strakes on suppressing VIV were investigated briefly in the absence of grids. Helical strakes were simulated by wrapping wires spirally around the test tube. The diameters of the single wires used in Test 35 and Test 36 were  $\frac{5}{32}$  inches (8.2% of a diameter) and  $\frac{1}{4}$  inches (13.1% of a diameter) respectively, and the helical spacing (pitch) between successive wraps was set to 16 inches (8.41 diameters). In both tests, the wind speed was advanced to a value where the peak vibration magnitude was found. The steady state vibration amplitudes at several other wind speeds were also recorded. The reduction of vibration response resulting from helical strakes was very impressive: The peak vibration magnitudes

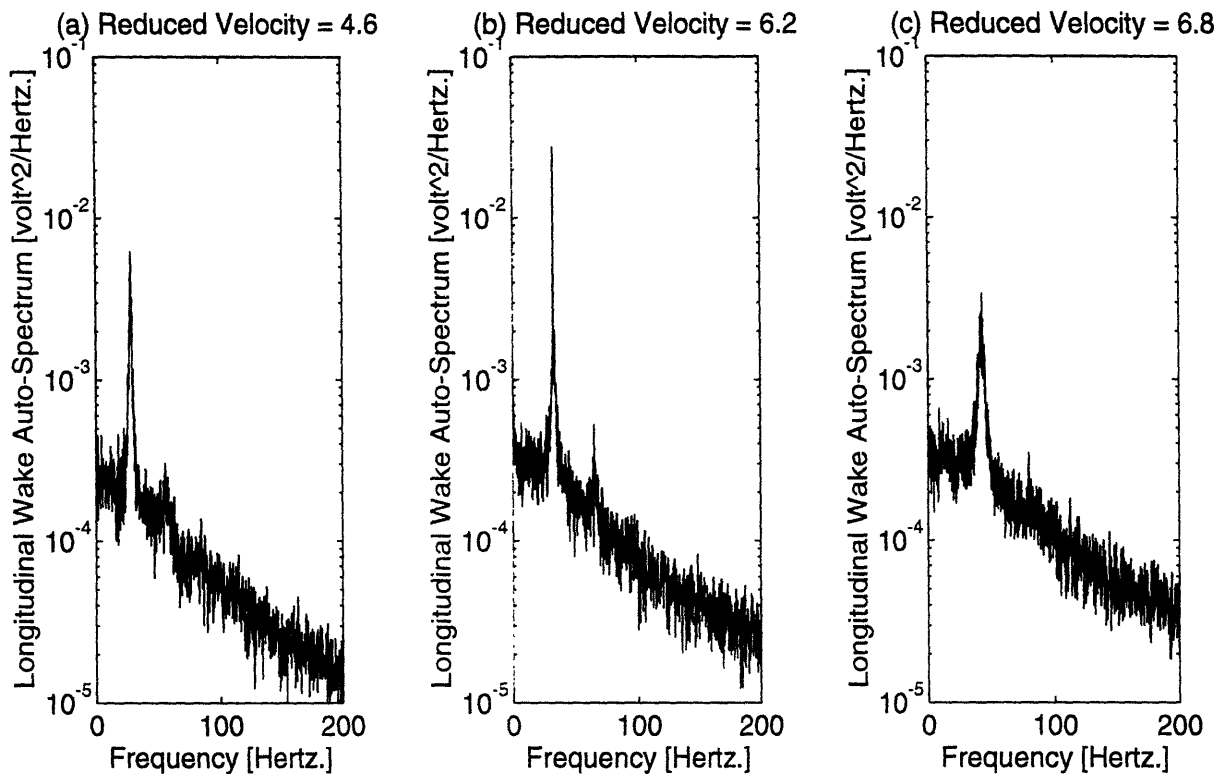


Figure 2-18: Test 29 (case 1, turbulence intensity 9.9%): power spectral density functions of the wake velocity in the longitudinal direction at three different reduced velocities.

were 0.15 and 0.14 diameters respectively, compared to 0.30 diameters without helical strakes (Test 28), a 50% response reduction.

### 2.5.2 Results of transient tests

Having studied the effect of free-stream turbulence on VIV, we now turn our attention to the effect of low-frequency variations in wind speed. Two transient tests were conducted for each of the three grid-turbulence cases. Test 31 was a representative of the six transient tests.

Test 31 was conducted with an experimental set-up that was identical to Test 29, where grid A was installed 30 inches upstream of the model plane. The low-frequency varying wind speed was achieved by continuous changes of dynamic pressure, through manually-controlled adjustments of the pitch angle of the tunnel fan. The time trace of the dynamic pressure was recorded by the Spectrum Analyzer, so that the time trace of the instantaneous wind speed could be inferred. The time trace of the corresponding in-line and cross-flow transient motions of the model were also collected by the Spectrum Analyzer.

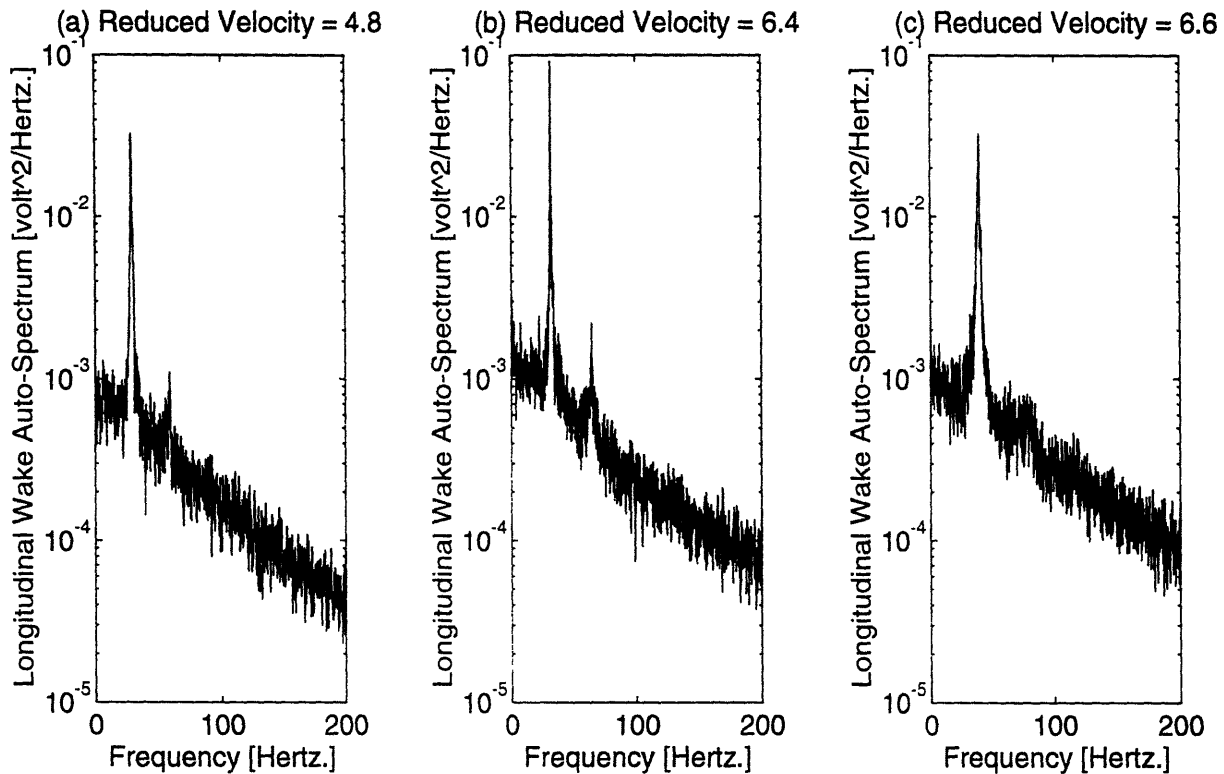


Figure 2-19: Test 32 (case 2, turbulence intensity 7.5%): power spectral density functions of the wake velocity in the longitudinal direction at three different reduced velocities.

Figure 2-22 shows the time trace of the measured wind speed expressed in terms of reduced velocities for Test 31, and Figure 2-23 shows the time trace of the corresponding cross-flow transient motion of the model at its mid-span. The transient motion of the model vividly demonstrates how the unsteady wind speed typically prevented the VIV response from developing to its steady state: vibration builds up as the wind speed moves toward the critical velocity, sustains as the wind speed stays within a critical interval, and decays as the wind speed moves away from the critical velocity. This helps to explain why large amplitude steady state lock-in vibrations of structural members under ideal conditions are not frequently observed in practice.

## 2.6 Summary of test results

The results of wind tunnel experiments on a 1.903 inch diameter carbon-fiber tube are summarized as follows:

- At a Reynolds number of approximately 26,000, intense turbulence (up to 10%) does not drastically disrupt the vortex shedding or reduce the magnitude of vibrations on a flexible cylinder. Vortex shedding still remains highly correlated

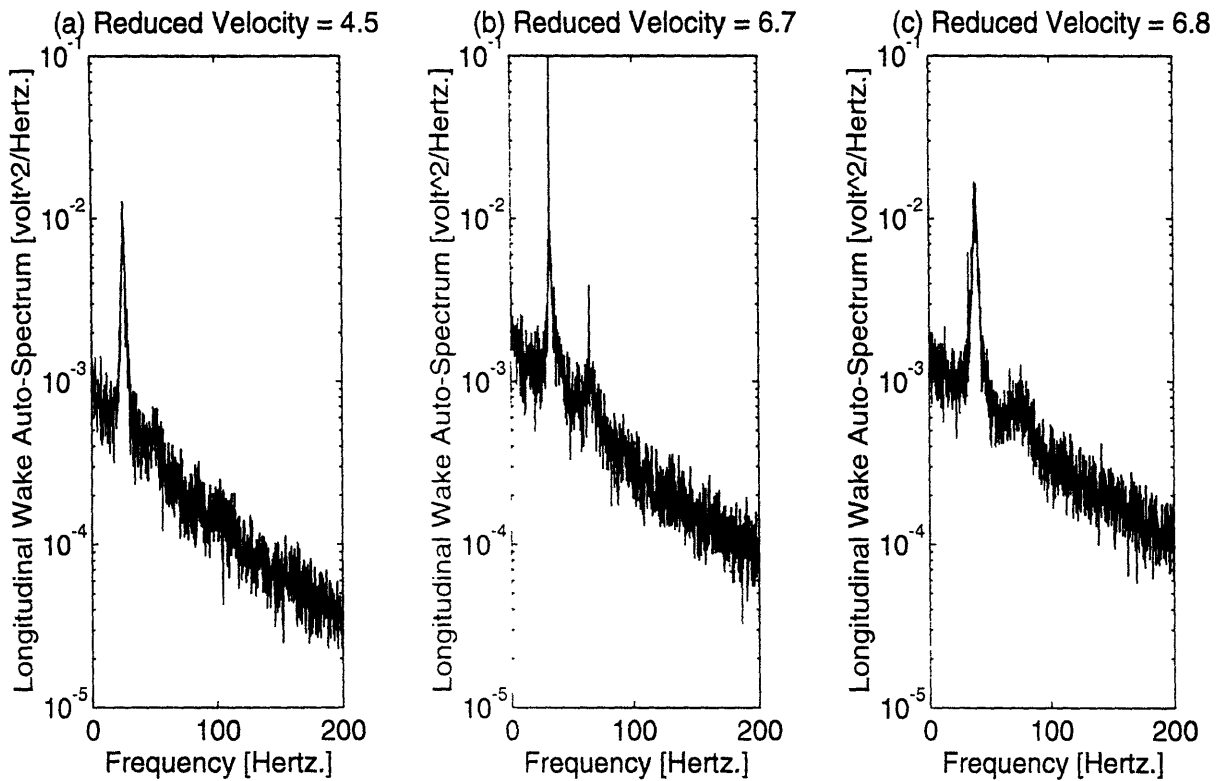


Figure 2-20: Test 37 (case 3, turbulence intensity 7.7%): power spectral density functions of the wake velocity in the longitudinal direction at three different reduced velocities.

over half of the total length of the flexible cylinder in intense turbulence. However, the hysteresis effect on the response magnitude does seem to decrease as turbulence intensity increases.

- Free-stream turbulence up to 10% tends to broaden the Strouhal peak and to reduce higher order harmonics of vortex shedding in the wake.
- Helical strakes are very effective in suppressing VIV response. A single  $\frac{1}{4}$  inch diameter wire (0.131 diameter) was responsible for a 50% response magnitude reduction on a 1.903 inch diameter flexible cylinder.
- Low-frequency variation in wind speed typically prevents VIV response from reaching steady state.

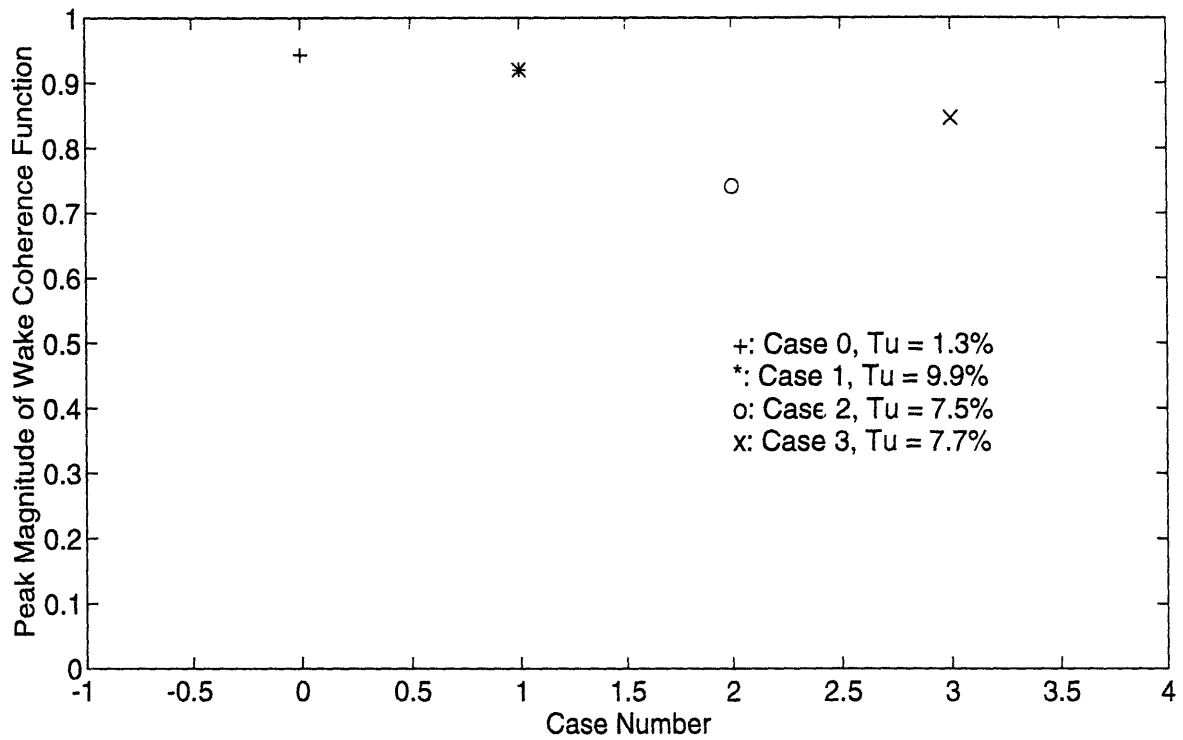


Figure 2-21: Peak magnitudes of averaged wake coherence functions *vs.* turbulence intensities, Cases 0, 1, 2, 3.



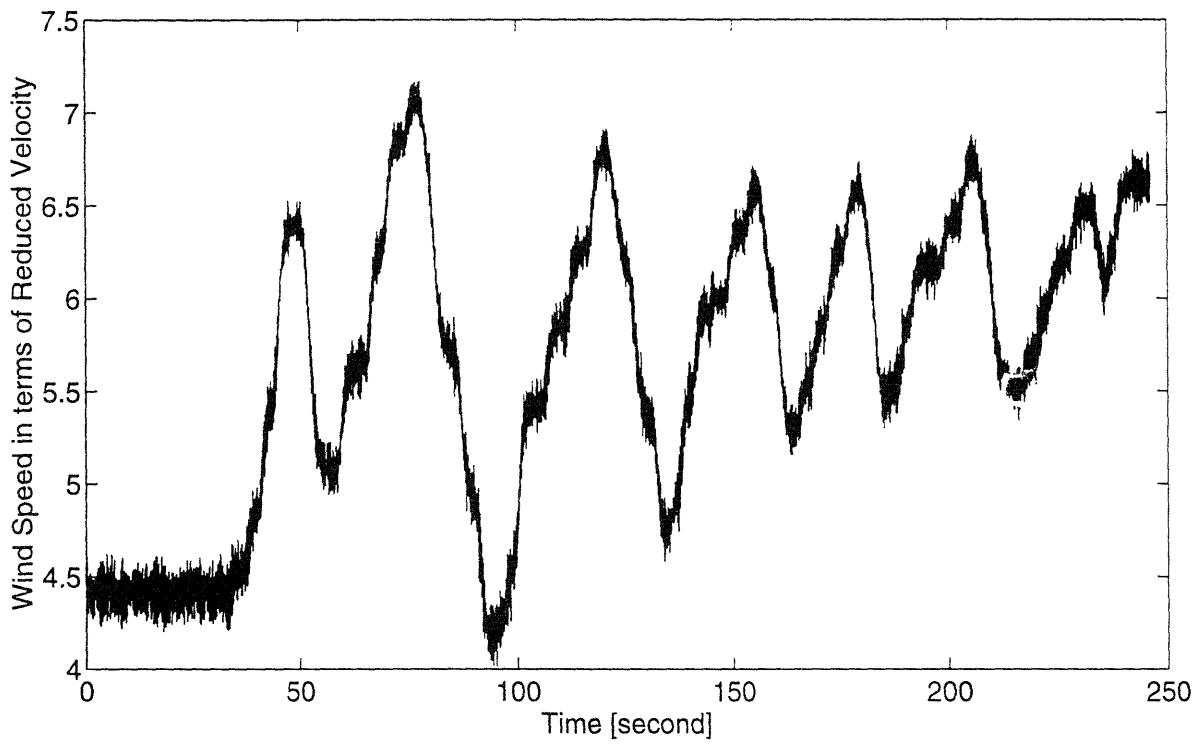


Figure 2-22: Time trace of the wind speed, Test 31 (case one, turbulence intensity 9.9%)

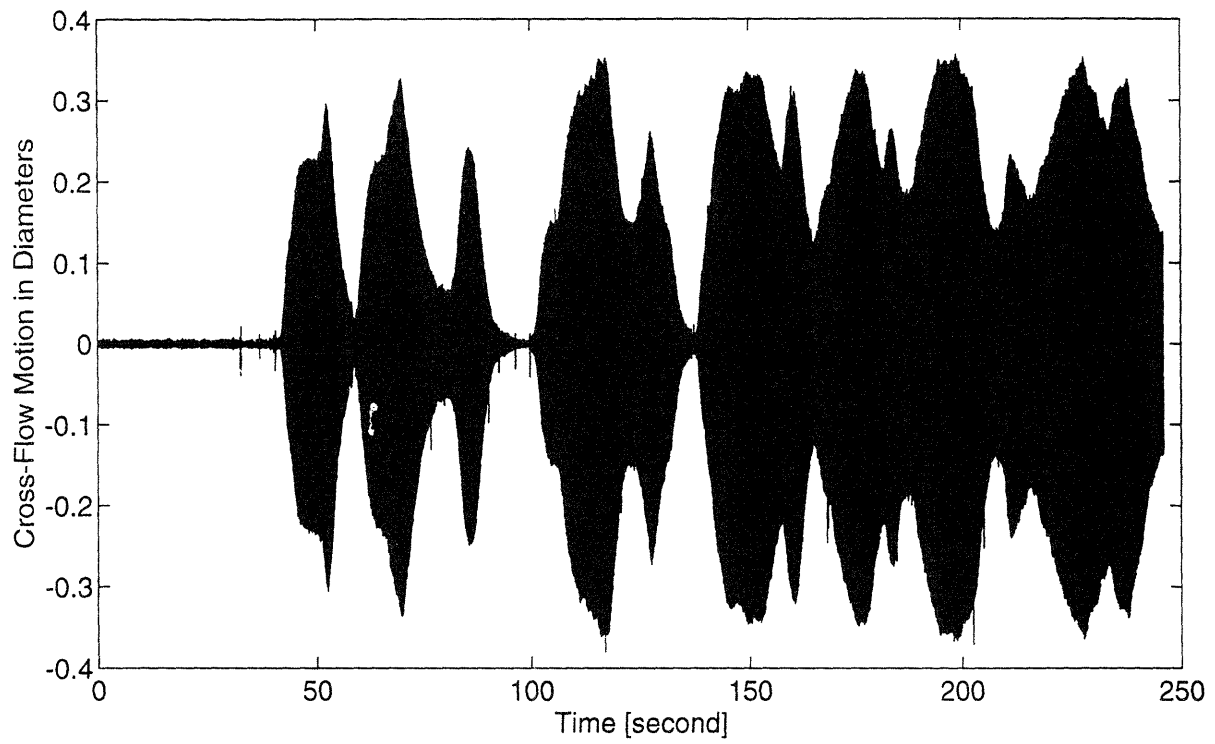


Figure 2-23: Time trace of the cross-flow transient motion, Test 31 (case one, turbulence intensity 9.9%)

# Chapter 3

## Time Domain VIV Prediction Model

### 3.1 Overview

Structural members of offshore platforms exposed in natural wind may vibrate as a result of vortex shedding. Strong vibrations are observed to occur at random time intervals separated intermittently by weak or no vibrations, since natural wind varies its speed and direction in a random fashion. The random variation of the natural windspeed causes the vortex shedding frequency to vary continuously over time. Vibrations start to develop when the vortex shedding frequency is in the vicinity of the natural frequency of the member, and continue to rise as long as the windspeed stays within a narrow range of flow velocities. The rise time depends on the structural damping, as well as the natural frequency of the member. The range of flow velocities which permit strong vibrations, or the critical velocity interval, is often defined in terms of the reduced velocity of the member.

Natural wind-induced vibration of structural members has resulted in fatigue damage to offshore platforms during fabrication and transportation, and flarebooms during in-service conditions [16]. It is important to accurately predict vibrations and the resulting fatigue damage caused by natural wind, to avoid potential disasters.

When the Vortex-Induced Vibration (VIV) of a flexible cylinder is dominated by the resonant response of a single mode, then by modal analysis, the response of the cylinder may be modeled in terms of an equivalent single degree of freedom (SDOF) oscillator. This oscillator has the properties of the responding resonant mode of the cylinder.

In this chapter, a time domain VIV prediction model is proposed, where the VIV of a flexible cylinder in unsteady winds can be predicted in the time domain by an

equivalent Single Degree of Freedom (SDOF) oscillator. A step-by-step procedure of implementing the proposed VIV prediction model is discussed. Examples are presented to evaluate the performance of the proposed VIV prediction model.

## 3.2 Mathematical basis of the VIV prediction model

In this section, a time domain VIV prediction model is proposed. The VIV of a flexible cylinder in unsteady winds is modeled as the response of an equivalent SDOF oscillator which has the properties of the responding resonant mode. The equivalent excitation force acting on the SDOF oscillator is first derived from the given time trace of the wind speed: then the transient vibration response is computed as the output of the SDOF oscillator. To further increase the implementation speed, the SDOF oscillator is replaced by an equivalent Auto Regressive Moving Average (ARMA) filter.

### 3.2.1 Derivation of equivalent excitation force

In this section, the excitation force is derived from the time trace of the instantaneous wind speed based on the assumption that the instantaneous lift coefficient takes a constant value which corresponds to the steady state vibration amplitude at the instantaneous wind speed. The derived sequence of excitation force is used later as the input to the SDOF oscillator.

When a SDOF oscillator is subjected to sinusoidal excitation at a resonant natural frequency, the oscillator will respond at the excitation frequency. Vortex shedding in wind may cause an elastic cylinder to develop such resonant oscillations. As the wind speed is increased or decreased so that the vortex shedding frequency approaches the natural frequency of the elastic cylinder, the vortex shedding frequency locks onto the cylinder natural frequency over a range of flow velocities. The resultant vibrations occur at or close to the natural frequency of the cylinder. The resonant excitation range of cross flow oscillation is found to depend on the mass ratio of the member [12]. In air, where the mass ratio is large, this excitation range extends over the reduced velocity values of approximately 4.75 to 8 [33]. At any windspeed within this reduced velocity range, the cylinder undergoes narrow-band cross-flow oscillations close to the natural frequency, with a preferred mode shape that is determined by the end conditions of the cylinder. The vibration amplitude, which is defined as the peak magnitude of oscillations along the cylinder, is typically large (above 1% of a diameter) [31]. The maximum value of vibration amplitudes falls within the reduced velocity range of 5.5 to 6.5 [33]. At windspeeds outside the reduced velocity range of 4.5 to 8, the cylinder undergoes broad-band cross-flow oscillations without any dominant frequencies, and the vibration amplitude is small (less than 1% of a diameter) [31].

It has been shown [16] that fatigue damage due to VIV is contributed almost exclusively by narrow-band oscillations. From now on, we will neglect broad-band oscillations and focus our attention exclusively on narrow-band oscillations. Since the narrow-band oscillation of the flexible cylinder is dominated by the resonant oscillation of a single mode, we will further assume that the cylinder undergoes pure sinusoidal cross-flow oscillations at this mode when the windspeed is within the critical velocity band.

Based on the single-mode assumption, steady state vibration amplitudes of an elastic cylinder can be expressed as a function of the steady wind speed expressed in terms of reduced velocities

$$\begin{aligned} \frac{A(V)}{A_{max}} &= f(V_r) \\ &= f\left(\frac{V}{f_n D}\right) \end{aligned} \quad (3.1)$$

where  $A(V)$  is the steady state vibration amplitude of the flexible cylinder at a constant flow speed  $V$ .  $A_{max}$  is the maximum vibration amplitude, presumably at the critical windspeed  $V_{crit}$ .  $A_{max}$  can be predicted using various VIV design methodologies, such as **DnV**, **BS 8100**, **ESDU 85038** and **Brown & Root**, etc. A complete review of these methodologies was documented in [30].  $f_n$  and  $D$  are, respectively, the natural frequency and the diameter of the cylinder.  $f(V_r)$  is a real function that relates the flow speed to the steady state vibration amplitude of the cylinder that is excited by the flow at that speed, and is defined as the steady-state response function.  $f(V_r)$  can be determined based on experimental evidence [31] [12]. Different expressions of this function resulting from the models proposed by various authors are given below.

- **DnV** [10] [9]

$$f(V_r) = \begin{cases} 1 & 4.7 \leq V_r \leq 8.0 \\ 0 & \text{otherwise} \end{cases} \quad (3.2)$$

- **BS 8100** [6]

$$f(V_r) = \begin{cases} \frac{(3.6 - 0.52V_r)V_r^2}{25} & 3.85 \leq V_r \leq 6.90 \\ 0 & \text{otherwise} \end{cases} \quad (3.3)$$

- **ESDU 85038** [12] and **Brown & Root** [29]

$$f(V_r) = \begin{cases} e^{-\left(1 - \frac{V_r}{(V_r)_{crit}}\right)^2 104.5 \left(\frac{m\zeta}{\rho D^2}\right)^{1.8}} & 4.25 \leq V_r \leq 5.25 \\ 0 & \text{otherwise} \end{cases} \quad (3.4)$$

• Fei & Vandiver [13]

$$f(V_r) = \begin{cases} V_r - 5.0 & 5.0 \leq V_r \leq 6.0 \\ 2(6.5 - V_r) & 6.0 \leq V_r \leq 6.5 \\ 0 & \text{otherwise} \end{cases} \quad (3.5)$$

Single mode dominance of VIV response of an elastic structure over a critical velocity range suggests that the response of the cylinder may be modeled as the output of an equivalent SDOF oscillator which has the properties of the responding resonant mode. In fact, this is possible by constructing a proper transformation between the windspeed and the amplitude of resonant excitations at the corresponding windspeed. Consider the following governing equation of a SDOF oscillator excited by a constant magnitude sinusoid at the resonant frequency  $\omega_n$ :

$$\ddot{x} + 2\zeta\omega_n\dot{x} + \omega_n^2x = f_a \cos \omega_n t \quad (3.6)$$

along with the following initial conditions:

$$\begin{aligned} x(0) &= x_0 \\ \dot{x}(0) &= \dot{x}_0 \end{aligned}$$

where  $x(t)$  is the transient vibration response of the oscillator.  $\omega_n$  and  $\zeta$  are the undamped natural frequency and the damping coefficient of the oscillator.  $f_a$  is the magnitude of the modal excitation force per unit modal mass of the oscillator and is to be determined from the time trace of the instantaneous wind speed. Assuming that the wind speed is held at a constant value of  $V$ , the solution of the transient vibration response is given by

$$x(t) = e^{-\zeta\omega_n t} \left[ x_0 \cos \omega_d t + \frac{\dot{x}_0 + x_0 \zeta \omega_n - \frac{f_a}{2\zeta\omega_n} \sin \omega_n t}{\omega_d} \right] + \frac{f_a}{2\zeta\omega_n^2} \sin \omega_n t \quad (3.7)$$

where  $\omega_d$  is the damped natural frequency of the system, and

$$\omega_d = \omega_n \sqrt{1 - \zeta^2} \quad (3.8)$$

The solution of steady state vibrations can be obtained from Equation 3.7 as  $t$  approaches infinity

$$x(t) = A(V)\sin \omega_n t = \frac{1}{2\zeta\omega_n^2} f_a(V)\sin \omega_n t \quad (3.9)$$

where  $A(V)$  is the steady state vibration amplitude at the given constant wind speed  $V$ , and is given by

$$A(V) = \frac{1}{2\zeta\omega_n^2} f_a(V) \quad (3.10)$$

Combining Equations 3.1 and 3.10, the amplitude of the harmonic excitation force at the resonant frequency can be expressed in terms of the steady windspeed as follows.

$$f_a(V) = 2\zeta\omega_n^2 A_{max} f\left(\frac{V}{f_n D}\right) \quad (3.11)$$

Equation 3.11 implies that by defining such a transformation between the wind-speed and the amplitude of the harmonic excitation force at the resonant frequency, the vibration amplitude of a flexible cylinder excited by a constant windspeed can be predicted by a SDOF oscillator under the equivalent harmonic excitation. Of course, this relationship between the amplitude of the excitation force and the wind speed is valid in case of the steady wind, where the wind speed is held at a constant value and the wind direction does not change.

To extend VIV prediction to any wind speed distribution  $V(t)$ , an important approximation is necessary at this point which has proven to be quite accurate. The excitation  $f_a(V)$  evaluated above is the magnitude of the periodic lift force which is required to drive the cylinder to the steady state vibration amplitude corresponding to the wind speed  $V$ . Since the lift coefficient changes with vibration amplitudes, the approximation is made here that as the cylinder vibration rises toward the steady state value, the periodic excitation force magnitude stays constant. In other words, during finite rise time, the lift coefficient is assumed to be constant at the value which would correspond to the final steady state vibration amplitude. With this approximation we may estimate the excitation which corresponds to any wind speed  $V(t)$  by the following formula:

$$\begin{aligned} f_a(t) &= f_a(V(t)) \\ &= 2\zeta\omega_n^2 A_{max} f\left(\frac{V(t)}{f_n D}\right) \end{aligned}$$

$$= 2\zeta\omega_n^2 A_{max} f(V_r(t)) \quad (3.12)$$

### 3.2.2 Prediction of transient vibrations of a flexible cylinder

Due to changes in wind speed  $V(t)$  and subsequently in reduced velocity  $V_r(t)$ , the vibration response of a flexible cylinder will be modulated in amplitude. In this section, transient vibrations of a flexible cylinder are predicted as a standard convolution integral of the time varying excitation force,  $f_a(t) \cos \omega_n t$ , and the impulse response function of the SDOF oscillator which has the same resonant properties.

Consider the following differential equation governing the motion of a SDOF oscillator excited by an external force  $f_a(t) \cos \omega_n t$ :

$$\ddot{x} + 2\zeta\omega_n \dot{x} + \omega_n^2 x = f_a(t) \cos \omega_n t \quad (3.13)$$

along with the initial conditions:

$$\begin{aligned} x(0) &= x_0 \\ \dot{x}(0) &= \dot{x}_0 \end{aligned}$$

The solution to Equation 3.13 can be expressed in terms of a convolution integral as follows.

$$x(t) = (c_1 + ic_2) \exp [(-\zeta + i\sqrt{1 - \zeta^2})\omega_n t] + \int_0^t f_a(\tau) \cos \omega_n \tau \times h(t - \tau) d\tau \quad (3.14)$$

where  $c_1$  and  $c_2$  are real constants that are determined by the initial conditions.  $i$  is the unit of pure imaginary numbers, and  $i = \sqrt{-1}$ .  $h(t)$  is called the impulse response function of the oscillator, and

$$h(t) = \begin{cases} \frac{1}{\omega_d} \exp(-\zeta\omega_n t) \sin \omega_d t & t \geq 0 \\ 0 & t < 0 \end{cases} \quad (3.15)$$

The first term on the right hand side of Equation 3.14 depends only on the initial conditions, and the magnitude of this term decays exponentially with time. Therefore it can be neglected for large time. The second term is an integral that expresses the transient motion due to the external force  $f(t)$ . This integral is called the *Duhamel integral*. If we neglect the contribution from the initial conditions, the motion of the SDOF oscillator can be expressed in terms of the *Duhamel integral*:



$$x(t) = \int_0^t f_a(\tau) \cos \omega_n \tau \times h(t - \tau) d\tau \quad (3.16)$$

$$= \frac{1}{\omega_d} \int_0^t f_a(\tau) \cos \omega_n \tau \times e^{-\zeta \omega_n (t - \tau)} \sin \omega_d (t - \tau) d\tau \quad (3.17)$$

Combining Equations 3.12 and 3.17, the transient vibration amplitude of a flexible cylinder excited by unsteady wind can be expressed in terms of the wind speed as follows.

$$\begin{aligned} x(t) &= \frac{1}{\omega_d} \int_0^t 2\zeta \omega_n^2 A_{max} f(V_r(\tau)) \cos \omega_n \tau \times e^{-\zeta \omega_n (t - \tau)} \sin \omega_d (t - \tau) d\tau \\ &= \frac{2\zeta \omega_n^2 A_{max}}{\omega_d} \int_0^t f(V_r(\tau)) \cos \omega_n \tau \times e^{-\zeta \omega_n (t - \tau)} \sin \omega_d (t - \tau) d\tau \end{aligned} \quad (3.18)$$

To calculate the transient vibrations by Equation 3.18 requires values of  $A_{max}$  and  $f(V_r)$ , as well as  $V(t)$ .  $A_{max}$  is the maximum cross-flow vibration amplitude at the critical wind speed  $V_{crit}$ . It depends on the values of the cross-flow lift force, the mass ratio and the structural damping ratio. Various design methodologies in predicting  $A_{max}$  exist in the literature [12] [6] [29], and a complete review of these prediction methodologies is documented in [30]. As an example for the illustration purpose, the **Brown & Root** [29] response amplitude prediction methodology will be briefly presented in the next section.

$f(V_r)$  is the steady-state response function that relates the flow speed (expressed in reduced velocity) to the steady state anti-node vibration amplitude at this speed. It was determined primarily from experiments, and varies under different test conditions. Various experimentally determined values of  $f(V_r)$  are summarized in the previous section.

$V(t)$  is the instantaneous wind speed. It is often treated as a random process. A realization of this random process can either be obtained from field measurements or from numerical simulations. Since the wind speed cannot be expressed in analytical form, the transient vibration predictions, or equivalently the convolution integral, has to be implemented numerically. The cost of the numerical convolution in the time domain increases linearly with the size of the wind speed sequence, which in turn is determined by the total duration and the sampling frequency of the wind speed. For compilation of long-term response statistics, the time domain numerical convolution scheme is not attractive.

To expedite the prediction implementation process, the concepts of state variables and state equations have been introduced. The current state of the SDOF system is represented by a vector which contains the number of variables sufficient to allow

the computation of future behavior of the system. These variables are called state variables and the vector that contains the state variables is called the state vector. In the case of a SDOF oscillator, for example, the state variables are  $x$  and  $\dot{x}$ , and the state vector is  $[x, \dot{x}]$ . The main idea of introducing state variables and state vectors is to replace the original second-order differential equation that governs the displacement response of the SDOF oscillator under an arbitrary excitation, by a first order differential equation (the so-called state equation) that contains the state vector. The state equation is then solved analytically using matrix manipulations and vector calculus. After a considerable amount of algebraic operations which are presented in Appendix A, the displacement response of the SDOF oscillator can be implemented as the solution of the following equivalent linear difference equation

$$x(t_{k+2}) - a_1 x(t_{k+1}) + a_2 x(t_k) = b_1 u(t_{k+1}) + b_2 u(t_k) \quad (3.19)$$

where

$$\begin{aligned} u(t_k) &= \frac{1}{\omega_n^2} f_a(t_k) \cos \omega_n t_k \\ &= 2\zeta A_{max} f(V_r(t_k)) \cos \omega_n t_k \\ b_1 &= 1 - \alpha \left( \beta + \frac{\zeta \omega_n}{\omega_d} \gamma \right) \\ b_2 &= \alpha^2 + \alpha \left( \frac{\zeta \omega_n}{\omega_d} \gamma - \beta \right) \\ a_1 &= -2\alpha\beta \\ a_2 &= \alpha^2 \\ \omega_d &= \omega_n \sqrt{1 - \zeta^2} \\ \alpha &= e^{-\zeta \omega_n h} \\ \beta &= \cos \omega_d h \\ \gamma &= \sin \omega_d h \\ t_k &= k \times h \\ h &= \text{increment of time steps} \end{aligned}$$

The numerical implementation of the transient vibration prediction of a flexible cylinder by a difference equation has computational advantages over that by numerical convolutions. This scheme is numerically speedy since the calculation of the response at the present time is explicit, *i.e.*, only requires simple addition operations of the response in the past and the excitation at the present and in the past. This scheme is also accurate since the solution of the state equation is exact at sampling points [3]. Details of the state equation and its solution derivation are presented in Appendix A.

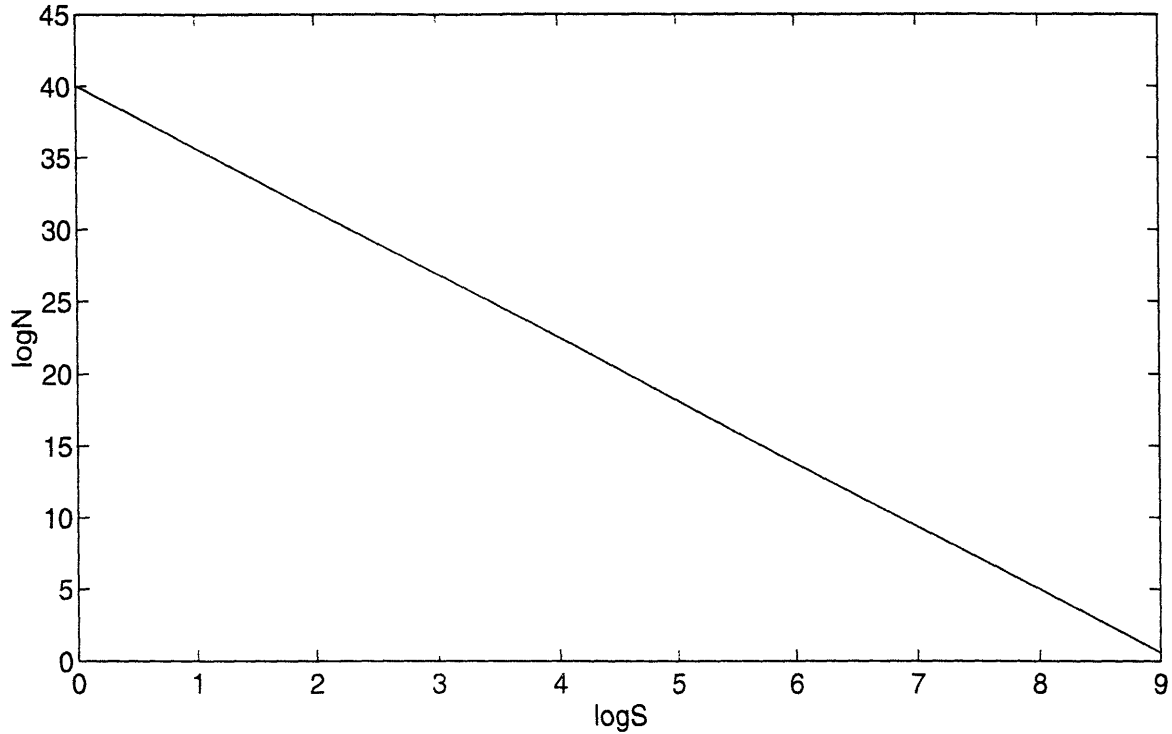


Figure 3-1: A generic  $S - N$  curve

### 3.2.3 Assessment of fatigue damage

If the response is deterministic and cyclic, the response and the number of cycles to fatigue failure can be defined as

$$NS^m = N_0 S_0^m = c \quad (3.20)$$

where  $S$  [ $\text{kg}\cdot\text{m}^{-1}\cdot\text{s}^{-2}$ ] is the stress range, for cyclic stresses. the stress range is twice the amplitude of cyclic stresses.  $N$  is the number of cycles to fatigue failure at the stress range  $S$ .  $S_0$  and  $N_0$  are the reference values of the stress range and the number of cycles to fatigue damage respectively.  $m$  and  $c$  are positive constants that are related to material properties. Equation 3.20 is known as an  $S - N$  curve, and it can be graphically presented as in Figure 3-1.

When the stress range is not a constant, such as in the case of vortex-induced oscillations of flexible cylinders in unsteady wind. Equation 3.20 cannot be used without additional assumptions. The Palmgren-Miner rule postulates that the accumulation of fatigue damage is linear [21]. Thus the fatigue damage due to the application of  $n_\sigma$  cycles at the stress range  $\sigma$  is

$$\Delta_\sigma = \frac{n_\sigma}{N_\sigma} \quad (3.21)$$

where  $N_\sigma$  is the number of cycles to failure at the stress range  $\sigma$  ( $N_\sigma \geq n_\sigma$ ). Under variable stress ranges, the total fatigue damage is

$$\begin{aligned} \Delta &= \sum_{\text{all } \sigma} \Delta_\sigma \\ &= \sum_{\text{all } \sigma} \frac{n_\sigma}{N_\sigma} \end{aligned} \quad (3.22)$$

The summation includes all variable stress ranges. Fatigue failure occurs when  $\Delta$  reaches unity. Substituting Equation 3.20 into Equation 3.22, we have

$$\Delta = c^{-1} \sum_{\text{all } \sigma} n_\sigma \sigma^m \quad (3.23)$$

In assessing the fatigue damage due to variable stress ranges in the time domain, it is more convenient to accumulate the fatigue damage over different cycles, rather than over different stress levels. Fatigue damage resulting from the  $i$ th stress cycle at stress range  $\sigma_i$  is

$$\Delta_i = \frac{1}{N_i} \quad (3.24)$$

where  $N_i$  is the number of cycles to fatigue failure at the stress range  $\sigma_i$ . The total fatigue damage that accumulates over the duration of applied stress cycles can be expressed as follows:

$$\begin{aligned} \Delta &= \sum_{i=1}^n \Delta_i \\ &= \sum_{i=1}^n \frac{1}{N_i} \\ &= c^{-1} \sum_{i=1}^n \sigma_i^m \end{aligned} \quad (3.25)$$

where  $n$  is the total number of applied stress cycles over the duration of the wind-induced vibrations.

### Converting vibration amplitudes to stress ranges

For a flexible pinned-pinned cylinder oscillating at the first mode in a sinusoidal mode shape, the transient vibration amplitude of the cylinder at an anti-node of the cylinder can be rewritten from Equation 3.18 as follows:

$$v(t) = A(t) \sin(\omega_d t + \phi(t)) \quad (3.26)$$

where  $A(t)$  is the envelope of the vibration amplitudes and  $\phi(t)$  is the instantaneous phase angle. The resulting bending moment at the anti-node can be expressed as follows:

$$M(t) = EI k^2 A(t) \sin(\omega_d t + \phi)$$

where  $M(t)$  is the instantaneous bending moment at the anti-node.  $E$  is the Young's modulus of the cylinder.  $I$  is the moment of inertia of the cylinder.  $k = \frac{\pi}{L}$  is the wave number at the first mode. The resulting stress range at the anti-node occurring on the surface of the cylinder can be expressed as follows:

$$\begin{aligned} \sigma(t) &= 2 \times \frac{M(t)}{I} \times \frac{D}{2} \\ &= \frac{E \pi^2 D}{L^2} \times A(t) \end{aligned} \quad (3.27)$$

For a boundary condition other than pinned-pinned, the mode shape of oscillations is not sinusoidal.  $F_i$ , a strain response parameter, may be derived to define the maximum strain as a function of the maximum deflection.  $F_i$  may be determined from stress analysis, measurements or finite element models. For the simple case of a pinned-pinned beam,  $F_i = \pi^2 = 9.87$ . The stress-deflection relationship shown in Equation 3.27 can be generalized for different boundary conditions as follows:

$$\sigma(t) = \frac{E F_i D}{L^2} \times A(t) \quad (3.28)$$

Table 3.1 presents computed values of  $F_i$  (at first mode) for typical boundary conditions.

Combining Equations 3.25 and 3.28, the total damage over the duration of applied cyclic stresses can be expressed in terms of the envelope of transient vibration amplitudes.

$$\Delta = c^{-1} \left( \frac{EF_1 D}{L^2} \right)^m \sum_{i=1}^n A_i^m \quad (3.29)$$

where  $A(t)$  is the envelope of the transient vibration amplitudes  $x(t)$  that were derived from Equation 3.18.  $A_i$  is the discrete sequence of  $A(t)$  sampled at  $f_n$ , the natural frequency of the member.  $b$  and  $c$  are real constants that are related to material properties. These are the parameters necessary to define a specific  $S-N$  curve.

The fatigue damage rate,  $\mathcal{D}$ , can be calculated as below.

$$\mathcal{D} = \frac{\Delta}{n} f_n = \frac{f_n}{nc} \left( \frac{EF_1 D}{L^2} \right)^m \sum_{i=1}^n A_i^m \quad (3.30)$$

### 3.3 Implementation of the prediction procedure

Based on the theory that was developed in the last section, the time domain VIV prediction of a flexible cylinder can be implemented by the following step by step procedure:

- **Predicting the maximum vibration amplitude.** To determine  $A_{max}$ , the maximum steady state vibration amplitude for the flexible cylinder expressed in diameters, we use the following formulation

$$\frac{A_{max}}{D} = \frac{3.82\gamma_i C_L}{\left[ 1 + 0.19 \left( \frac{2\pi St^2 K_s}{C_L} \right) \right]^{3.35}} \quad (3.31)$$

where  $\gamma_i$  is a mode shape parameter that depends on the boundary conditions of the cylinder. Values of  $\gamma_i$  for typical boundary conditions of a flexible cylinder are listed in Table 3.2.  $C_L$  is the root mean squared (r.m.s.) lift force coefficient based on stationary cylinders, and it depends on the Reynolds number. The variation of the lift force coefficient with the Reynolds number is shown in Figure 3-2.  $St$  is the Strouhal number, and it depends on the Reynolds number.  $St = 0.2$  is usually a good first guess for most members in the subcritical Reynolds number regime.  $K_s$  is the stability parameter, or the reduced damping, and  $K_s = \frac{2m\delta}{\rho D^2}$ .

It is worth pointing out that the recommended lift force coefficient function shown in Figure 3-2 is more conservative, particularly in the critical and supercritical regimes, than that was originally proposed by *Brown & Root* [29]. We [30] believe that there is insufficient evidence, at the present time, to warrant the use of a lift coefficient as low as 0.1, as obtained from stationary cylinder

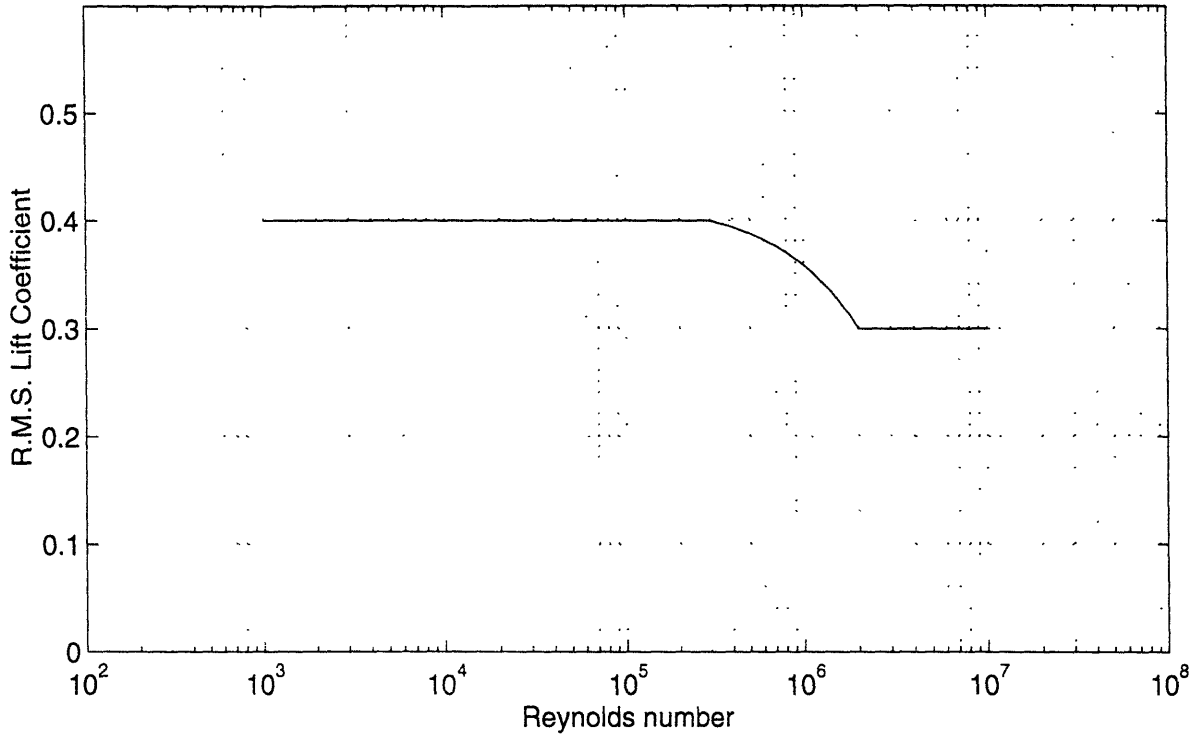


Figure 3-2: Variation of the r.m.s. lift force coefficient with Reynolds number, from Rudge & Fei (1991)

studies. The lift force coefficient in Figure 3-2 varies linearly for the Reynolds number from  $3 \times 10^5$  to  $2 \times 10^6$ . The effects of surface roughness and atmospheric turbulence are also disregarded in this simple model. These parameters have been shown on stationary cylinders to cause the transition from subcritical to supercritical flow to occur at a lower nominal Reynolds number, thereby reducing the lift coefficient obtained at the velocity of interest. In the future, as relevant data becomes available, we recommend that this lift coefficient function be modified accordingly.

The aforementioned prediction formula for maximum steady state vibration amplitude was first proposed by Brown & Root [29], and was recommended by Rudge et al [30] [31].

- **Sampling the wind speed.** in order to be able to catch the vibration cycles of the cylinder accurately, the wind speed data need to be sampled at a sampling frequency that is high enough compared to the natural frequency of the cylinder. The desired wind speed data can be achieved by resampling the original wind data at a higher rate using lowpass interpolation. Lowpass interpolation is done by the matlab built-in function `interp` [24]. In case real wind speed data is not available, the desired wind speed samples may be simulated. A time

history of a Gaussianly distributed wind speed samples with a target windspeed spectrum can be generated, by providing Gaussianly distributed white noise as input to an optimum Auto Regressive Moving Average (ARMA) filter, which best simulates the target spectrum [28]. This method consists of finding an ARMA digital filter that matches the statistical properties of the wind speed at the location where the cylinder is placed. The sequence of resampled or simulated wind speed samples is denoted by  $V(t)$ .

- **Constructing the equivalent excitation force.** Once the time trace of the desired wind speed data is obtained, the excitation force acting on the equivalent SDOF oscillator can be constructed through two steps. The first step is to express the wind speed in terms of reduced velocity that corresponds to the responding mode of the cylinder. The second step is to transform the dimensionless windspeed to the amplitude of the periodic excitation force, through Equation 3.12. In implementing the second step, the steady-state response function, which relates the flow speed to the steady state vibration amplitude excited by the flow at this wind speed, is required. Fei & Vandiver [13] proposed the use of the following model in wind-induced vibration problems:

$$f(V_r) = \begin{cases} 0 & V_r \leq 5.0 \text{ or } V_r \geq 6.5 \\ V_r - 5.0 & 5.0 \leq V_r \leq 6.0 \\ 2(6.5 - V_r) & 6.0 \leq V_r \leq 6.5 \end{cases} \quad (3.32)$$

Figure 3-3 shows the model proposed by Fei & Vandiver. Models proposed by other authors were listed in Section 3.2.

The time trace of the corresponding excitation force (per unit mass) which is defined in Equation 3.19 can be expressed as follows:

$$\begin{aligned} \omega_n^2 u(t) &= f_a(t) \cos \omega_n t \\ &= 2\omega_n^2 \zeta A_{max} f(V_r(t)) \cos \omega_n t \end{aligned} \quad (3.33)$$

- **Calculating the transient vibration amplitudes.** Once the time trace of the excitation force is derived, the transient displacement response of the cylinder at an anti-node of the cylinder can be solved from the linear difference equation 3.19. In order to advance the solution in the time domain, proper initial values of vibration amplitudes at two consecutive time intervals are required. For the cylinder that starts to vibrate from a stationary state, it is convenient to set the initial conditions as follows:



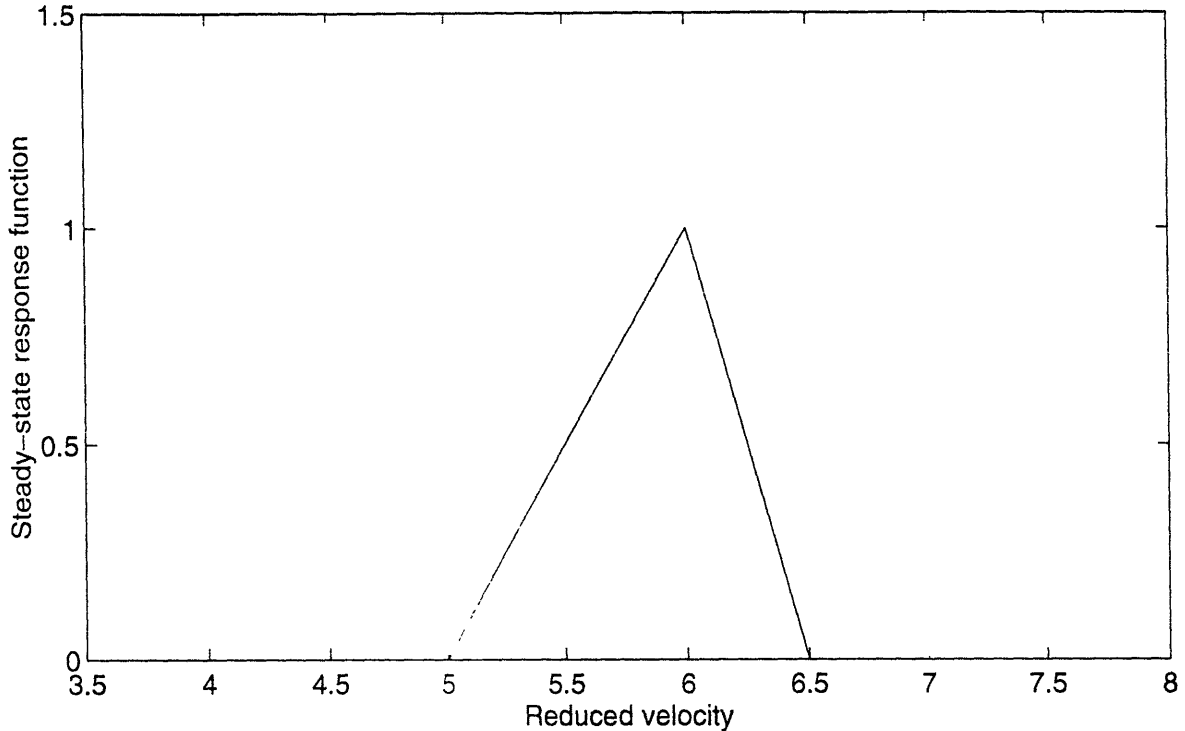


Figure 3-3: steady-state response function. proposed by Fei & Vaniver

$$\begin{aligned} x(1) &= 0 \\ x(2) &= 0 \end{aligned}$$

- Assessing the resulting fatigue damage.** Once the time trace of VIV amplitudes has been solved, the corresponding envelope of the transient motion  $A(t)$  (where  $A(t) = \{A(t), i = 1, n\}$ ) which consists of the peak values of the transient vibration amplitudes  $x(t)$  can be collected. The total fatigue damage over the duration of stress cycles can be calculated using Equation 3.29 for a prescribed  $S-N$  curve. Fatigue failures are deemed to occur if the total damage exceeds 1.

### 3.4 Examples

In this section, examples will be given to evaluate the performance of the proposed time domain VIV model on a 1.903 inch diameter carbon fiber tube. The tube is pinned at both ends and is allowed to vibrate freely in between. The tube that presented is the same as the test cylinder that was built for our wind tunnel experiments

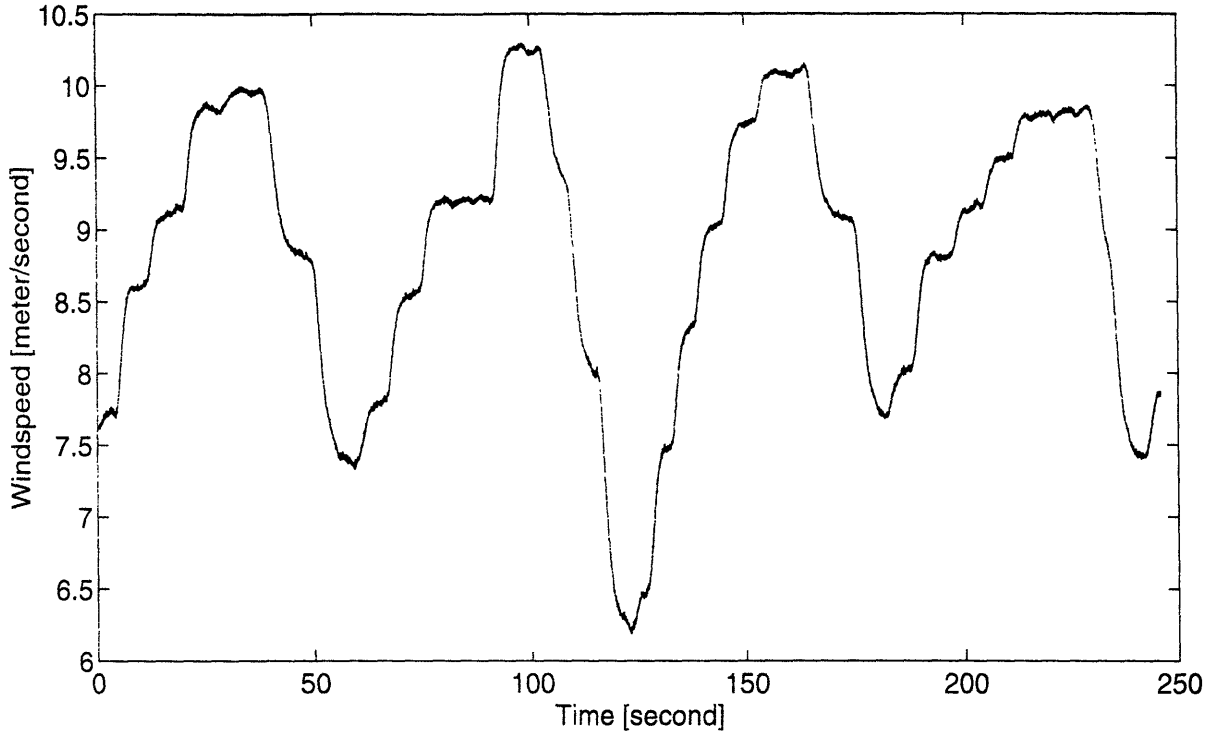


Figure 3-4: Time trace of the measured windspeed in metric units

that were described in the previous chapter. The main parameters of the tube were documented in Rudge & Fei [30] and Nicholls [26] and are summarized briefly as follows:

- Total length ( $L$ ) = 2.0955 [m] or 82.5 [in]
- Outside diameter ( $D$ ) = 0.0483 [m] or 1.903 [in]
- Wall thickness ( $t$ ) = 0.0023 [m] or 0.089 [in]
- Mass density ( $\rho_m$ ) = 1597.674 [ $\text{kg}\cdot\text{m}^{-3}$ ] or 3.100 [ $\text{slug}\cdot\text{ft}^{-3}$ ]
- Natural frequency (first mode  $f_1$ ) = 32.375 [ $\text{s}^{-1}$ ]
- Structural damping ratio in air ( $\zeta$ ) = 0.35%
- Young's modulus ( $E$ ) =  $7.7 \times 10^6$  [psi] or  $5.3 \times 10^4$  [MPa].

The maximum steady state vibration amplitude is predicted first by using the Brown & Root [29] prediction model. The solution sequence for predicting the maximum steady state vibration amplitude of the tube is listed step by step in Table 3.3.

Four cases are presented to test the validity of various time domain VIV prediction models. In case one, the transient vibrations of the test tube at its mid-span are predicted following the step-by-step procedure in Table 3.3. Predictions are compared with the wind tunnel measurements. The measured time histories of the instantaneous wind speed are used in predictions. Figure 3-4 shows the time trace of the instantaneous wind speed. This wind speed sequence was sampled continuously for 246 seconds at a sampling frequency of 512 Hertz. In case two, the effect of using different steady-state response functions is assessed. The predicted transient vibrations using each of the steady-state response functions proposed by **DnV**, **BS 8100**, **ESDU** and **Fei & Vandiver** with identical input wind speed sequences are compared with the measured transient vibrations. In case three, the effect of downsampling the original wind speed sequence on the accuracy of predictions is studied. The original wind speed sequence is re-sampled at two lower frequencies. The predicted transient vibrations corresponding to the downsampled wind speed sequences are compared with the measured transient vibrations. In case four, the effect of using the mean wind speed to predict transient vibrations is studied. The predicted transient vibrations based on the mean wind speed are compared with the wind-tunnel measurements.

### 3.4.1 Case one: predictions *v.s.* wind tunnel measurements

In this case, the transient vibrations of the cylinder corresponding to the wind speed shown in Figure 3-4 are predicted using the step-by-step implementation procedure that was described in Section 3.3. The steady-state response function proposed by Fei & Vandiver [13] is used in constructing the sequence of excitation force from the sequence of the corresponding wind speed samples. The predictions will be shown to have remarkable accuracy when compared with the wind tunnel measurements.

Figure 3-5 shows the time trace of the wind speed expressed in terms of reduced velocities. The wind speed is seen to vary considerably with time but is within the excitation range of the first mode of the cylinder.

Figure 3-6 shows the time trace of the equivalent excitation force derived from the time trace of the corresponding windspeed by Equation 3.12, using the steady-state response function proposed by Fei & Vandiver [13] in Equation 3.32.

Figure 3-7 shows the time trace of the predicted transient vibration amplitudes of the test tube under the excitation force that was shown in Figure 3-6.

The envelope of the predicted transient vibrations, consisting of the peaks (local minima and local maxima) of the transient vibration amplitudes, is shown in Figure 3-8. The envelope of the measured transient vibrations at the mid-span of the test tube is also shown in the same figure for comparison. This comparison clearly demonstrates the accuracy of the prediction.

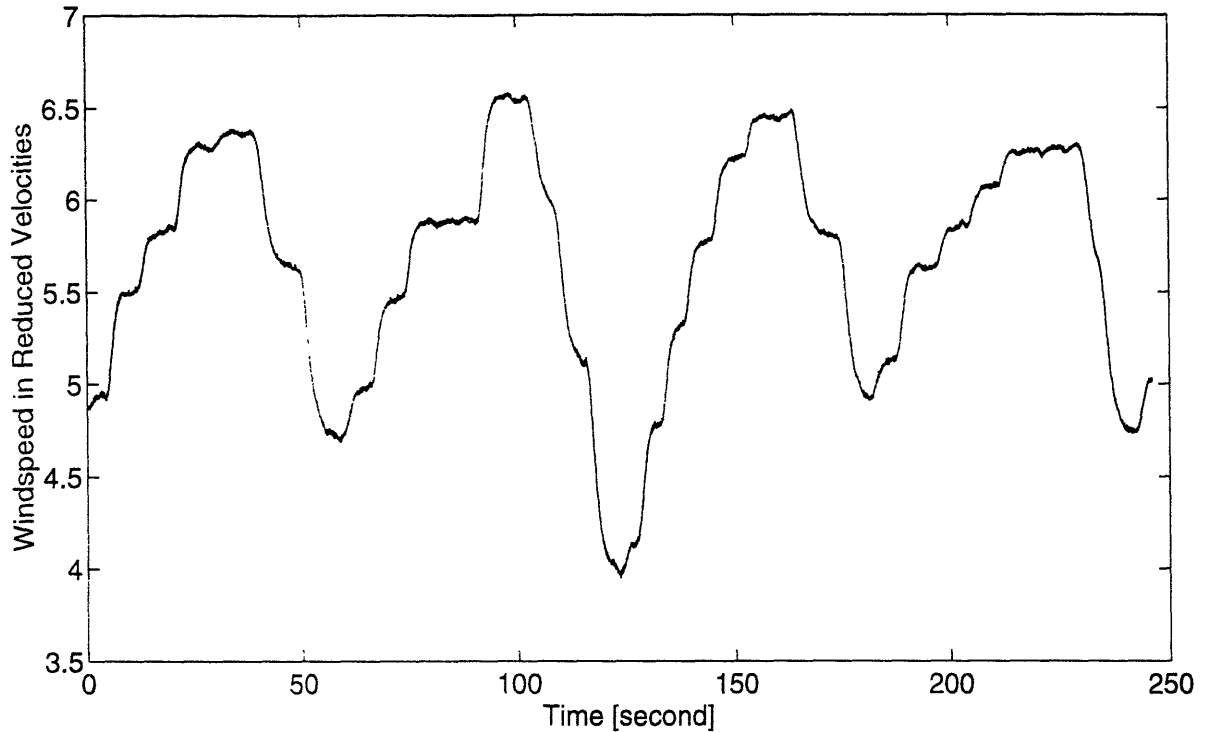


Figure 3-5: Time trace of the measured windspeed expressed in terms of reduced velocities

### 3.4.2 Case two: effect of different steady-state response functions

In this case, the effect of different steady-state response functions  $f(V_r)$  on transient response predictions is studied for identical input sequences of the wind speed samples. Four different steady-state response functions are studied: **DnV**, **BS 8100**, **ESDU 85038/Brown & Root** and **Fei & Vandiver**. For each proposed steady-state response function, the time trace of the wind speed is chosen to be identical to that shown in Figure 3-4; the corresponding excitation force and the transient vibrations are predicted; and the envelope of predicted transient vibrations are then compared with the envelope of measured transient vibrations.

Figure 3-9 shows the predicted transient vibration envelope using the steady-state response function proposed by **DnV**, as well as the measured transient vibration envelope. The steady-state response function proposed by **DnV** was shown in Equation 3.2. **DnV** assumes a constant steady state vibration amplitude in the reduced velocity range of 4.7 to 8.0, thus neglecting possible response reduction at off-critical wind speeds. It is clear from Figure 3-9 that such an assumption over-predicts the response magnitudes, and consequently leads to a conservative estimation in fatigue damage rate. As a conclusion, any reasonable steady-state response function leading to an acceptable vibration prediction should therefore allow for response reduction at

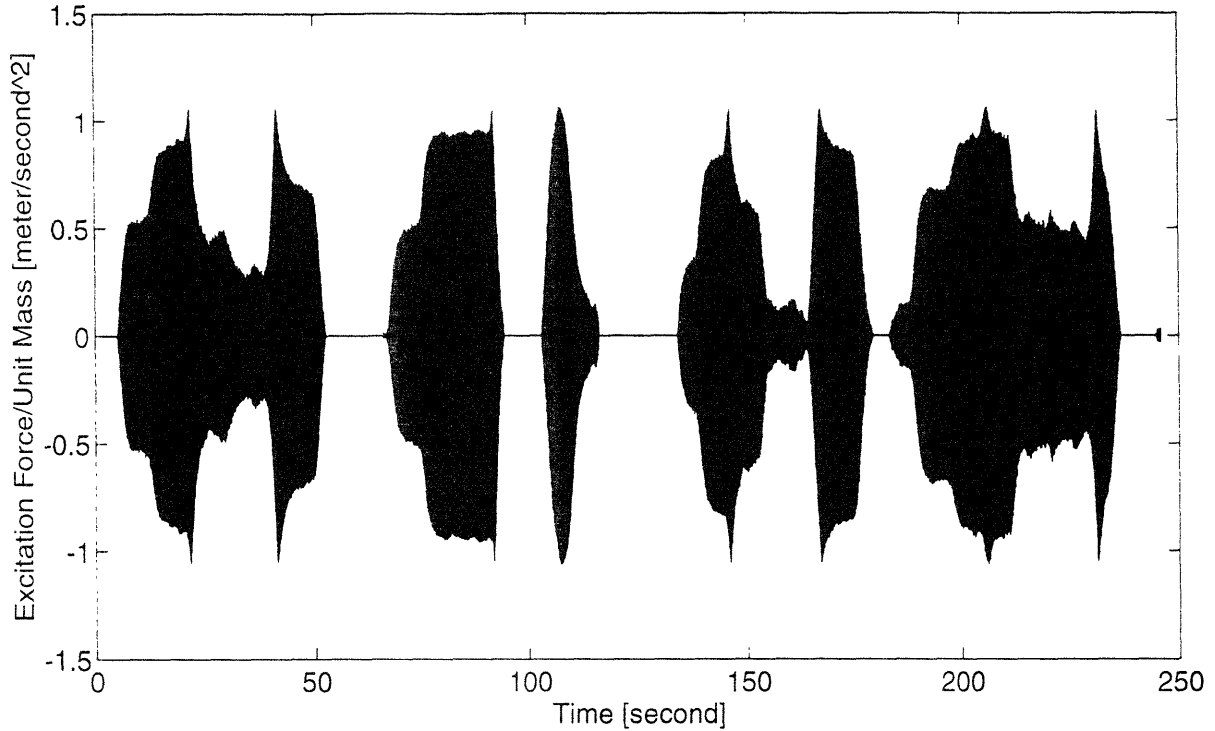


Figure 3-6: Time trace of the predicted excitation force acting on the SDOF oscillator, in newtons per unit mass

off-critical wind speeds.

Figure 3-10 shows the predicted transient vibration envelope using the steady-state response function proposed by **BS 8100**, as well as the measured transient vibration envelope. The steady-state response function proposed by **BS 8100** was shown in Equation 3.3. Although **BS 8100** allows for the steady state vibration amplitude to vary with the reduced velocity when the reduced velocity is within 3.85 to 6.90, as demonstrated by the predicted vibration amplitudes over time, the match in vibration amplitudes between the prediction and the measurement at the corresponding time is poor. Specifically, **BS 8100** is not able to identify the exact locations of the peak vibration amplitude; and **BS 8100** is conservative since it shows much smaller decay in vibration amplitudes when the wind speed moves out of the excitation range, compared with the measurements. These two differences in predictions and measurements reveal the two corresponding drawbacks of the **BS 8100** model. First, the proposed excitation range ( $3.85 \leq V_r \leq 6.90$ ) does not agree with the measurements. Second, the tails of this response function are too broad. Consequently, the **BS 8100** model will lead to an overly conservative estimation in fatigue damage rate.

Figure 3-11 shows the predicted transient vibration envelope using the steady-state response function proposed by **ESDU 85038** and **Brown & Root**, as well

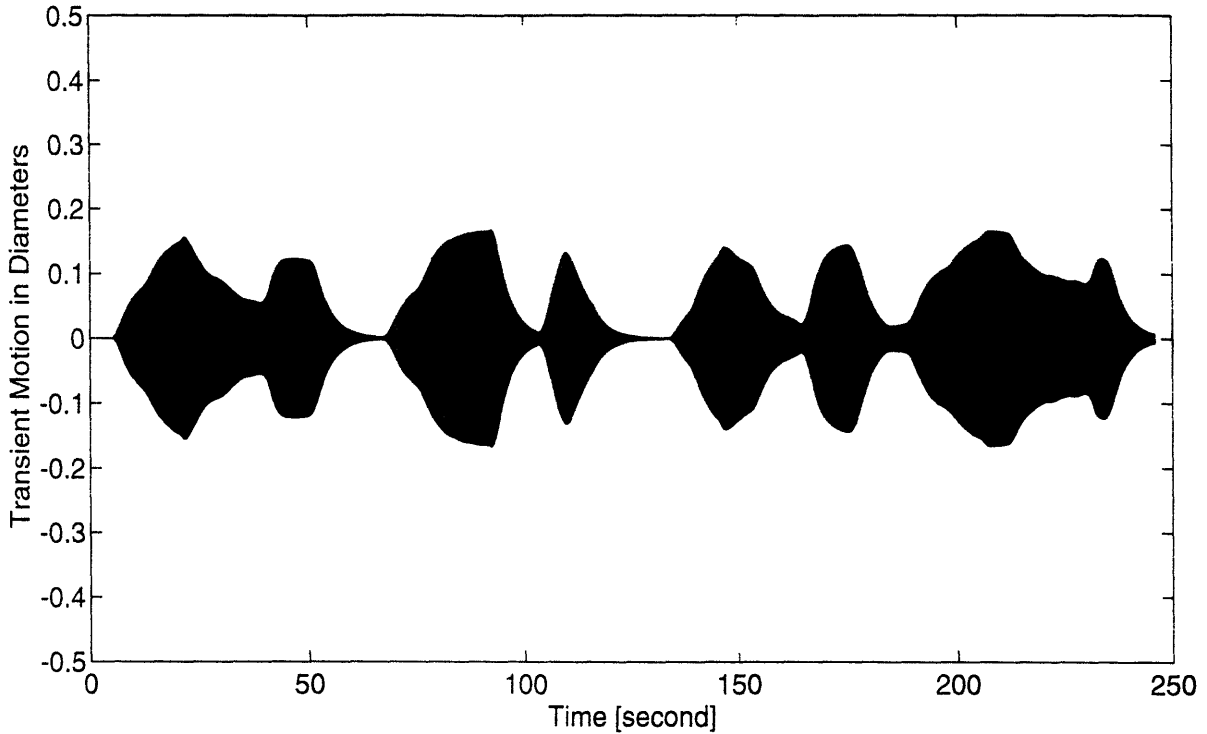


Figure 3-7: Time trace of the predicted transient vibrations at the mid-span of the cylinder, in diameters, from the proposed method

as the measured transient vibration envelope. The steady-state response function proposed by **ESDU 85038** was shown in Equation 3.4. The **ESDU 85038** model offers more flexibility. First, it allows the steady state vibration amplitudes to vary with the reduced velocity when the reduced velocity is within 4.25 to 5.25. Second, it allows the shape of the steady-state response function to vary with the  $K_s$  value, resulting in larger response for smaller  $K_s$ . The range of reduced velocity from 4.25 to 5.25 is too small. This results in inaccurate amplitude predictions and also a time shift in amplitudes between the predictions and the measurements, reflecting that the proposed excitation range ( $4.25 \leq V_r \leq 5.25$ ) does not agree with the measurements. Figure 3-11 reveals that the flexibility offered by the **ESDU 85038** model does not improve the prediction, but may rather lead to an under-predicted response which is undesirable for design purposes.

Figure 3-12 shows the predicted transient vibration envelope using the steady-state response function proposed by **Fei & Vandiver**, as well as the measured transient vibration envelope. This is a reproduction of Figure 3-8 shown in Case one. Close match in vibration amplitudes between the prediction and the measurement at the corresponding time indicates the success of the simple **Fei & Vandiver** model. More specifically, the proposed excitation range ( $5 \leq V_r \leq 6.5$ ) seems to agree well with measurements since the prediction accurately captures the rise and decay cycles of

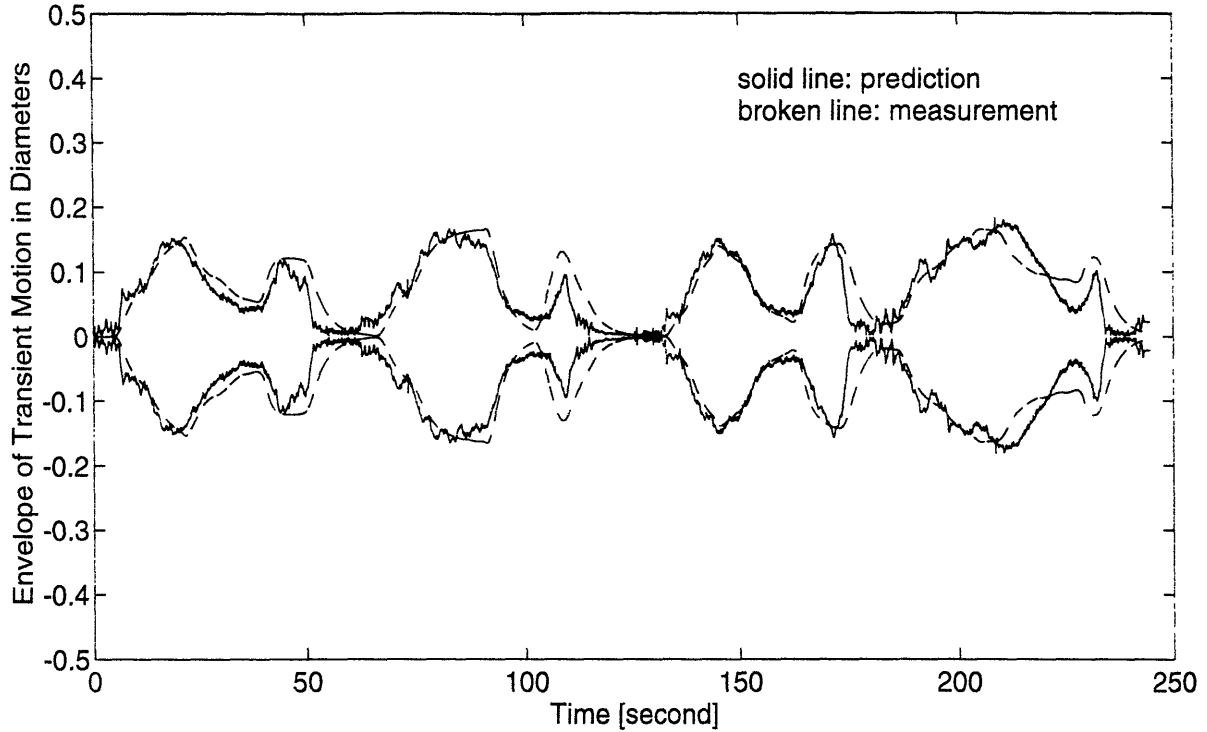


Figure 3-8: Envelope of the predicted and the measured transient vibration amplitudes at the mid-span of the cylinder, in diameters

the measured transient vibrations; the shape of the steady-state response function seems to be reasonable because of the close match in slopes of the rise and decay amplitudes between the prediction and the measurement.

### 3.4.3 Case three: effect of downsampling the wind speed

In this case, the effect of downsampling the original wind speed sequence on transient vibration predictions is studied. The original sequence of the wind speed (shown in Figure 3-4) with the sampling frequency of 512 Hertz is downsampled at two much lower sampling rates, 0.1 Hertz (period of 10 seconds) and 0.025 Hertz (period of 40 seconds). Corresponding transient vibrations are predicted for each of the two downsampled time traces of the wind speed and then compared with the measurements originally sampled at 512 Hertz.

Suppose  $V_1[i]$  and  $V_2[j]$  are, respectively, the discrete-time representations of the continuous-time signal  $V(t)$  with different sampling frequencies. Both discrete sequences can be related to the underlying continuous signal as follows:

$$V_1[i] = V(iT_1) \tag{3.34}$$

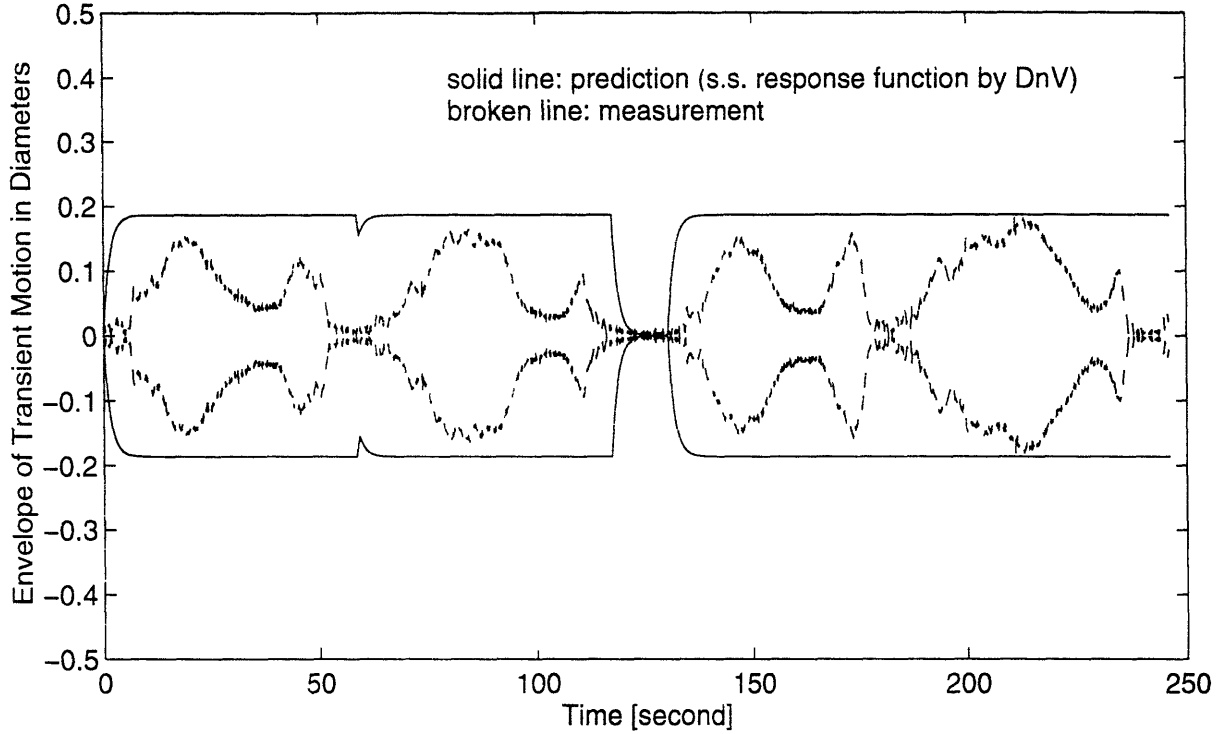


Figure 3-9: Comparison of the predicted and the measured transient vibration envelopes. Steady-state response function proposed by **DnV** is used for prediction.

$$V_2[j] = V(jT_2) \quad (3.35)$$

where  $i$  and  $j$  are, respectively, integers that represent the indices of the sequences  $V_1[i]$  and  $V_2[j]$ .  $T_1$  and  $T_2$  are, respectively, the sampling periods (inverse of the sampling frequency) of the sequences  $V_1[i]$  and  $V_2[j]$ .

$V_1[i]$  and  $V_2[j]$  can then be related to each other through Equations 3.34 and 3.35 as below

$$V_2[n] = V_1\left[\frac{nT_2}{T_1}\right] = V(nT_2) \quad (3.36)$$

Figure 3-13 shows the time traces of the original wind speed sequence  $V_1[i]$  with a sampling frequency of 512 Hertz ( $T_1 = 1.95 \times 10^{-3}$  seconds) and the downsampled wind speed sequence  $V_2[j]$  with a sampling frequency of 0.1 Hertz ( $T_2 = 10$  seconds). According to Equation 3.36,  $V_2[j]$  can be derived from  $V_1[i]$  through Equation 3.36 as follows:



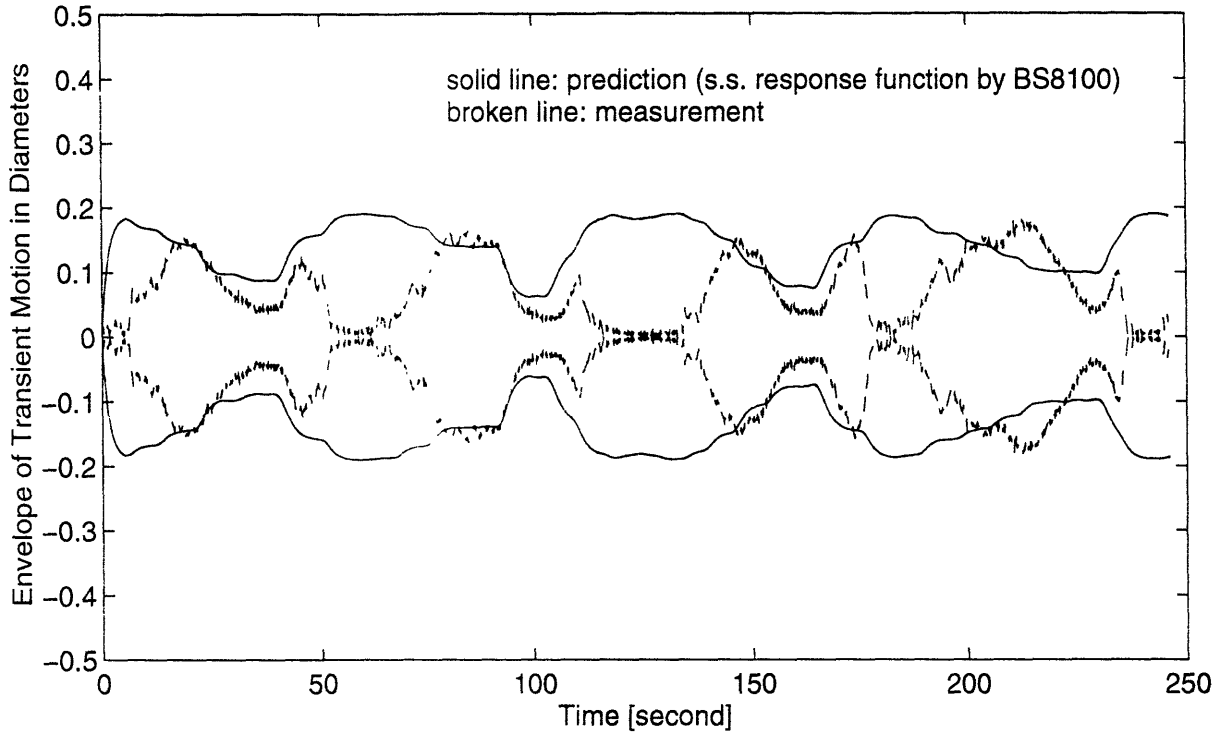


Figure 3-10: Comparison of the predicted and the measured transient vibration envelopes. Steady-state response function proposed by **BS 8100** is used for prediction.

$$\begin{aligned}
 V_2[j] &= V_1\left[\frac{jT_2}{T_1}\right] \\
 &= V_1[5120j]
 \end{aligned}
 \tag{3.37}$$

A total of 25 samples are taken in the downsampled wind speed sequence, and the total length of the sequence is 240 seconds. The downsampled wind speed sequence is found to be a good approximation to the original wind speed sequence, as shown in Figure 3-13. However, a sampling frequency of 0.1 Hertz may not be the optimal choice for natural winds as it was suggested by Figure 3-13, since the generated unsteady windspeed sequence does not resemble the behavior of natural winds.

Figure 3-14 shows the corresponding time traces of the envelopes of the predicted transient vibrations and the measured transient vibrations. To assure the accuracy of response predictions, the values of the windspeed between sampling points have been linearly interpolated. Linear interpolation of the windspeed tends to smooth the predicted response, but overall, the prediction seems to be a good approximation of the measurement.

Figure 3-15 shows the time traces of the original wind speed sequence  $V_1[i]$  with a

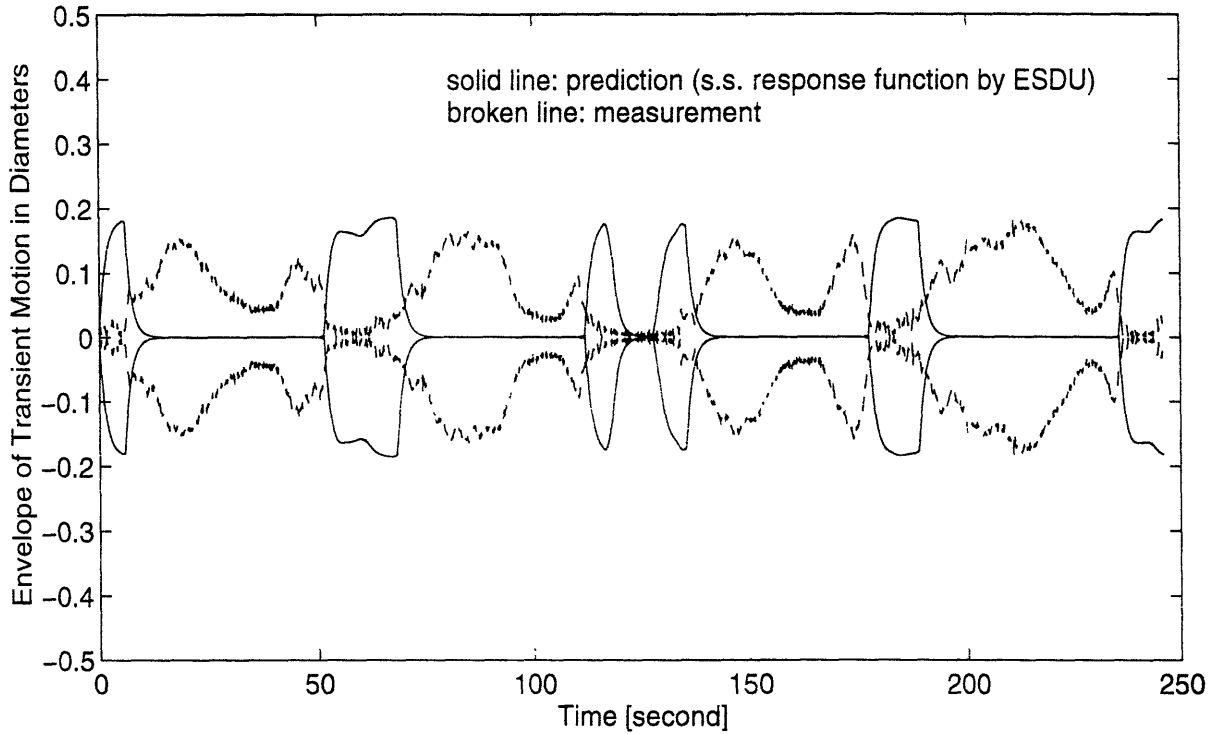


Figure 3-11: Comparison of the predicted and the measured transient vibration envelopes. Steady-state response function proposed by **ESDU 85038/Brown & Root** is used for prediction.

sampling frequency of 512 Hertz ( $T_1 = 1.9 \times 10^{-3}$  seconds) and the downsampled wind speed sequence  $V_3[k]$  with a sampling frequency of 0.025 Hertz ( $T_3 = 40$  seconds). According to Equation 3.36, the values of  $V_3[k]$  can be derived from the values of  $V_1[i]$  as follows:

$$\begin{aligned}
 V_3[n] &= V_1\left[\frac{nT_3}{T_1}\right] \\
 &= V_1[20480n]
 \end{aligned}
 \tag{3.38}$$

A total of 7 samples are taken in the new sequence, and the total length of the sequence is 240 seconds. Due to many fewer samples, the downsampled wind speed sequence no longer approximates the original wind speed sequence. Consequently, the transient response prediction based on downsampled wind speed sequence cannot be expected to resemble the measurement.

Figure 3-16 shows the corresponding time traces of the envelopes of the predicted transient vibrations and the measured transient vibrations. Fewer numbers of samples (caused by low sampling rates) remove the high-frequency components of the wind-

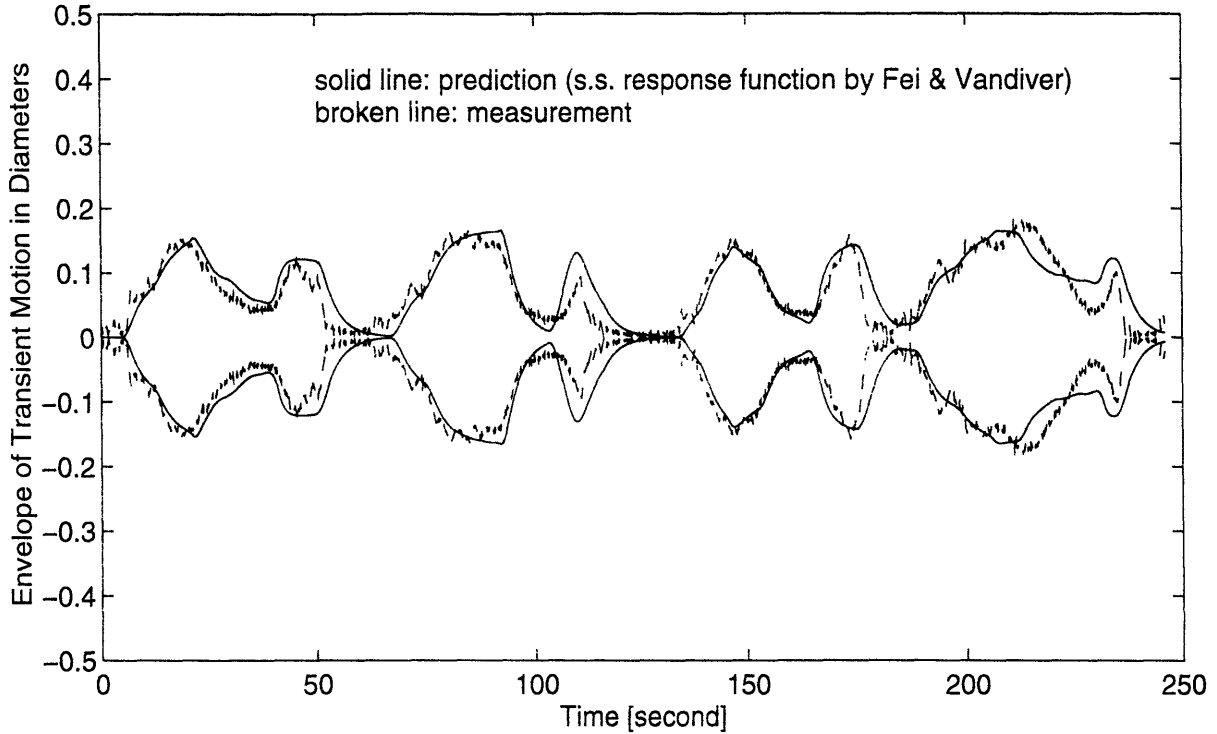


Figure 3-12: Comparison of the predicted and the measured transient vibration envelopes. Steady-state response function proposed by **Fei & Vandiver** is used for prediction.

speed, and (in the mean time) increase the steadiness of the windspeed. Consequently, the predicted transient vibrations show less transient effects and more tendency towards steady state. The inconsistency between the prediction and the measurement, caused by an inadequate sampling frequency of the wind speed, will inevitably result in a poor fatigue assessment.

### 3.4.4 Case four: effect of using mean windspeed

In this case, the effect of using the mean windspeed on transient response predictions is studied. The purpose of this study is to show why steady-state response predictions based on the mean windspeed (such as hourly mean windspeed) could lead to an unsatisfactory fatigue damage assessment.

A mean wind speed sequence is constructed, and the corresponding transient vibration response is predicted based on the SDOF algorithm. This mean wind speed sequence has the same length as the original wind speed sequence. The value of the mean wind speed sequence at any time is a constant equal to the mean of the original wind speed sequence over the entire 246 seconds. Figure 3-17 shows the time traces of the original wind speed sequence and the mean wind speed sequence expressed in

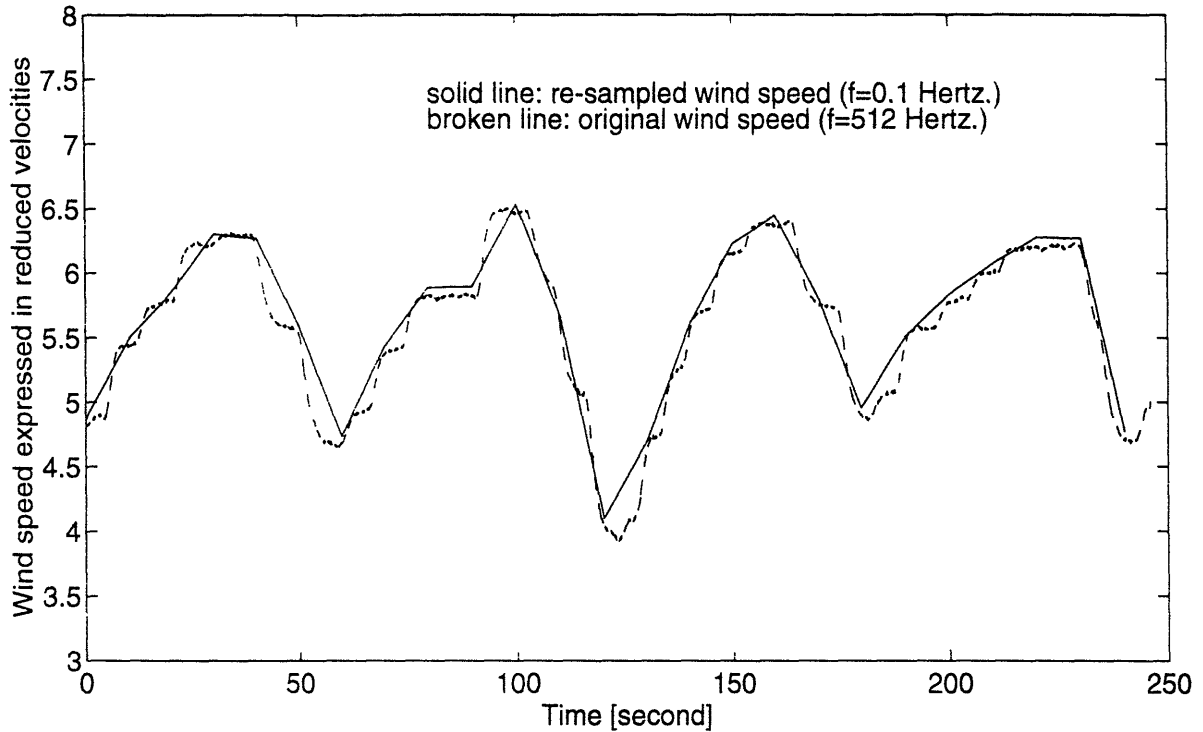


Figure 3-13: Time traces of the original wind speed (sampling frequency of 512 Hertz) and the downsampled wind speed (sampling frequency of 0.1 Hertz)

terms of reduced velocities. The purpose of constructing the new wind speed sequence is to simulate the consequence of using hourly mean windspeed in predicting the VIV response and fatigue damage of real offshore structures.

Figure 3-18 shows the corresponding time traces of the envelopes of the predicted transient vibrations based on the mean wind speed and the measured transient vibrations. The predicted transient vibrations based on the mean wind speed are clearly steady-state vibrations, except for the small rise time at the beginning. Compared to the measurement with high-frequency resolution, the predicted steady-state vibrations are unrealistic, and could contribute to an overly conservative estimate in fatigue damage rate, especially when the mean wind speed happens to be close to the critical velocity of the structural member.

It is implied that a VIV design methodology based on the hourly mean windspeed could grossly over-calculate the occurrence of steady-state vibrations. Current design prediction methods generally assume that when the critical velocity of a given structural member is located within a particular bin of the hourly mean windspeed from a mean windspeed scatter diagram, then it is adequate to compute the steady state response of the member. The frequency of encountering that critical windspeed is equal to the probability of encountering that mean windspeed bin which brackets the

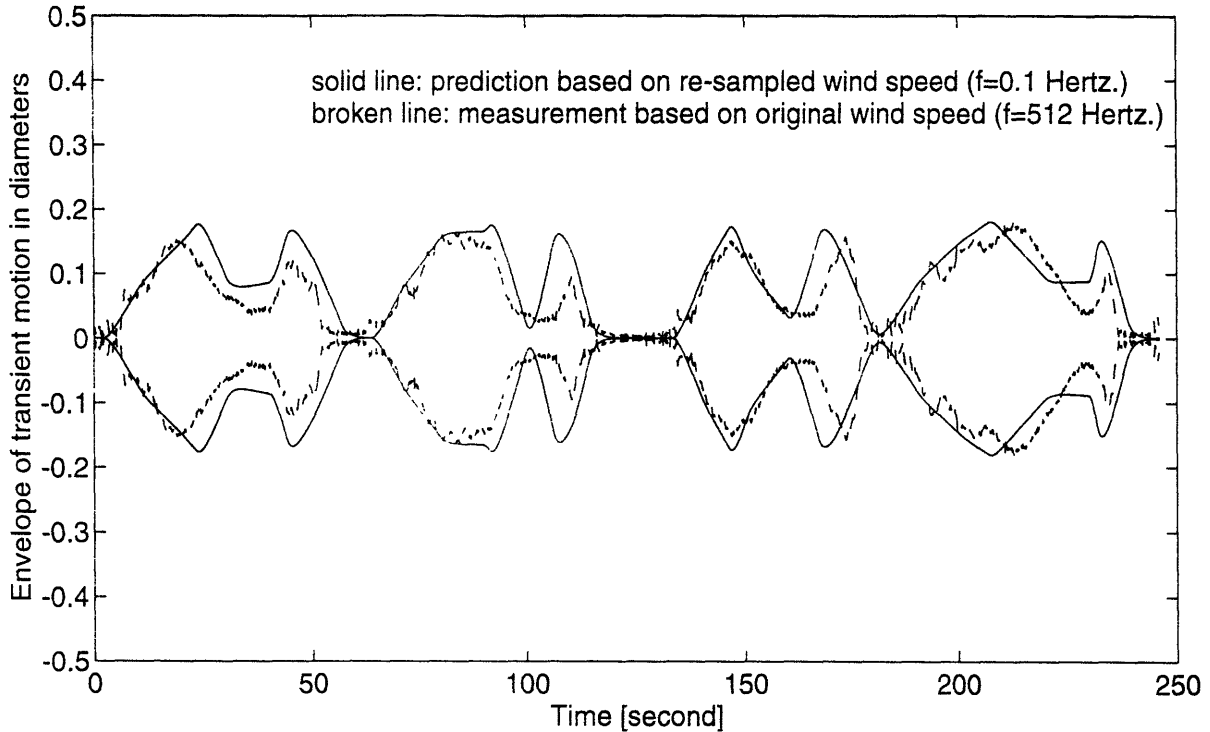


Figure 3-14: Time traces of the envelopes of the measured transient vibrations (sampling frequency of 512 Hertz) and the predicted transient vibrations (sampling frequency of 0.1 Hertz)

critical velocity of the member. These methods will predict a fatigue damage rate which depends on the size of the bin, resulting in a large value of fatigue damage for a coarse discretization of the mean windspeed scatter diagram.

### 3.5 Summary

In this chapter, a time domain SDOF model for predicting VIV of structural members in unsteady winds has been proposed. For a given time trace of the wind speed, the model constructs the corresponding time trace of the excitation force which depends on a particular steady-state response function. The transient vibrations are predicted as the result of time domain convolution between the excitation force and the impulse response function of the SDOF oscillator which has the resonant properties of the target structural member.

Four examples have been presented to illustrate the use of the proposed time domain SDOF model on VIV prediction of a 1.903 inch diameter carbon-fiber tube. In the first example, the proposed time domain VIV prediction model was implemented by a step-by-step procedure: first, a time trace of the wind speed has been selected;

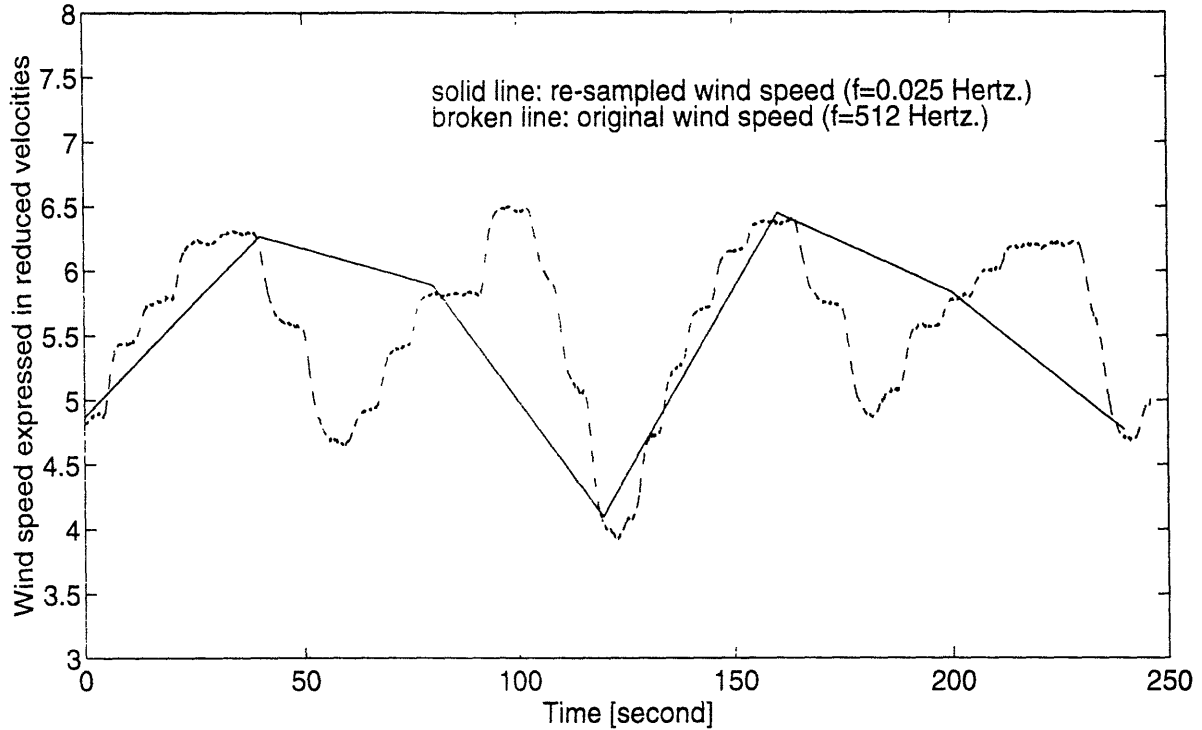


Figure 3-15: Time traces of the original wind speed (sampling frequency of 512 Hertz) and the downsampled wind speed (sampling frequency of 0.025 Hertz)

second, the corresponding excitation force has been derived; third, the corresponding transient vibrations of the target cylinder at its mid-span have been predicted. In transforming the wind speed to the corresponding excitation force, the steady-state response function proposed by Fei & Vandiver [13] has been used. The predicted transient vibrations have shown remarkable accuracy as compared to the measured transient vibrations.

In the second example, the effect of different steady-state response functions on the accuracy of the proposed VIV prediction model have been examined. The steady-state response function proposed by **DnV** and **BS 8100** have shown to overly predict the occurrence of steady state vibrations as compared to the measurements, and consequently lead to an unrealistically high estimate in fatigue damage rate. The steady-state response functions proposed by **ESDU 85038** and **Brown & Root** have allowed the flexibility of appreciable response reductions at off-critical windspeeds, but have failed to identify an excitation range consistent with the measurements. This failure may ultimately lead to a non-conservative estimate in fatigue damage rate. The simple steady-state response function proposed by **Fei & Vandiver** has shown remarkable success as compared to the measurements. First, it identifies the excitation range consistent with the measurements. Second, it allows for response reductions at off-critical windspeeds which are also consistent with the measurements.

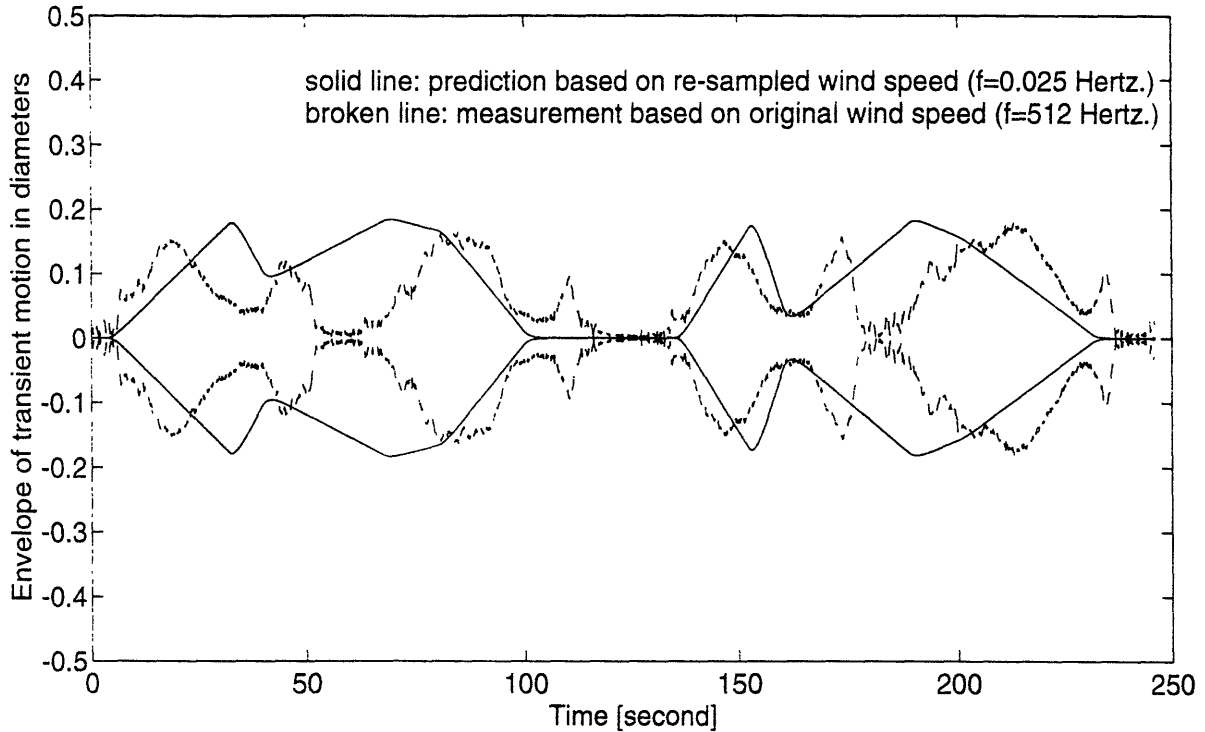


Figure 3-16. Time traces of the envelopes of the measured transient vibrations (sampling frequency of 512 Hertz) and the predicted transient vibrations (sampling frequency of 0.025 Hertz)

In the third example, the effect of downsampling the wind speed sequence on the accuracy of the proposed VIV prediction model has been studied. A downsampled wind speed sequence with a sampling frequency of 0.1 Hertz (sampling period of 10 seconds) has been found as a reasonable approximation to the original mean speed with a much higher sampling frequency. Not surprisingly, the corresponding predicted transient vibrations have also shown reasonable agreement with the measurements. On the other hand, a downsampled wind speed sequence with a sampling frequency of 0.025 Hertz (sampling period of 40 seconds) has shown tremendous deviation from the original wind speed. Consequently, the corresponding predicted transient vibrations are totally inconsistent with the measurements. It is conclusive that a high sampling frequency is necessary to ensure the resemblance between the sampled wind speed sequence and the continuous-time wind speed signal, and consequently to ensure the accuracy of response and fatigue damage assessment. It will be shown in the next chapter that the minimum sampling frequency is related to the dynamic rise time of the oscillator.

In the fourth example, the effect of using the mean windspeed to predict the transient vibrations has been studied. The predicted response based on a 246-second mean

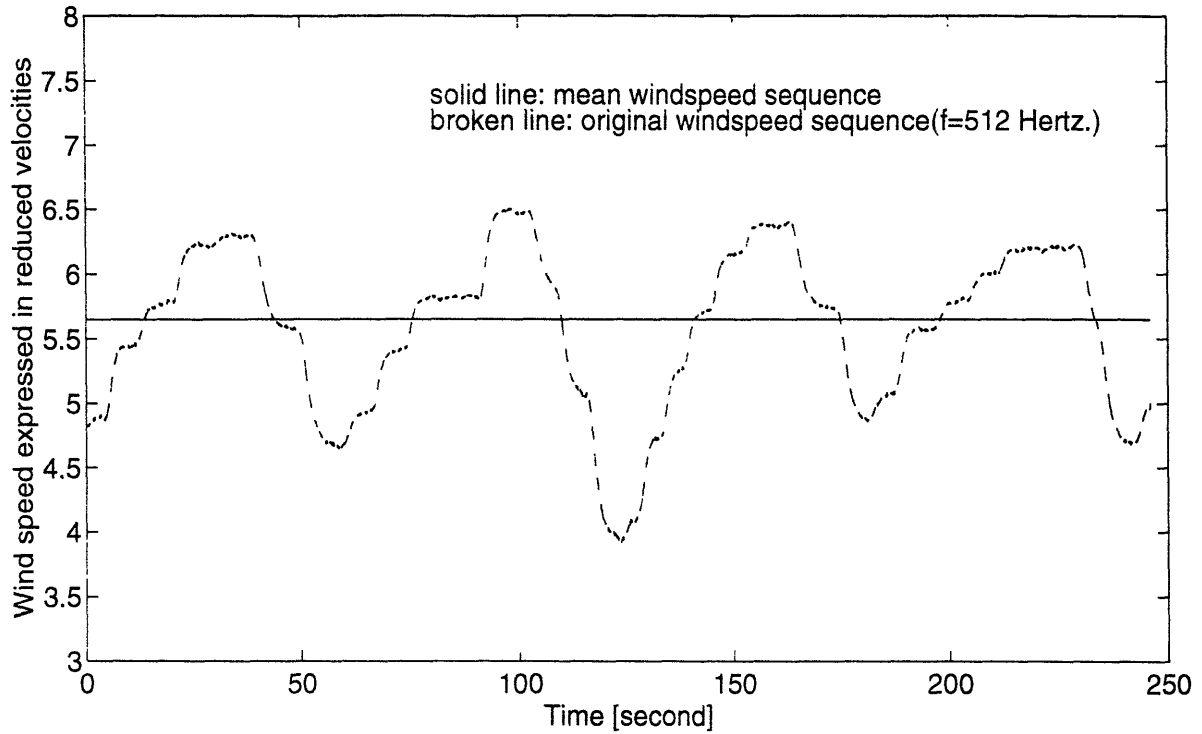


Figure 3-17: Time traces of the original wind speed sequence (sampling frequency of 512 Hertz) and the mean wind speed sequence

of the original windspeed sequence is essentially steady-state vibrations, remarkably inconsistent with the measured transient vibrations. It is implied that a VIV prediction based on the hourly mean wind speed could grossly over-calculate the occurrence of steady-state vibrations, and may lead to an overly conservative estimate in fatigue damage rate, especially when the hourly mean wind speed coincides with the critical velocity of the member.



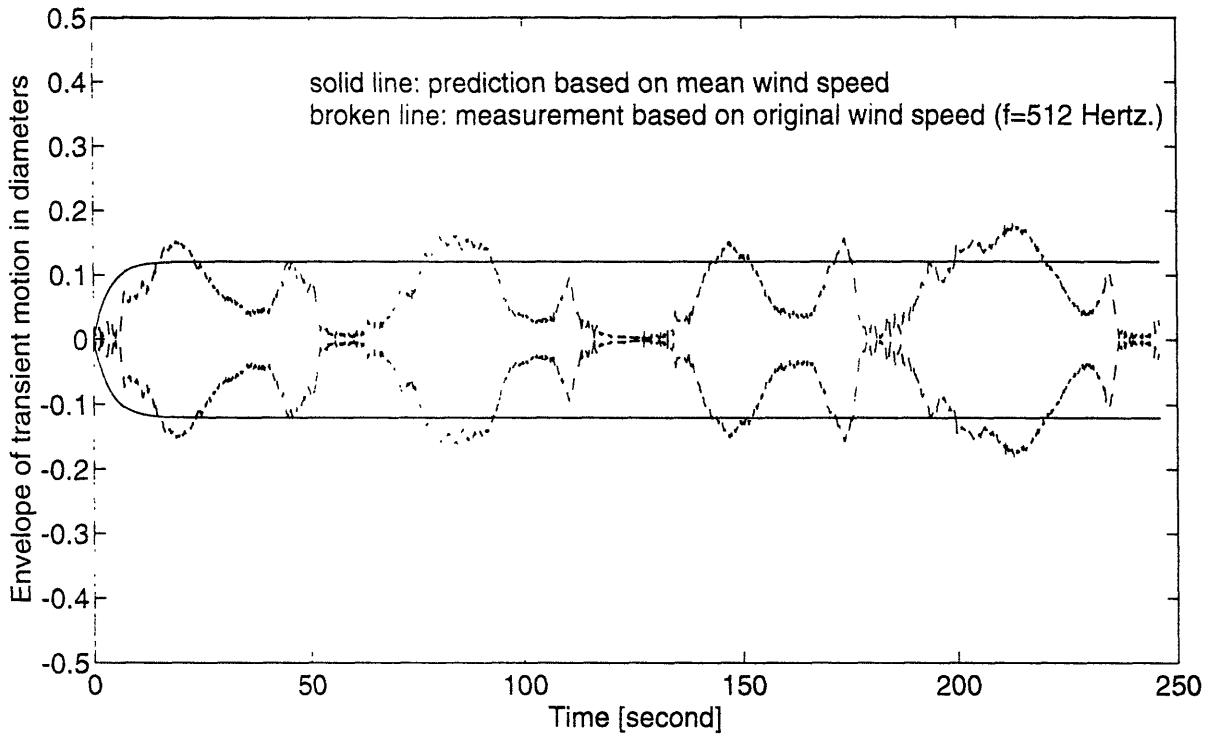


Figure 3-18: Time traces of the envelopes of the measured transient vibrations (sampling frequency of 512 Hertz) and the predicted transient vibrations corresponding to the mean wind speed sequence

Boundary Conditions	$F_i$
Free-Fixed	3.52
Pinned-Pinned	9.87
Fixed-Pinned	20.4
70% Fixity [16]	22.4
Fixed-Fixed	28.2

Table 3.1: Values of  $F_i$  for different boundary conditions, from Rudge & Fei (1991)

Boundary Conditions	$\gamma_i$
Free-Fixed	1.304
Pinned-Pinned	1.155
Fixed-Pinned	1.161
70% Fixity [16]	1.163
Fixed-Fixed	1.167

Table 3.2: Values of  $\gamma_i$  for different boundary conditions, from Rudge & Fei (1991)

Variable Name	Variable Symbol	Variable Value	SI units
$D$	outside diameter	0.0483	[m]
$t$	wall thickness	0.0023	[m]
$f_1$	natural frequency	32.375	[s <sup>-1</sup> ]
$\rho_m$	mass density	1597.674	[kg·m <sup>-3</sup> ]
$\gamma_i$	mode shape parameter	1.155	
$\zeta$	damping coefficient	0.35%	
$V_{crit}$	critical velocity	7.82	[m·s <sup>-1</sup> ]
$Re$	Reynolds number	26,068	
$St$	Strouhal number	0.2	
$C_L$	lift force coefficient	0.42	
$K_s$	stability parameter	8.57	
$A_{max}$	maximum amplitude	0.0092	[m]
$A_{max}/D$	maximum amplitude	0.19	

Table 3.3: Prediction of the maximum vibration amplitude

# Chapter 4

## Probabilistic Models for VIV Predictions

### 4.1 Motivation

Natural wind-induced vibrations of structural members have been the source of fatigue damage to offshore platforms during fabrication and transportation and to flarebooms during in-service conditions. To avoid failures, it is important for designers to be able to predict such vibrations as well as the resulting fatigue damage.

Current response prediction methods generally assume that when the mean wind speed is within the critical wind speed range for a given structural member, then it is adequate to compute the steady state response of the member. However, practical experience has revealed [16] that these methods *over-predict* the response, and, predict structural failures *too* frequently.

One explanation of the over-conservatism was suggested by Rudge et. al [31]. They found that the frequency of occurrence of steady state vibrations at the critical wind velocity is greatly *over-estimated*, since it is assumed that ideal conditions, which require low turbulence and increasing wind speeds, allow lock-in to develop to its fullest extent at which peak amplitudes are seen. This explanation was later supported by the results of wind tunnel experiments described in Chapter 3.

Figures 3-5 and 3-8 showed, respectively, the time traces of the instantaneous windspeed and the corresponding transient vibration peaks of a flexible cylinder from a typical transient test described in Chapter 3. It is clear from the figures that, although the mean wind speed was ideal for lock-in conditions, unsteady fluctuations in the wind speed typically prevented vortex-excited vibrations from reaching steady state amplitudes. The Brown & Root formula [29] predicted that the maximum steady state vibration amplitude would be 0.193 diameters. 0.191 diameters was the maximum measured vibration amplitude in a test where the windspeed was increased monotonically and steady state vibration amplitudes at different windspeeds were

measured. In the transient test the duration of time that the wind speed stayed within the critical velocity range for the member was less than the transient buildup time for this lightly damped vibration mode, and maximum amplitude response rarely occurred. Under ideal steady state lock-in conditions, mid-span vibration amplitudes of 0.19 diameters were observed.

In this chapter and the next, a probabilistic model is proposed in which three discount factors contributing to the fatigue damage reduction of structural members in random winds are identified. The first factor is caused by the fluctuations of the instantaneous windspeed around its mean, and can be determined by the PDF of the instantaneous windspeed and the critical velocity of the structural member. The second factor is caused by the finite rise time of the structural response, and is predicted in terms of the ratio of the expected duration of a visit to the rise time of the structural response. The third factor is the over estimation of response caused by discretizing the PDF of the mean windspeeds into rather broad bins. The conservative assumption is often made that if the critical windspeed for a member coincides with any part of a discrete bin then the probability of encountering that critical windspeed is equal to the probability of encountering that bin. This fails to account for lower off-critical response within a bin. The wider the bin the worse the error. The proposed model is illustrated by worked examples. The results of the probabilistic model are verified with the results of the time domain VIV model with the input of the raw windspeed data.

## 4.2 Analysis of time scales

There are two time scales that determine the vibration amplitude and the fatigue damage rate of a flexible cylinder in random winds. One is the duration of a visit by the wind speed to the critical velocity interval. The other is the rise time of the structural vibration response.

### 4.2.1 Duration of a visit by the wind speed to an interval $[a, b]$

Duration of a visit by the wind speed to an interval  $[a, b]$  is defined as the undisrupted length of time that wind speed spends between levels  $a$  and  $b$ . The definition of the duration of a visit by wind speed to an interval can be illustrated in Figure 4-1.  $\mathcal{T}_{[a,b]}$ , the duration of a visit to the interval  $[a, b]$ , starts with either an upcrossing of the windspeed at level  $a$  or a downcrossing of windspeed at level  $b$ , and ends with either an upcrossing at  $b$  or a downcrossing at  $a$ .

In the case of random winds, the duration of a visit by the wind speed to an interval is a random variable that depends on the mean rates of crossings by the wind speed

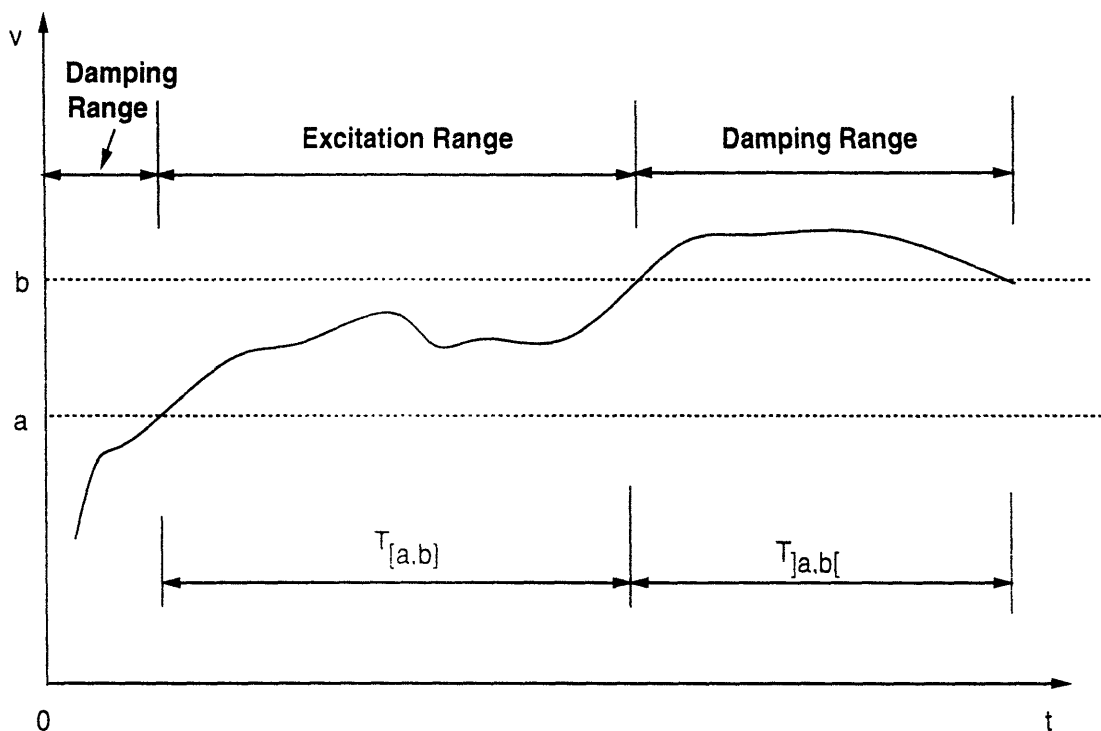


Figure 4-1: Duration of a visit by the wind speed to an interval  $[a, b]$

at levels  $a$  and  $b$ . The exact distribution of the duration of a visit by wind speed to an interval is not known except for very few processes [11]. However, the exact mean can be calculated as follows, provided that the wind speed is a stationary random process:

Consider the successive times  $\mathcal{T}_{[a,b]}$  and  $\mathcal{T}_{]a,b[}$  which a stationary random process  $V(t)$  spends, respectively, within  $[a, b]$  and outside  $[a, b]$ . To derive the mean value  $E[\mathcal{T}_{[a,b]}]$ , we need to apply a nonlinear transformation to the windspeed process  $V(t)$ . Let  $X(t)$  be a random process that can be derived from  $V(t)$  in the following way:

$$X(t) = y - (V(t) - a)(V(t) - b) \quad (4.1)$$

where  $y$  is an arbitrary positive real constant.

This transformation, as expressed in Equation 4.1, establishes a nonlinear mapping from  $V(t)$  to  $X(t)$ . Specifically, the windspeed samples within the velocity interval  $[a, b]$  are mapped to the samples of the process  $X(t)$  which have the values greater or equal to  $y$ ; whereas the windspeed samples outside the interval  $[a, b]$  are mapped to the samples of the process  $X(t)$  which have the values less than  $y$ . Therefore, calculating the mean duration of a visit by the windspeed to the interval  $[a, b]$  is equivalent to calculating the mean length of stay by the process  $X(t)$  above the level  $y$ .

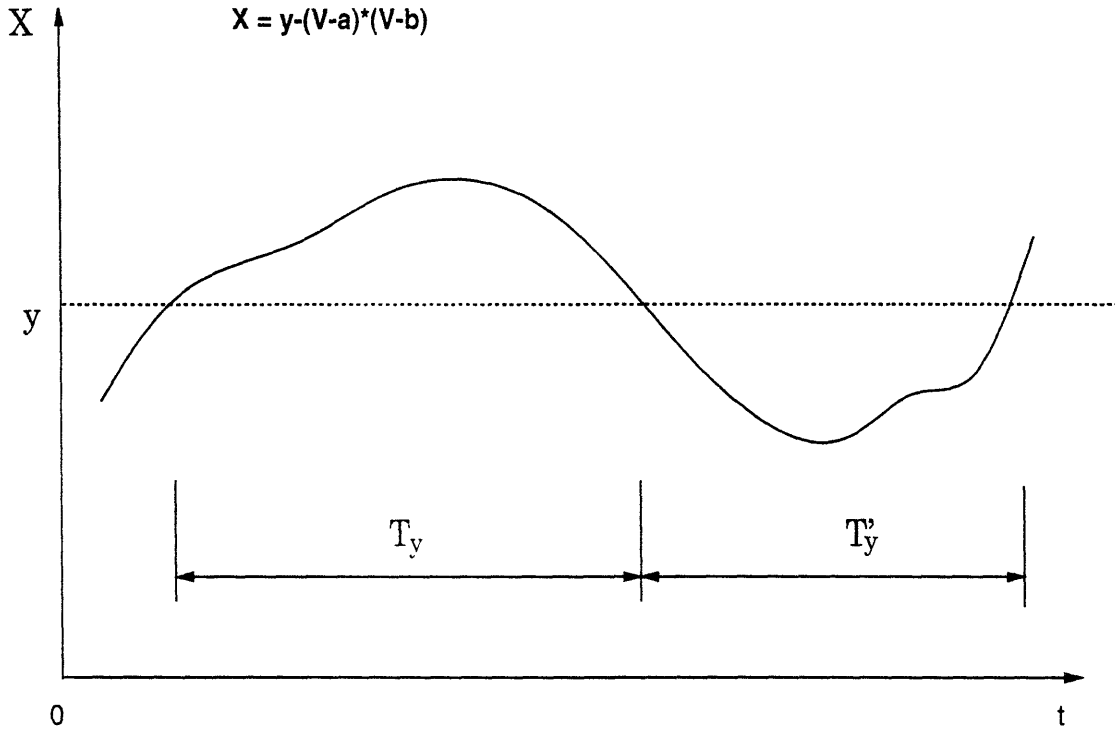


Figure 4-2: Durations of stay above and below a fixed threshold  $y$

Figure 4-2 shows the time history of the process  $X(t)$ , which is derived from the windspeed process  $V(t)$  shown in Figure 4-1. through the nonlinear transformation expressed in Equation 4.1.  $T_y$  and  $T'_y$  are, respectively, the successive times which  $X(t)$  spends above and below the threshold  $y$ . Since  $a \leq V \leq b$  corresponds to  $X \geq y$ , thus  $T_y = \mathcal{T}_{[a,b]}$ . In the following, we will derive  $E[T_y]$  in terms of the statistics of  $X(t)$ , then express  $E[\mathcal{T}_{[a,b]}]$  in terms of the statistics of  $V(t)$ .

$E[T_y]$ , the mean value of  $T_y$ , can be expressed as below for a stationary random process  $X(t)$  [39] (this is true if the windspeed process  $V(t)$  is stationary).

$$E[T_y] = \frac{1 - F_X(y)}{\mu_y^-} \quad (4.2)$$

where  $F_X(y)$  is the CDF of the process  $X(t)$  evaluated at  $y$ .  $\mu_y^+$  is the mean rate of crossing the level  $X(t) = y$  at positive slopes.

Since  $a \leq V \leq b$  corresponds to  $X \geq y$ , the probability of the windspeed within the critical velocity interval is equivalent to the probability that the derived process  $X(t)$  exceeds the level  $y$ . Since each upcrossing at the level  $X(t) = y$  corresponds to either a simultaneous upcrossing at the level  $V(t) = a$  or a simultaneous downcrossing at the level  $V(t) = b$ , the frequency of crossing the level  $X(t) = y$  at positive

slopes is equivalent to the frequency of crossing the level  $V(t) = a$  at positive slopes and crossing the level  $V(t) = b$  at negative slopes. Therefore,  $F_X(y)$  and  $\mu_y^+$  can be related to the statistics of  $V(t)$  as follows.

$$1 - F_X(y) = F_V(b) - F_V(a) \quad (4.3)$$

$$\begin{aligned} \mu_y^+ &= \nu_a^+ + \nu_b^- \\ &= \nu_a^+ + \nu_b^+ \end{aligned} \quad (4.4)$$

where  $F_V(b)$  and  $F_V(a)$  are, respectively, the CDFs of the windspeed process  $V(t)$  evaluated at  $b$  and  $a$ .  $\nu_a^+$  is the mean rate of crossing the level  $V(t) = a$  at positive slopes.  $\nu_b^+$  and  $\nu_b^-$  are the mean rates of crossing the level  $V(t) = b$  at positive and negative slopes respectively. Since every up-crossing is followed by a down-crossing,  $\nu_b^+ = \nu_b^-$ . The mean rate of crossing the level  $V(t) = \theta$  can be expressed as follows [39].

$$\nu_\theta^+ = \nu_\theta^- = \frac{1}{2} \int_{-\infty}^{\infty} |\dot{v}| p_{V\dot{V}}(\theta, \dot{v}) d\dot{v} \quad (4.5)$$

where  $p_{V\dot{V}}(v, \dot{v})$  is the joint PDF of the random process  $V(t)$  and its time derivative process  $\dot{V}(t)$ .

Substituting Equations 4.3 and 4.4 into Equation 4.2, we arrive at the equation for the mean duration of a visit by the windspeed to the critical interval  $[a, b]$ .

$$E[\mathcal{T}_{[a,b]}] = \frac{F_V(b) - F_V(a)}{\nu_a^+ + \nu_b^+} \quad (4.6)$$

It is worth noticing that Equation 4.6 is exactly the same as the result by Ditlevsen [11], where he analyzed the first outpassage time by a stationary, ergodic random process.

It is clear from Equation 4.6 that the mean duration of an undisrupted visit to a velocity interval depends not only on the probability distribution of the wind speed process  $V(t)$ , but also on the properties of its time derivative process  $\dot{V}(t)$ , due to the dependence of Equation 4.6 on the mean rates of crossings. If the windspeed can be described as a Gaussian process, then closed-form expressions for  $F_V(x)$ ,  $\nu_x^+$  and  $E[\mathcal{T}_{[a,b]}]$  are available as below.

$$F_V(x) = \int_0^x \frac{1}{\sqrt{2\pi}\sigma_V} \exp\left(-\frac{(v - \bar{V})^2}{2\sigma_V^2}\right) dv \quad (4.7)$$

$$\nu_x^+ = \frac{1}{2\pi} \frac{\sigma_{\dot{V}}}{\sigma_V} \exp\left(-\frac{(v - \bar{V})^2}{2\sigma_V^2}\right) \quad (4.8)$$

$$E[\mathcal{T}_{[a,b]}] = \frac{\int_a^b \frac{1}{\sqrt{2\pi}\sigma_V} \exp\left(-\frac{(v-\bar{V})^2}{2\sigma_V^2}\right) dv}{\frac{1}{2\pi} \frac{\sigma_V}{\sigma_{\dot{V}}} \left\{ \exp\left(-\frac{(a-\bar{V})^2}{2\sigma_V^2}\right) + \exp\left(-\frac{(b-\bar{V})^2}{2\sigma_V^2}\right) \right\}} \quad (4.9)$$

Mean upcrossing rates of non-Gaussian random processes can be determined from related Gaussian processes, through a univariate, nonlinear transformation [15] as follows.

Suppose  $F_V(v)$  and  $p_V(v)$  are the CDF and the PDF of the wind speed  $V(t)$  respectively, and  $\sigma_V$  and  $\sigma_{\dot{V}}$  are the standard deviations of the wind speed and the time derivative of the wind speed respectively. Our objective is to derive the mean upcrossing rate of the process  $V(t)$  in terms of the above quantities.

First, a Gaussian random process  $\tilde{Y}(t)$  is derived from the wind speed process  $V(t)$  through a non-linear transformation. The mean upcrossing rate of the process  $V(t)$  at level  $V(t) = \theta$  can be obtained from that of the derived Gaussian process  $\tilde{Y}(t)$  at a corresponding level. Let  $\tilde{Y}$  be a Gaussian random process of the same sampling rate and total length as  $V(t)$ , which consists of random variables  $\tilde{Y}_i$  of zero mean and unit variance. Then there exists a real function  $h(\tilde{Y}_i)$  such that

$$V_i = h(\tilde{Y}_i) = F_V^{-1}(\Phi(\tilde{Y}_i)) \quad (4.10)$$

where  $\Phi$  is the CDF of  $\tilde{Y}_i$  and  $\Phi(\tilde{Y}_i) = \frac{1}{\sqrt{2\pi}} \int_{-\infty}^{\tilde{Y}_i} \exp(-0.5\tilde{y}^2) d\tilde{y}$ . Since both  $F_V$  and  $\Phi$  are monotones,  $h$  is guaranteed to possess one to one mapping. The mean rate of crossing the level  $\theta$  by the process  $V(t)$  can be obtained from the mean rate of crossing the level  $\tilde{y} = h^{-1}(\theta)$  by the Gaussian process  $\tilde{Y}(t)$ , since  $V(t)$  and  $\tilde{Y}(t)$  upcross the level  $c$  and  $\tilde{y}$  respectively at the same instant. Thus the mean rate of crossing the level  $\theta$  by  $V(t)$  can be expressed as the mean rate of crossing the level  $\tilde{y} = h^{-1}(\theta)$  by the Gaussian process  $\tilde{Y}(t)$

$$\nu_{\theta}^+ = \frac{\sigma_{\dot{\tilde{Y}}}}{\sqrt{2\pi}} \phi(h^{-1}(\theta)) \quad (4.11)$$

where  $\phi$  is the PDF of  $\tilde{Y}_i$  and  $\phi(\tilde{Y}_i) = \frac{1}{\sqrt{2\pi}} \exp(-0.5\tilde{Y}_i^2)$ .

To calculate  $\nu_{\theta}^+$  requires finding the value of  $\sigma_{\dot{\tilde{Y}}}$ . Next  $\sigma_{\dot{\tilde{Y}}}$  is expressed in terms of the statistics of the original processes  $V(t)$  and  $\dot{V}(t)$ . First a new random process  $\tilde{V}(t)$  is defined that can be derived from the process  $V(t)$  as follows

$$\tilde{V}(t) = \frac{V(t) - E[V]}{\sigma_V} \quad (4.12)$$

where  $E[V]$  and  $\sigma_V$  are the mean and the standard deviation of the random process  $V(t)$ . The derived process  $\tilde{V}(t)$  has a zero mean and a unit variance. Furthermore,



the following equations hold for  $\tilde{V}(t)$ :

$$F_{\tilde{V}}(\tilde{v}) = F_V(v) \quad (4.13)$$

$$p_{\tilde{V}}(\tilde{v}) = \sigma_V p_V(v) \quad (4.14)$$

$$\sigma_{\dot{\tilde{V}}} = \frac{\sigma_{\dot{V}}}{\sigma_V} \quad (4.15)$$

where  $F_{\tilde{V}}(\tilde{v})$  and  $p_{\tilde{V}}(\tilde{v})$  are the CDF and the PDF of the random process  $\tilde{V}(t)$ , and  $\sigma_{\dot{\tilde{V}}}$  is the standard deviation of the process  $\dot{\tilde{V}}(t)$ .

Combining the equations 4.10 and 4.13, the process  $\tilde{V}(t)$  can be related to the process  $\tilde{Y}(t)$ :

$$\tilde{V}(t) = h^*(\tilde{Y}(t)) = F_V^{-1}(\Phi(\tilde{Y})) \quad (4.16)$$

Since  $\tilde{Y}(t)$  and  $\dot{\tilde{Y}}(t)$  are independent, as stationary Gaussian processes, the process  $\dot{\tilde{V}}(t)$  has zero mean and variance given as below

$$\sigma_{\dot{\tilde{V}}}^2 = E \left[ \left( \frac{dh^*(\tilde{Y})}{d\tilde{Y}} \right)^2 \right] \times E \left[ \left( \dot{\tilde{Y}}(t) \right)^2 \right] \quad (4.17)$$

That yields  $\sigma_{\dot{\tilde{V}}}^2 = \sigma_{\dot{\tilde{Y}}}^2 \eta^2$ , where  $\eta$  is given by:

$$\eta = \sqrt{\int_{-\infty}^{\infty} \frac{\phi^3(\xi) d\xi}{\{p_{\tilde{V}}[F_V^{-1}(\Phi(\xi))]\}^2}} \quad (4.18)$$

Finally, the mean upcrossing rate by the wind speed process  $V(t)$  at level  $\theta$  can be expressed more explicitly as

$$\nu_{\theta}^+ = \frac{1}{2\pi\eta} \frac{\sigma_{\dot{V}}}{\sigma_V} e^{-0.5\tilde{y}^2} \quad (4.19)$$

where  $\tilde{y}$  is given by:

$$\tilde{y} = \Phi^{-1} \left( F_{\tilde{V}} \left( \frac{\theta - E[V]}{\sigma_V} \right) \right) \quad (4.20)$$

$\sigma_V$  and  $\sigma_{\dot{V}}$  are, respectively, the standard deviations of the windspeed and the time derivative of the windspeed. Both quantities are necessary to calculate the mean up-

crossing rates of the windspeed, as indicated by Equation 4.19.

$\sigma_{\dot{V}}$  is a measure of the turbulence level and may be estimated in a rational way [2].  $\sigma_{\dot{V}}$  is not commonly reported and a database needs to be established from high sampling rate raw windspeed data. As part of this research,  $\sigma_{\dot{V}}$  has been estimated from a database measured at one marine site over a wide range of mean windspeeds and turbulence levels. This is reported in Chapter 6.

In absence of the database of local windspeed measurements, both  $\sigma_V$  and  $\sigma_{\dot{V}}$  can be obtained alternatively by integrating a proper power spectral density function of the wind speed  $S_V(f)$ :

$$\sigma_V = \sqrt{\int_0^{f_\infty} S_V(f) df} \quad (4.21)$$

$$\sigma_{\dot{V}} = 2\pi \sqrt{\int_0^{f_\infty} f^2 S_V(f) df} \quad (4.22)$$

where  $S_V(f)$  is the power spectral density function of the wind speed. The windspeed spectrum can be either obtained from local windspeed measurements, or can be adopted from a standard spectrum model with similar wind conditions.  $f_\infty$  is the cut-off frequency beyond which the wind speed spectrum is not valid. For example, the cut-off frequency could be half the sampling frequency of the windspeed measurements on which the spectrum model is based. A word of caution to derive  $\sigma_{\dot{V}}$  by integrating the windspeed spectrum is that  $f^2 S_V(f)$  may not resemble the true spectrum for  $\dot{V}$  to give an accurate estimate of  $\sigma_{\dot{V}}$ . To be confident in using this approach, one should compare the estimate with the true value of  $\sigma_{\dot{V}}$  derived directly from raw windspeed records. Derivations of  $\sigma_{\dot{V}}$  from high sampling rate raw windspeed data will be presented in Chapter 6.

In summary, for a given PDF and wind statistics such as  $\bar{V}$ ,  $\sigma_V$  and  $\sigma_{\dot{V}}$ , the calculation of the mean upcrossing rate by the non-Gaussian process  $V(t)$  involves the following steps:

- The first step is to define a Gaussian process  $\tilde{Y}(t)$  from the wind speed process  $V(t)$ , through a non-linear transformation. Since the CDFs of both processes are monotone, the transformation function  $h^*$  is guaranteed to possess one to one mapping. In general,  $h^*$  can only be derived numerically.
- The second step is to calculate  $\eta$  and  $\tilde{\gamma}$  numerically by Equations 4.18 and 4.20. Then the mean upcrossing rate can be calculated by Equation 4.19.

The calculated mean upcrossing rates by the wind speed can be used directly to calculate the mean duration of a visit by the wind speed to the critical velocity interval, by Equation 4.6. The mean duration of a visit by the wind speed to the critical velocity interval will be shown later in this chapter to determine the fatigue damage of a structure in random winds.

## 4.2.2 Rise time of structural response

As the excitation force is switched on, the structure needs a finite amount of time to build up its vibration amplitude towards a steady state value. The transient response envelope of a single degree of freedom oscillator with a constant sinusoidal excitation at the natural frequency  $f_n$  is approximated by the following equation

$$A(t) = A_{max}(1 - e^{-\zeta\omega_n t}) \quad (4.23)$$

where  $A(t)$  is the instantaneous vibration amplitude envelope at time  $t$  after the excitation has begun and  $A_{max}$  is the steady state vibration amplitude.  $\zeta$  is the structural damping ratio measured in still air.  $\omega_n$  is the natural frequency of the  $n$ -th mode in radians per second.

The rise time of structural response is defined as the duration required to build up to  $(1 - e^{-1})$  of the steady state value, from an initial stationary state. From this definition:

$$t_r = -\frac{1}{\zeta\omega_n} \ln\left(\frac{1}{e}\right) \quad (4.24)$$

$$= \frac{1}{\zeta\omega_n} = \frac{T}{2\pi\zeta} \quad (4.25)$$

where  $T$  is the undamped vibration period. Clearly, the rise time of structural response depends on the structural damping ratio and the natural frequency of the structure. For lightly damped structures, such as members on oil production platforms, the rise time can exceed 100 or more periods of vibration.

## 4.3 Introduction of a Gaussian windspeed approximation

In the analysis of random winds, the Gaussian windspeed approximation is very attractive because the PDF of the Gaussian windspeed  $p_V(v)$  only depends on two statistics, namely the mean windspeed  $\bar{V}$  and the standard deviation of the instanta-

neous windspeed  $\sigma_V$ :

$$p_V(v) = \frac{1}{\sqrt{2\pi}\sigma_V} \exp\left(-\frac{(v - \bar{V})^2}{2\sigma_V^2}\right)$$

Before the Gaussian windspeed approximation is employed to develop the probabilistic prediction methodology, it will be verified using real maritime wind data.

Raw wind data with varying mean windspeeds and turbulence levels are used. These wind data are a product of a measurement program sponsored by the Statoil Joint Industry Project on Maritime Turbulent Wind Field Measurements and Models. Project members included: Amoco Norway Oil Company, Conoco Norway Inc., Elf Aquitaine Norge A/S, Exxon Production Research Company, A/S Norske Shell, Norsk Hydro, Statoil and Saga Petroleum A/S. The database consists of several hundred hours of high quality wind data, obtained at exposed sites on the western coast of Norway. The raw wind data were grouped in many 40-minute raw windspeed records with a sampling frequency of 0.85 Hertz. The 40-minute mean windspeed varies between 13 [m·s<sup>-1</sup>] and 31 [m·s<sup>-1</sup>], and the turbulence level varies between 7% and 30%. A description of the wind measurement program and some wind data may be found in Odd Jan Andersen and Jorgen Lovseth [2].

To verify this assumption, the mean duration of a visit by the windspeed into any fixed critical velocity interval was calculated from the measured windspeed records by the following two methods. For any 40-minute windspeed record, the first method was to calculate the mean duration from the definition given by Equation 4.6; while the second method was to calculate the sample wind statistics  $\bar{V}$ ,  $\sigma_V$  and  $\sigma_{\dot{V}}$  from the raw windspeed record, and to calculate the mean duration based on the Gaussian windspeed assumption implied by Equation 4.9. To distinguish the two different methods, let us denote the mean duration of a visit calculated by the first method and the second method as the numerical duration and the Gaussian duration respectively. Since the underlying instantaneous windspeed may not be a Gaussian process, the numerical duration and the Gaussian duration are not the same in general. The comparison between these two durations shall indicate the adequacy of the Gaussian windspeed approximation.

The numerical duration was calculated in the following way. For each 40-minute windspeed record, the cumulative distribution functions of the windspeed evaluated at the lower and the upper bound of the critical velocity interval,  $F_V(a)$  and  $F_V(b)$ , were estimated as the fraction of the windspeed samples less than or equal to  $a$  and  $b$  respectively. The mean upcrossing rates at  $a$  and  $b$ , denoted as  $\nu_a^+$  and  $\nu_b^+$  respectively, were estimated as the number of the windspeed samples which up-crossed the levels  $a$  and  $b$  per 40 minutes. One upcrossing at the level  $x$  was recorded at time  $t_i$  when  $V(t_i) < x$  and  $V(t_{i+1}) \geq x$ , where  $t_i$  and  $t_{i+1}$  are the two adjacent sampling

points. The numerical duration was estimated by Equation 4.6 for known quantities of  $F_V(a)$ ,  $F_V(b)$ ,  $\nu_a^-$  [s<sup>-1</sup>] and  $\nu_b^+$  [s<sup>-1</sup>].

The Gaussian duration was calculated in the following way. Let  $\{V_i\}$  be the wind-speed samples in one 40-minute record. Then  $\bar{V}$  and  $\sigma_V$  were calculated as follows.

$$\bar{V} = \frac{1}{N} \sum_{i=1}^N V_i \quad (4.26)$$

$$\sigma_V = \sqrt{\frac{1}{N-1} \sum_{i=1}^N (V_i - \bar{V})^2} \quad (4.27)$$

where  $N = 2048$  is the total number of windspeed samples in one 40-minute wind-speed record.

To calculate  $\sigma_{\dot{V}}$ , a sequence of  $\dot{V}_i$  was derived from the windspeed sequence  $V_i$  using the central difference scheme:

$$\dot{V}_i = \frac{V_{i-2} - V_i}{2\Delta t} \quad (4.28)$$

where  $\Delta t$  is the sampling period, or the time increment of the windspeed sequence. The central difference scheme is a numerical difference scheme with high order of accuracy. The truncation error is second order, compared to first order by forward difference scheme.

Once  $\{\dot{V}_i\}$  was derived from Equation 4.28,  $\sigma_{\dot{V}}$  was calculated as follows.

$$\sigma_{\dot{V}} = \sqrt{\frac{1}{N-3} \sum_{i=1}^{N-2} \dot{V}_i^2} \quad (4.29)$$

After wind statistics  $\bar{V}$ ,  $\sigma_V$  and  $\sigma_{\dot{V}}$  were derived from windspeed samples using Equations 4.27, 4.28 and 4.29, the Gaussian duration  $E[\mathcal{T}_{[a,b]}]$  was calculated using Equation 4.9.

A systematic implementation of the verification process is as follows. A set of critical velocities was selected to represent typical offshore structural members. The critical velocities range from 3 [m·s<sup>-1</sup>] to 45 [m·s<sup>-1</sup>]. Three groups of windspeed records were also selected. The first group (group 1) consisted of the windspeed records for which the 40-minute mean windspeeds fell between 14.5 [m·s<sup>-1</sup>] and 15.5 [m·s<sup>-1</sup>], the second group (group two) consisted of the windspeed records with 40-minute mean windspeeds which fell between 19.5 [m·s<sup>-1</sup>] and 20.5 [m·s<sup>-1</sup>], and the third group (group three) consisted of the windspeed records for which the 40-minute

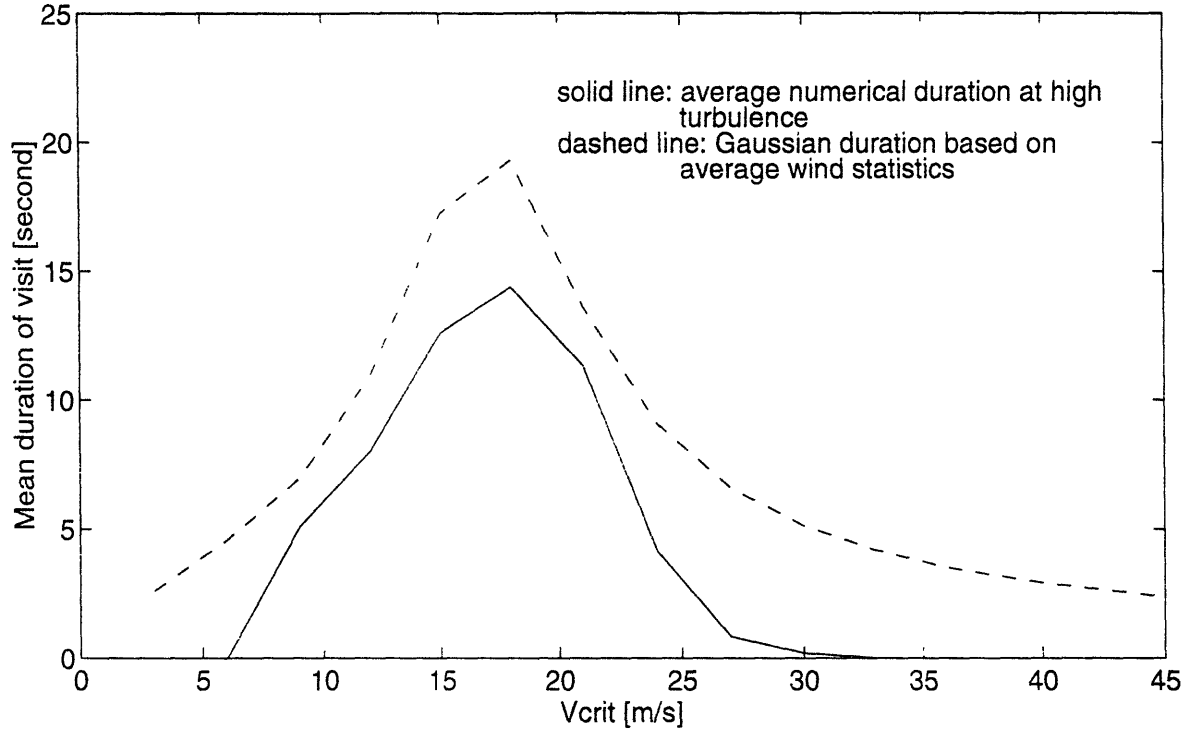


Figure 4-3: Variation of average numerical and Gaussian durations with critical velocities, from the 12 windspeed records in group 1 with large turbulence (17%)

mean windspeeds fell between  $24 \text{ [m}\cdot\text{s}^{-1}]$  and  $26 \text{ [m}\cdot\text{s}^{-1}]$ . For each individual windspeed record, the wind statistics ( $\bar{V}$ ,  $\sigma_V$  and  $\sigma_V$ ) and the numerical duration were calculated.

In each group with the same mean windspeed, the calculated turbulence intensity values for different records varied due to different thermal stability conditions. The wind records were therefore divided into two or three sub-groups according to their turbulence levels. In each sub-group, the wind statistics and the numerical duration were averaged, and the Gaussian duration was calculated from the average wind statistics.

For example, in group 1, there were a total of 15 windspeed records, each with the 40-minute mean windspeed within  $(14.5, 15.5) \text{ [m}\cdot\text{s}^{-1}]$ . 12 windspeed records have the turbulence intensity values greater than 13%, representing unstable atmospheric thermal conditions. The average turbulence intensity value for these 12 records is 17%. The other 3 windspeed records had turbulence intensity values less than 10%, representing stable thermal conditions. The average turbulence intensity value for these 3 records is 8%. Figure 4-3 shows the average numerical durations and the average Gaussian durations as functions of critical velocities from the 12 windspeed records in group 1 with large turbulence (average turbulence intensity 17%). Fig-

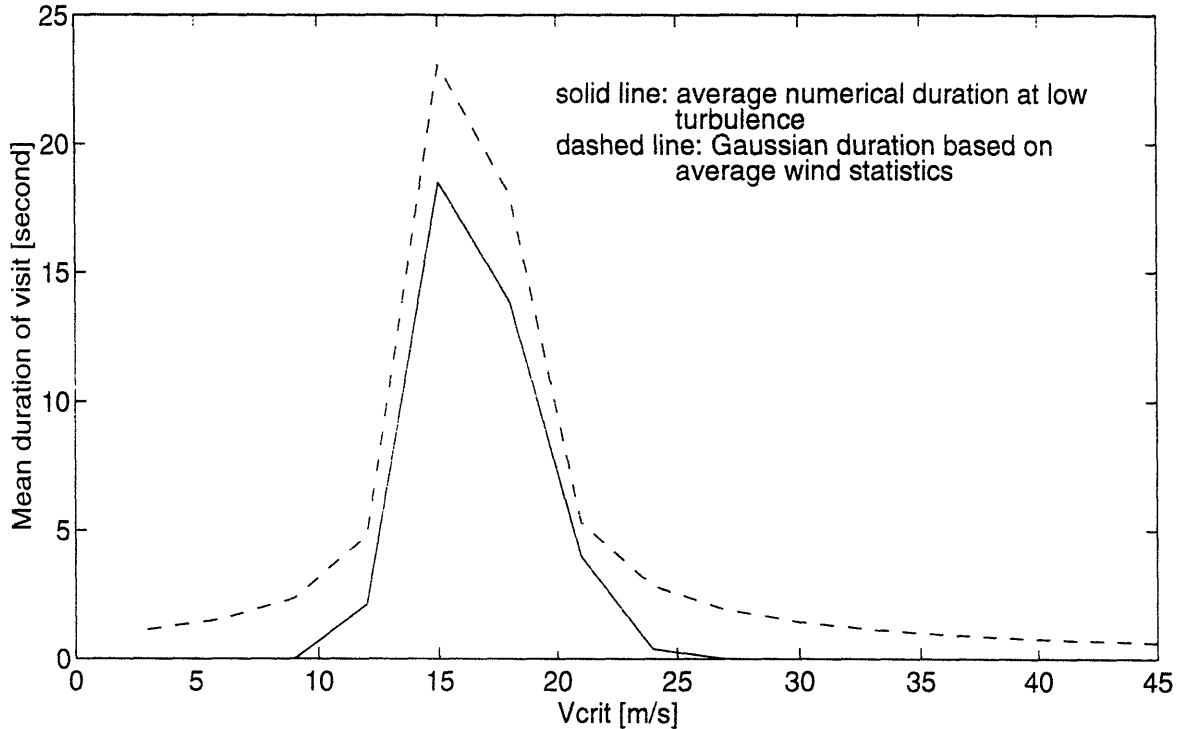


Figure 4-4: Variation of average numerical and Gaussian durations with critical velocities, from the 3 windspeed records in group 1 with small turbulence (8%)

Figure 4-4 shows the average numerical durations and the average Gaussian durations as functions of critical velocities from the 3 windspeed records in group 1 with small turbulence (average turbulence intensity 8%).

Both figures show that the maximum values of the mean duration occurs at the critical velocity approximately equal to the average mean windspeed, which is about 15 [m·s<sup>-1</sup>]. The values of the mean duration decay quickly as the critical velocity moves away from the average mean windspeed. A long duration of a visit in the critical velocity interval would allow the structural response to develop towards the maximum. This is entirely consistent with the fact that the maximum vibration amplitude occurs when the critical velocity equals the mean windspeed. Smaller turbulence results in a bigger but narrower peak in the duration *vs.* critical velocity curve. This is because a smaller magnitude of velocity fluctuations increases the chance for the windspeed to stay within the critical velocity interval when the critical velocity is equal to the mean windspeed. It decreases the chance for the windspeed to cross into the critical velocity interval when the critical velocity far from the mean windspeed.

Both figures also show that the Gaussian duration is consistently larger than the average numerical duration at all values of critical velocities. In Figures 4-3 and 4-

4, the maximum Gaussian duration is 25% and 35% larger than the corresponding average numerical duration. Analysis of group 2 and group 3 reveals the similar results. Since a conservative estimate in the expected duration leads to a conservative estimate in fatigue damage rate, the Gaussian windspeed model is a useful and conservative predictor of fatigue damage rate.

## 4.4 Development of probabilistic prediction methodology

Let us denote  $\mathcal{D}(\bar{V})$  as the fatigue damage rate of a structural member with real wind conditions and finite rise time;  $\mathcal{D}_{s.s.}$  as the fatigue damage rate of a structural member with a constant windspeed at  $V_{crit}$  and instant rise time;  $\mathcal{D}_0(\bar{V})$  as the fatigue damage rate of a structural member with real wind conditions and instant rise time. Among all these three fatigue damage rates,  $\mathcal{D}(\bar{V})$  is the one that a real structural member experiences and that we are trying to predict;  $\mathcal{D}_{s.s.}$  is the maximum damage rate that arises from steady-state vibrations at the critical velocity, and it can be predicted using standard design methodology such as Brown & Root;  $\mathcal{D}_0(\bar{V})$  is introduced to isolate the effects of real wind conditions and finite rise time. The expected fatigue damage rate can be expressed below as functions of both  $\mathcal{D}_{s.s.}$  and  $\mathcal{D}_0(\bar{V})$

$$E[\mathcal{D}(\bar{V})] = \mathcal{D}_{s.s.} \times \frac{E[\mathcal{D}(\bar{V})]}{\mathcal{D}_{s.s.}} \quad (4.30)$$

$$= \mathcal{D}_{s.s.} \times \frac{E[\mathcal{D}_0(\bar{V})]}{\mathcal{D}_{s.s.}} \times \frac{E[\mathcal{D}(\bar{V})]}{E[\mathcal{D}_0(\bar{V})]} \quad (4.31)$$

$$= \mathcal{D}_{s.s.} \times \gamma_0 \times \gamma_1 \quad (4.32)$$

where  $E[x]$  denotes the expected value of a random variable  $x$ .  $\gamma_0 = \frac{E[\mathcal{D}_0(\bar{V})]}{\mathcal{D}_{s.s.}}$  is a discount factor to account for instantaneous fluctuations of windspeed alone.  $\gamma_1 = \frac{E[\mathcal{D}(\bar{V})]}{E[\mathcal{D}_0(\bar{V})]}$  is a discount factor to account for finite rise time of structural response alone.

To predict the expected fatigue damage rate requires the values of  $\mathcal{D}_{s.s.}$  and the two discount factor  $\gamma_0$  and  $\gamma_1$ .  $\mathcal{D}_{s.s.}$  can be calculated using standard methods once  $A_{max}$  has been estimated. Probabilistic predictions for both  $\gamma_0$  and  $\gamma_1$  will be presented next.



#### 4.4.1 Predicting $\gamma_0$ , the fatigue damage discount factor due to instantaneous fluctuations of windspeed

Let  $V(t)$  be the time trace of the instantaneous wind speed normal to the cylinder and  $A_0(t)$  be the time trace of the corresponding instant rise vibration amplitudes in cross-flow direction. In other words, the value of the continuous-time series  $A_0(t)$  at any instant  $t_i$ ,  $A_0(t_i)$ , is the steady state vibration amplitude corresponding to the instantaneous wind speed  $V(t_i)$ . By definition,  $A_0(t_i)$  can be derived from the corresponding  $V(t_i)$  as expressed below, where we define  $A_0^*(t_i)$  as the ratio of  $A_0(t_i)$ , the steady state vibration amplitude at a particular reduced velocity  $V_r(t_i) = \frac{V(t_i)}{f_n D}$ , to  $A_{max}$ , the maximum steady state vibration amplitude at the critical wind speed  $V_{crit}$ :

$$A_0^*(t_i) = \frac{A_0(t_i)}{A_{max}} = f(V_r(t_i)) \quad (4.33)$$

$$= f\left(\frac{V(t_i)}{f_n D}\right) \quad (4.34)$$

where  $V(t_i)$  and  $V_r(t_i)$  are random variables that denote the instantaneous wind speed and the corresponding reduced velocity at time  $t_i$ .  $A_0(t_i)$  is a random variable that denotes the instant rise vibration amplitude at the instantaneous wind speed  $V(t_i)$ .  $A_{max}$  is the maximum steady state vibration amplitude, occurring at the critical wind speed  $V_{crit}$ .  $A_{max}$  can be predicted using various VIV design methodologies, such as **DnV**, **BS 8100**, **ESDU 85038** and **Brown & Root**, etc. A complete review of these methodologies was documented in [30].  $D$  is the diameter of the structural member and  $f_n$  is the natural frequency of the cylinder in Hertz.  $f(V_r)$  is the steady-state response function. It is a real function that relates the reduced velocity to the corresponding steady state vibration amplitude of the structural member. It can be determined based on experimental evidence [31] [12]. Different expressions of this function resulting from the models proposed by various authors were given in Chapter 3.

Equation 4.33 shows the relationship between the random variable  $V_r(t_i)$  and the derived random variable  $A_0(t_i)$ . Next, the probability distribution and resulting fatigue damage of instant rise vibration amplitudes will be derived from the probability distribution of the wind speed. For simplicity, upper case letters are used to denote random variables, while lower case letters are used to denote values of random variables, such as arguments of PDF's. For example,  $V$  and  $V_r$  are used to denote the random variables  $V(t_i)$  and  $V_r(t_i)$  respectively, and  $v$  is used to denote the value of the random variable  $V$ .

## Probability density function of response amplitude

Let us denote  $p_V(v)$  as the PDF of the wind speed;  $p_{V_r}(v_r)$  as the PDF of the wind speed expressed in terms of reduced velocity;  $p_{A_0}(a_0)$  as the PDF of instant rise vibration amplitudes;  $p_{A_0^*}(a_0^*)$  as the PDF of normalized instant rise vibration amplitudes. Our immediate goal is to derive  $p_{A_0^*}(a_0^*)$  from  $p_{V_r}(v_r)$ . Such a derivation is possible if the steady-state vibration response function,  $f(v_r)$ , possesses one-to-one mapping. Consider:

$$v_r = f^{-1}(a_0^*) = g(a_0^*) \quad (4.35)$$

where  $g(a_0^*)$  is the inverse function of  $f(v_r)$ .

Based on the theory of random variables, the probability distribution function of instant rise vibration amplitudes can be derived from that of the wind speed as follows:

$$p_{A_0^*}(a_0^*) = p_{V_r}(g(a_0^*)) \left| \frac{dg(a_0^*)}{da_0^*} \right| \quad (4.36)$$

If  $f(v_r)$  is not a monotone, the range of variations of  $v_r$  can be partitioned into segments within each of which the function is a monotone and

$$p_{A_0^*}(a_0^*) = \sum_l p_{V_r}(g_l(a_0^*)) \left| \frac{dg_l(a_0^*)}{da_0^*} \right| \quad (4.37)$$

where  $g_l(a_0^*)$  is the inverse mapping in the  $l$ -th segment. For the model of  $f(v_r)$  in Equation 3.5 proposed by Fei & Vandiver (Equation 3.5), there are two such non-zero monotonic segments.

## Fatigue damage assessment

If the response is deterministic and cyclic, the response and the number of cycles to fatigue failure can be defined by an  $S - N$  curve

$$NS^m = c \quad (4.38)$$

where  $S$  is the stress range, for cyclic stresses.  $S$  is twice the amplitude of cyclic stresses.  $N$  is the number of cycles to fatigue failure at the stress range  $S$ .  $m$  and  $c$  are positive constants that are related to material properties.

Let  $\mathcal{D}(t)$  denote the fraction of damage accumulated per unit time due to a random stress  $S(t)$ . According to Lin [21], the expectation of  $\mathcal{D}(t)$  can be expressed as follows:

$$E[\mathcal{D}(t)] = 2^m c^{-1} E[M_T(t)] \int_0^\infty \sigma^m p_\Sigma(\sigma, t) d\sigma \quad (4.39)$$

where  $\sigma(t)$  is the peak of the random stress  $S(t)$ ,  $p_\Sigma(\sigma, t)$  is the probability density function of stress peaks at time  $t$ .  $E[M_T(t)]$  is the expected number of peaks of the stress per unit time.

If the random stress  $S(t)$  is a stationary, narrow-band process, then the number of positive stress peaks per unit time is the center frequency of the stress spectrum,  $f_c$ .

$$E[M_T(t)] = f_c \quad (4.40)$$

And the expected fatigue damage rate is

$$E[\mathcal{D}] = 2^m f_c c^{-1} \int_0^\infty \sigma^m p_\Sigma(\sigma) d\sigma \quad (4.41)$$

For a flexible cylinder vibrating at its first mode with an amplitude  $A$ , the response amplitude spectrum will be narrow band with a peak at the natural frequency. Therefore,  $f_c = f_n$ . Furthermore, the maximum bending stress can be related to the maximum displacement response  $A$  as follows:

$$\begin{aligned} \Sigma &= E \times \epsilon \\ &= E \times \left(\frac{D}{L}\right)^2 \times \frac{F_i}{2} \times \frac{A}{D} \\ &= \frac{EDF_i}{2L^2} \times A \end{aligned} \quad (4.42)$$

where  $E$  is the Young's Modulus of the material.  $\epsilon$  is the maximum bending strain.  $F_i$  is the strain response parameter which relates the maximum deflection to the maximum strain. It varies with different boundary conditions [30], as shown in Table 3.1. For a pinned-pinned beam,  $F_i = \pi^2 = 9.87$ .  $D$  and  $L$  are, respectively, the diameter and the total length of the member.

Because they are linearly related, the PDF of the peaks of random stresses,  $p_\Sigma(\sigma)$ , can be calculated from the PDF of the peaks of the displacement response,  $p_A(a)$ , through Equation 4.42.

$$p_\Sigma(\sigma) = \frac{1}{\frac{EDF_i}{2L^2}} p_A\left(\frac{\sigma}{\frac{EDF_i}{2L^2}}\right)$$

$$= \frac{2L^2}{EDF_i} p_A\left(\frac{2L^2\sigma}{EDF_i}\right) \quad (4.43)$$

Combining Equations 4.41 and 4.43, the fatigue damage rate can be expressed in terms of the distribution of the peaks of the displacement response:

$$\begin{aligned} E[\mathcal{D}] &= 2^m f_n c^{-1} \int_0^\infty \sigma^m p_\Sigma(\sigma) d\sigma \\ &= f_n c^{-1} \left(\frac{EDF_i}{L^2}\right)^m \int_0^\infty a^m p_A(a) da \\ &= f_n c^{-1} \left(\frac{EDF_i}{L^2}\right)^m \int_0^{A_{max}} a^m p_A(a) da \end{aligned} \quad (4.44)$$

The expected fatigue damage rate assuming instant rise time.  $E[\mathcal{D}_0]$ , can be expressed as follows after replacing random variable  $A$  by  $A_0$  and changing variables from  $A_0$  to  $A_0^*$ :

$$\begin{aligned} E[\mathcal{D}_0] &= f_n c^{-1} \left(\frac{EDF_i}{L^2}\right)^m \int_0^{A_{max}} a_0^m p_{A_0}(a_0) da_0 \\ &= f_n c^{-1} \left(\frac{EDF_i}{L^2}\right)^m \int_0^1 (A_{max} a_0^*)^m p_{A_0^*}(a_0^*) da_0^* \\ &= f_n c^{-1} \left(\frac{EDF_i}{L^2} A_{max}\right)^m \int_0^1 (a_0^*)^m p_{A_0^*}(a_0^*) da_0^* \end{aligned} \quad (4.45)$$

$E[\mathcal{D}_0]$  can be further expressed in terms of the PDF of the wind speed expressed in terms of reduced velocity, after using Equation 4.37 in evaluating Equation 4.45:

$$E[\mathcal{D}_0] = f_n c^{-1} \left(\frac{EDF_i}{L^2} A_{max}\right)^m \int_0^1 (a_0^*)^m \sum_l p_{V_r}(g_l(a_0^*)) \left| \frac{dg_l(a_0^*)}{da_0^*} \right| da_0^* \quad (4.46)$$

Equation 4.46 is used to calculate the expected fatigue damage rate of a structural member assuming instant rise to steady state amplitudes, for a given PDF of the instantaneous wind speed.

Since unsteadiness of the wind speed has been considered, the fatigue damage rate predicted by Equation 4.46 is expected to be smaller than the fatigue damage rate resulting from steady state vibrations at the critical velocity of the member  $V_{crit}$ . Next we shall compare  $E[\mathcal{D}_0]$  against  $\mathcal{D}_{s,s.}$ , the fatigue damage rate resulting from steady state vibrations.

Let us denote  $\mathcal{D}_{s,s.}$  as the fatigue damage rate resulting from steady state vibra-

tions with a constant amplitude  $A_{max}$ . Steady state vibrations with amplitude  $A_{max}$  is the worst scenario in terms of fatigue damage accumulations. Therefore  $\mathcal{D}_{s.s.}$  is the largest value of fatigue damage rates among all possible wind conditions. In case of steady state vibrations, the probability distribution of vibration amplitudes consists of an impulse at  $A_{max}$  with a unit area and zero elsewhere. Consequently  $\mathcal{D}_{s.s.}$  can be calculated from Equation 4.44 with proper modifications.

$$\begin{aligned}\mathcal{D}_{s.s.} &= \left(\frac{E}{L^2}\right)^m \int_0^{A_{max}} a^m p_A(a) da \\ &= \left(\frac{E}{L^2}\right)^m A_{max}^m\end{aligned}\quad (4.47)$$

Now we are ready to calculate  $\gamma_0$ , the ratio of the fatigue damage rate assuming instant rise time of structural response to the fatigue damage rate with steady state vibrations at the critical velocity, by combining Equations 4.45 and 4.47:

$$\begin{aligned}\gamma_0 &= \frac{E[\mathcal{D}_0]}{\mathcal{D}_{s.s.}} \\ &= \frac{A_{max}^m \int_0^1 (a_0^*)^m p_{A_0^*}(a_0^*) da_0^*}{A_{max}^m} \\ &= \int_0^1 (a_0^*)^m \sum_l p_{V_r}(g_l(a_0^*)) \left| \frac{dg_l(a_0^*)}{da_0^*} \right| da_0^*\end{aligned}\quad (4.48)$$

From Equation 4.48, the determinants of  $\gamma_0$  include:  $m$ , the exponent of the  $S-N$  curve, which depends on the material properties of the structural member;  $f(v_r)$  or  $g_l(a_0^*)$ , the steady-state response function or its inverse function, which depends on selection of one of many different models proposed by various authors.  $p_{V_r}(v_r)$ , which in turn depends on  $p_V(v)$  and  $V_{crit}$ , the PDF of the wind speed and the critical wind speed respectively. Among the three determinants,  $p_{V_r}(v_r)$  can change considerably with different PDF's of wind speed and different critical wind speeds resulting from different structural members. Consequently, for any arbitrarily specified distribution of the wind speed,  $\gamma_0$  can only be calculated numerically by Equation 4.48.  $\gamma_0$  does not depend on the exact vibration mode shape and therefore does not depend on the particular boundary conditions or fixity of the member. It does depend indirectly on these quantities because the value of the reduced velocity  $V_r$  depends on the natural frequency.

However, for the case that the wind speed distribution can be fully specified by a few parameters, such as the mean and the variance for Gaussian PDF's, then it is possible to present graphically the values of  $\gamma_0$  as functions of these parameters for the whole class of windspeed distributions. For example, if the wind speed distribu-

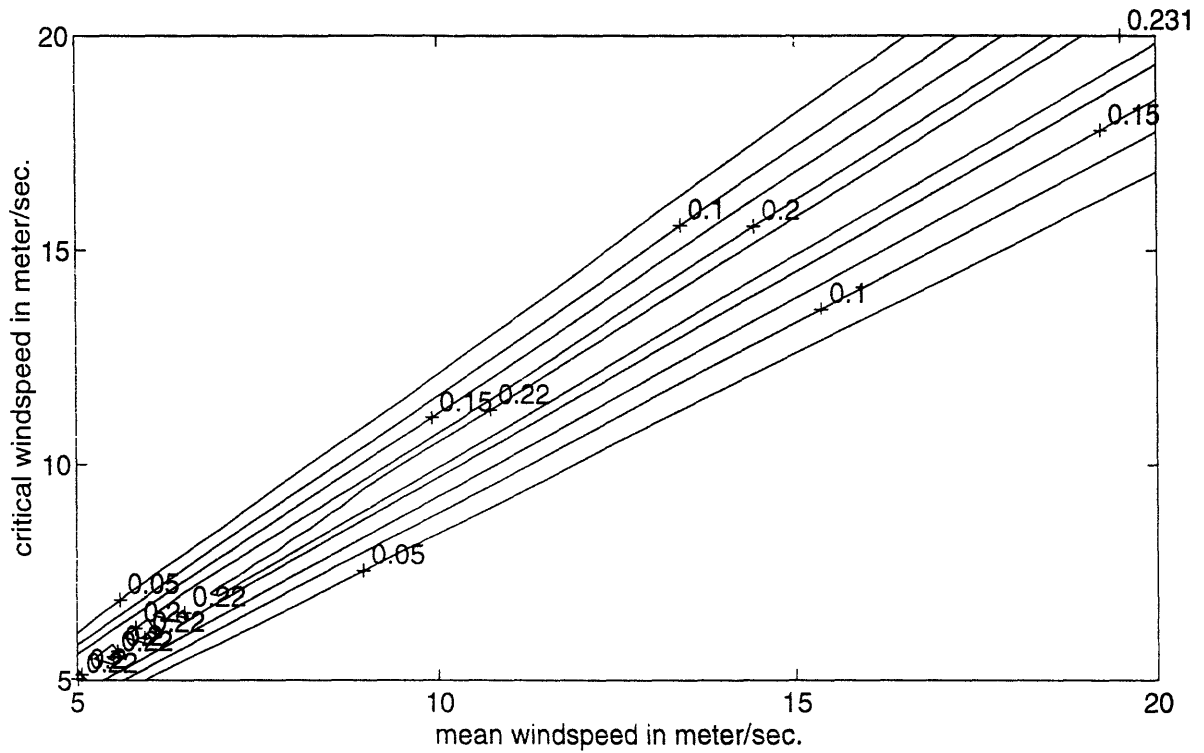


Figure 4-5: Values of  $\gamma_0$  as functions of mean wind speed  $\bar{V}$  and the critical wind speed of the structural member  $V_{crit}$  for Gaussianly-distributed windspeed and the turbulence intensity of 10%.

tion is Gaussian, then the value of  $\gamma_0$  can be determined by values of  $m$ ,  $f(v_r)$ ,  $\bar{V}$ ,  $\sigma_V$  and  $V_{crit}$ . If we further fix the values of  $m$  and  $f(v_r)$ , then  $\gamma_0$  only depends on the following three parameters:  $\bar{V}$ ,  $\sigma_V$  and  $V_{crit}$ . Therefore, in the case that the wind speed distribution is Gaussian,  $\gamma_0$  can be presented in the form of a 3-dimensional contour plot for different values of  $\bar{V}$ ,  $\sigma_V$  and  $V_{crit}$ .

Figure 4-5 shows a 2-dimensional contour plot for values of  $\gamma_0$  as functions of  $\bar{V}$  and  $V_{crit}$ . In this Figure, the wind speed distribution is assumed to be Gaussian, and the standard deviation of the wind speed  $\sigma_V$  is assumed to be 10% of the mean wind speed;  $m$  is assigned to a value of 3.74, a typical value for steel members; The model proposed by Fei & Vandiver (Equation 3.5) is used for  $f(v_r)$ .

The mean windspeed is itself a random variable and it is not always right at the critical velocity of the member. Even though there are instances when the mean windspeed happens to be at the critical velocity of the member, fluctuations of the instantaneous windspeed would allow the member to develop critical responses as well as off-critical responses. Off-critical response amplitudes are less than critical response amplitudes, thus making smaller contributions to fatigue damage accumulations than critical responses do. Therefore,  $\gamma_0$  is always less than 1. As shown in

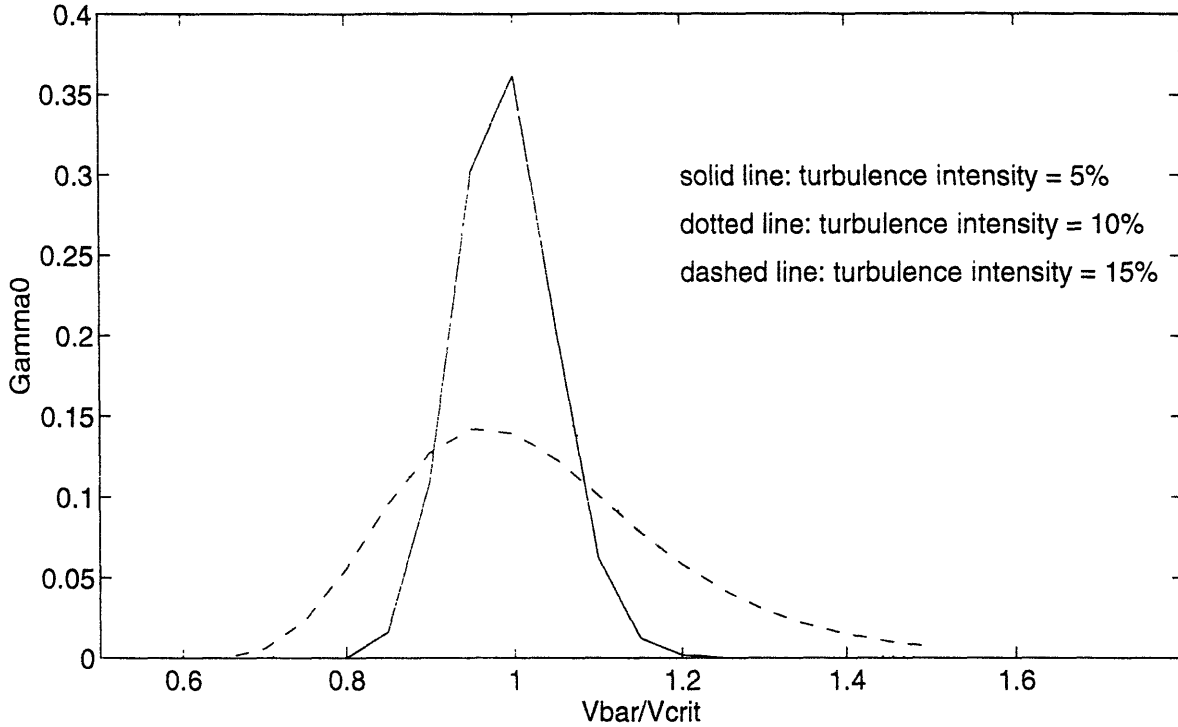


Figure 4-6: Variation of  $\gamma_0$  as functions of  $\frac{\bar{V}}{V_{crit}}$  at different turbulence intensity levels.

Figure 4-5 for a 10% turbulence level, the maximum value of  $\gamma_0$  is less than 0.25, indicating that an estimate of fatigue damage rate based on conservative maximum steady state vibrations is four times as big as the fatigue damage rate based on instant rise time model.

Values of  $\gamma_0$  decay quickly as the mean windspeed moves away from the critical velocity, indicating the wind conditions are not favorable in developing VIV. Values of  $\gamma_0$  also varies with the standard deviation of the windspeed. The smaller the standard deviation, the more that the windspeed looks like steady-state, and the larger will be the value of  $\gamma_0$ .

Figure 4-6 shows the variations of  $\gamma_0$  with mean windspeeds at turbulence intensity levels ( $\frac{\sigma_V}{\bar{V}}$ ) of 5%, 10% and 15% respectively. In this figure, the instantaneous windspeed was assumed to be Gaussian. The mean windspeeds were normalized by an arbitrary chosen value of  $V_{crit}$ . As we will show later in this chapter when the probabilistic model was verified using real maritime wind data, for Gaussianly-distributed instantaneous windspeeds,  $\gamma_0$  depends only on  $\frac{\bar{V}}{V_{crit}}$  and the turbulence intensity level  $\frac{\sigma_V}{\bar{V}}$ .

In current design codes, the conservative assumption is often made that if the critical windspeed for a member coincides with any part of a discrete windspeed bin

then the probability of encountering that critical windspeed is equal to the probability of encountering that bin. The effect of a finite bin size will be studied in Chapter 5.

#### 4.4.2 Predicting $\gamma_1$ , the fatigue damage discount factor due to structural response rise time

The natural fluctuation of the wind speed often does not allow fully developed vibrations. The actual fatigue damage rate of structural members in natural winds, therefore, depends on the relative length of the duration of visit to the rise time of a structural response mode. To model the effect of finite rise time, it is postulated that  $\gamma_1$ , the fatigue damage discount factor caused by the finite rise time of structural response, is a function that has the following form:

$$\gamma_1 = \frac{E[\mathcal{D}]}{E[\mathcal{D}_0]} = q(m, \zeta\omega_n E[\mathcal{T}_{[a,b]}]) \quad (4.49)$$

where  $[a, b]$  is defined as the critical velocity interval of a structural member. Values of  $a$  and  $b$  are determined by  $V_{crit}$ .  $\mathcal{T}_{[a,b]}$  is the duration of a visit by the windspeed to the interval  $[a, b]$ .  $\zeta\omega_n E[\mathcal{T}_{[a,b]}]$  is the ratio of  $E[\mathcal{T}_{[a,b]}]$ , the mean duration of a visit by the wind speed to the critical velocity interval  $[a, b]$ , to  $\frac{1}{\zeta\omega_n}$ , the structural rise time. This ratio is defined as  $r$ .  $\mathcal{D}$  is the correct fatigue damage rate of the structural member excited by random winds accounting for finite rise time.  $\mathcal{D}_0$  is the fatigue damage rate assuming instant rise time.  $q(m, r)$  is a real function that relates the fatigue damage reduction factor  $\gamma_1$  to  $r$ , the ratio of the duration of a visit by the wind speed to rise time.  $m$  is the exponent from the  $S - N$  curve expression in Equation 4.38.

The function  $q$  can be estimated by *Monte Carlo* simulations using the following steps:

- *Generating Wind Speed.* A time history of a Gaussianly distributed wind speed with a specified spectrum <sup>1</sup> can be generated by providing Gaussianly distributed white noise, as input to an optimum AutoRegressive MovingAverage

---

<sup>1</sup>The windspeed spectrum was defined as [27]:

$$S_V(f) = \frac{320 \times (0.1\bar{V}_{10})^2 \times (0.1Z)^{0.45}}{(1 + \bar{f}^n)^{\frac{2}{3n}}} \quad (4.50)$$

where  $\bar{f} = 172 \times f \times (0.1Z)^{\frac{2}{3}} \times (0.1\bar{V}_{10})^{-0.75}$ ;  $n = 0.468$ ;  $S_V(f)$  is the power spectral density at frequency  $f$  in Hertz;  $Z$  is the height above sea level in meters;  $\bar{V}_{10}$  is the 1 hour mean wind speed at 10 meters above sea level. This formula results from extensive windspeed measurements at Sletringen, Norway, and has been proposed as a model spectrum for design of North Sea structures [27].



filter, which best simulates the target spectrum [28]. The generated wind speed is denoted by  $V(t)$ . This simulation may of course be replaced by using real wind data.

- *Calculating the Excitation Force and Response.* Due to single mode dominance of VIV response, the vibration of the cylinder is regarded as the same as that of an equivalent single degree of freedom oscillator which has been obtained using the techniques of modal analysis.

$$m\ddot{x} + 2\zeta\omega_n\dot{x} + \omega_n^2x = f_a \cos \omega_n t \quad (4.51)$$

where  $x(t)$  is the mid-span vibration response amplitude of the cylinder to the given excitation.  $\zeta$  is the measured structural damping ratio of the cylinder.  $\omega_n$  is the natural frequency of the  $n$ th mode in radians per second and  $f_a$  is the amplitude of the modal excitation force per unit modal mass of the oscillator and is to be determined from the generated wind speed. Assuming that the wind speed is held at a constant value of  $V(t_i)$ , the vibration of the cylinder would eventually reach a steady state given by

$$x(t_i) = A(t_i) \sin \omega_n t = \frac{1}{2\zeta\omega_n^2} f_a(t_i) \sin \omega_n t \quad (4.52)$$

where  $A(t_i)$  is the steady state vibration amplitude, and is given by

$$A(t_i) = \frac{f_a(t_i)}{2\zeta\omega_n^2} \quad (4.53)$$

The  $\sin \omega_n t$  term accounts for the periodicity of the lift force and is assumed to be independent and uncoupled from the amplitude modulation caused by variations in  $V(t_i)$ . At any given time  $t_i$ , the amplitude of the excitation force,  $f_a(t_i)$ , can be derived from the value of the instantaneous wind speed  $V(t_i)$  in a way such that the corresponding steady state vibration amplitude at the wind-speed  $V(t_i)$  could be predicted in terms of the steady-state response function as follows:

$$A(t_i) = \frac{f_a(t_i)}{2\zeta\omega_n^2} = A_{max} f(V_r(t_i)) \quad (4.54)$$

or, equivalently

$$f_a(t_i) = 2\zeta\omega_n^2 A_{max} f(V_r(t_i)) \quad (4.55)$$

At this point an important approximation is necessary which has proven to be quite accurate. The excitation  $f_a(t_i)$  evaluated above is derived from the steady state magnitude of the periodic lift force which would be required to drive the cylinder to the steady state response amplitude corresponding to the reduced velocity. Since the lift coefficient changes with response amplitudes, the approximation is made here that as the cylinder vibration rises toward the steady state value, the periodic excitation force magnitude stays constant. In other words, during finite rise time, the lift coefficient is assumed to be constant at the value which would correspond to the final steady state response amplitude. With this approximation we may estimate the excitation which corresponds to any wind speed  $V(t)$ .

Due to changes in wind speed  $V(t_i)$  and therefore changes in reduced velocity  $V_r(t_i)$ , the vibration response will be modulated in amplitude. These modulations in response may be estimated by a standard convolution integral of the time varying excitation force,  $f_a(t_i)$ , and the impulse response function for the oscillator, as follows.

$$x(t) = \frac{1}{\omega_d} \int_0^t f_a(\tau) \cos(\omega_n \tau) e^{-\zeta \omega_n (t-\tau)} \times \sin(\omega_d (t-\tau)) d\tau \quad (4.56)$$

where  $\omega_d$  is the damped natural frequency and  $\omega_d = \omega_n \sqrt{1 - \zeta^2}$ .

- *Calculating the fatigue damage rates.* Vibrations of an elastic cylinder cause cyclic bending stresses, which result in fatigue damage. The fatigue damage,  $\Delta_i$ , resulting from the  $i$ th cycle of stresses, can be expressed as below.

$$\Delta_i = \frac{1}{N_i} \quad (4.57)$$

where  $N_i$  is the number of cycles to fatigue failure at the stress range  $\sigma_i$ , for cyclic stresses.  $\sigma_i$  is twice the amplitude of cyclic stresses. The total fatigue damage accumulated over the duration of stresses,  $\Delta$ , could be expressed as the sum of  $\Delta_i$  over the total number of the applied cyclic stresses,  $n$ , as follows.

$$\Delta = \sum_{i=1}^n \Delta_i \quad (4.58)$$

$$= \sum_{i=1}^n \frac{1}{N_i} \quad (4.59)$$

$$= c^{-1} \sum_{i=1}^n \sigma_i^m \quad (4.60)$$

where  $c$  and  $m$  are the constants of the  $S - N$  curve that were shown in Equation 4.38. By virtue of the relationship between the peaks of vibrations and the peaks of stresses shown in Equation 4.42,  $\Delta$  could be further expressed in terms of the peaks of vibrations as follows

$$\Delta = c^{-1} \left( \frac{EDF_i}{L^2} \right)^m \sum_{i=1}^n X_i^m \quad (4.61)$$

where  $X(t)$  is the envelope of the transient vibration  $x(t)$  that was derived from Equation 4.56.  $X_i$  is the discrete sequence of  $X(t)$  sampled at  $f_n$ , the natural frequency of the member.  $E$  is the Young's modulus of the material.  $F_i$  is the strain response parameter. It varies with different boundary conditions (see Table 3.1). For a pinned-pinned beam,  $F_i = 9.87$ .  $D$  and  $L$  are, respectively, the diameter and the total length of the member.

The fatigue damage rate,  $\mathcal{D}$ , can be calculated as below.

$$\mathcal{D} = \frac{\Delta}{n} f_n = \frac{f_n}{nc} \left( \frac{EDF_i}{L^2} \right)^m \sum_{i=1}^n X_i^m \quad (4.62)$$

The fatigue damage rate assuming instant rise time,  $\mathcal{D}_0$ , can also be calculated as below.

$$\mathcal{D}_0 = \frac{f_n}{nc} \left( \frac{EDF_i}{L^2} \right)^m \sum_{i=1}^n (A_0)_i^m \quad (4.63)$$

where  $(A_0)_i$  is the steady state vibration amplitude at the wind speed  $V_i$ .

The ratio of the fatigue damage rates between finite rise time and instant rise time can be expressed as follows.

$$\frac{\mathcal{D}}{\mathcal{D}_0} = \frac{\sum_{i=1}^n X_i^m}{\sum_{i=1}^n (A_0)_i^m} \quad (4.64)$$

- *Calculating the Time Scales.*

A time history of a Gaussianly distributed wind speed with a target spectrum was created as the output of an ARMA filter, as previously described. The mean duration of a visit by the wind speed to the critical velocity interval and the rise time of the natural mode were also calculated from Equations 4.6 and

4.25 respectively. based on the wind statistics derived from the simulated wind speed record. The ratio between the two time scales as defined previously as  $r = \zeta\omega_n E[\mathcal{T}_{[a,b]}]$  was computed.

For each simulated time history of Gaussianly distributed wind speed, a single pair of values  $(\frac{\mathcal{D}}{\mathcal{D}_0}, r)$  was formed. This pair relates  $\frac{\mathcal{D}}{\mathcal{D}_0}$ , the ratio of actual fatigue damage rate to that assuming instant rise, to  $r$ , the ratio of the mean duration of a visit by the windspeed (to the critical velocity interval) to rise time.

The above steps were repeated to generate wind speed records with different hourly means, to calculate the fatigue damage rates of a single structural member, and to find the durations of a visit by the wind speed to the critical velocity interval, until a considerable number of such pairs  $(\frac{\mathcal{D}}{\mathcal{D}_0}, r)$  were formed. An empirical relationship between  $\frac{\mathcal{D}}{\mathcal{D}_0}$  and  $r$  was identified as the curve which minimizes the least square error to the results of the *Monte Carlo* simulations.

The following empirical expressions were identified as the best fit to the results of the *Monte Carlo* simulations based on the least square error technique.

$$\gamma_1 = \frac{E[\mathcal{D}]}{E[\mathcal{D}_0]} = \begin{cases} 1 - \exp(-0.9359r^{0.2541}) & m = 3.0 \\ 1 - \exp(-0.7093r^{0.2859}) & m = 3.74 \\ 1 - \exp(-0.5718r^{0.3085}) & m = 4.38 \end{cases} \quad (4.65)$$

where  $r = \zeta\omega_n E[\mathcal{T}_{[a,b]}]$ . Equation 4.65 is plotted in Figure 4-7 with the results of the numerical simulations.

Figure 4-7 shows that  $\gamma_1$  increases as  $r$  increases, but decreases as  $m$  increases. It means that the effect of finite rise on fatigue damage diminishes for long durations of visit to the critical windspeed interval (steady state vibrations at constant winds are an extreme example) or for members with short rise times (large structural damping ratio, for example). Values of  $\gamma_1$  corresponding to values of  $m$  different from 3.0, 3.74 or 4.38 can be either interpolated from Figure 4-7 when  $m$  is between 3.0 and 4.38, or calculated based on the same technique of *Monte Carlo* simulations described above for other values of  $m$ .

The reason why  $\gamma_1$  is insensitive to the ratio  $\frac{\bar{V}}{V_{crit}}$  is illustrated by Figure 4-8. Figure 4-8 shows the normalized values of both  $\gamma_0$  and  $\gamma_1$  as functions of  $\frac{\bar{V}}{V_{crit}}$ , where  $\gamma_0$  was predicted by the probabilistic model assuming Gaussian windspeed and  $\frac{\sigma_V}{\bar{V}} = 0.09$ . To find the variation of  $\gamma_1$  with  $\frac{\bar{V}}{V_{crit}}$ , the variation of the Gaussian duration with  $V_{crit}$  were taken from Figure 4-4, where the Gaussian durations were calculated based on the average wind statistics derived from the raw windspeed records. These records exhibit a mean windspeed close to 15 [m·s<sup>-1</sup>] and 8% turbulence intensity. The maximum Gaussian duration was 23 seconds. Two values of structural rise time were selected so that  $r$ , the ratio of the mean duration to the rise time could be formed and  $\gamma_1$  could be calculated. One rise time was 100 seconds, and the maximum

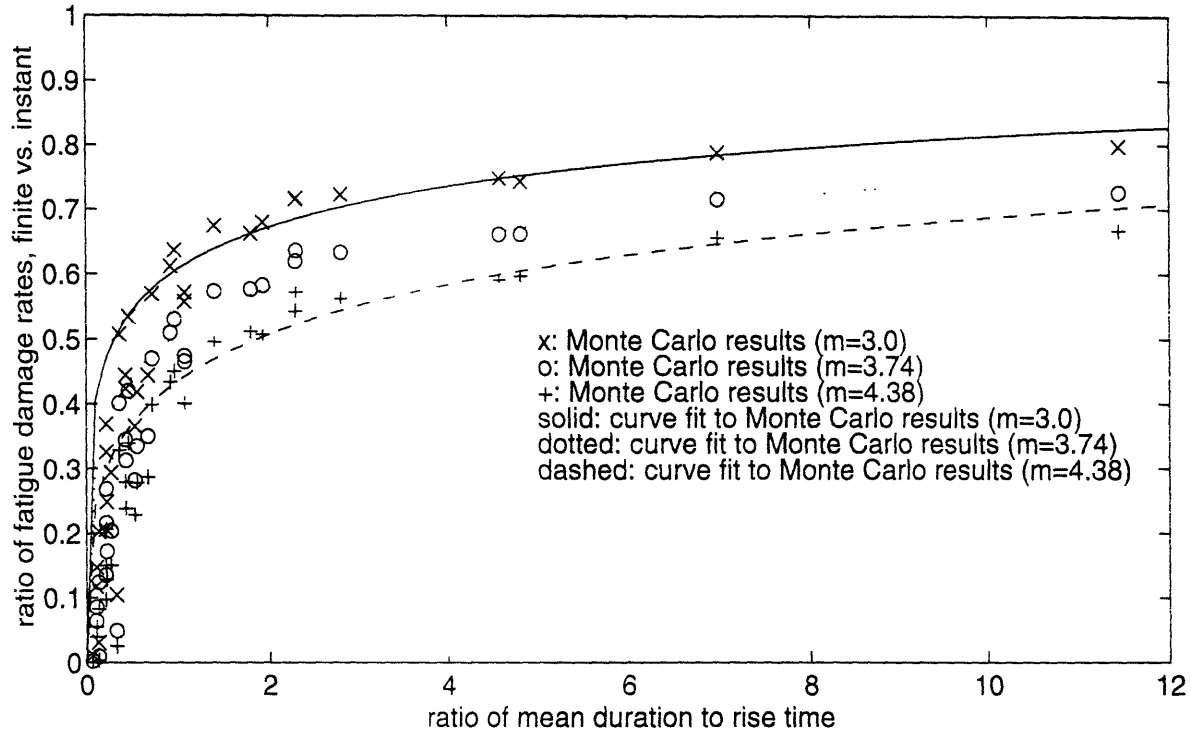


Figure 4-7: Variation of  $\gamma_1$  with  $r$ , the ratio of the mean duration of a visit to structural response rise time

value of  $r$  was 0.23. The second rise time was 10 seconds, and the maximum value of  $r$  was 2.3. According to Figure 4-11, 0.23 and 2.3 represent the small and large extreme values of  $r$ . The two different  $r$  versus  $V_{crit}$  curves corresponding to different values of the rise time were formed. Values of  $r$  were further translated into values of  $\gamma_1$  based on the following equation:

$$\gamma_1 = 1 - \exp(-0.7093r^{0.2859}) \quad (4.66)$$

This equation was from the results of *Monte Carlo* numerical simulations shown in Equation 4.65, assuming a  $S - N$  curve with  $m = 3.74$ .

For each of the two rise times,  $(\gamma_1)_{max}$  was the maximum value of  $\gamma_1$ . Values of  $\frac{\gamma_1}{(\gamma_1)_{max}}$  were plotted against  $\frac{\bar{V}}{V_{crit}}$  in Figure 4-8, where  $\bar{V} = 15 \text{ [m}\cdot\text{s}^{-1}\text{]}$ .

Figure 4-8 reveals that  $\gamma_0$  is far more sensitive to the values of  $\frac{\bar{V}}{V_{crit}}$  than  $\gamma_1$  is. It means that the shape of  $\gamma$  ( $\gamma_0 \times \gamma_1$ ) versus  $\frac{\bar{V}}{V_{crit}}$  curve is controlled by  $\gamma_0$ . This fact considerably simplifies the development of a model which corrects the prediction error caused by discretizing the mean windspeed. Such a model will be discussed in Chapter 5.

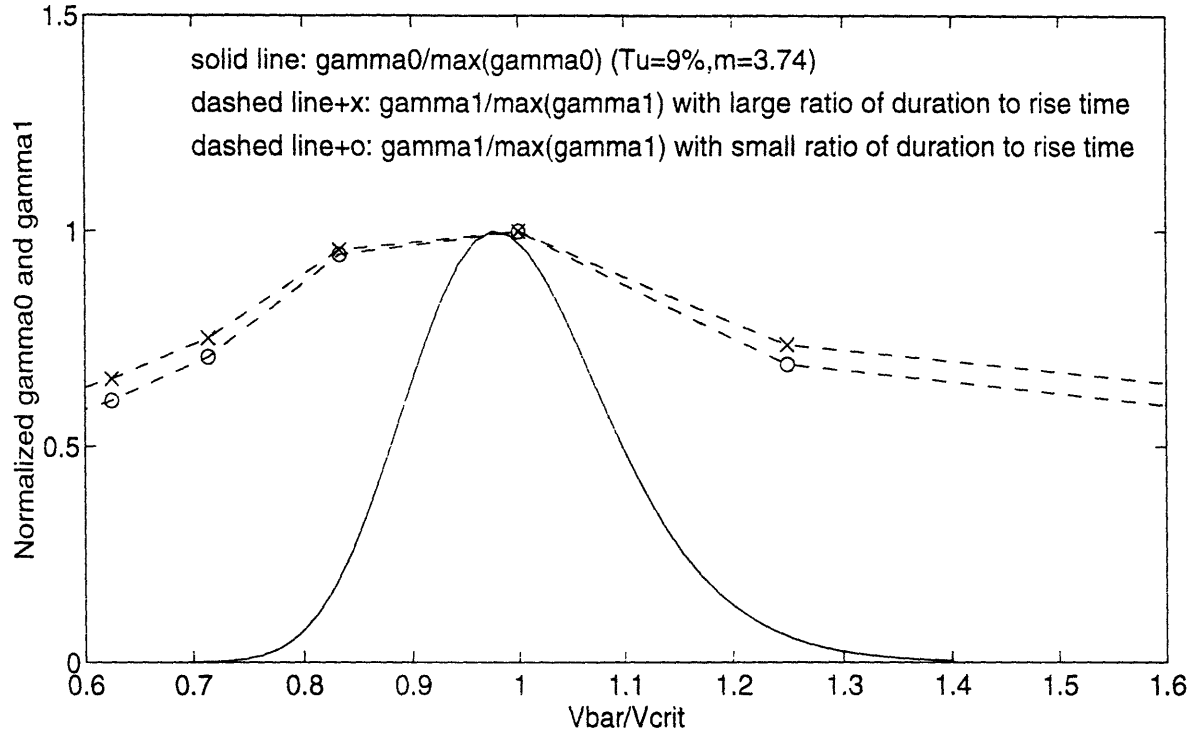


Figure 4-8: Variation of  $\frac{\gamma_0}{(\gamma_0)_{max}}$  and  $\frac{\gamma_1}{(\gamma_1)_{max}}$  with  $\frac{\bar{V}}{V_{crit}}$

## 4.5 Examples

### 4.5.1 Implementing the probabilistic model

An example is given to demonstrate the implementation of the proposed probabilistic model. The fatigue damage rate of a flexible cylinder is predicted based on the probabilistic model. The cylinder, a tube made of carbon-fiber, is assumed to have pinned-pinned ends. Structural parameters of the cylinder, such as the total length, diameter and the natural frequency, are described in Table 4.1.

For the purpose of illustrating the use of the proposed probabilistic model, we assume that both the PDF and the power spectral density function of the wind speed are given. The PDF of the wind speed is assumed to be Gaussian with a PDF  $p_V(v)$ , a mean  $\bar{V}$  and a variance  $\sigma_V^2$ . The Gaussian assumption was shown to be a conservative and useful approximation to natural winds.

$$p_V(v) = \frac{1}{\sqrt{2\pi}\sigma_V} \exp\left(-\frac{(v - \bar{V})^2}{2\sigma_V^2}\right) \quad (4.67)$$

where  $\bar{V}$  is the hourly mean wind speed, and  $\sigma_V$  is the standard deviation of the wind speed. Values of both quantities will be assigned below in **Step 1**.

The wind speed spectrum is defined by Equation 4.50. Reiterating

$$S_V(f) = \frac{320 \times (0.1\bar{V}_{10})^2 \times (0.1Z)^{0.45}}{(1 + \tilde{f}^n)^{\frac{5}{3n}}}$$

where  $\tilde{f} = 172 \times f \times (0.1Z)^{\frac{2}{3}} \times (0.1\bar{V}_{10})^{-0.75}$ ;  $n = 0.468$ ;  $S_V(f)$  [ $\text{m}^2 \cdot \text{s}^{-1}$ ] is the power spectral density function at frequency  $f$  [ $\text{s}^{-1}$ ];  $Z$  [m] is the height above sea level;  $\bar{V}_{10}$  is the hourly mean wind speed at 10 meters above sea level. The member is assumed to be at 10 meters above sea level, thus  $Z=10$  meters and  $\bar{V}_{10} = \bar{V}$ .

It is important to recognize that wind speeds may behave quite differently in different geographic areas. The use of the wind speed spectrum defined by Equation 4.50 may not generalize to all environments.

### Step 1: to estimate $\sigma_V$ and $\sigma_{\dot{V}}$

To assess the fatigue damage discount factor  $\gamma_1$  requires calculating the mean duration of a visit by the wind speed to the critical velocity interval, from wind statistics. The required wind statistics are the standard deviations of the wind speed,  $V$ , and its time derivative,  $\dot{V}$ . In this example, we assume that a database of local wind statistics from which the values of both standard deviations can be derived is not available, but that the power spectral density function of the windspeed given in Equation 4.50 is adequate to describe the local wind environment. Consequently we have to estimate the values of both standard deviations from the given power spectral density function of the windspeed, after a value of  $\bar{V}_{10}$  is assigned.

The hourly mean wind speed is assumed to be at the critical velocity of the member. The critical velocity  $V_{crit}$  is defined to correspond to a reduced velocity value of 6, at which the maximum steady state vibration of the tube would be achieved based on the observation of the results from the wind tunnel experiments.

$$\bar{V} = \bar{V}_{10} = 6.0f_n D = 9.38 \text{ [m} \cdot \text{s}^{-1}] \quad (4.68)$$

The standard deviation of the wind speed,  $\sigma_V$ , and the standard deviation of the wind acceleration,  $\sigma_{\dot{V}}$ , are calculated using Equations 4.21 and 4.22. The cut-off frequency is chosen to be 0.425 Hertz, half of the sampling frequency of the windspeed measurements from which the windspeed spectrum was derived.

After the cut-off frequency is defined, both  $\sigma_V$  and  $\sigma_{\dot{V}}$  can be calculated as follows.

$$\sigma_{\bar{V}} = \sqrt{\int_0^{0.425} S_V(f) df} = 0.8880 \text{ [m}\cdot\text{s}^{-1}\text{]}$$

$$\sigma_{\bar{V}^2} = 2\pi \sqrt{\int_0^{0.425} f^2 S_V(f) df} = 0.5001 \text{ [m}\cdot\text{s}^{-2}\text{]}.$$

The above integrations were implemented numerically using *Simpson's* rule. 1000 frequency intervals were evenly divided between 0 and 0.45 Hertz, which corresponds to a frequency resolution of  $4.5 \times 10^{-4}$  Hertz.

The critical reduced velocity interval was defined as [5, 6.5], consistent with results of our wind tunnel experiments. The corresponding lower and upper bounds of the critical velocity interval were 7.82 and 10.16 meters per second respectively. The cumulative distribution function of the windspeed at the lower and upper bounds of the critical velocity interval was calculated to be 0.03931 and 0.8114 respectively, based on the assumption of Gaussianly-distributed windspeed and using the PDF from Equation 4.67.

## Step 2: to calculate $E[\mathcal{T}_{[a,b]}]$ and $\frac{1}{\zeta\omega_n}$

To calculate  $E[\mathcal{T}_{[a,b]}]$ , the mean duration of a visit by the wind speed to the critical velocity interval, requires the values of the mean upcrossing rates by the wind speed at levels  $a = 7.82 \text{ [m}\cdot\text{s}^{-1}\text{]}$  and  $b = 10.16 \text{ [m}\cdot\text{s}^{-1}\text{]}$  respectively. Since the wind speed is assumed to be Gaussian, the mean upcrossing rate at a level  $\theta$  is known as follows:

$$\nu_{\theta}^+ = \frac{1}{2\pi} \frac{\sigma_V}{\sigma_{\bar{V}}} \exp\left(-\frac{(\theta - \bar{V})^2}{2\sigma_{\bar{V}}^2}\right) \quad (4.69)$$

Using the above equation and the values of  $\sigma_V$  and  $\sigma_{\bar{V}}$ , the mean upcrossing rates at levels  $a$  and  $b$  are 0.0191 and 0.0607 per second respectively.

Having obtained all of its determinants, the mean duration of a visit by the wind speed to the critical velocity interval can be calculated as follows.

$$\begin{aligned} E[\mathcal{T}_{[a,b]}] &= \frac{F_V(b) - F_V(a)}{\nu_a^+ + \nu_b^-} \\ &= \frac{0.8114 - 0.0393}{0.0191 + 0.0607} \\ &= 9.6753 \text{ [s]} \end{aligned}$$

Another key time scale is the rise time of the structural response, and it can be



calculated directly from the structural parameters as follows.

$$\begin{aligned}\frac{1}{\zeta\omega_n} &= \frac{1}{0.0035 \times 2 \times 3.1416 \times 32.375} \\ &= 1.4045 \text{ [s]}\end{aligned}$$

The ratio of the two time scales is  $r = \zeta\omega_n E[\mathcal{T}_{[a,b]}] = 9.6753/1.4045 = 6.8885$ . In other words the mean duration of visit is 6.9 times the rise time of the structural member.

### Step 3: to predict $\gamma$

To predict the combined fatigue damage discount factor  $\gamma$ , or the ratio of the fatigue damage rate with real wind conditions to the fatigue damage rate with steady state conditions, we need to calculate the following two quantities. The first quantity is  $\gamma_0$ , or the ratio of the fatigue damage rate assuming instant rise time to the fatigue damage rate with steady state conditions.  $\gamma_0$  accounts for the effect of instantaneous windspeed fluctuations on structural fatigue damage alone, and it can be calculated using Equation 4.48, Reiterating as follows:

$$\gamma_0 = \int_0^1 (a_0^*)^m \sum_l p_{v_r}(g_l(a_0^*)) \left| \frac{dg_l(a_0^*)}{da_0^*} \right| da_0^* \quad (4.70)$$

where  $f(v_r)$  is the steady-state response function.  $g_l(a_0^*)$  is the inverse mapping of the function  $f(v_r)$  in the  $l$ -th segment, and it is only defined when  $0 \leq a_0^* \leq 1$ . For the model of  $f(v_r)$  proposed by Fei & Vandiver [13] there are two such non-zero monotonic segments, namely  $g_1(a_0^*)$  and  $g_2(a_0^*)$ . In this example, functions  $f(v_r)$ ,  $g_1(a_0^*)$  and  $g_2(a_0^*)$  that were proposed by Fei & Vandiver are used:

$$f(v_r) = \begin{cases} v_r - 5.0 & 5.0 \leq v_r \leq 6.0 \\ 2(6.5 - v_r) & 6.0 \leq v_r \leq 6.5 \\ 0 & \text{otherwise} \end{cases} \quad (4.71)$$

$$g_1(a_0^*) = 5.0 + a_0^* \quad (4.72)$$

$$g_2(a_0^*) = 6.5 - 0.5a_0^* \quad (4.73)$$

$p_{v_r}(v_r)$  is the PDF of the windspeed expressed in terms of reduced velocities. Based on the theory of random variables,  $p_{v_r}(v_r)$  can be expressed directly in terms of  $p_V(v)$ , the PDF of the windspeed:

$$\begin{aligned}
p_{V_r}(v_r) &= f_n D \times p_V(f_n D \times v_r) \\
&= \frac{V_{crit}}{6} \times p_V\left(\frac{V_{crit}}{6} \times v_r\right)
\end{aligned} \tag{4.74}$$

Equation 4.70 for calculating the value of  $\gamma_0$  can be re-organized as follows after the substitutions of Equations 4.72, 4.73, 4.74:

$$\gamma_0 = \int_0^1 \frac{V_{crit}}{6} (a_0^*)^m \left\{ p_V\left(\left(5 + a_0^*\right) \frac{V_{crit}}{6}\right) + 0.5 p_V\left(\left(6.5 - 0.5 a_0^*\right) \frac{V_{crit}}{6}\right) \right\} da_0^* \tag{4.75}$$

Since the PDF of the windspeed is assumed to be Gaussian,  $\gamma_0$  can be calculated numerically for any given value of  $m$  (exponent of  $S - N$  curve). In this example, Integration in Equation 4.75 is implemented numerically using the *Trapezoidal's* rule. The value of the exponent of the  $S - N$  curve is chosen to be 3.74. 1000 uniformly-distributed intervals are divided between the lower and upper limit of the integration. The corresponding value of  $\gamma_0$  from the numerical integration is 0.2116.

The second quantity needed for the combined fatigue damage discount factor is  $\gamma_1$ , or the ratio of the fatigue damage rates between the probabilistic model and instant rise time model, which takes into account of the finite rise time of structural response. This ratio was assumed to depend only on  $r$ , the ratio of the mean duration to rise time, and can be calculated by Equation 4.65. Assuming the exponent of the  $S - N$  curve to be 3.74 (this is a typical value for steel, not carbon fiber, but is used here for example purposes only), the ratio of fatigue damage rates may be calculated as follows.

$$\begin{aligned}
\gamma_1 &= 1 - \exp(-0.7093 r^{0.2859}) \\
&= 1 - \exp(-0.7093 \times 6.8885^{0.2859}) \\
&= 0.7082
\end{aligned}$$

The combined fatigue damage discount factor,  $\gamma$ , is the product of  $\gamma_0$  and  $\gamma_1$ :

$$\begin{aligned}
\gamma &= \gamma_0 \times \gamma_1 \\
&= 0.2116 \times 0.7082 \\
&= 0.15
\end{aligned}$$

The result shows that the combined fatigue damage discount factor is 0.15 or equivalently, the increase in fatigue life of structural members in real wind conditions

is about 7 times as that based on conservative steady state vibrations. Between the two factors contributing to the fatigue damage rate reduction factor, the effect of the instantaneous windspeed fluctuations alone seems to be a dominant factor in this example, because of a large value of  $r$ . But the effect of finite rise time could be important when the duration to rise time ratio is small, as in the case when the mean windspeed does not coincide with the critical velocity of the member.

Table 4.1 summaries the use of the three step implementation of the probabilistic model on the worked example.

section	variable name	variable symbol	variable value	SI units
<b>input</b>	$L$	total length	2.0955	[m]
	$D$	outside diameter	0.0483	[m]
	$t$	wall thickness	0.0023	[m]
	$f_1$	natural frequency	32.375	[s <sup>-1</sup> ]
	$V_{crit}$	critical velocity	9.38	[m·s <sup>-1</sup> ]
	$\zeta$	structural damping ratio	0.35%	
	$Z$	height above sea level	10	[m]
<b>step 1</b>	$\bar{V}$	mean windspeed	9.38	[m·s <sup>-1</sup> ]
	$\sigma_V$	standard deviation of windspeed	0.8880	[m·s <sup>-1</sup> ]
	$\sigma_{\bar{V}}$	standard deviation of $\bar{V}$	0.5001	[m·s <sup>-2</sup> ]
	$a$	lower bound of the critical velocity interval	7.82	
	$b$	upper bound of the critical velocity interval	10.16	
	$F_V(a)$	CDF of windspeed at $a$	0.0393	
	$F_V(b)$	CDF of windspeed at $b$	0.8114	
<b>step 2</b>	$\eta$	non-normality factor	1.00	
	$\nu_a^+$	mean upcrossing rate at $a$	0.0191	[s <sup>-1</sup> ]
	$\nu_b^+$	mean upcrossing rate at $b$	0.0607	[s <sup>-1</sup> ]
	$E[\mathcal{T}_{[a,b]}]$	mean duration of visit to interval $[a, b]$	9.6753	[s]
	$\zeta\omega_1 E[\mathcal{T}_{[a,b]}]$	ratio of mean duration of visit to rise time	6.8885	
<b>step 3</b>	$m$	exponent of $S - N$ curve	3.74	
	$\gamma_0 = \frac{E[\mathcal{D}_0]}{\mathcal{D}_{*,*}}$	fatigue damage discount factor caused by instantaneous windspeed fluctuations	0.2116	
	$\gamma_1 = \frac{E[\mathcal{D}_1]}{E[\mathcal{D}_0]}$	fatigue damage discount factor caused by finite rise time of structural response	0.7082	
	$\gamma = \frac{E[\mathcal{D}_1]}{\mathcal{D}_{*,*}}$	combined fatigue damage discount factor	0.15	
	$\frac{1}{\gamma} = \frac{\mathcal{D}_{*,*}}{E[\mathcal{D}_1]}$	increase in fatigue life	6.67	

Table 4.1: Summary of a worked example of the proposed probabilistic model

## 4.5.2 Using the probabilistic model based on wind statistics from raw wind data

In this example, the fatigue damage of a structural member of Exxon's Harmony and Heritage platforms during transpacific tow is evaluated using both the probabilistic model and the time domain VIV model. Our confidence in the probabilistic model will be increased if the fatigue damage predicted by both models is comparable.

A real structural member of Exxon's Harmony and Heritage platforms is selected from Grundmeier et al. [16]. The structural parameters of the member is given below.

- Diameter = 0.51 [m] (20 [in]).
- Natural Frequency = 4.25 [ $s^{-1}$ ].
- Critical Velocity = 12.96 [ $m \cdot s^{-1}$ ].
- Length = 24.38 [m] (80 [ft]).
- Structural Damping = 0.15 %.

Figure 4-9 shows a time trace of the instantaneous windspeed at approximately 375 feet above the water during a transpacific tow [7]. The record is 30 minutes long and is sampled at 2 Hertz. This windspeed record will be input for both prediction models. The sample statistics of this record are as follows:

- $\bar{V} = 12.64$  [ $m \cdot s^{-1}$ ] (28.27 [mph]).
- $\sigma_V = 0.90$  [ $m \cdot s^{-1}$ ] (2.01 [mph]).
- $\sigma_{\dot{V}} = 0.34$  [ $m \cdot s^{-2}$ ].
- *kurtosis* = 2.95 (close to the Gaussian value of 3.0).

Table 4.2 shows the values of  $\frac{1}{\gamma}$  predicted from both the probabilistic model and the time domain VIV model. Since  $\gamma$  was defined as the fatigue discount factor (the ratio of the fatigue damage rate with real conditions to the fatigue damage rate with

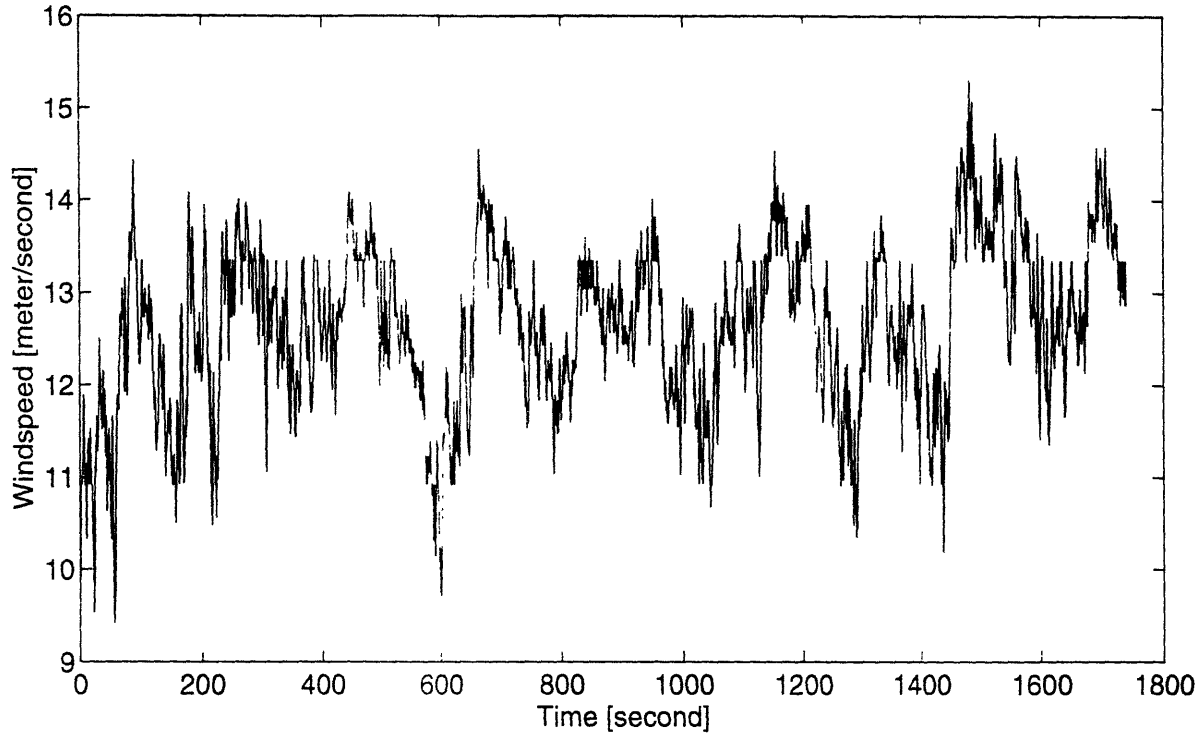


Figure 4-9: Time trace of the windspeed from transpacific tow, from Campbell (1992)

steady-state conditions at a mean windspeed equal to  $V_{crit}$ ),  $\frac{1}{\gamma}$  is the effective increase in fatigue life compared to the estimate based on maximum steady-state vibrations. The values of  $\frac{1}{\gamma}$  (increase in fatigue life) predicted by the time domain model are 4.90, 6.83 and 8.93, depending on the values of the exponent of the  $S - N$  curve. These values are relatively low because the mean windspeed happens to be close to the critical velocity of the member, which increases the probability of large-amplitude vibrations. It is expected that the values of  $\frac{1}{\gamma}$  increase significantly as the critical velocity of individual members moves away from the mean windspeed.

It is apparent that the predictions from the probabilistic model agree well with

$m$	$\gamma^{-1}$	
	time domain VIV model	probabilistic model
3.0	4.90	4.82
3.74 (API-X')	6.83	6.60
4.38 (API-X)	8.93	8.54

Table 4.2: Results of the predictions from both time domain VIV model and the probabilistic model

the predictions from the time domain VIV model, thus giving confidence to the prediction model. However, a single record is not sufficient to validate the approach. This is done in the next section using an extensive data base.

## 4.6 Verification of probabilistic prediction methodology using high sampling rate real wind data

In this section, the fatigue damage of a real structural member exposed in a marine site is predicted using both the probabilistic model and the time domain VIV model. Wind data with varying mean windspeeds and turbulence levels will be used.

A real structural member is selected from Harmony and Heritage platforms [16]. The structural parameters of the member is given below.

- Diameter = 0.91 [m] (36 [in]).
- Total length = 33.53 [m] (110 [ft]).
- Natural frequency = 4.13 [ $s^{-1}$ ].
- Critical velocity = 22.64 [ $m \cdot s^{-1}$ ].
- Structural damping = 0.15%.

The wind data are utilized in the following way. For each 40-minute long wind-speed record, the time domain VIV model developed in Chapter 3 was used to calculate the corresponding time series of transient vibrations.  $\gamma_0$  was calculated directly from the raw windspeed data through the steady-state response function  $f(v_r)$ . Estimates of  $\gamma_1$  were calculated from the transient vibrations. For comparison, wind statistics were calculated directly from the time series of each 40-minute windspeed record. These wind statistics include the 40-minute mean windspeed,  $\bar{V}$ , the standard deviation of the windspeed,  $\sigma_V$ , and the standard deviation of the time derivative of the windspeed,  $\sigma_{\dot{V}}$ . Based on these wind statistics, the probabilistic model proposed in this chapter was used to predict the values of  $\gamma_0$  and  $\gamma_1$ . These predicted values of  $\gamma_0$  and  $\gamma_1$  were then compared with the results from the time domain model.

In order to improve the time domain statistics of the estimates, 2 hour long wind-speed records were created by grouping together 3 similar 40-minute records. The

values of  $\gamma$  predicted by both the probabilistic model and the time domain model were compared based on the procedure described in the previous paragraph.

An important assumption was made in the predictions using the probabilistic model. The instantaneous windspeed is assumed to be a Gaussian process. This assumption enables closed-form solutions to the probabilistic model for both  $\gamma_0$  and  $\gamma_1$  that only depend on a limited number of parameters. The Gaussian assumption for the instantaneous windspeed greatly simplifies the design process for fatigue-resistant structural members caused by vortex-induced vibrations. This assumption was proven to be useful and conservative from the analysis of raw windspeed data earlier in this chapter.

#### 4.6.1 Verifying $\gamma_0$

By definition from Equation 4.48:

$$\begin{aligned}\gamma_0 &= \frac{E[\mathcal{D}_0]}{\mathcal{D}_{s.s.}} \\ &= \int_0^1 (a_0^*)^m \sum_l p_{V_r}(g_l(a_0^*)) \left| \frac{dg_l(c_0^*)}{da_0^*} \right| da_0\end{aligned}\quad (4.76)$$

where  $E[\mathcal{D}_0]$  is the expected fatigue damage rate assuming instant (zero) structural rise time.  $\mathcal{D}_{s.s.}$  is the fatigue damage rate resulting from steady state vibrations at the critical velocity of the member.  $p_{V_r}(x)$  is the PDF of the instantaneous windspeed expressed in terms of the reduced velocity.  $g_l(a_0^*)$  is the inverse mapping of the steady-state response function ( $f(v_r)$ ) in the  $l$ -th segment. For the model of  $f(v_r)$  proposed by Fei & Vandiver (Equation 3.5) there are two such non-zero monotonic segments, namely  $g_1(a_0^*)$  and  $g_2(a_0^*)$ . They are given as follows:

$$g_1(a_0^*) = 5.0 + a_0^* \quad (4.77)$$

$$g_2(a_0^*) = 6.5 - 0.5a_0^* \quad (4.78)$$

Since  $V_r = \frac{V}{f_n D}$  and  $V$  are linearly related, the PDF of the windspeed expressed in terms of the reduced velocity can be expressed directly in terms of the PDF of the windspeed as follows.

$$p_{V_r}(v_r) = f_n D \times p_V(f_n D \times v_r)$$

$$= \frac{V_{crit}}{6} \times p_V\left(\frac{V_{crit}}{6} \times v_r\right) \quad (4.79)$$

where  $p_V(x)$  is the PDF of the instantaneous windspeed.

Equation 4.76 can be re-written in the following form after the corresponding terms in the equation are replaced by Equations 4.77, 4.78 and 4.79.

$$\gamma_0 = \frac{V_{crit}}{6} \int_0^1 (a_0^*)^m \{p_V(v_1) + 0.5p_V(v_2)\} da_0^* \quad (4.80)$$

where

$$\begin{aligned} v_1 &= \frac{(5 + a_0^*)V_{crit}}{6} \\ v_2 &= \frac{(6.5 - 0.5a_0^*)V_{crit}}{6} \end{aligned}$$

Since the PDF of the windspeed is assumed to be Gaussian with a mean  $\bar{V}$  and a standard deviation of  $\sigma_V$ , then  $p_V(x) = \frac{1}{\sqrt{2\pi}\sigma_V} \exp\left(-\frac{(x-\bar{V})^2}{2\sigma_V^2}\right)$ . After algebraic manipulations, the value of  $\gamma_0$  can be shown to only depend on three dimensionless parameters given as below.

$$\begin{aligned} \gamma_0 &= \gamma_0\left(\frac{\sigma_V}{\bar{V}}, \frac{\bar{V}}{V_{crit}}, m\right) \\ &= \gamma_0\left(T_u, \frac{\bar{V}}{V_{crit}}, m\right) \end{aligned} \quad (4.81)$$

where  $T_u = \frac{\sigma_V}{\bar{V}}$  is the turbulence intensity level.

Equations 4.80 and 4.81 show that for given values of the turbulence intensity level, the ratio of the mean windspeed to the critical velocity of the member and the slope of the  $S - N$  curve,  $\gamma_0$  of the probabilistic model can be calculated by means of numerical integration. While the critical velocity of the member is a known quantity for a given structural member, values of  $\bar{V}$  and  $\sigma_V$  need to be specified. These two wind statistics can be calculated directly from the windspeed samples.

To test the Gaussian assumption for the estimation of  $\gamma_0$ , a series of 40-minute continuous windspeed samples was used. Let  $\{V_i\}$  be the windspeed samples of a 40-minute record but re-sampled at the natural frequency of the member. Let  $\{A_i\}$  be the envelope of the transient vibration amplitudes assuming instant structural rise time.  $A_i$  was calculated directly from the instantaneous windspeed as follows:



$$A_i = f\left(\frac{V_i}{f_n D}\right) \times A_{max} \quad (4.82)$$

where  $f(v_r)$  is the steady-state response function. A model for  $f(v_r)$  proposed by Fei & Vandiver [13] is recommended and is given below.

$$f(V_r) = \begin{cases} V_r - 5.0 & 5.0 \leq V_r \leq 6.0 \\ 2(6.5 - V_r) & 6.0 \leq V_r \leq 6.5 \\ 0 & \text{otherwise} \end{cases} \quad (4.83)$$

where  $A_{max}$  is the maximum steady state vibration amplitude at the critical velocity of the member. As shown later,  $\gamma_0$  is independent of the value of  $A_{max}$ , there is no need to calculate the value of  $A_{max}$  at this point.

By definition,  $\gamma_0$  was calculated as follows.

$$\begin{aligned} \gamma_0 &= \frac{E[\mathcal{D}_0]}{\mathcal{D}_{s.s.}} \\ &= \frac{\sum_{i=1}^n A_i^m}{\sum_{i=1}^n A_{max}^m} \\ &= \frac{\sum_{i=1}^n \left(f\left(\frac{V_i}{f_n D}\right)\right)^m}{n} \end{aligned} \quad (4.84)$$

where  $n$  is the total number of natural vibration periods in 40 minutes.

Figure 4-10 shows the values of  $\gamma_0$  calculated from Equation 4.84 as a function of the ratio of the mean windspeed to the critical velocity of the member. These raw wind records have turbulence intensity between 9% to 11%. The values of  $\gamma_0$  predicted by the probabilistic model, as shown in Equation 4.80, are also plotted as a function of the ratio of the mean windspeed to the critical velocity of the member at the turbulence intensity of 9% and 11%. The predictions are shown to agree well with the true values of  $\gamma_0$  directly calculated from the windspeed records.

#### 4.6.2 Verifying $\gamma_1$

By definition in Equation 4.49:

$$\gamma_1 = \frac{E[\mathcal{D}]}{E[\mathcal{D}_0]} \quad (4.85)$$

The probabilistic model states that  $\gamma_1$  is determined by the ratio of the mean du-

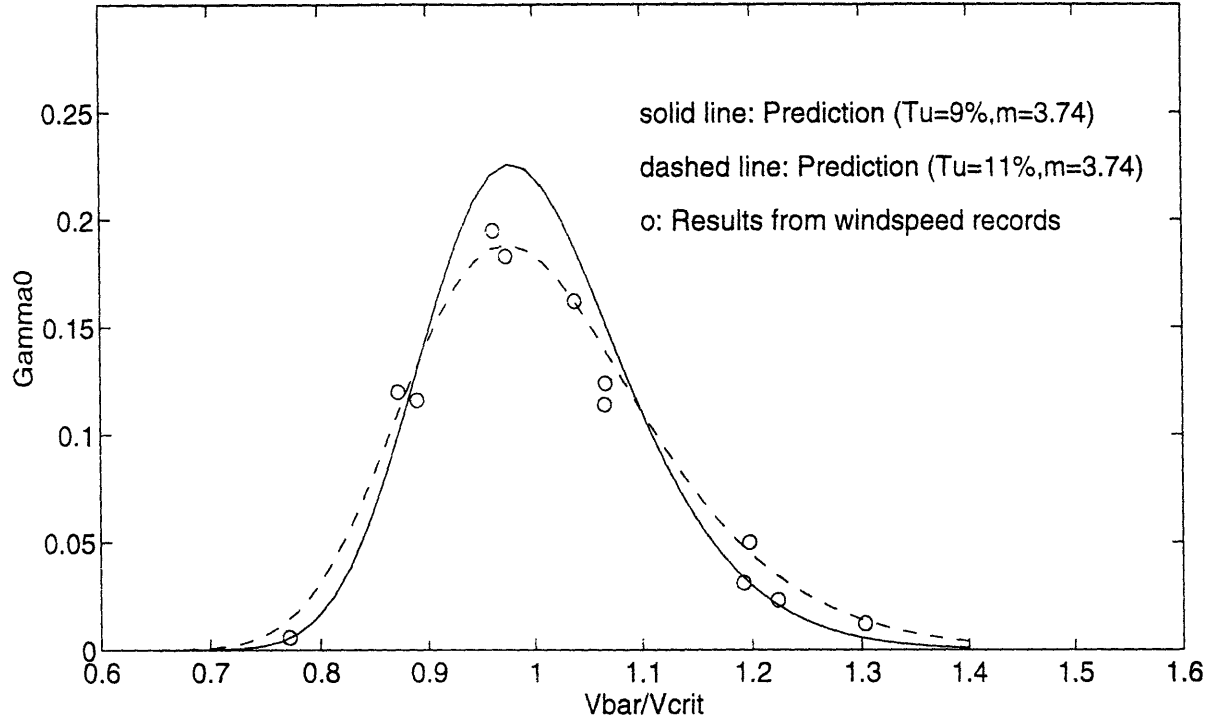


Figure 4-10: Variation of  $\gamma_0$  with the ratio of the mean wind speed to the critical velocity of the member

ration of a visit by the wind speed into the critical velocity interval to the structural rise time. This relationship was established by the empirical formula given below as a result from *Monte Carlo* numerical simulations.

$$r = \zeta \omega_n E[\mathcal{T}_{[a,b]}]$$

$$\gamma_1 = \begin{cases} 1 - \exp(-0.9359r^{0.2541}) & m = 3.00 \\ 1 - \exp(-0.7093r^{0.2859}) & m = 3.74 \\ 1 - \exp(-0.5718r^{0.3085}) & m = 4.38 \end{cases} \quad (4.86)$$

where  $E[\mathcal{T}_{[a,b]}]$  is the mean duration of a visit by the wind speed into the critical velocity interval  $[a, b]$ .  $E[\mathcal{T}_{[a,b]}]$  is given below for any given PDF of the wind speed  $p_V(x)$ .

$$E[\mathcal{T}_{[a,b]}] = \frac{F_V(b) - F_V(a)}{\nu_a^+ + \nu_b^-} \quad (4.87)$$

where  $F_V(x)$  is the CDF of the wind speed evaluated at  $x$ .  $\nu_x^+$  is the mean rate of crossing the level  $V = x$  at positive slopes. If the instantaneous wind speed is a Gaussian process, then  $E[\mathcal{T}_{[a,b]}]$  can be expressed explicitly in terms of the wind statistics

such as  $\bar{V}$ ,  $\sigma_V$  and  $\sigma_{\dot{V}}$ , and the values of  $a$  and  $b$  as follows

$$E[\mathcal{T}_{[a,b]}] = \frac{\int_a^b \frac{1}{\sqrt{2\pi}\sigma_V} \exp\left(-\frac{(v-\bar{V})^2}{2\sigma_V^2}\right) dv}{\frac{1}{2\pi} \frac{\sigma_V}{\sigma_{\dot{V}}} \left\{ \exp\left(-\frac{(a-\bar{V})^2}{2\sigma_V^2}\right) + \exp\left(-\frac{(b-\bar{V})^2}{2\sigma_V^2}\right) \right\}} \quad (4.88)$$

After simplifications,  $E[\mathcal{T}_{[a,b]}]$  can be shown to depend only on three quantities:  $\frac{\sigma_V}{\sigma_{\dot{V}}}$ ,  $\frac{\sigma_{\dot{V}}}{\bar{V}}$  and  $\frac{\bar{V}}{V_{crit}}$ . These will significantly simplify the implementation of the probabilistic model since this model only requires input of few wind statistics such as  $\bar{V}$ ,  $\sigma_V$  or  $T_u$ , and  $\sigma_{\dot{V}}$ .

To validate the empirical formula for predicting  $\gamma_1$  from the ratio of the mean duration to the structural rise time, the time domain VIV model developed in Chapter 3 was used to calculate the values of  $\gamma_1$  from a series of 40-minute windspeed records. For each windspeed record, the transient vibrations of the member were calculated. The value of  $\gamma_1$  is the ratio of the fatigue damage rate resulting from transient vibrations to the fatigue damage rate assuming the instant structural rise time. Let  $X_i$  be the envelope of the transient vibration amplitudes sampled at the vibration frequency over a period of 40 minutes.  $X_i$  was the output of the time domain VIV model. Let  $A_i$  be the envelope of the vibrations assuming instant structural rise time.  $A_i$  was calculated directly from the windspeed record by Equation 4.82. Then  $\gamma_1$  can be calculated as follows.

$$\begin{aligned} \gamma_1 &= \frac{E[\mathcal{D}]}{E[\mathcal{D}_0]} \\ &= \frac{\sum_{i=1}^n X_i^m}{\sum_{i=1}^n A_i^m} \end{aligned} \quad (4.89)$$

where  $n$  is the total number of vibration cycles in 40 minutes.

To estimate the value of  $E[\mathcal{T}_{[a,b]}]$  which corresponded to the value of  $\gamma_1$  from Equation 4.89, wind statistics were calculated from the same 40-minute windspeed records which were used to calculate  $\gamma_1$ . These wind statistics included the 40-minute mean windspeed,  $\bar{V}$ , the standard deviation of the windspeed,  $\sigma_V$ , and the standard deviation of the time derivative of the windspeed,  $\sigma_{\dot{V}}$ . The value of  $E[\mathcal{T}_{[a,b]}]$  was then calculated using Equation 4.88. This value of  $E[\mathcal{T}_{[a,b]}]$  was an estimate of the mean duration of a visit using a Gaussianly-distributed windspeed model. This Gaussian windspeed had the identical values of  $\bar{V}$ ,  $\sigma_V$  and  $\sigma_{\dot{V}}$  as those of the true windspeed (which may not have been Gaussian). The estimated mean duration for the Gaussian windspeed model was consistently longer than that of the actual windspeed record, as was shown when the Gaussian assumption was introduced earlier in this chapter. Therefore, Equation 4.88 will give a conservative estimate of  $E[\mathcal{T}_{[a,b]}]$ .

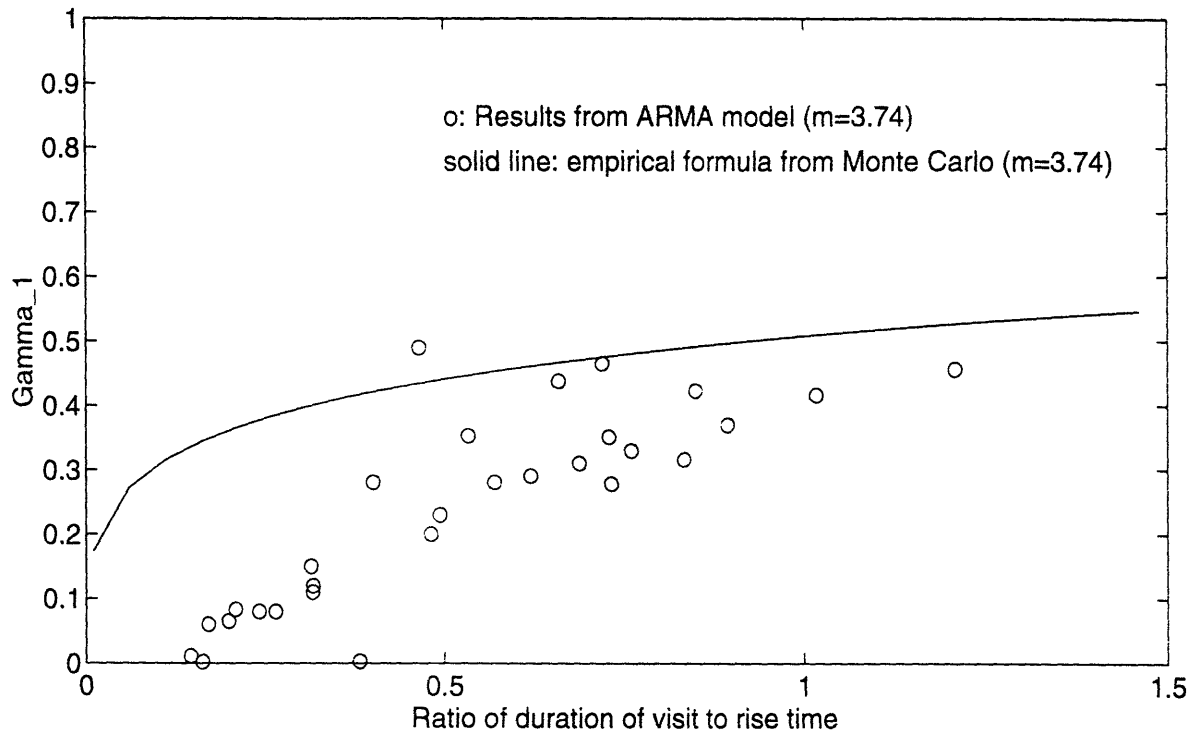


Figure 4-11: Variation of  $\gamma_1$  with the ratio of the mean duration to the rise time

Figure 4-11 shows the variation of  $\gamma_1$  with the ratio of the mean duration to the rise time as computed by the empirical formula in Equation 4.86, and compared to the pairs  $(\zeta\omega_n E[\mathcal{T}_{[a,b]}], \gamma_1)$  calculated from the time domain VIV model using Equations 4.88 and 4.89. The empirical formula is seen to provide a conservative prediction of  $\gamma_1$ .

### 4.6.3 Verifying the predictions based on longer-term wind data

In this section, 2 hour long stationary windspeed records have been assembled from the wind data base. 6 such files have been constructed, each consisting of 3 selected 40-minute single files. These six files have (2 hour) mean windspeeds ranging from 14 [m·s<sup>-1</sup>] to 29 [m·s<sup>-1</sup>]. For each of the 6 files, values of  $\gamma$  are calculated for the selected structural member using both the time domain model and the probabilistic model. In using the probabilistic model, the wind statistics such as  $T_u$  and  $\sigma_V$  are estimated directly from the 2 hour long windspeed records.

Figure 4-12 shows the values of  $\gamma$  calculated from both models as a function of  $\frac{V_{visit}}{V_T}$  assuming the slope of  $S - N$  curve is 3.74. The results from the probabilistic

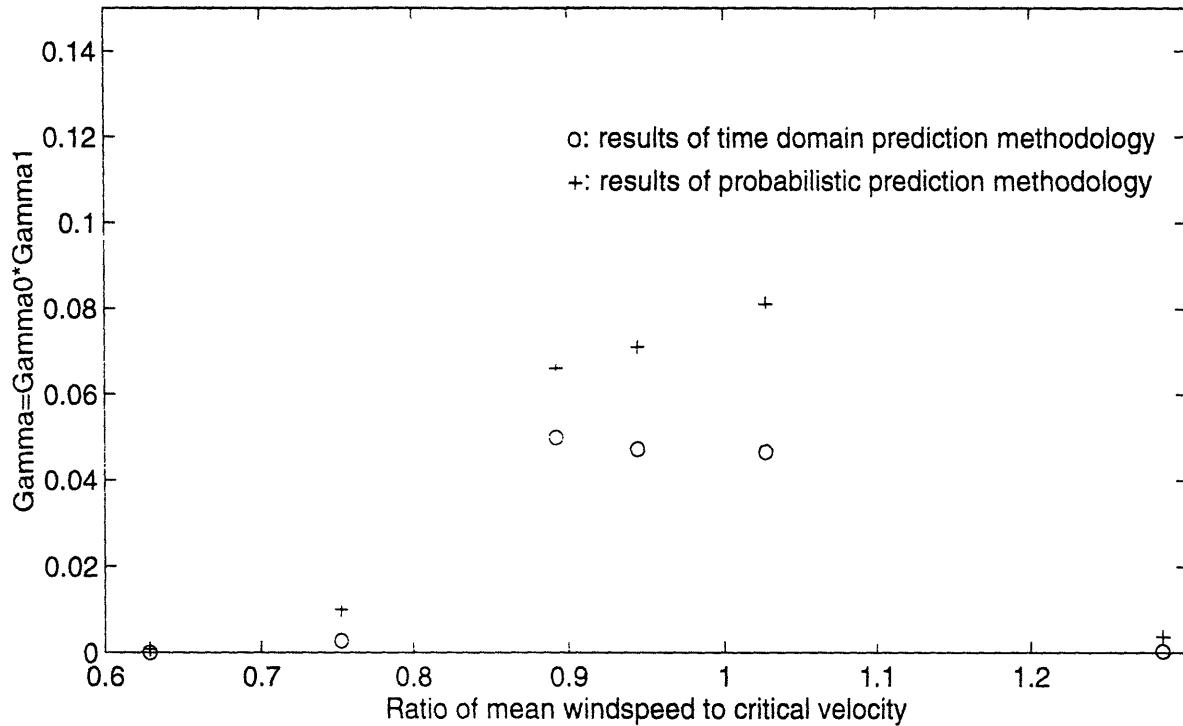


Figure 4-12: Values of  $\gamma$  as a function of  $\frac{\bar{V}}{V_{crit}}$  based on the time domain model and the probabilistic model. slope of  $S - N$  curve = 3.74. Reduced velocity range is from 3.8 to 7.7

model are consistently higher than those from the time domain model, which shows the conservative nature of the probabilistic model. Never the less, the peak value of  $\gamma$  from the probabilistic model is less than 0.1, which would give a greater than 10 increase in the fatigue life of the member compared to the steady state estimate.

## 4.7 Summary

A probabilistic model is proposed to predict the fatigue damage of an offshore structural member caused by natural winds. This model assumes that natural wind is a Gaussianly-distributed random process with a given mean windspeed and standard deviation. After analyzing relevant wind statistics and structural parameters, this model identifies two factors which would significantly improve the fatigue damage estimate. The probabilistic model is illustrated through worked examples.

The probabilistic model is verified against the time domain model using high sampling rate real windspeed data. These wind data were recorded in a typical maritime wind environment. For a typical offshore structural member and a given windspeed record, the time domain predictions were based on the raw windspeed

records, while the probabilistic predictions were carried out based on the sample wind statistics that are derived from the raw windspeed records. Results revealed that the assumption of Gaussianly-distributed natural windspeeds leads to a slightly conservative estimate of fatigue damage, but nonetheless yields a factor of more than 10 increase in fatigue life when compared to conventional fatigue damage estimates based on steady state vibrations at the critical windspeed.

# Chapter 5

## Effects of Discretizing the PDF of Mean Windspeeds

### 5.1 Fatigue damage of a structural member when the mean windspeed is a random variable

The annual estimated fatigue damage rate should take into account the PDF of the mean windspeed. Suppose that the mean windspeed is a continuous random variable with a specified PDF,  $p_{\bar{v}}(\bar{v})$ , as shown in Figure 5-1. The expected value of the fatigue damage discount factor can be expressed in terms of  $p_{\bar{v}}(\bar{v})$  as follows:

$$\begin{aligned} E[\gamma] &= \int_{-\infty}^{\infty} \gamma(\bar{v}) p_{\bar{v}}(\bar{v}) d\bar{v} \\ &= \int_{-\infty}^{\infty} \gamma_0(\bar{v}) \gamma_1(\bar{v}) p_{\bar{v}}(\bar{v}) d\bar{v} \end{aligned} \quad (5.1)$$

where  $\gamma(\bar{v}) = \gamma_0(\bar{v}) \times \gamma_1(\bar{v})$  is the fatigue damage discount factor at a constant mean windspeed  $\bar{v}$ , where  $\gamma(\bar{v})$  was defined earlier in Chapter 4 as the ratio of the “true” fatigue damage rate to the fatigue damage rate calculated assuming steady state vibrations at the critical velocity.  $\gamma(\bar{v})$  can be calculated numerically based on the probabilistic model that was proposed in Chapter 4. However, Equation 5.1 is not directly useful because  $p_{\bar{v}}(\bar{v})$  is rarely known in functional forms.

### 5.2 The scatter diagram of the mean windspeed and the effect of finite bin sizes

In practice, the probability of the mean windspeed is often expressed in a form known as a scatter diagram. In a scatter diagram, the mean windspeed axis is evenly divided into a certain number of intervals, known as velocity bins. Each velocity bin has a

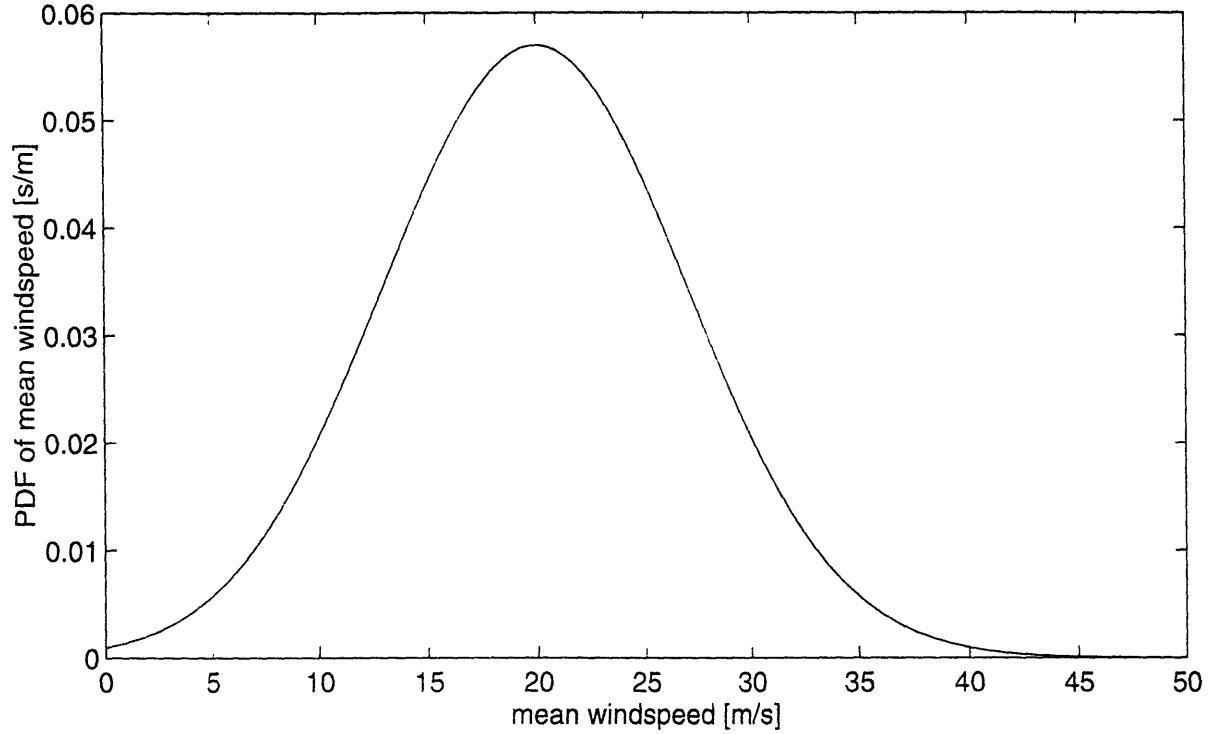


Figure 5-1. PDF of mean windspeed

width called the bin size, and is assigned with a probability value equal to the fraction of time that the windspeed occurs within that bin. The sum of the probabilities over all the bins is equal to 1. Within each velocity bin, the mean windspeed is assumed to be uniformly distributed. Figure 5-2 shows a typical scatter diagram with 9 velocity bins. The bin size is  $5 \text{ [m}\cdot\text{s}^{-1}]$ .

Equation 5.1 must be modified to allow the probability of the mean windspeed to be expressed in terms of a scatter diagram. Assume that there are  $n$  velocity bins, each with a bin size  $\Delta\bar{V}$ . Let  $\bar{V}_j$  and  $\bar{V}_{j+1}$  be the lower and the upper bound of the  $j$ -th velocity bin, where  $j$  is an integer between 1 and  $n$ , and  $\bar{V}_{j+1} = \bar{V}_j + \Delta\bar{V}$ . Let  $P_j$  the probability associated with the  $j$ -th bin. Then, Equation 5.1 can be rewritten as follows.

$$\begin{aligned}
 E[\gamma] &= \int_{-\infty}^{\infty} \gamma(\bar{v}) p_{\bar{v}}(\bar{v}) d\bar{v} \\
 &= \sum_{j=1}^n \int_{\bar{V}_j}^{\bar{V}_{j+1}} \gamma(\bar{v}) \frac{P_j}{\Delta\bar{V}} d\bar{v} \\
 &= \sum_{j=1}^n P_j \frac{1}{\Delta\bar{V}} \int_{\bar{V}_j}^{\bar{V}_{j+1}} \gamma(\bar{v}) d\bar{v}
 \end{aligned}$$



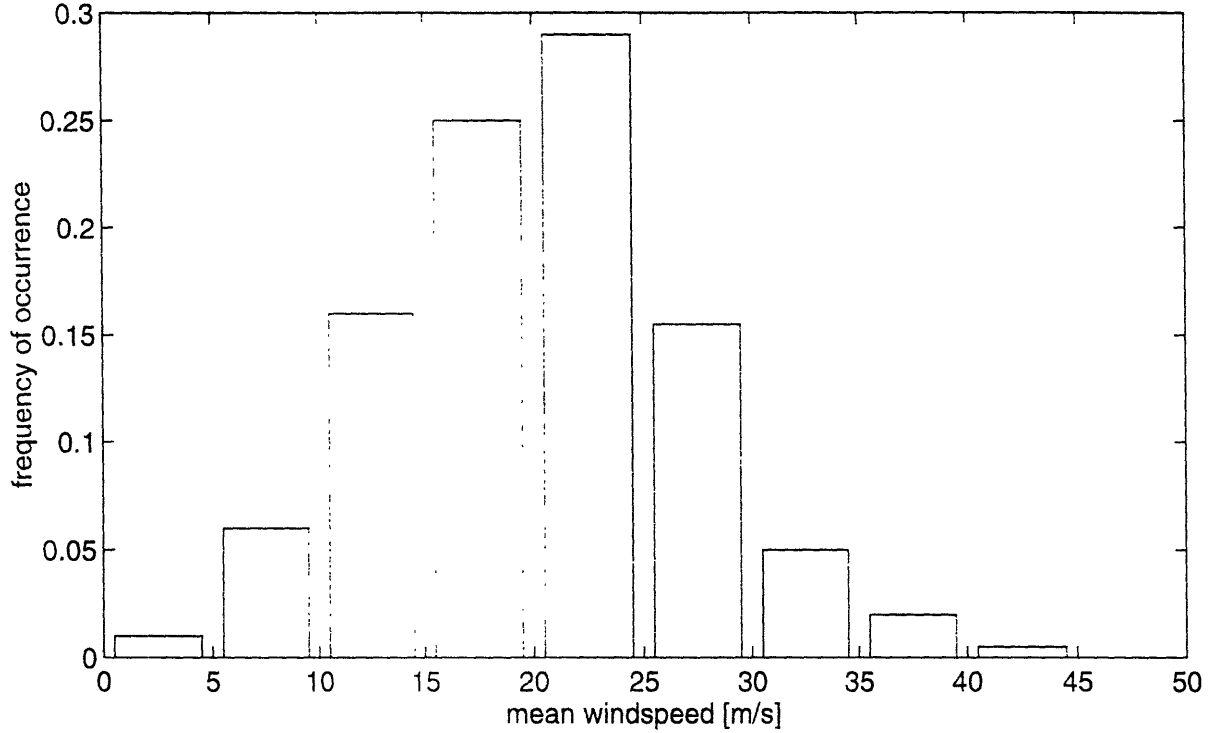


Figure 5-2: A scatter diagram of mean windspeed

$$= \sum_{j=1}^n P_j \bar{\gamma}_j \quad (5.2)$$

where  $\bar{\gamma}_j = \frac{1}{\Delta V} \int_{V_j}^{V_{j+1}} \gamma(\bar{v}) d\bar{v}$  is the average value of  $\gamma$  in the  $j$ -th velocity bin.

Equation 5.2 shows that  $E[\gamma]$  can be calculated as follows.  $\gamma$  is calculated numerically as a function of the mean windspeed, using the probabilistic model proposed in Chapter 4; then the integral is evaluated within each velocity bin to calculate  $\bar{\gamma}_j$ .  $E[\gamma]$  is then the probability-weighted sum of the  $\bar{\gamma}_j$  over all possible velocity bins.  $E[\gamma]$  accounts for the effect of the discretization of this scatter diagram on the ratio of the "true" fatigue damage rate to the fatigue damage rate from steady state vibrations at the critical velocity of the member.

Since  $\gamma$  decays quickly as the mean windspeed moves away from the critical velocity of the member, as shown in the contour plot (Figure 4-5) for values of  $\gamma_0$  in Chapter 4, the summation in Equation 5.2 needs to be carried out only over those velocity bins near  $V_{crit}$  where  $\bar{\gamma}_j$  is not small. A numerically efficient method to calculate  $E[\gamma]$  is to identify the velocity bin which brackets  $V_{crit}$  (call it the  $k$ -th bin) and start calculating  $\bar{\gamma}_k$  at the  $k$ -th velocity bin. The next two velocity bins for which the  $\bar{\gamma}_j$  is to be calculated and added to the sum are the  $(k-1)$ -th bin and the  $(k+1)$ -th bin. The summation continues independently in both directions as the velocity bins

move progressively more distant from  $V_{crit}$ , until velocity bins are reached where the  $\bar{\gamma}_j$  is below a pre-determined level. The evaluation is considered to be finished when the summation stops in both directions.

### 5.2.1 Approximating $E[\gamma]$

To calculate the exact value of  $E[\gamma]$  requires an appreciable amount of numerical computation. A simple but crude estimate of  $E[\gamma]$  is as follows.

$$\begin{aligned} E[\gamma] &= \gamma(\bar{V} = V_{crit}) \times P_k \\ &= \gamma_{max} \times P_k \end{aligned} \quad (5.3)$$

where  $\hat{E}[\gamma]$  denotes an approximation to  $E[\gamma]$ .  $P_k$  is the probability of the velocity bin which brackets the critical velocity of the member.  $\gamma_{max} = \gamma(V_{crit})$  is the value of  $\gamma$  when the mean windspeed equal to the critical velocity of the member.

By definition,  $E[\gamma]$  and  $\hat{E}[\gamma]$  are related through the following equation:

$$\begin{aligned} E[\gamma] &= \frac{E[\gamma]}{\hat{E}[\gamma]} \times \hat{E}[\gamma] \\ &= \gamma_{bin} \times \hat{E}[\gamma] \end{aligned}$$

where  $\gamma_{bin}$  is defined as the ratio of  $E[\gamma]$  to  $\hat{E}[\gamma]$ . It is clear that  $\gamma_{bin}$  is a factor which corrects the approximation of Equation 5.3 to the “true” fatigue damage reduction factor.

To see whether  $\hat{E}[\gamma]$  is a good approximation to  $E[\gamma]$ , let us look at  $\gamma_{bin}$  when the scatter diagram is assumed flat, *i.e.*, all  $P_j$  are equal.

$$\begin{aligned} \gamma_{bin} &= \frac{E[\gamma]}{\hat{E}[\gamma]} \\ &= \frac{\sum_{j=1}^n P_j \bar{\gamma}_j}{\gamma_{max} P_k} \\ &= \frac{\sum_{j=1}^n \bar{\gamma}_j}{\gamma_{max}} \\ &= \frac{\sum_{j=1}^n \bar{\gamma}_j \Delta \bar{V}}{\gamma_{max} \Delta \bar{V}} \end{aligned} \quad (5.4)$$

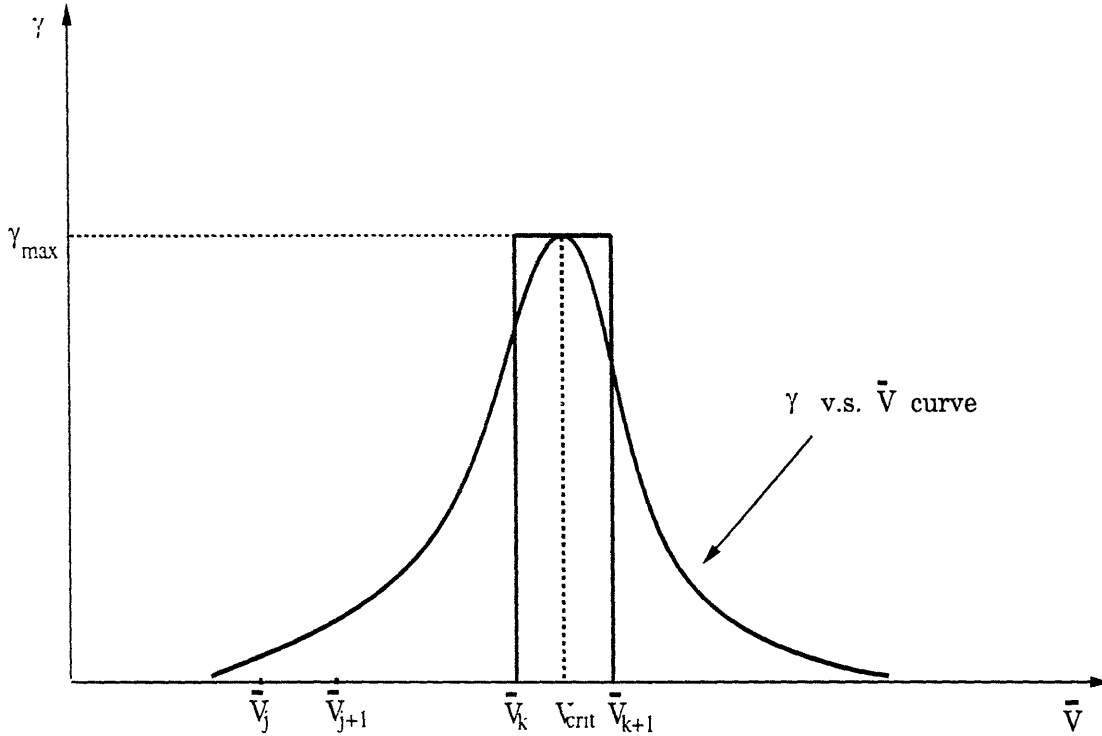


Figure 5-3: Variation of  $\gamma$  with mean windspeeds

$\gamma_{bin}$  becomes easier to interpret through Figure 5-3, which shows the values of  $\gamma$  as a function of mean windspeed. In this figure,  $j$ -th velocity bin is denoted by the interval  $[\bar{V}_j, \bar{V}_{j+1}]$ . The numerator of  $\gamma_{bin}$  shown in Equation 5.4 is the area under the  $\gamma$  curve; while the denominator is the area of the rectangle with the height equal to  $\gamma_{max}$  and width equal to the bin size.

As an example, the values of  $\gamma_{bin}$  for a typical structural member have been calculated for different values of bin size and turbulence intensity levels. Figure 5-4 shows the values of  $\gamma_{bin}$  as a function of the bin size to critical velocity ratio for a particular structural member with the following characteristics.

- critical velocity ( $V_{crit}$ ) = 12.96 [m·s<sup>-1</sup>].
- natural frequency ( $f_n$ ) = 4.25 [s<sup>-1</sup>].
- structural damping ( $\zeta$ ) = 0.15%.

The following assumptions were made:

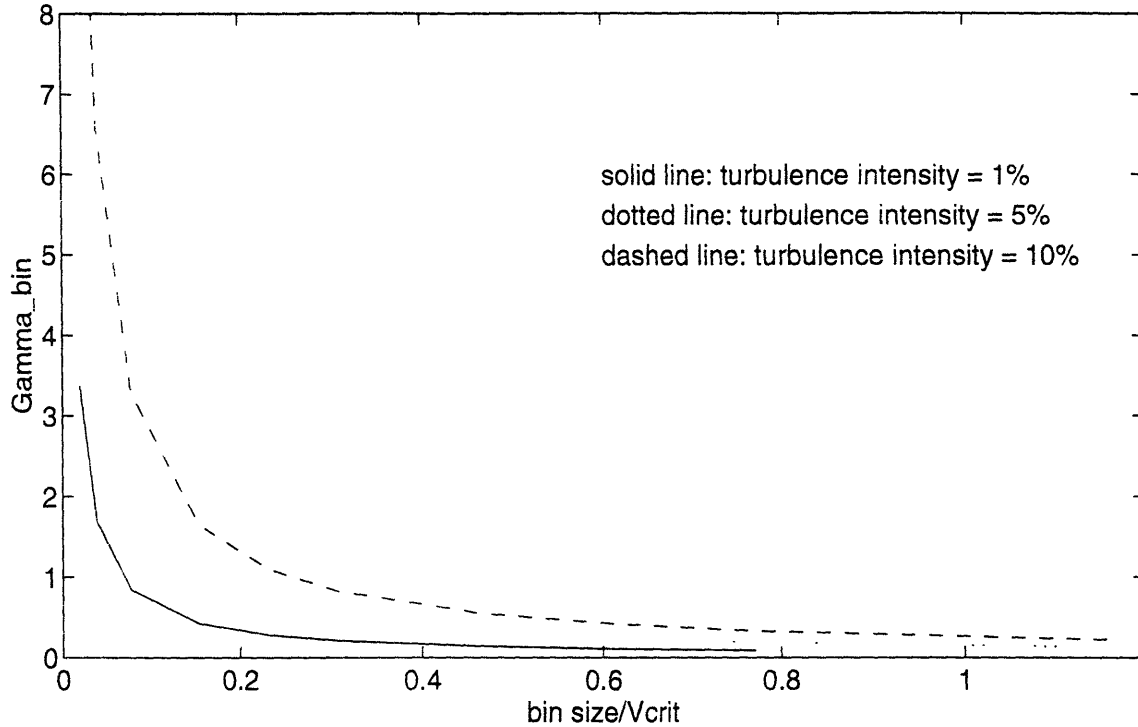


Figure 5-4: Variation of  $\gamma_{bin}$  with bin sizes, from a numerical example

1. The instantaneous windspeed was assumed Gaussian with a specified mean and turbulence intensity.
2. The scatter diagram of mean windspeeds was assumed to be flat. *i.e.*, the mean windspeed was equally likely over the significant width of the  $\gamma$  vs.  $\bar{V}$  curve (see Figure 5-3).
3. Although  $\frac{\sigma_V}{\sigma_v}$  may vary with mean windspeed, for this example,  $\frac{\sigma_V}{\sigma_v}$  was 0.38 [ $s^{-1}$ ].
4. The exponent of  $S - N$  curve ( $m$ ) was fixed. For this example,  $m$  was 3.74.

Fixing the above parameters left  $\gamma_{bin}$  dependent only on the bin size and the turbulence intensity level. As the bin size was changed, the numerator in Equation 5.4 did not change, but the denominator changed in proportion to the bin size. Hence  $\gamma_{bin}$  is inversely proportional to the bin size  $\Delta\bar{V}$ . Increasing turbulence increases  $\gamma_{bin}$ , because it increases the off-critical response found outside of the central bin.

There is a bin size for which  $\gamma_{bin} = 1.0$ . This particular choice of the bin size, called the critical bin size, occurs when  $\hat{E}[\gamma]$ , the simple approximation, is equal to the “true” fatigue damage reduction factor,  $E[\gamma]$ . For a bin size smaller than the critical bin size,  $\gamma_{bin}$  is greater than 1, meaning that the approximation  $\hat{E}[\gamma]$  underestimates the real fatigue damage. For a bin size greater than the critical bin size,  $\gamma_{bin}$  is less than 1, meaning that the approximation,  $\hat{E}[\gamma]$ , is conservative. For the above example, the critical values of the ratio of bin size to the critical velocity are 0.07, 0.15 and 0.27 for turbulence intensity levels of 1%, 5% and 10% respectively. In other words, for  $V_{crit}$  of 12.96 [m·s<sup>-1</sup>], then the critical values of the bin size are 0.91, 1.95 and 3.51 [m·s<sup>-1</sup>] at respective turbulence levels. These values may vary depending on different values of  $m$ , and also on  $\frac{\sigma_V}{\sigma_V}$ ,  $\gamma_0$ ,  $\gamma_1$  and structural parameters. Hence, a task remaining is to eliminate the dependence of  $\gamma_{bin}$  on so many parameters.

### 5.2.2 A model for $\gamma_{bin}$

Since  $\hat{E}[\gamma]$  (approximate fatigue damage discount factor) is much easier to calculate than  $E[\gamma]$  (the “true” fatigue damage discount factor), it is of practical significance to find an expression for  $\gamma_{bin}$  which depends only on the bin size to critical velocity ratio, turbulence intensity and the slope of the  $S - N$  curve. However,  $\gamma_{bin}$  may also depend on  $\gamma_1$ , which is determined by the ratio of the mean duration of visit to rise time. It may be expected that quantities such as the wind statistics  $\sigma_V$ ,  $\sigma_V$  and the structural rise time could also be important. However, Figure 4-8 shows that the shape of the  $\gamma$  versus  $\frac{\bar{V}}{V_{crit}}$  curve is insensitive to  $\gamma_1$  and is controlled by  $\gamma_0$ . Since only the shape of the  $\gamma$  curve matters in determining the value of  $\gamma_{bin}$ , the development of a model for  $\gamma_{bin}$  can be considerably simplified. A model for  $\gamma_{bin}$  thus looks like the following.

$$\gamma_{bin} = \mathcal{F}\left(m, \frac{\Delta \bar{V}}{V_{crit}}, T_u\right) \quad (5.5)$$

where  $m$  is the exponent of the  $S - N$  curve,  $T_u$  is the turbulence intensity.

The function  $\mathcal{F}$  can be estimated by numerical experiments using the following steps.

- **Calculate  $\gamma_0$  as a function of mean windspeed.** Using the steady-state response function presented in Equation 3.5, the value of  $\gamma_0$  can be calculated by Equation 4.75. Reiterating:

$$\gamma_0 = \int_0^1 (a_0^*)^m \frac{V_{crit}}{6} \left\{ p_1 \cdot \left( \frac{(5 + a_0^*) V_{crit}}{6} \right) + 0.5 p_1 \cdot \left( \frac{(6.5 - 0.5 a_0^*) V_{crit}}{6} \right) \right\} da_0^*$$

where  $V_{crit}$  is the critical velocity of the member.  $p_V(x) = \frac{1}{\sqrt{2\pi}\sigma_V} \exp\left(-\frac{(x-\bar{V})^2}{2\sigma_V^2}\right)$  is the PDF of the instantaneous windspeed.  $\bar{V}$  and  $\sigma_V$  are, respectively, the mean and the standard deviation of the instantaneous windspeed.

After simplification, the value of  $\gamma_0$  is found to depend on the following parameters:

$$\begin{aligned}\gamma_0 &= \gamma_0\left(\frac{\sigma_V}{\bar{V}}, \frac{\bar{V}}{V_{crit}}, m\right) \\ &= \gamma_0(T_u, \frac{\bar{V}}{V_{crit}}, m)\end{aligned}$$

where  $T_u$  is the turbulence intensity.

- **Calculate  $\gamma_1$  as a function of mean windspeed.**  $\gamma_1$  depends upon the mean duration of a visit by the windspeed to the critical velocity interval and upon the structural rise time.

The mean duration of a visit by the windspeed to the critical velocity interval,  $E[\mathcal{T}_{[a,b]}]$ , was expressed in Equation 4.6. Reiterating:

$$E[\mathcal{T}_{[a,b]}] = \frac{F_V(b) - F_V(a)}{\nu_a^+ + \nu_b^+}$$

where  $F_V(x)$  is the CDF of the instantaneous windspeed evaluated at  $x$ .  $a$  and  $b$  are, respectively, the lower and upper bounds of the critical velocity interval,  $a = \frac{5}{6}V_{crit}$  and  $b = \frac{6.5}{6}V_{crit}$ .  $\nu_x^+$  is the mean rate of crossing the level  $V(t) = x$  at positive slopes. If the instantaneous windspeed is assumed to be a Gaussian process, then  $\nu_x^+ = \frac{1}{2\pi} \frac{\sigma_V}{\sigma_V} \exp\left(-\frac{(x-\bar{V})^2}{2\sigma_V^2}\right)$ , where  $\sigma_V$  is the standard deviation of the time derivative of the instantaneous windspeed. The mean duration of visit can be further expressed as follows.

$$E[\mathcal{T}_{[a,b]}] = \frac{\int_a^b \frac{1}{\sqrt{2\pi}\sigma_V} \exp\left(-\frac{(x-\bar{V})^2}{2\sigma_V^2}\right) dx}{\frac{1}{2\pi} \frac{\sigma_V}{\sigma_V} \left\{ \exp\left(-\frac{(a-\bar{V})^2}{2\sigma_V^2}\right) + \exp\left(-\frac{(b-\bar{V})^2}{2\sigma_V^2}\right) \right\}} \quad (5.6)$$

The above equation for  $E[\mathcal{T}_{[a,b]}]$  shows that for given values of  $a$  and  $b$ , the mean duration of a visit to  $[a, b]$  depends not only on the mean windspeed  $\bar{V}$  and the standard deviation  $\sigma_V$  through the PDF of the windspeed, but also on the ratio  $\frac{\sigma_{\dot{V}}}{\sigma_V}$  through upcrossing rates.

To implement the probabilistic model, it is necessary to be able to estimate  $\sigma_{\dot{V}}$  and  $\sigma_V$  from knowledge of prevailing weather conditions.  $\sigma_V$  is a measure of the turbulence level and may be estimated in a rational way.  $\sigma_{\dot{V}}$  is not commonly reported and a database needs to be established from high sampling rate raw windspeed data. As part of this research,  $\sigma_{\dot{V}}$  has been estimated from a database measured at one marine site over a wide range of mean windspeeds and turbulence levels. This is reported in Chapter 6.

For illustrative purposes, a constant value of  $\frac{\sigma_{\dot{V}}}{\sigma_V}$  ( $=0.38 \text{ [s}^{-1}\text{]}$ ) is used here to calculate the mean duration of a visit to the critical interval at different mean windspeeds.  $\frac{\sigma_{\dot{V}}}{\sigma_V}$  may vary with mean windspeed. More complete analysis on  $\sigma_{\dot{V}}$  from raw windspeed data is given in Chapter 6.

Equation 5.6 showed that  $E[\mathcal{T}_{[a,b]}]$  only depends on  $\frac{\sigma_{\dot{V}}}{\sigma_V}$ ,  $\frac{\sigma_V}{\bar{V}}$  and  $\frac{\bar{V}}{V_{crit}}$ . After  $E[\mathcal{T}_{[a,b]}]$  is found,  $\gamma_1$  can be calculated based on the empirical formulae shown in Equation 4.65. These empirical formulae were the best fit to the results of *Monte Carlo* numerical simulations based on the least square error technique (see Chapter 4 for details).

$$r = \zeta \omega_n E[\mathcal{T}_{[a,b]}]$$

$$\gamma_1 = \frac{E[\mathcal{D}]}{E[\mathcal{D}_0]} = \begin{cases} 1 - \exp(-0.9359r^{0.2541}) & m = 3.00 \\ 1 - \exp(-0.7093r^{0.2859}) & m = 3.74 \\ 1 - \exp(-0.5718r^{0.3085}) & m = 4.38 \end{cases}$$

where  $\zeta$  and  $\omega_n$  are, respectively, the structural damping coefficient and the natural frequency of the structural member in radians per second.

- **Calculate  $\gamma_{bin}$ .** Values of  $\gamma$  at different mean windspeeds are calculated as the product of  $\gamma_0$  and  $\gamma_1$ . The  $\gamma$  vs. mean windspeeds curve is then constructed for fixed values of the turbulence intensity and  $m$ , the exponent of the  $S-N$  curve.

Next, for a given bin size  $\Delta\bar{V}$ , the mean windspeed bins are constructed.  $\bar{\gamma}_j$  is calculated numerically at each bin as the average value of  $\gamma$  within that bin. The actual integration of  $\gamma$  within each bin may be approximated using the rectangular scheme. After the values of  $\bar{\gamma}_j$  are calculated over all velocity bins,

$\gamma_{bin}$  is calculated as follows.

$$\gamma_{bin} = \frac{\sum_{j=1}^n \bar{\gamma}_j}{\gamma_{max}} \quad (5.7)$$

where  $\gamma_{max} = \gamma(V_{crit})$  is the value of  $\gamma$  at the mean windspeed equal to  $V_{crit}$ .

Since  $\bar{\gamma}_j$  decays quickly as the mean windspeed moves away from  $V_{crit}$ , the actual summation in Equation 5.7 is confined to a limited range of mean windspeeds.

Equation 5.7 provides a value of  $\gamma_{bin}$  for a given structural member at fixed values of the bin size, turbulence intensity and the exponent of the  $S - N$  curve. In order to account for different values of bin size and the turbulence level, a model for  $\gamma_{bin}$  is proposed as follows:

$$\begin{aligned} \gamma_{bin} &= \mathcal{F}_m\left(m, \frac{\Delta\bar{V}}{V_{crit}}, T_u\right) \\ &= \left(\frac{\Delta\bar{V}}{V_{crit}}\right)^{-1} \mathcal{F}_m(T_u) \end{aligned} \quad (5.8)$$

where  $\mathcal{F}_m(T_u)$  is a real function of  $T_u$ , the turbulence intensity. The subscript  $m$  indicates that the functional form of  $\mathcal{F}_m$  depends on the choice of a particular  $S - N$  curve. The fact that  $\gamma_{bin}$  is inversely proportional to  $\Delta\bar{V}$  is clear in Equation 5.4, where the denominator is proportional to  $\Delta\bar{V}$  while the numerator does not change with  $\Delta\bar{V}$ .

Next we will show how the functional form of  $\mathcal{F}_m(T_u)$  for a specified  $S - N$  curve was derived based on the numerical values of  $\gamma_{bin}$  which were calculated from Equation 5.7. Without loss of generality, let us assume that  $m = 3.74$ .

First, a set of turbulence intensity levels were specified at which the values of  $\gamma_{bin}$  were to be evaluated. This set covered the range of turbulence intensity levels that might occur in maritime winds. In this example, the turbulence intensity levels were set at 1%, 5%, 10%, 15% and 20%.

At turbulence intensity equal to 1%, the bin size was varied from 0.25 [ $\text{m}\cdot\text{s}^{-1}$ ] to 15 [ $\text{m}\cdot\text{s}^{-1}$ ] (corresponding to a  $\frac{\Delta\bar{V}}{V_{crit}}$  value from 0.02 to 1.16 at  $V_{crit} = 12.96$  [ $\text{m}\cdot\text{s}^{-1}$ ]), and  $\gamma_{bin}$  was calculated using Equation 5.7 at each bin size. The variation of  $\gamma_{bin}$  with different values of  $(\frac{\Delta\bar{V}}{V_{crit}})^{-1}$  was found to fit well by a straight line through the origin using the least square error technique. The slope of this line was the value of  $\mathcal{F}_m$  at a fixed turbulence level.



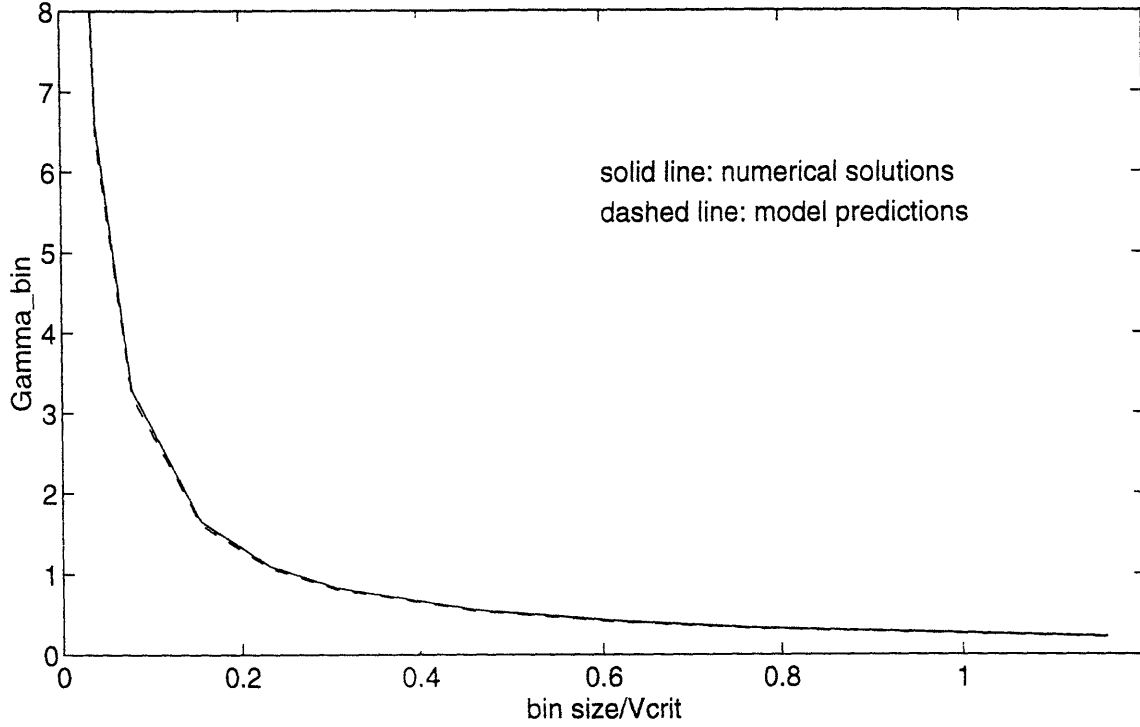


Figure 5-5: Variation of  $\gamma_{bin}$  with bin sizes at turbulence intensity = 10%, numerical solution *v.s.* model prediction.  $m = 3.74$

The above process was repeated to calculate the values of  $\mathcal{F}_m$  at turbulence intensity equal to 5%, 10%, 15% and 20%. The variation of  $\mathcal{F}_m$  with turbulence intensity level was found to be well represented by a third-order polynomial expressed below.

$$\mathcal{F}_{m=3} = T_u^2 + 1.98T_u + 0.04 \quad (5.9)$$

where  $T_u = \frac{\sigma_v}{V}$  is the turbulence intensity level.

Combining Equations 5.8 and 5.9, a model for  $\gamma_{bin}$  can be expressed as below for  $m = 3.74$ .

$$\gamma_{bin} = \left( \frac{\Delta \bar{V}}{V_{crit}} \right)^{-1} (T_u^2 + 1.98T_u + 0.04) \quad (5.10)$$

Figure 5-5 shows for the example, the values of  $\gamma_{bin}$  (calculated from Equation 5.7) as a function of the bin size to the critical velocity ratio at 10% turbulence intensity. The values of  $\gamma_{bin}$  from this example are compared with the values of  $\gamma_{bin}$  predicted by the model in Equation 5.10.

$m$	$\mathcal{F}_m$				
	$T_u = 1\%$	$T_u = 5\%$	$T_u = 10\%$	$T_u = 15\%$	$T_u = 20\%$
$m = 3.00$	0.074	0.143	0.237	0.336	0.436
$m = 3.74$	0.065	0.143	0.254	0.370	0.488
$m = 4.38$	0.059	0.140	0.250	0.366	0.483

Table 5.1: Values of  $\mathcal{F}_m$  at different values of turbulence and the exponent of the  $S - N$  curve

The functional form of  $\mathcal{F}_m$  is different for different values of  $m$  (from different  $S - N$  curves). To derive a functional form of  $\mathcal{F}_m$  at a different value of  $m$ , values of  $\gamma_{bin}$  need to be calculated using Equation 5.7 for different values of  $\frac{\Delta\bar{V}}{V_{crit}}$  and  $T_u$ . Then  $\mathcal{F}_m$  at different turbulence intensity levels can be calculated from the values of  $\gamma_{bin}$  using Equation 5.8. Table 5.1 shows the values of  $\mathcal{F}_m$  as functions of turbulence intensity levels at  $m = 3.00$ ,  $m = 3.74$  and  $m = 4.38$  respectively. These values of  $m$  span the values recommended by the U.K. Department of Energy [38] for most welded joints and the American Petroleum Institute [1].

The numerical values of  $\mathcal{F}_m$  in Table 5.1 for  $m = 3.00$  and  $m = 4.38$  were also found to be fit well by third-order polynomials expressed as follows.

$$\mathcal{F}_{m=3.00} = T_u^2 + 1.73T_u + 0.06 \quad (5.11)$$

$$\mathcal{F}_{m=4.38} = 3T_u^2 + 1.84T_u + 0.04 \quad (5.12)$$

As a summary to Equations 5.10, 5.11 and 5.12, a model for  $\gamma_{bin}$  for  $m = 3.00$ ,  $m = 3.74$  and  $m = 4.38$  can be expressed as follows.

$$\gamma_{bin} = \begin{cases} \left(\frac{\Delta\bar{V}}{V_{crit}}\right)^{-1}(T_u^2 + 1.73T_u + 0.06) & m = 3.00 \\ \left(\frac{\Delta\bar{V}}{V_{crit}}\right)^{-1}(T_u^2 + 1.98T_u + 0.04) & m = 3.74 \\ \left(\frac{\Delta\bar{V}}{V_{crit}}\right)^{-1}(3T_u^2 + 1.84T_u + 0.04) & m = 4.38 \end{cases} \quad (5.13)$$

Equation 5.13 is able to model  $\gamma_{bin}$  as a function of the ratio of the bin size to the critical velocity of a member, turbulence intensity and different  $S - N$  curves. It is strictly valid when all the underlying assumptions hold. These assumptions include:

- The scatter diagram of mean windspeeds is flat locally over the significant width of the  $\gamma$  vs.  $\bar{V}$  curve.
- The instantaneous windspeed is a Gaussian random process.

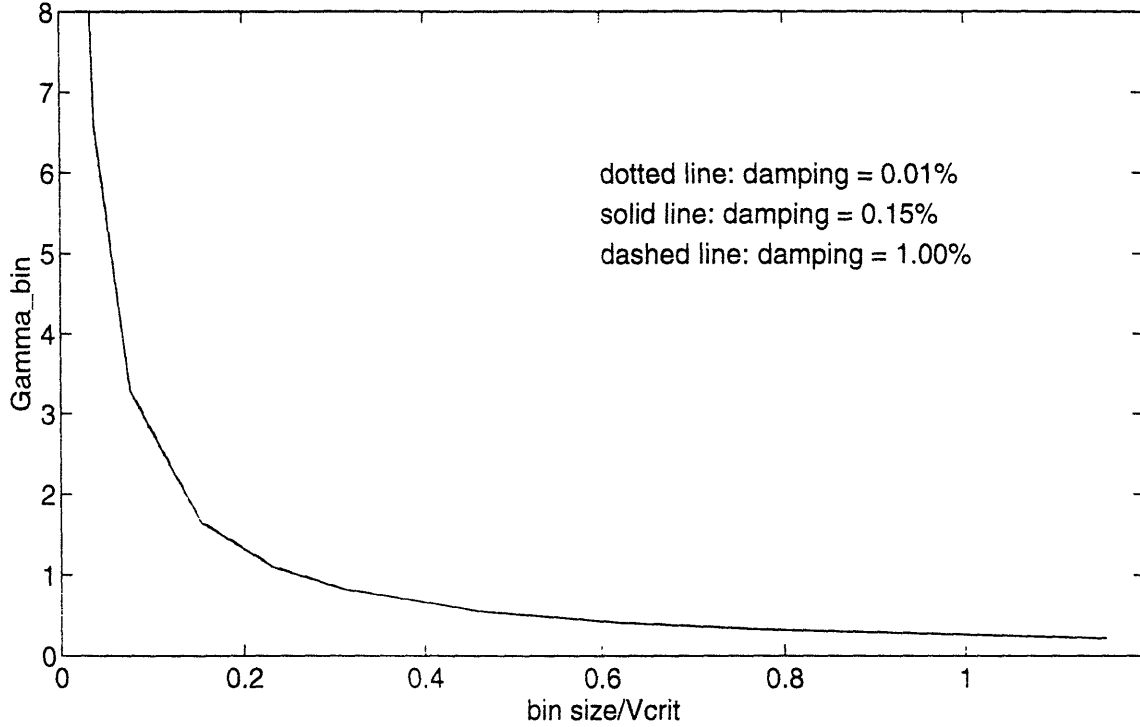


Figure 5-6: Variations of  $\gamma_{bin}$  with  $\frac{\Delta \bar{V}}{V_{crit}}$  at  $T_u = 10\%$  for different values of structural damping,  $m = 3.74$

- A constant  $\frac{\sigma_{\bar{V}}}{\sigma_V}$  at all mean windspeeds.
- A constant structural damping ratio = 0.15%.

The insensitivity of  $\gamma_1$  to  $\gamma_{bin}$  is further demonstrated by a numerical example. Consider three cases with identical values of structural parameters and wind statistics except for different values of structural damping coefficients. The values of structural damping coefficients for the three cases are  $\zeta_1 = 0.01\%$ ,  $\zeta_2 = 0.15\%$  and  $\zeta_3 = 1.0\%$  respectively. For each case, turbulence intensity level was fixed at 10% and  $m$  was fixed at 3.74.  $\gamma_{bin}$  was calculated from Equation 5.7 at different bin sizes so that  $\gamma_{bin}$  vs.  $\frac{\Delta \bar{V}}{V_{crit}}$  curve at turbulence intensity level of 10% can be plotted in Figure 5-6.

Figure 5-6 shows that values of  $\gamma_{bin}$  are insensitive to the structural damping. Since structural damping only influences the value of  $\gamma_{bin}$  through the ratio of the mean duration to the rise time, this figure further supports that the shape of the  $\gamma$  vs.  $\bar{V}$  curve is controlled by  $\gamma_0$ .

As a summary, the model for  $\gamma_{bin}$  shown in Equation 5.13 is robust and applicable to the situations when the scatter diagram of mean windspeeds is flat locally at  $V_{crit}$

and when the instantaneous windspeed is approximately Gaussian.

### 5.3 Summary

Since the mean windspeed is a random process typically specified by a scatter diagram, estimated fatigue damage of structural members must account for the width of the wind velocity bins. The expected value of fatigue damage is a probability (of occurrence) weighted integral of the predicted fatigue damage over all possible wind velocity bins. However, to find the exact fatigue damage based on integration is not practically attractive because of excessive amount of numerical computations.

A simple but crude estimate of the exact fatigue damage has been found to be the product of the fatigue damage when the mean windspeed is at the critical velocity of the member and the probability of the wind velocity bin which brackets the critical velocity of the member. A model is proposed to correct the crude estimate to the exact fatigue damage using a correction factor. Exact values of fatigue damage based on numerical integrations over various wind velocity bin sizes suggest that this correction factor depends on the ratio of the velocity bin size to the critical velocity of the structural member, the turbulence intensity level and the slopes of the  $S - N$  curve. This model correctly shows that a large ratio of the velocity bin size to the critical velocity or a small turbulence intensity level leads to a small factor, or a small expected fatigue damage. The model yields satisfactory predictions as compared to the results of numerical integrations.

# Chapter 6

## Characteristics of Natural Winds

It was shown in Chapter 3 that unsteady fluctuations of the instantaneous windspeed typically prevent vortex-excited vibrations from reaching steady state amplitudes. Natural winds exhibit random variations in both amplitudes and directions, which make impact on fatigue problems of offshore structural members. Reliable predictions of their fatigue lives, therefore, require thorough understanding of how natural winds behave.

In this chapter, characteristics of natural winds are studied. Review of existing knowledge on natural winds revealed lack in the quantitative understanding of the wind statistics which determine the duration of a visit by the windspeed to an interval. This led us to estimate these wind statistics from high sampling rate raw windspeed data. These new wind statistics enable us to assess fatigue damage of wind sensitive offshore structural members based on the probabilistic model proposed in Chapter 4.

### 6.1 Review of existing knowledge on natural winds

The wind is a movement of free air caused by large-scale thermal currents in the atmosphere above the earth's surface. The wind speed in the atmosphere varies stochastically in time and geographic distribution. To study random variations of winds in both magnitude and direction requires analytical tools such as probability and statistics.

Let  $\mathbf{V}(x, y, z, t) = \{U(x, y, z, t), V(x, y, z, t), W(x, y, z, t)\}$  be a vector representing the instantaneous windspeed at time  $t$  and at location  $(x, y, z)$ . Here  $x$ ,  $y$  and  $z$  are the three orthogonal axes of Cartesian coordinate system, where  $z$  denotes the vertical direction (to the earth surface),  $x$  and  $y$  denotes the longitudinal and transverse direction yet to be specified in the horizontal plane.  $U(x, y, z, t)$ ,  $V(x, y, z, t)$  and  $W(x, y, z, t)$  are, respectively, the corresponding instantaneous velocity components in longitudinal, transverse and vertical directions.

At any location  $(x, y, z)$ , the instantaneous windspeed  $\{U(t), V(t), W(t)\}$  is defined as the sum of two subsequent three-dimensional random processes  $\{\bar{U}(t), \bar{V}(t), \bar{W}(t)\}$  and  $\{u(t), v(t), w(t)\}$ , where  $\{\bar{U}(t), \bar{V}(t), \bar{W}(t)\}$  is the average windspeed over a specified time period, and  $\{u(t), v(t), w(t)\}$  is the fluctuating windspeed, or turbulence.

$$U(t) = \bar{U}(t) + u(t) \quad (6.1)$$

$$V(t) = \bar{V}(t) + v(t) \quad (6.2)$$

$$W(t) = \bar{W}(t) + w(t) \quad (6.3)$$

where bar denotes time-averaging.

The average windspeed can be interpreted as a moving average over a specified time period (for example, 1-hour period). The average windspeed could change over time, but the change of the average windspeed with time is much slower than that of the fluctuating windspeed.

The average windspeed could also vary with the length of the averaging period. It is conventional to define a mean windspeed as the average over one hour. Consequently, the corresponding average windspeed is called the hourly average windspeed. The hourly mean convention is chosen because the period of 1 hour coincides with a minimum in the windspeed spectrum [32]. The low spectral value implies that the rate of energy change from hour to hour is slow, which corroborates the choice of one hour as a good statistical period.

However, the hourly average windspeed may not be appropriate to use directly for VIV predictions. In Chapter 3, we investigated the effect of using the mean windspeed on the accuracy of VIV predictions. We concluded that use of mean windspeed grossly over-predicts the occurrence of steady state vibrations.

The following is a review of the existing knowledge of the characteristics of the mean (time-average) and the fluctuating windspeed. Most material that is presented below can be found in Lawson [19], Sachs [32] and Liu [22].

## 6.1.1 Hourly average windspeed

### Windspeed profile

Hourly average windspeed varies with height in a form which can be described by either a logarithmic law or a power law.

- **Logarithmic law**

$$\bar{U}(z) = \frac{U_*}{\kappa} \ln \frac{z}{z_0} \quad (6.4)$$

- **Power law**

$$\bar{U}(z) = \bar{U}(z_r) \left( \frac{z}{z_r} \right)^\alpha \quad (6.5)$$

where  $\bar{U}(z)$  is the hourly average windspeed at height  $z$  above ground;  $U_*$  is the shear velocity or friction velocity, which by definition is equal to  $\sqrt{\frac{\tau_0}{\rho}}$ , where  $\tau_0$  is the stress of wind at ground level and  $\rho$  is the air density;  $\kappa$  is the von Karman constant equal to 0.4 approximately;  $z_0$  is the roughness of ground, which is an effective height of ground roughness elements;  $\bar{U}(z_r)$  is the wind speed at any reference height,  $z_r$ , which is conventionally defined at 10 meters above ground; and  $\alpha$  is the power-law exponent, which depends on roughness and other conditions.

The logarithmic law is based on physical principles, assuming the shear stress is constant. The Power law only approximates the variation (of windspeed) over part of the height range, but nevertheless is more popular in engineering applications due to its easy use.

### Probability distribution functions

As it varies with time, the hourly average windspeed at any location is a random variable which can be best described by probability density functions (PDF) or cumulative distribution functions (CDF). The following three functions are commonly used:

- Rayleigh distribution

$$F_{\bar{U}}(y) = 1 - \exp\left(-\frac{\pi y^2}{4(E[\bar{U}])^2}\right) \quad (6.6)$$

- Gaussian distribution

$$p_{\bar{U}}(y) = \frac{1}{\sqrt{2\pi}\sigma_{\bar{U}}} \exp\left(-\frac{(y - E[\bar{U}])^2}{2\sigma_{\bar{U}}^2}\right) \quad (6.7)$$

- Weibull distribution

$$F_{\bar{U}}(y) = 1 - \exp\left(-\left(\frac{y}{c}\right)^k\right) \quad (6.8)$$

where  $p_{\bar{U}}(y)$  and  $F_{\bar{U}}(y)$  are the PDF and the CDF of the hourly average windspeed, where  $p_{\bar{U}}(y) = \frac{dF_{\bar{U}}(y)}{dy}$ ;  $\bar{U}$  is the hourly average windspeed;  $E[\bar{U}]$  is the ensemble average of the hourly average windspeed  $\bar{U}$ ;  $\sigma_{\bar{U}}$  is the standard deviation of the hourly

average windspeed:  $c$  and  $k$  are the mode and the slope of the Weibull distribution respectively.

The Rayleigh distribution is rather simple because it depends only on one parameter, the mean of the hourly average windspeed, but it is only a crude approximation. Gaussian and Weibull distributions are two-parameter (both mean and standard deviation of the hourly average windspeed) probability models that yield better results.

### 6.1.2 Turbulence

Sachs [32] described the fluctuating windspeed as follows:

Quantitatively, however, the wind variations over a short period ( $\approx 1$  hour) are entirely random about the mean speed over that period. Further, the random pattern is the same, at all times, for any wind-measurement site where conditions remain the same.

#### Probability distribution functions of turbulence

According to the remarks by Sachs, it is reasonable to model the fluctuating windspeed as a stationary Gaussian random process. Its PDF is Gaussian with an ensemble mean of zero and a variance of  $\sigma_u^2$ :

$$p_u(y) = \frac{1}{\sqrt{2\pi}\sigma_u} \exp\left(-\frac{y^2}{2\sigma_u^2}\right) \quad (6.9)$$

#### Autocorrelation functions of turbulence

$R_u(\tau)$ ,  $R_v(\tau)$  and  $R_w(\tau)$  are the three autocorrelation functions of turbulence corresponding to the longitudinal, transverse, and vertical components of the fluctuating velocity,  $u(t)$ ,  $v(t)$ , and  $w(t)$  respectively.

Mathematically,  $R_u(\tau)$ ,  $R_v(\tau)$  and  $R_w(\tau)$  are defined as

$$R_u(\tau) = E[u(t)u(t + \tau)] \quad (6.10)$$

$$R_v(\tau) = E[v(t)v(t + \tau)] \quad (6.11)$$

$$R_w(\tau) = E[w(t)w(t + \tau)] \quad (6.12)$$

where  $E[x]$  denotes the ensemble average of a random process  $x$ .  $\tau$  is the time lag between the same signal.  $R_u(\tau)$ ,  $R_v(\tau)$  and  $R_w(\tau)$  are called the longitudinal, transverse and vertical autocorrelation function of turbulence. Notice that the above



defined autocorrelation functions depend only on the time lag  $\tau$  because the fluctuating windspeed  $u(t)$ ,  $v(t)$ ,  $w(t)$  are assumed to be stationary random processes. In general, the autocorrelation functions depend on both the instantaneous time  $t$  and the time lag  $\tau$ .

### Power spectral density functions of turbulence

The power spectral density function represents variations of wind energy with different frequencies. There are three power spectral density functions of turbulence,  $S_u(f)$ ,  $S_v(f)$  and  $S_w(f)$ , corresponding to the longitudinal, transverse and vertical components of the fluctuating velocity,  $u(t)$ ,  $v(t)$  and  $w(t)$  respectively.

Mathematically,  $S_u(f)$ ,  $S_v(f)$  and  $S_w(f)$  are defined as

$$S_u(f) = \int_{-\infty}^{\infty} e^{-i2\pi f\tau} R_u(\tau) d\tau \quad (6.13)$$

$$S_v(f) = \int_{-\infty}^{\infty} e^{-i2\pi f\tau} R_v(\tau) d\tau \quad (6.14)$$

$$S_w(f) = \int_{-\infty}^{\infty} e^{-i2\pi f\tau} R_w(\tau) d\tau \quad (6.15)$$

where  $R_u(\tau)$ ,  $R_v(\tau)$  and  $R_w(\tau)$  are longitudinal, transverse and vertical autocorrelation functions of turbulence defined in Equations 6.10, 6.11 and 6.12.  $f$  [Hertz] is frequency in Hertz.  $i$  is the unit of imaginary numbers, and  $i = \sqrt{-1}$ .  $S_u(f)$ ,  $S_v(f)$  and  $S_w(f)$  are called the longitudinal, transverse and vertical power spectral density functions of turbulence.

Different longitudinal wind spectrum formulae proposed by various investigators are presented as follows:

- **Davenport spectrum** [23]

$$\frac{f S_u(f)}{U_*^2} = \frac{4x^2}{(1+x^2)^{4/3}} \quad (6.16)$$

- **Von Karman spectrum** [34]

$$\frac{f S_u(f)}{U_*^2} = \frac{4\beta \frac{fL_*^2}{U}}{\left[1 + 70.8 \left(\frac{fL_*^2}{U}\right)^2\right]^{5/6}} \quad (6.17)$$

- **Kareem spectrum** [18]

$$\frac{f S_u(f)}{U_*^2} = \frac{335 \frac{f L_u^x}{\bar{U}(10)}}{(1 + 71 \frac{f L_u^x}{\bar{U}(10)})^{5/3}} \quad (6.18)$$

- **North Sea spectrum** [27]

$$S_u(f) = \frac{320 \times (0.1 \bar{U}_{10})^2 \times (0.1 Z)^{0.45}}{(1 + \tilde{f}^n)^{\frac{5}{3n}}} \quad (6.19)$$

where  $f$  [ $s^{-1}$ ] is the frequency.  $U_*$  [ $m \cdot s^{-1}$ ] is friction velocity.  $x = \frac{1200f}{\bar{U}(10)}$ , where  $\bar{U}(10)$  is the hourly average windspeed at 10 meters above ground.  $\beta$  is a parameter determined by surface roughness and has a value ranging from 4.0 to 6.5, it decreases as surface roughness increases.  $L_u^x$  is the longitudinal length scale of longitudinal turbulence which will be defined later.  $\tilde{f} = 172 \times f \times (0.1 Z)^{\frac{2}{3}} \times (0.1 \bar{U}_{10})^{-0.75}$ , where  $n = 0.468$  and  $Z$  [m] is the height above sea level.

The Davenport spectrum model is commonly used for land-based structures. The Von Karman spectrum model can be used in applications in which the effect of the low-frequency component could be important. The Kareem spectrum and the North Sea spectrum were proposed for sea-based structures. Various spectrum formulae tend to agree in that they approach the Kolmogorov limit at high frequencies, but they differ at low frequencies.

### Turbulence intensity

Turbulence intensity measures the amplitude of the fluctuating windspeed. It is defined as follows:

$$\begin{aligned} T_u(z) &= \frac{\sqrt{E[u^2]}(z)}{\bar{U}(z)} \\ &= \frac{u'(z)}{\bar{U}(z)} \end{aligned} \quad (6.20)$$

where  $u'(z) = \sqrt{E[u^2]}(z)$  is the r.m.s. value of the fluctuating windspeed in longitudinal direction. Again,  $E[x]$  denotes the ensemble average of a random process  $x$ .

Turbulence intensity varies with height and temperature gradient along the height. Due to the presence of the earth's boundary layer, the shear gradient in the velocity profile is the largest close to the ground. Large shear near the ground generates high turbulence. Strong negative temperature gradients (lower temperature at higher

height) create strong atmospheric convection which generates large velocity fluctuations, thus creating large turbulence.

### Integral scales of turbulence

Integral scales of turbulence are measures of the average size of the turbulent eddies of the flow. There are altogether nine integral scales of turbulence, corresponding to the three dimensions of the eddies associated with the longitudinal, transverse, and vertical components of the fluctuating velocity,  $u$ ,  $v$ , and  $w$ . For example,  $L_u^x$ ,  $L_u^y$  and  $L_u^z$  are, respectively, measures of the average longitudinal, transverse, and vertical size of the eddies associated with the longitudinal fluctuating windspeed.

Mathematically,  $L_u^x$  is defined as

$$L_u^x = \frac{1}{u'^2} \int_0^\infty R_{u_1 u_2}(x) dx \quad (6.21)$$

where  $R_{u_1 u_2}(x)$  is the spatial cross-correlation function of the longitudinal velocity components  $u_1 \equiv u(x_1, y_1, z_1, t)$  and  $u_2 \equiv u(x_1 + x, y_1, z_1, t)$ , and  $R_{u_1 u_2} = E[u_1 u_2]$ , where  $E[x]$  denotes the ensemble average of a random process  $x$ . Similar definitions apply to the other integral turbulence scales.

### 6.1.3 Wind directionality effects

Wind effects on structural members depend not only on the magnitude of the windspeeds, but on the associated wind directions as well. Wind directionality is important in both aerodynamic and structural perspectives. For example, wind-induced vibrations of a flexible cylinder depend on the direction of instantaneous winds. Considerable change in the wind direction in a short period alone could effectively disrupt established vibrations in one direction. Therefore it is important to study wind directionality effects.

Most of the existing knowledge on wind directionality effects is in the context of structural reliability, where extreme wind speeds and directions are of primary concern. Continuous joint probability distributions of extreme wind speeds and directions have been studied, but so far no credible models have been proposed in the literature, according to Simiu & Scanlan [34].

For applications to wind-induced vibrations, distribution functions of wind speed and direction are valuable. However to obtain such wind statistics could be a formidable task since the instantaneous windspeed in any direction is a derived random process that depends on both the instantaneous wind speed and direction, both being random processes.

We shall make the assumption that when estimating the response of a particular member, the direction of the windspeed does not change with time. If we define the direction of the windspeed as longitudinal, then the uni-directional assumption implies  $V(t) = W(t) = 0$ . Such an assumption would significantly reduce the degree of difficulty in dealing with two random variables at the same time and allow us to concentrate on the random characteristics of the wind speed alone. However, the consequence of this assumption on fatigue damage estimation remains to be studied.

## 6.2 Estimating desirable wind statistics from raw windspeed data

Fluctuations of the instantaneous windspeed typically prevent the structure from reaching steady-state vibrations by not allowing the windspeed to stay sufficiently long in the critical velocity interval. To understand the impact of the instantaneous windspeed on the fatigue damage accumulation of wind sensitive structural members requires wind statistics which determine the duration of a visit into an interval. Such wind statistics include:

- $p_U(u)$ , PDF of the instantaneous windspeed.
- $T_u = \frac{\sigma_U}{\bar{U}}$ , the turbulence intensity, where  $\sigma_U$  is the standard deviation of the instantaneous windspeed and  $\bar{U}$  is the mean windspeed.
- $\sigma_{\dot{U}}$ , the standard deviation of the time derivative of the instantaneous windspeed.

The PDF of the instantaneous windspeed, which carries the values of the mean windspeed  $\bar{U}$  and the standard deviation  $\sigma_U$ , explains why in real winds, steady-state vibrations at  $U_{crit}$  do not happen frequently. This PDF, along with  $U_{crit}$ , is used to calculate the value of  $\gamma_0$ .  $\sigma_U$  and  $\sigma_{\dot{U}}$  determine the mean duration and ultimately the value of  $\gamma_1$ . These wind statistics can only be estimated from high-frequency windspeed measurements over a wide range of velocities and elevations above the sea surface.

In the following sections, a database, which contains high sampling frequency wind data, measured at a typical maritime environment, is briefly described. Wind statistics estimated from the database are analyzed and presented.

### 6.2.1 The wind database

The wind database described here contains high sampling frequency wind data representative of typical maritime conditions [2]. The database includes wind speed measurements at different elevations. Windspeed samples were recorded with a frequency of 0.85 Hertz, and were grouped into 40 minute long records. Each record contains 2048 samples.

### 6.2.2 $p_U(u)$

A short-term windspeed record can be decomposed into a mean(time-average over the entire record length) windspeed and fluctuating windspeed. Since the mean windspeed and the fluctuating windspeed appear to be uncorrelated [32], instantaneous windspeed may be modeled as a Gaussian random process with the PDF given below:

$$p_U(u) = \frac{1}{\sqrt{2\pi}\sigma_U} \exp\left(-\frac{(u - \bar{U})^2}{2\sigma_U^2}\right) \quad (6.22)$$

where  $\bar{U}$  is the average windspeed over the entire record length. In this case,  $\bar{U}$  denotes the 40-minute mean windspeed.  $\sigma_U$  is the standard deviation of the windspeed.

In Chapter 4, analysis of raw windspeed has revealed that the assumption of Gaussianly-distributed instantaneous windspeed leads to a satisfactory prediction of  $\gamma_0$  and a conservative prediction of  $\gamma_1$ . Therefore, it is safe to predict the fatigue damage of offshore structural members based on the Gaussian windspeed assumption.

### 6.2.3 $T_u$

The turbulence intensity is defined here as follows:

$$T_u = \frac{\sigma_U}{\bar{U}} \quad (6.23)$$

where  $T_u$  is the turbulence intensity.  $\sigma_U$  is the standard deviation of the 40-minute windspeed.  $\bar{U}$  is the 40-minute mean windspeed.

Figure 6-1 shows  $T_u$  as a function of  $\bar{U}$  at three different elevations. Each pair of  $(\bar{U}, T_u)$  was calculated numerically from a 40-minute windspeed record as follows.

$$\bar{U} = \frac{1}{2048} \sum_{i=1}^{2048} U_i$$

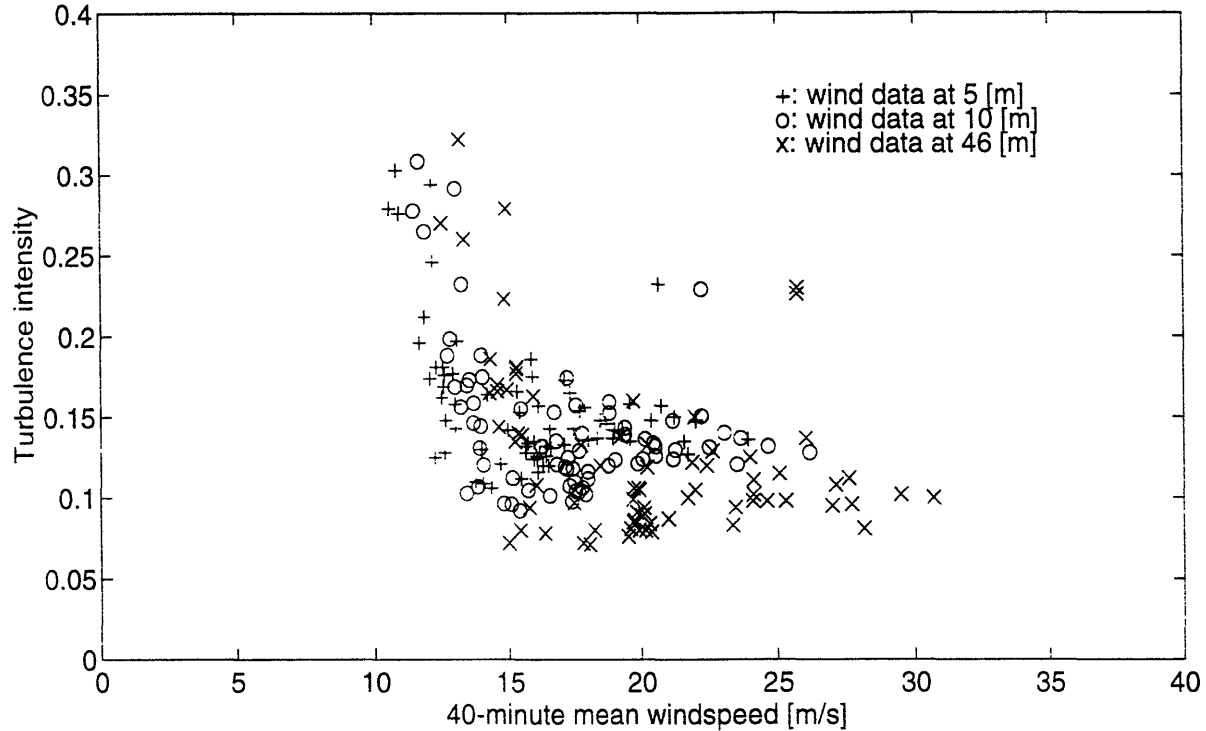


Figure 6-1: Variation of  $T_u$  with  $\bar{U}$  at three different elevations, from high sampling rate raw windspeed data

$$\sigma_U = \sqrt{\frac{1}{2047} \sum_{i=1}^{2048} (U_i - \bar{U})^2}$$

$$T_u = \frac{\sigma_U}{\bar{U}}$$

The observed turbulence levels range from 7% to 33%, and show poor correlation with the mean windspeeds. The scatter of the turbulence is caused by differences in the atmospheric stability. When the atmosphere is stable, the turbulence is generated only by the shear gradient in the velocity profile, resulting in a low turbulence intensity. When the atmosphere is unstable, the turbulence is generated not only by the shear gradient in the velocity profile, but also by unstable atmospheric convection, resulting in a large turbulence intensity. A strong atmospheric instability is characterized by a strong negative temperature gradient in the vertical direction (higher temperature close to ground).

Turbulence intensity depends on the mean windspeed  $\bar{U}$ , the elevation and the temperature gradient. Large mean windspeeds increase the turbulence production, thus increasing the turbulence intensity. Velocity fluctuations are the largest close to the surface due to large shear gradients in the windspeed profile. Negative temperature gradients cause atmospheric instability and result in a large turbulence level.

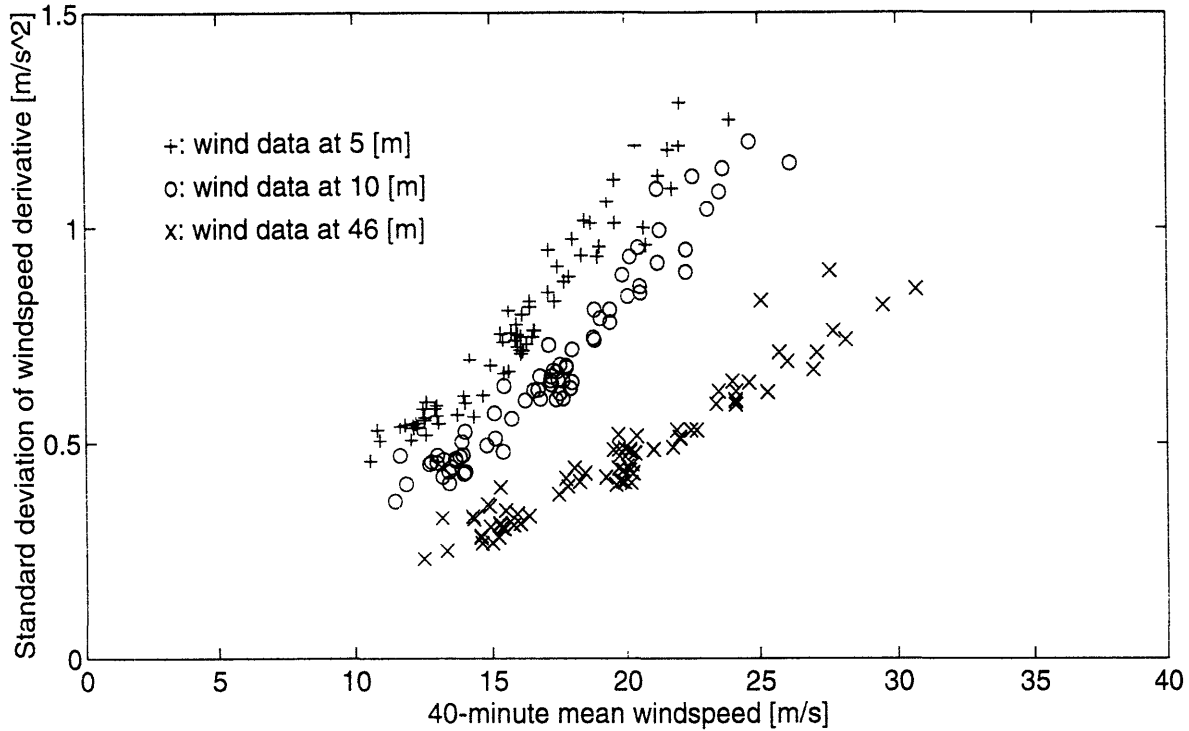


Figure 6-2: Variation of  $\sigma_{\dot{U}}$  with  $\bar{U}$  at three different elevations. from high sampling rate raw windspeed data

#### 6.2.4 $\sigma_{\dot{U}}$

$\sigma_{\dot{U}}$  is an important parameter to determine the upcrossing statistics, which in turn determine the mean duration of a visit by the windspeed to the critical velocity interval of a structural member. A sequence of  $\dot{U}$  can be obtained by taking the time derivative of the corresponding windspeed sequence  $U$ .

Since the differentiation operation on the digitized windspeed sequence is entirely numerical, the accuracy of the numerical differentiation scheme is of great concern. A good numerical differentiation scheme is one which has minimum round-off error as the number of samples increases. For example, the central difference scheme is superior to the forward difference scheme, since, as the number of samples increases, the round-off error of the central difference scheme decreases quadratically, while the round-off error of the forward difference scheme decreases linearly.

For any 40-minute windspeed record,  $\sigma_{\dot{U}}$  can be calculated as the sample standard deviation of the sequence  $\dot{U}$ . Figure 6-2 shows the observed  $\sigma_{\dot{U}}$  as a function of  $\bar{U}$  at three different elevations. Every pair,  $(\bar{U}, \sigma_{\dot{U}})$ , was derived numerically from a 40-minute raw windspeed record using the method described above. A total of 83

40-minute records were evaluated.

At a given elevation, Figure 6-2 shows that  $\sigma_{\bar{U}}$  is highly correlated with  $\bar{U}$ .  $\sigma_{\bar{U}}$  increases with  $\bar{U}$ , suggesting higher rates of turbulence production at higher windspeeds. At a constant value of  $\bar{U}$ ,  $\sigma_{\bar{U}}$  decreases as elevation increases. This is because the presence of the earth's boundary layer causes a larger shear gradient in the velocity profile near the surface, which in turn generates more turbulence and contributes to a larger  $\sigma_{\bar{U}}$ .

Based on the wind data that was presented in Figure 6-2, the relationship between  $\sigma_{\bar{U}}$  and  $\bar{U}$  at different elevations can be approximated by the following empirical formula:

$$\sigma_{\bar{U}} = \begin{cases} 0.0649\bar{U} - 0.2648 & z = 5 \text{ [m]} \\ 0.0608\bar{U} - 0.3725 & z = 10 \text{ [m]} \\ 0.0347\bar{U} - 0.2206 & z = 46 \text{ [m]} \end{cases} \quad (6.24)$$

Readers should be cautious in applying the above empirical formulae since they depend on data from a single maritime site. It may not be applicable to land-based wind environments.

### 6.3 Summary

Existing knowledge on wind statistics have been reviewed. Most of the available wind statistics are based on the hourly average windspeed, which is found inappropriate to use directly for predicting VIV and fatigue damage of wind sensitive structural members.

Wind statistics as input to the proposed probabilistic model were estimated from a high sampling frequency wind database measured at one marine site over a wide range of mean windspeeds and turbulence levels. The windspeed database consists of many 40-minute windspeed records with a sampling frequency of 0.85 Hertz.

The observed turbulence intensity depends on the mean windspeed, the elevation and the temperature gradient. Difference in temperature gradients causes poor correlation between the turbulence intensity and the mean windspeed.

The observed values of  $\sigma_{\bar{U}}$  show high correlation with the mean windspeed which is insensitive to atmosphere stability. At a given elevation,  $\sigma_{\bar{U}}$  increases with the mean windspeed.  $\sigma_{\bar{U}}$  decreases as elevation increases.



# Chapter 7

## The Design of Fatigue Resistant Structural Members Excited by Natural Winds

In this chapter, a design methodology for fatigue resistant structural members excited by natural winds is proposed based on the probabilistic model. The proposed design methodology is illustrated by examples.

### 7.1 Design procedure

A procedure is recommended to estimate the fatigue damage rate for a structural member exposed in natural winds. The prediction procedure consists of the following four steps:

- **Step 1: Predict  $\mathcal{D}_{s,s}$ .**  $\mathcal{D}_{s,s}$  is the fatigue damage rate of a structural member due to steady state vibrations at the critical velocity. It is the maximum fatigue damage rate that the member could experience among all possible wind conditions.  $\mathcal{D}_{s,s}$  is predicted based on the following steps.

1. *Calculate  $A_{max}$ .*  $A_{max}$ , the maximum amplitude of steady state vibrations, is predicted by the **Brown & Root** formula [29] as follows.

$$\frac{A_{max}}{D} = \frac{3.82\gamma_i C_L}{\left[1 + 0.19 \left(\frac{2\pi S_z^2 K_s}{C_L}\right)\right]^{3/5}} \quad (7.1)$$

where  $D$  [m] is the diameter of the cylinder.  $\gamma_i$  is the mode shape parameter that depends on the boundary conditions of the cylinder vibrating in the lowest mode. Values of  $\gamma_i$  for typical boundary conditions of a flexible cylinder are listed in Table 7.1 [31].  $C_L$  is the root mean squared (r.m.s.)

lift force coefficient based on stationary cylinder measurements, and it depends on the Reynolds number. The variation of the lift force coefficient with the Reynolds number is shown in Figure 7-1 [29].  $S_t$  is the Strouhal number, and it depends on the Reynolds number.  $S_t = 0.2$  is usually a good first guess for most members in the subcritical Reynolds number regime.  $K_s$  is the stability parameter, or the reduced damping.  $K_s = \frac{2m\delta}{\rho D^2}$ , where  $m$  [ $\text{kg}\cdot\text{m}^{-1}$ ] is the mass per unit length of the cylinder,  $\delta = 2\pi\zeta$  where  $\zeta$  is the structural damping ratio measured in still air,  $\rho$  [ $\text{kg}\cdot\text{m}^{-3}$ ] is the density of the air.

It is worth pointing out that the recommended lift force coefficient function shown in Figure 7-1 is more conservative, particularly in the critical and supercritical regimes, than that was originally proposed by **Brown & Root** [29]. We [30] believe that there is insufficient evidence, at the present time, to warrant the use of a lift coefficient as low as 0.1, as obtained from stationary cylinder studies. The lift force coefficient in Figure 7-1 varies linearly for the Reynolds number from  $3 \times 10^5$  to  $2 \times 10^6$ . The effects of surface roughness and atmospheric turbulence are also disregarded in this simple model. These parameters have been shown on stationary cylinders to cause the transition from subcritical to supercritical flow to occur at a lower nominal Reynolds number, thereby reducing the lift coefficient obtained at the velocity of interest. In the future, as relevant data becomes available, we recommend that this lift coefficient function be modified accordingly.

Boundary Conditions	$\gamma_i$	$F_i$
Free-Fixed	1.304	3.52
Pinned-Pinned	1.155	9.87
Fixed-Pinned	1.161	20.4
70% Fixity [16]	1.163	22.4
Fixed-Fixed	1.167	28.2

Table 7.1: Values of  $\gamma_i$  and  $F_i$  for different boundary conditions

2. Calculate  $\mathcal{D}_{s.s.}$ .  $\mathcal{D}_{s.s.}$  [ $\text{s}^{-1}$ ] is the fatigue damage rate assuming steady state vibrations. Its inverse is the number of seconds to fatigue failure.  $\mathcal{D}_{s.s.}$  is calculated from  $A_{max}$  and a specified  $S - N$  curve as follows.

$$\begin{aligned} \mathcal{D}_{s.s.} &= f_n c^{-1} \left( E \times F_i \times \frac{D^2}{L^2} \times \frac{A_{max}}{D} \times \text{SCF} \right)^m \\ &= \frac{f_n}{N_0} \left( \frac{E}{S_0} \times F_i \times \frac{D^2}{L^2} \times \frac{A_{max}}{D} \times \text{SCF} \right)^m \end{aligned}$$

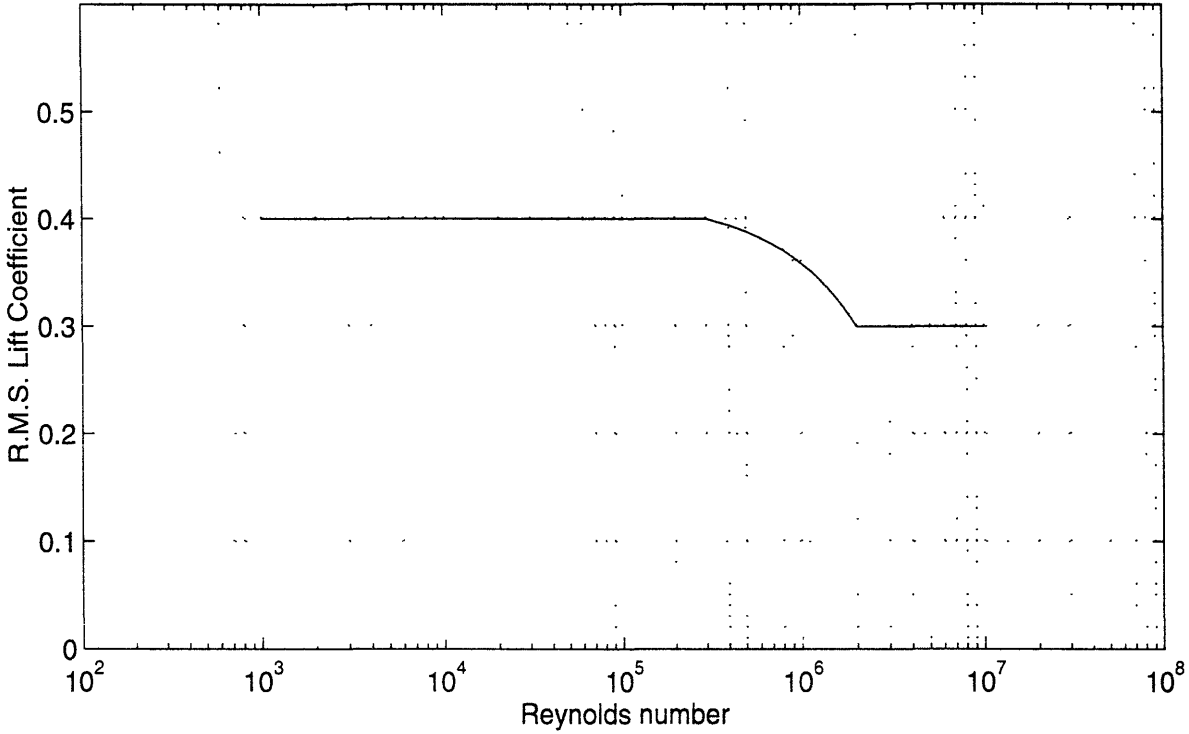


Figure 7-1: Variation of the r.m.s. lift force coefficient with Reynolds number, from Rudge & Fei (1991)

where  $f_n$  [ $s^{-1}$ ],  $D$  [m] and  $L$  [m] are, respectively, the natural frequency, the diameter and the total length of the structural member.  $E$  [ $kg \cdot m^{-1} \cdot s^{-2}$ ] is the Young's modulus.  $F_i$  is the strain response parameter. It defines the maximum strain as a function of the maximum deflection and the cylinder boundary conditions [30]. Values of  $F_i$  with different boundary conditions are shown in Table 7.1. For a pinned-pinned beam,  $F_i = \pi^2 = 9.87$ . SCF is the stress concentration factor, A typical SCF = 2.0 to 4.0.  $c$  and  $m$  are positive constants that are defined by the  $S - N$  curve as follows.

$$NS^m = N_0 S_0^m = c$$

where  $S$  [ $kg \cdot m^{-1} \cdot s^{-2}$ ] is the stress range, for cyclic stresses, the stress range is twice the amplitude of cyclic stresses.  $N$  is the number of cycles to fatigue failure at the stress range  $S$ .  $S_0$  and  $N_0$  are the reference stress range and the number of cycles to fatigue failure at the reference stress range.  $m$  and  $c$  are positive constants that are related to material properties.  $m$  is usually between 3 and 4.

- **Step 2: Predict  $\gamma_{max}$ .**  $\gamma_{max}$  is the value of  $\gamma$  ( $=\gamma_0 \times \gamma_1$ ) evaluated with the mean windspeed equal to the critical velocity of the member, where  $\gamma$  is a fatigue discount factor which includes the effect of natural fluctuations of the windspeed around a constant mean windspeed and the effect of the structural rise time.  $\gamma_{max}$  can be calculated as follows.

$$\begin{aligned}
 V_{crit} &= 6f_n D \\
 a &= \frac{5V_{crit}}{6} \\
 b &= \frac{6.5V_{crit}}{6} \\
 E[\mathcal{T}_{a,b}] &= \frac{\int_a^b \frac{1}{\sqrt{2\pi}\sigma_V} \exp\left(-\frac{(v-V_{crit})^2}{2\sigma_V^2}\right) dv}{\frac{1}{2\pi} \frac{\sigma_V}{\sigma_V} \left\{ \exp\left(-\frac{(a-V_{crit})^2}{2\sigma_V^2}\right) + \exp\left(-\frac{(b-V_{crit})^2}{2\sigma_V^2}\right) \right\}} \\
 &= \frac{\Phi\left(\frac{1}{12T_u}\right) - \Phi\left(-\frac{1}{6T_u}\right)}{\frac{1}{2\pi} \frac{\sigma_V}{\sigma_V} \left\{ \exp\left(-\frac{1}{288T_u^2}\right) + \exp\left(-\frac{1}{72T_u^2}\right) \right\}} \quad (7.2)
 \end{aligned}$$

$$r_{max} = \zeta \omega_n E[\mathcal{T}_{a,b}] \quad (7.3)$$

$$(\gamma_0)_{max} = \frac{V_{crit}}{6\sqrt{2\pi}\sigma_V} \int_0^1 (a_0^*)^m \left\{ e^{-x_1(a_0^*)} + 0.5e^{-x_2(a_0^*)} \right\} da_0^* \quad (7.4)$$

$$x_1(a_0^*) = \frac{\left(\frac{5+a_0^*}{6} V_{crit} - V_{crit}\right)^2}{2\sigma_V^2}$$

$$x_2(a_0^*) = \frac{\left(\frac{6.5-0.5a_0^*}{6} V_{crit} - V_{crit}\right)^2}{2\sigma_V^2}$$

$$(\gamma_1)_{max} = \begin{cases} 1 - \exp(-0.9359r_{max}^{0.2541}) & m = 3.00 \\ 1 - \exp(-0.7093r_{max}^{0.2859}) & m = 3.74 \\ 1 - \exp(-0.5718r_{max}^{0.3085}) & m = 4.38 \end{cases} \quad (7.5)$$

$$\gamma_{max} = (\gamma_0)_{max} \times (\gamma_1)_{max} \quad (7.6)$$

where  $\Phi(x)$  is the CDF of the normal Gaussian distribution, and  $\Phi(x) = \int_{-\infty}^x \frac{1}{\sqrt{2\pi}} \exp(-\frac{1}{2}x^2) dx$ . Values of  $\Phi(x)$  are tabulated in most elementary probability books.  $a_0^*$  is the dummy variable representing the vibration amplitude normalized by  $A_{max}$ .

The integral in Equation 7.4 can only be carried out numerically since  $m$  is usually not an integer.

To calculate  $\gamma_{max}$  requires the values of  $\sigma_V$  and  $\sigma_V$ . In Chapter 6, the values of  $\sigma_V$  and  $\sigma_V$  were derived upon analyzing high sampling rate raw wind data in

a typical maritime environment. Results demonstrate the following characteristics of  $\sigma_V$  and  $\sigma_{\dot{V}}$ .

$\sigma_V$  depends on the mean windspeed, the height above the sea level and the stability of the atmosphere. High windspeed and low elevation generally contribute to a high value of  $\sigma_V$  (or turbulence intensity  $T_u$ ). However, atmospheric instability, which is a function of the vertical temperature gradient, could drastically change the value of turbulence intensity. Stability varies with weather patterns. Unstable conditions increase the turbulence level. It is therefore at the designer's discretion to specify a turbulence intensity level appropriate at a given mean windspeed equal to the critical windspeed of the member, at a given height above the sea level. However, 5% is recommended as a conservative low estimate of the turbulence intensity level. Low turbulence results in greater damage rates.

Unlike  $\sigma_V$ ,  $\sigma_{\dot{V}}$  is found highly correlated with  $\bar{V}$ . Equation 6.24 showed an empirical relationship between  $\sigma_{\dot{V}}$  and  $\bar{V}$  at different elevations. This relationship was derived directly from high sampling rate raw wind data in a typical maritime environment. It is valid when the mean windspeed is between 10 [m·s<sup>-1</sup>] and 30 [m·s<sup>-1</sup>], and when the elevation is between 5 [m] and 46 [m] above the sea level. Reiterating Equation 6.24:

$$\sigma_{\dot{V}} = \begin{cases} 0.0649\bar{V} - 0.2648 & z = 5 \text{ [m]} \\ 0.0608\bar{V} - 0.3725 & z = 10 \text{ [m]} \\ 0.0347\bar{V} - 0.2206 & z = 46 \text{ [m]} \end{cases}$$

Readers should be aware of the limitations of the above prediction model for  $\sigma_{\dot{V}}$ . It may not be applicable to a land-based wind environment, and may not be appropriate to use when the windspeed or the elevation are outside of the ranges specified above. However, 0.20 [m·s<sup>-2</sup>] is recommended as a conservative estimate of  $\sigma_{\dot{V}}$ . Damage rate increases as  $\sigma_{\dot{V}}$  decreases.

The calculation of  $\gamma_{max}$  can also be implemented graphically through three figures. Figure 7-2 shows the value of  $(\gamma_0)_{max}$  as a function of turbulence intensities at three different values of the slope of  $S - N$  curves. This value of  $(\gamma_0)_{max}$  is calculated using Equation 7.4. Since in real wind environments, turbulence intensity is almost always greater than 5%, the value of  $(\gamma_0)_{max}$  is almost always less than 0.4, resulting in a factor of 2.5 increase in real fatigue life.

To calculate  $(\gamma_1)_{max}$  requires the value of  $E[\mathcal{T}_{[a,b]}]$  evaluated at  $\bar{V}$  equal to  $V_{crit}$ , the expected duration of a visit by the windspeed into the critical velocity interval of the structural member. Figure 7-3 shows a contour plot of the expected

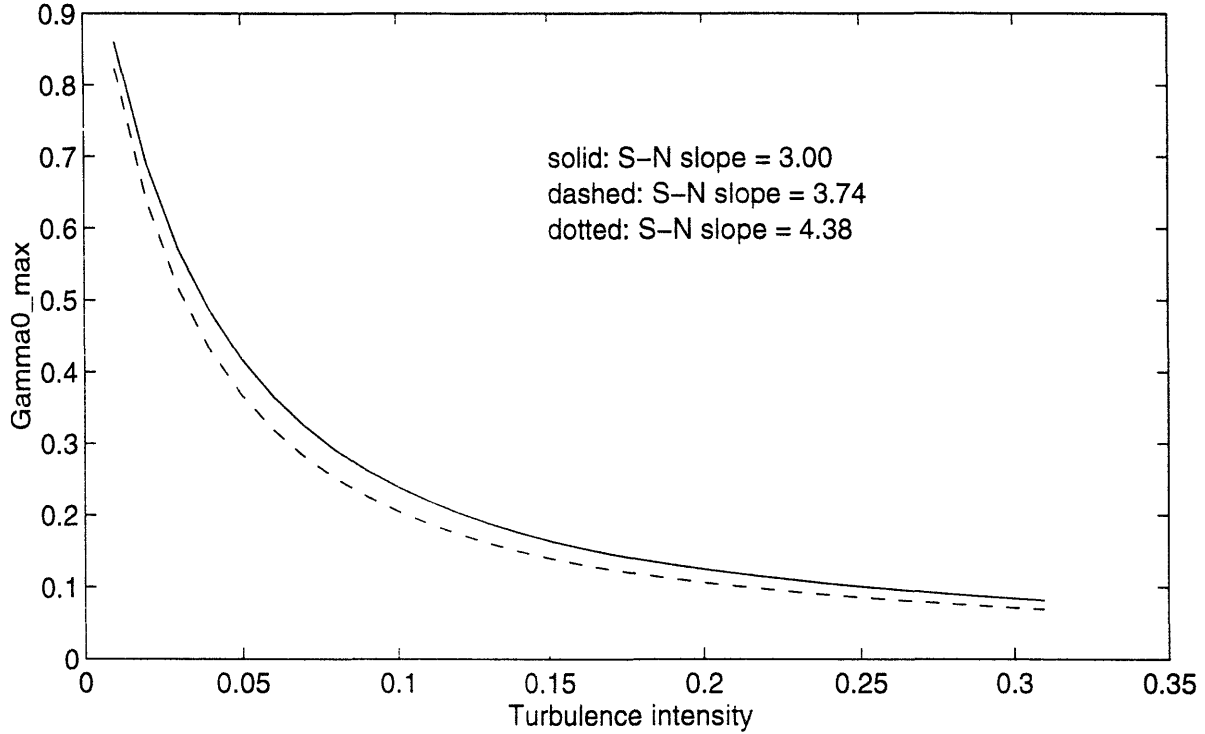


Figure 7-2: Variation of  $(\gamma_0)_{max}$  with turbulence intensities at three different values of the slope of  $S - N$  curves

duration (expressed in seconds) as a function of the critical windspeed and the turbulence intensity level. This plot of the expected duration, as denoted by  $\mathcal{T}$  [s], is calculated using Equation 7.2 but with the value of  $\sigma_{\dot{V}}$  fixed at  $1.0 \text{ [m}\cdot\text{s}^{-2}]$ . Since the expected duration of visit is inversely proportional to  $\sigma_{\dot{V}}$ , the value of  $E[\mathcal{T}_{[a,b]}]$  [s] at other values of  $\sigma_{\dot{V}}$  can be obtained by dividing  $\mathcal{T}$  by  $\sigma_{\dot{V}}$  as follows:

$$E[\mathcal{T}_{[a,b]}] = \frac{\mathcal{T}}{\sigma_{\dot{V}}} \quad (7.7)$$

where  $\sigma_{\dot{V}}$  should be expressed in metric units  $[\text{m}\cdot\text{s}^{-2}]$ . The value of  $\sigma_{\dot{V}}$  can be obtained either from a prediction model such as Equation 6.24, or from meteorological sources. Note that  $\mathcal{T}$  shown in Figure 7-3 is not a conservative estimate of the actual expected duration of visit.  $E[\mathcal{T}_{[a,b]}]$  can be as high as 5 times the value of  $\mathcal{T}$ , when  $0.20 \text{ [m}\cdot\text{s}^{-2}]$  is used as a conservative estimate of  $\sigma_{\dot{V}}$ .

Once  $E[\mathcal{T}_{[a,b]}]$  is derived from Figure 7-3 and Equation 7.7,  $(\gamma_1)_{max}$  can be calculated using Equations 7.3 and 7.5, or Figure 7-4.  $\gamma_{max}$  can be calculated using Equation 7.6; that is taking the product of  $(\gamma_0)_{max}$  and  $(\gamma_1)_{max}$ .

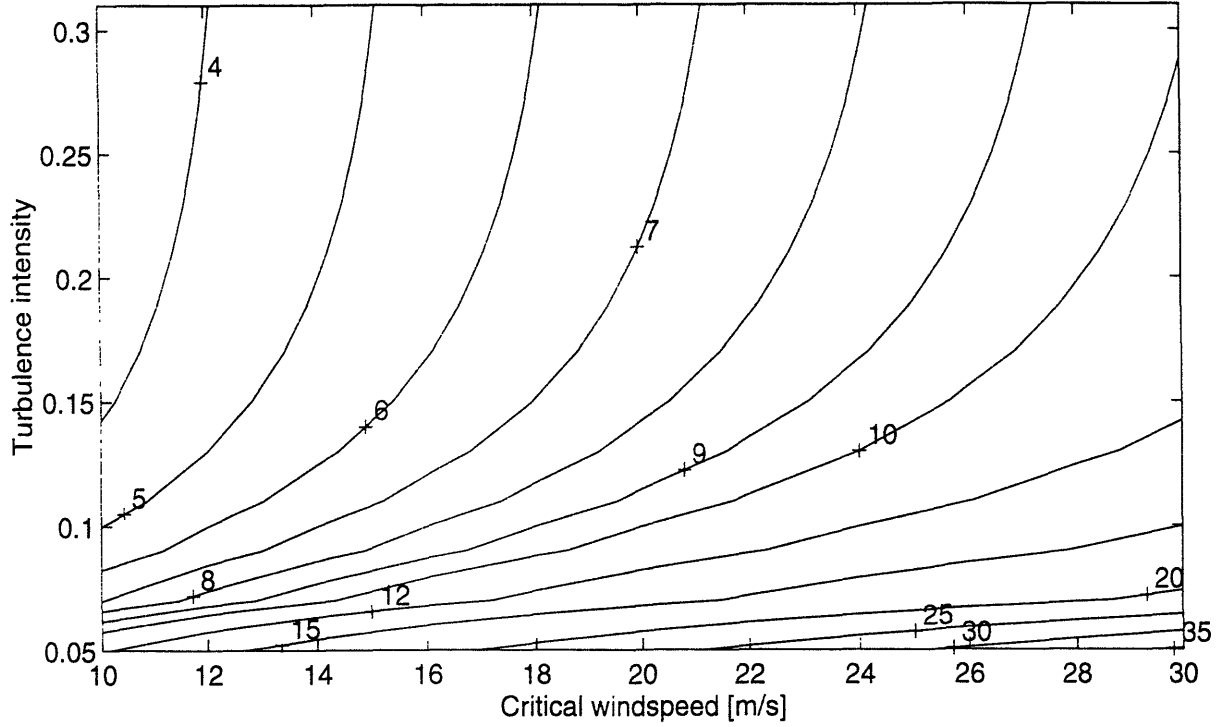


Figure 7-3: Variation of  $\mathcal{T}$  [s] with  $V_{crit}$  and turbulence intensity at  $\sigma_V = 1.0$  [ $\text{m}\cdot\text{s}^{-1}$ ]

- **Step 3: Predict  $\gamma_{bin}$ .**  $\gamma_{bin}$  is a factor which corrects the expected value of the fatigue damage rate  $E[\mathcal{D}]$  for errors introduced by discretizing the PDF of the mean wind velocity into finite width velocity bins.  $\gamma_{bin}$  is given below for various values of  $m$ , as a function of turbulence level.

$$\gamma_{bin} = \begin{cases} \left(\frac{\Delta\bar{V}}{V_{crit}}\right)^{-1}(T_u^2 + 1.73T_u + 0.06) & m = 3.00 \\ \left(\frac{\Delta\bar{V}}{V_{crit}}\right)^{-1}(T_u^2 + 1.98T_u + 0.04) & m = 3.74 \\ \left(\frac{\Delta\bar{V}}{V_{crit}}\right)^{-1}(3T_u^2 + 1.84T_u + 0.04) & m = 4.38 \end{cases}$$

where  $\Delta\bar{V}$  [ $\text{m}\cdot\text{s}^{-1}$ ] is the velocity bin size of the scatter diagram.  $T_u$  is the turbulence intensity level. The above empirical formula can also be shown in the forms of contour plots by Figures 7-5, 7-6 and 7-7. Each of these figures corresponds to a different  $S - N$  curve.

- **Step 4: Predict  $E[\mathcal{D}]$ .**  $E[\mathcal{D}]$ , the fatigue damage rate of a structural member exposed in natural winds, is predicted as follows.

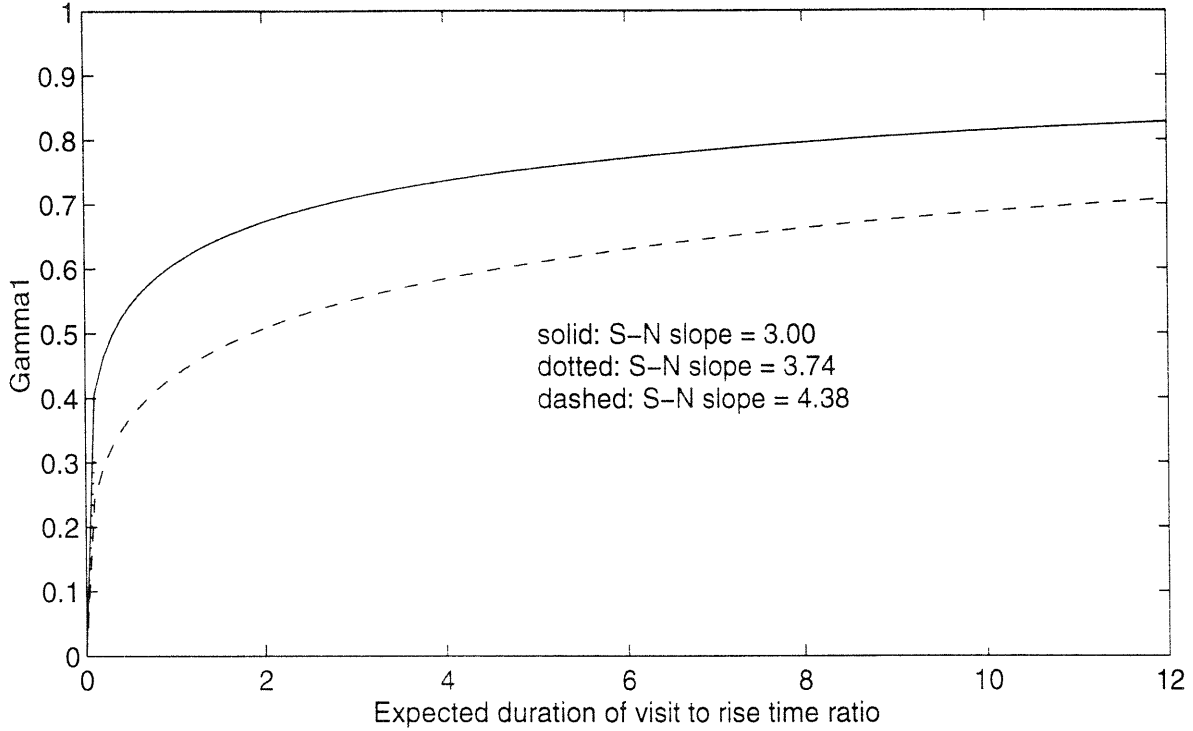


Figure 7-4: Variation of  $(\gamma_1)_{max}$  with  $r_{max}$  for three different  $S - N$  curves

$$E[\mathcal{D}] = \mathcal{D}_{s.s.} \times \gamma_{max} \times \gamma_{bin} \times P_k$$

where  $P_k$  is the probability of occurrence of the velocity bin which brackets the critical velocity of the member.

## 7.2 Examples

### 7.2.1 A worked example to illustrate the design procedure

The design procedure described above is illustrated in the following example.

A typical offshore structural member is selected from Grundmeier et al [16]. The structural parameters of the member are summarized as follows:

- Diameter ( $D$ ) = 0.6096 [m] or 24 [in]



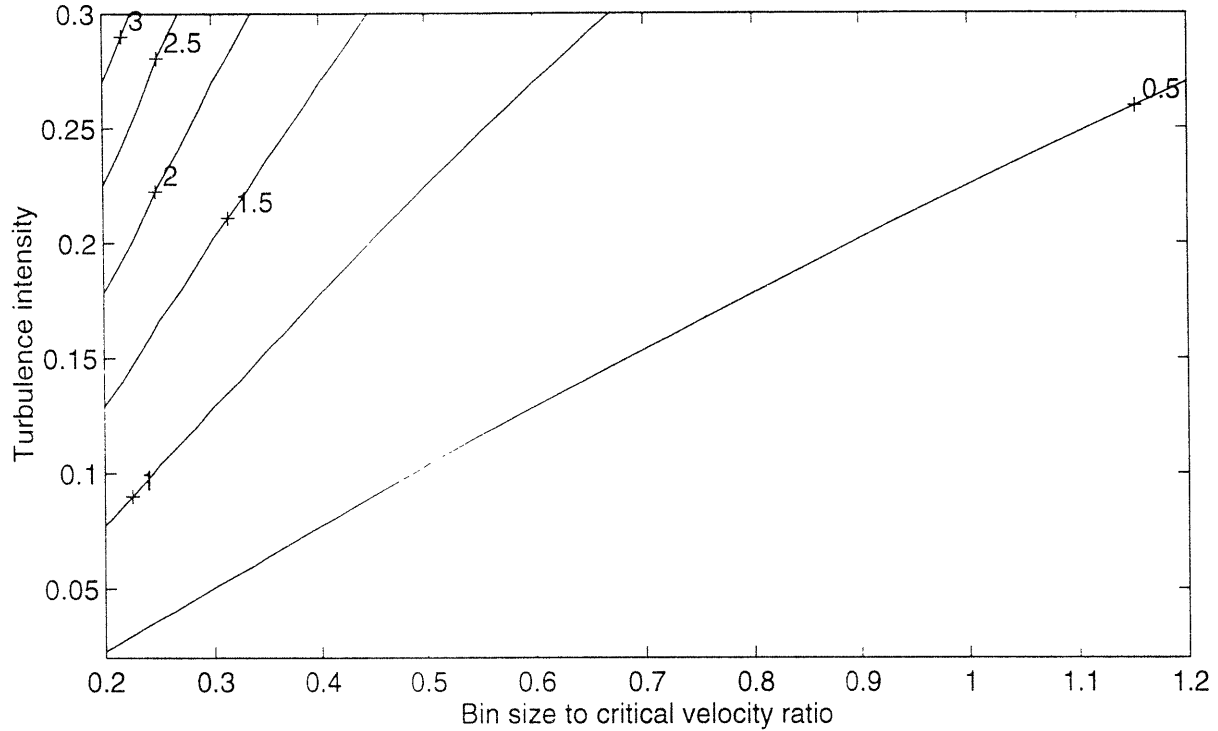


Figure 7-5: Contour plot of  $\gamma_{bin}$  as functions of velocity bin size and turbulence intensity, slope of  $S - N$  curve ( $m$ ) = 3.00

- Length ( $L$ ) = 24.38 [m] or 80 [ft]
- Thickness ( $t$ ) = 0.0127 [m] or 0.5 [in]
- Fundamental natural frequency ( $f_n$ ) = 5.37 [s<sup>-1</sup>]
- Critical velocity ( $V_{crit}$ ) = 19.62 [m·s<sup>-1</sup>]
- Structural damping ratio ( $\zeta$ ) = 0.002<sup>1</sup>
- Height above sea level ( $z$ ) = 46 [m]

An  $S - N$  curve typical for class T welded nodal joints [38] is selected. This  $S - N$  curve has the following characteristics:

<sup>1</sup>This is the value the author recommends for welded steel members. Also see [30].

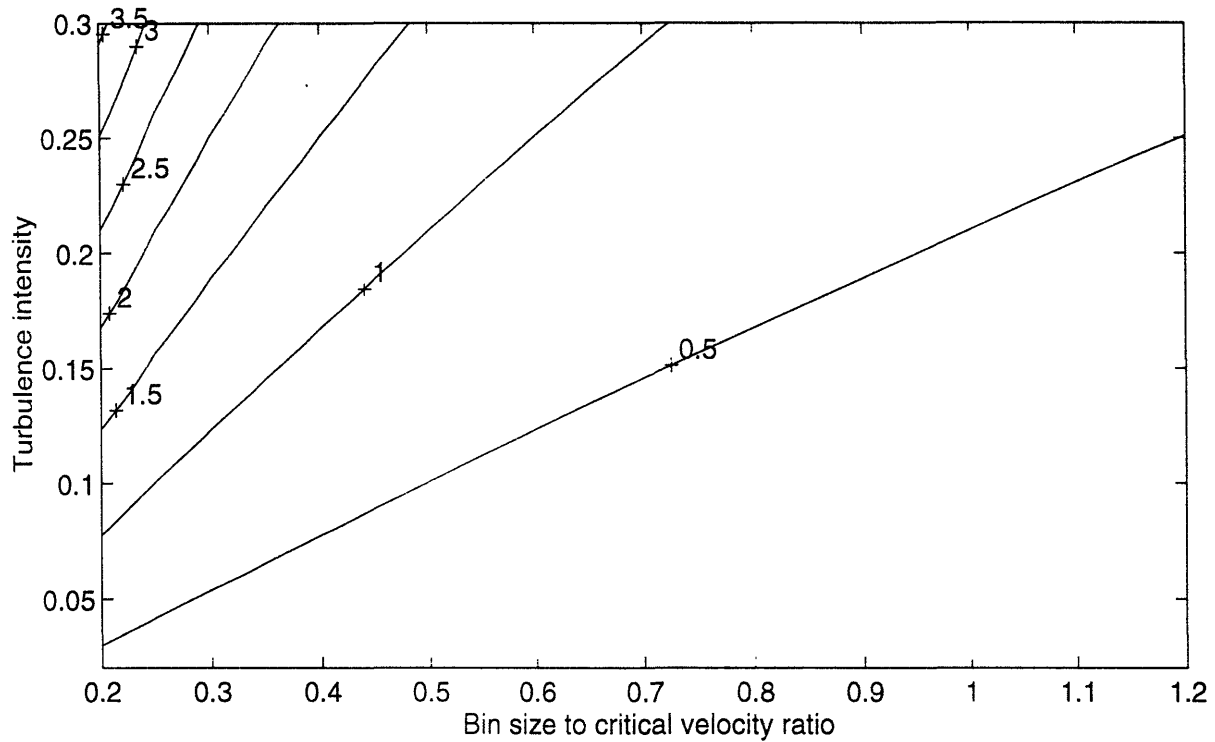


Figure 7-6: Contour plot of  $r_{bin}$  as functions of velocity bin size and turbulence intensity. slope of  $S - N$  curve ( $m$ ) = 3.74

$$NS^3 = N_0 S_0^3 = c \quad (7.8)$$

where  $S_0 = 90 \times 10^6$  [Pa] or  $[\text{kg} \cdot \text{m}^{-1} \cdot \text{s}^{-2}]$  is the reference stress range.  $N_0 = 2 \times 10^6$  is the number of cycles to fatigue failure at the reference stress range. This  $S - N$  curve will be assumed throughout the rest of this chapter.

To carry out the design calculation for this particular member, the wind statistics such as  $\sigma_V$ ,  $\sigma_{\dot{V}}$  and a scatter diagram which describes the long-term probability distribution of hourly mean windspeeds are desired. At the mean windspeed equal to  $V_{crit}$ , the turbulence intensity ( $T_u$ ) level is assumed to be 10%, a value typical for maritime wind environments. Therefore

$$\begin{aligned} \sigma_V &= V_{crit} \times T_u \\ &= 19.62 \times 0.1 \\ &= 1.96 [\text{m} \cdot \text{s}^{-1}] \end{aligned}$$

$\sigma_{\dot{V}}$  is assumed to depend on the mean windspeed by virtue of the empirical relationship that was derived directly from high sampling rate raw wind data. Applying

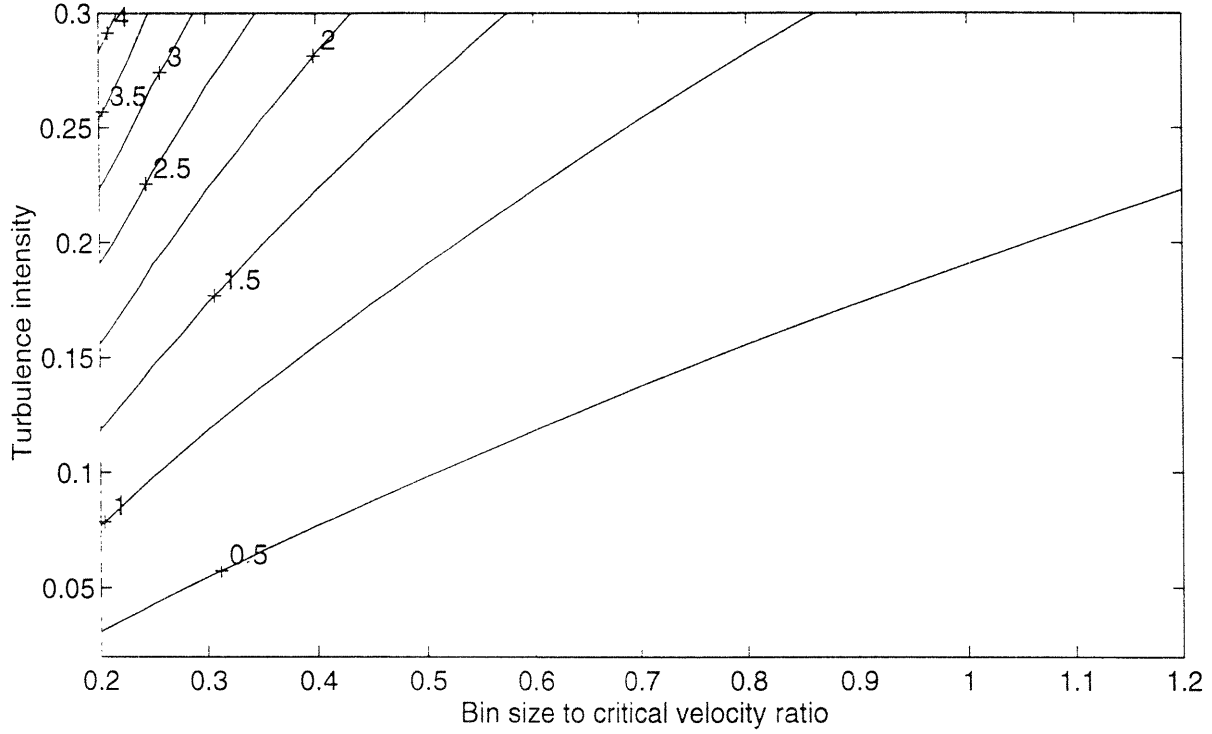


Figure 7-7: Contour plot of  $\gamma_{bm}$  as functions of velocity bin size and turbulence intensity, slope of  $S - N$  curve ( $m$ ) = 4.38

Equation 6.24.

$$\begin{aligned}
 \sigma_V &= 0.0347V_{crit} - 0.2206 \\
 &= 0.0347 \times 19.62 - 0.2206 \\
 &= 0.46 \text{ [m}\cdot\text{s}^{-2}]
 \end{aligned}$$

For the purpose of example only, the long-term hourly mean windspeed is assumed to be a stationary random process which can be described by the Rayleigh distribution with the following CDF and PDF:

$$\begin{aligned}
 F_Y(y) &= 1 - \exp\left(-\frac{\pi y^2}{4E^2[y]}\right) \\
 p_Y(y) &= \frac{dF_Y(y)}{dy} = \exp\left(-\frac{\pi y^2}{4E^2[y]}\right) \times \frac{\pi y}{2E^2[y]}
 \end{aligned}$$

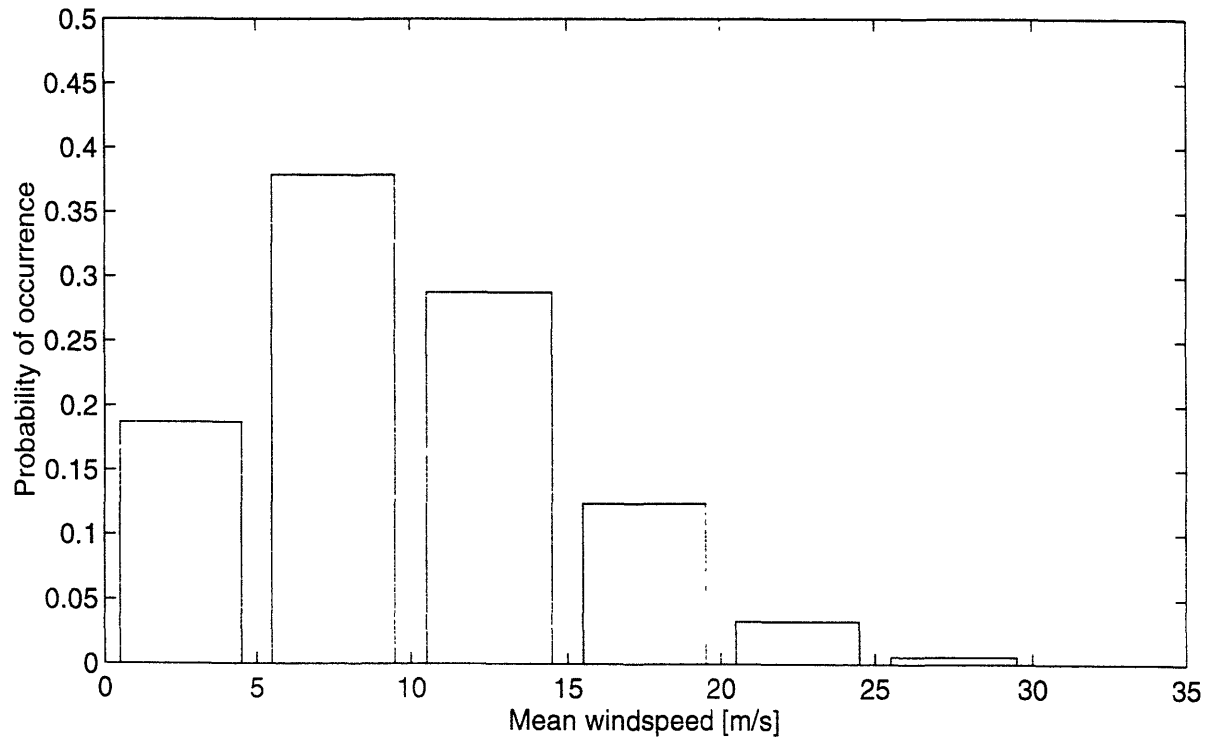


Figure 7-8: Scatter diagram of the long-term hourly mean windspeed

where  $F_Y(y)$  and  $p_Y(y)$  are, respectively, the CDF and the PDF of the Rayleigh distribution.  $E[y]$  is the ensemble average of the hourly mean windspeed. In this example,  $E[y]$  is fixed at 10 [m·s<sup>-1</sup>]. The scatter diagram of the hourly mean windspeed shows the probability distribution of the hourly mean windspeed discretized by a finite number of mean velocity bins. Figure 7-8 shows the scatter diagram of the hourly mean windspeed when the hourly mean windspeed is a Rayleigh-distributed random process with an overall mean of 10 [m·s<sup>-1</sup>]. In this figure, the size of each velocity bin is 5 [m·s<sup>-1</sup>], and the sum of probabilities over the entire group of velocity bins is equal to unity. This scatter diagram of the hourly mean windspeed will be assumed throughout the rest of this chapter. For this example  $V_{crit} = 19.62$  [m·s<sup>-1</sup>] which falls into the bin between 15 and 20 [m·s<sup>-1</sup>].  $P_k$  the probability of this bin is 0.13.

Based on the information provided above, the design calculation can be carried out step by step in Table 7.2, presented at the end of this chapter.

Table 7.2 shows that for this particular example, when the instantaneous fluctuations of the windspeed and the effect of finite bin size of mean windspeeds are considered, the estimated increase in fatigue life of a typical structural member could be more than 6 ( $= \frac{D_{s.s} \times P_k}{E[D]}$ ) as compared to that due to steady-state vibrations at the critical velocity.

## 7.2.2 The effect of different values of turbulence intensity

As mentioned in Chapter 6, the turbulence intensity level above the surface could vary significantly (from 5% to over 30% based on raw wind data, see Figure 6-1) with different degrees of atmospheric instability. Also, it is not uncommon that some structural members are exposed to high turbulent flows when placed in the wake of other structural members. Therefore, it is of practical interest to study how turbulence level affects the value of the fatigue damage discount factor.

In this section, the design calculation will be carried out for a typical structural member at various turbulence levels. The resultant combined fatigue damage discount factors are compared

A typical offshore structural member is selected from Grundmeier et al [16] with the following key structural parameters:

- Diameter ( $D$ ) = 0.6096 [m] or 24 [in]
- Length ( $L$ ) = 30.48 [m] or 100 [ft]
- Thickness ( $t$ ) = 0.0127 [m] or 0.5 [in]
- Fundamental natural frequency ( $f_n$ ) = 3.43 [s<sup>-1</sup>]
- Critical velocity ( $V_{crit}$ ) = 12.56 [m·s<sup>-1</sup>]
- Structural damping ratio ( $\zeta$ ) = 0.002
- Height above sea level ( $z$ ) = 46 [m]

Four different values of turbulence intensity, namely 5%, 10%, 20% and 30%, are selected. However, the values of  $\sigma_V$  are assumed to only depend on the mean wind-speed by virtue of Equation 6.24. At each of the four turbulence intensities, the design calculation is carried out in a similar step by step fashion illustrated in Table 7.2, and the key results are summarized in Table 7.3.

The results in Table 7.3 show that although high turbulence significantly reduces the fatigue damage rate when the mean windspeed equals the critical velocity of the member, the difference tends to diminish when the mean windspeed is considered as a random process described by a scatter diagram. This is because high turbulence actually increases the chance for the instantaneous windspeed to cross into the critical velocity interval when the mean windspeed is close but outside of the interval. This effect is accounted for by  $\gamma_{bin}$ .  $\gamma_{bin}$  increases with turbulence level. All factors considered, an increase in turbulence level is accompanied by a slight decrease in damage rate.

### 7.2.3 The effect of different values of $\sigma_V$

In Chapter 6, the statistical properties of natural winds in a typical maritime environment were studied. The value of  $\sigma_V$  was observed to be highly correlated with the mean windspeed. Furthermore, an empirical formula (Equation 6.24) was proposed to estimate the value of  $\sigma_V$  from the mean windspeed at different elevations. However, it is unknown if that relationship is also applicable to land-based or other wind environments. Therefore, it is of practical interest to investigate how the result of the proposed design calculation would vary as the value of  $\sigma_V$  changes.

In this section, a typical structural member is selected from Grandmeir et al [16], and the proposed design calculation is carried out at three different values of  $\sigma_V$ . The selected structural member has the following key structural parameters:

- Diameter ( $D$ ) = 0.6096 [m] or 24 [in]
- Length ( $L$ ) = 24.38 [m] or 80 [ft]
- Thickness ( $t$ ) = 0.0127 [m] or 0.5 [in]
- Fundamental natural frequency ( $f_n$ ) = 5.37 [s<sup>-1</sup>]
- Critical velocity ( $V_{crit}$ ) = 19.62 [m·s<sup>-1</sup>]
- Structural damping ratio ( $\zeta$ ) = 0.002
- Height above sea level ( $z$ ) = 46 [m]

Three cases are considered, each with a different value of  $\sigma_V$ . These three different values of  $\sigma_V$  are 0.20 [m·s<sup>-2</sup>], 0.46 [m·s<sup>-2</sup>] and 1.0 [m·s<sup>-2</sup>]. 0.46 [m·s<sup>-2</sup>] is a value of  $\sigma_V$  implied by the empirical formula shown by Equation 6.24 at the mean windspeed equal to the critical velocity, while 0.20 [m·s<sup>-2</sup>] and 1.0 [m·s<sup>-2</sup>] are respectively, the lower (conservative) and higher estimates of  $\sigma_V$ . For all three cases, the turbulence intensity level is fixed at 10%, a typical value observed in maritime wind environments.

For each of the three cases with different values of  $\sigma_V$ , the proposed design calculation is carried out in a step by step fashion identical to the worked example illustrated in Table 7.2. Table 7.4 summarizes the key results.

Table 7.4 confirms that the value of  $\sigma_V$  only affects the value of  $\gamma_{max}$  through the expected duration of a visit. A small value of  $\sigma_V$  leads to a long duration of a visit, which consequently leads to a large value of  $\gamma_{max}$ , or a small increase in fatigue life. However, the dependence of  $\gamma_{max}$  on  $\sigma_V$  is not very sensitive, as shown in Table 7.4. A 50% increase in the value of  $\sigma_V$  only results in a 10% reduction in  $\gamma_{max}$ . Therefore by choosing a conservative value of  $\sigma_V = 0.2$  the predictions of fatigue damage rate in other wind environments may be reasonably good.

#### 7.2.4 The effect of different values of $V_{crit}$

At a given wind site where the scatter diagram of mean windspeeds is known, one may identify a number of structural members susceptible to fatigue failure caused by VIV. Since structural members generally have different values of critical velocities, the probability of occurrence of the critical velocity bin (or the mean velocity bin which brackets the critical velocity) will vary. It is anticipated that the member associated with the highest probability of occurrence of the critical velocity bin may suffer substantial fatigue damage due to significant exposure to the critical velocity. The probability of occurrence of the critical velocity bin,  $P_k$ , accounts for the extent of exposure.

For any given member  $P_k$  must take into consideration not only the occurrence of the mean windspeed, but also the direction of the wind. Wind direction has not been explicitly discussed in this thesis due to limitations of time. However, it is straight forward to estimate the  $P_k$  of a critical velocity bin including the effects of wind direction if such direction information is available. One would sum up the probabilities of occurrence of mean windspeed bins so as to include all mean wind velocity and direction combinations which resulted in a vector component of the wind normal to the member which was at the critical windspeed. Such refinements are left to future work.

## 7.3 Summary

A design methodology for fatigue resistant structural members excited by natural winds is proposed based on probabilistic models. The design procedure consists of four steps. Step one predicts the fatigue damage rate of a structural member due to steady state vibrations at the critical velocity. Step two predicts the fatigue damage discount factors caused by the natural fluctuations of the windspeed and the finite rise time based on the input of relevant wind statistics. Step three predicts a factor which corrects the expected value of the fatigue damage rate for errors introduced by discretizing the PDF of the mean wind velocity into finite width velocity bins. Step four predicts the fatigue damage rate of a structural member caused by natural winds as the product of the factors from the previous three steps.

The design procedure has been illustrated by step by step examples using typical offshore structural members and realistic values of relevant wind statistics. Effects of different values of wind statistics on the results of design calculations have been presented by numerical examples.



Step Number	Symbol	Variable	Value	Units
0	$D$	member diameter	0.6096	[m]
	$L$	member length	24.38	[m]
	$f_n$	member natural frequency	5.37	[s <sup>-1</sup> ]
	$V_{crit}$	member critical velocity	19.62	[m·s <sup>-1</sup> ]
	$\zeta$	member structural damping	0.002	
1	$\gamma_1$	mode shape	1.163	
	$Re$	Reynolds number	$8.25 \times 10^6$	
	$C_L$	r.m.s. lift coefficient	0.3	
	$S_r$	Strouhal number	0.2	
	$K_s$	reduced damping	10.5	
	$\frac{A_{max}}{D}$	maximum amplitude to diameter ratio	0.05	
	$E$	Young's modulus	$209 \times 10^9$	[Pa]
	$F_r$	strain response parameter	22.4	
	SCF	stress concentration factor	3.0	
	$S_0$	reference stress range	$90 \times 10^6$	[Pa]
	$N_0$	number of stress cycles to failure	$2 \times 10^6$	
	$m$	slope of $S - N$ curve	3.0	
	$\mathcal{D}_{s,s}$	maximum fatigue damage rate	$3.1 \times 10^{-4}$	[s <sup>-1</sup> ]
2	$T_u$	Turbulence intensity	0.1	
	$(\gamma_0)_{max}$	fatigue discount factor 1	0.24	
	$\mathcal{T}$	duration of visit	10	[s]
	$\sigma_V$	s.t.d. of acceleration	0.46	[m·s <sup>-2</sup> ]
	$E[\mathcal{T}_{a,b}]$	expected duration of visit	21.73	[s]
	$t_r$	rise time	14.82	[s]
	$r_{max}$	duration to rise time ratio	1.47	
	$(\gamma_1)_{max}$	fatigue discount factor 2	0.64	
	$\gamma_{max}$	fatigue discount factor 1 & 2	0.15	
3	$\Delta V$	velocity bin size	5	[m·s <sup>-1</sup> ]
	$\gamma_{bin}$	bin size correction factor	0.95	
4	$P_k$	probability of occurrence	0.13	
	$\frac{E \mathcal{D}^1}{\mathcal{D}_{s,s} \times P_k}$	combined fatigue discount factor	0.14	
	$\frac{\mathcal{D}_{s,s} \times P_k}{E \mathcal{D}^1}$	increase in fatigue life	6.9	
	$E \mathcal{D}^1$	fatigue damage rate	$9.8 \times 10^{-9}$	[s <sup>-1</sup> ]

Table 7.2: Step by step implementation of the design procedure

$T_u$	5%	10%	20%	30%
$\sigma_V$ [ $\text{m}\cdot\text{s}^{-1}$ ]	0.63	1.26	2.51	3.77
$\sigma_V$ [ $\text{m}\cdot\text{s}^{-2}$ ]	0.215	0.215	0.215	0.215
$(\gamma_0)_{max}$	0.4	0.24	0.13	0.08
$(\gamma_1)_{max}$	0.71	0.63	0.60	0.59
$\gamma_{max}$	0.28	0.15	0.08	0.05
$\gamma_{bin}$	0.37	0.61	1.12	1.68
$P_k$	0.29	0.29	0.29	0.29
$\frac{E\mathcal{D}}{\mathcal{D}_{s.s.} \times P_k}$	0.10	0.09	0.09	0.08

Table 7.3: Variation of fatigue damage discount factor with turbulence intensity

$T_u$	10%	10%	10%
$\sigma_V$ [ $\text{m}\cdot\text{s}^{-2}$ ]	0.20	0.46	1.0
$(\gamma_0)_{max}$	0.24	0.24	0.24
$(\gamma_1)_{max}$	0.72	0.64	0.57
$\gamma_{max}$	0.17	0.15	0.14
$\gamma_{bin}$	0.95	0.95	0.95
$P_k$	0.13	0.13	0.13
$\frac{E\mathcal{D}}{\mathcal{D}_{s.s.} \times P_k}$	0.16	0.14	0.13

Table 7.4: Variation of fatigue damage discount factor with  $\sigma_V$

# Chapter 8

## Conclusions and Recommendations

### 8.1 Conclusions

The following key conclusions can be drawn based on the work of this thesis.

- Free-stream turbulence up to 10% does not drastically disrupt the vortex shedding or reduce the magnitude of vibrations on a flexible cylinder. However, low-frequency variation in windspeed typically prevents VIV response from reaching steady state, thus increasing the fatigue life of the structural member exposed in natural winds.
- A time domain model for predicting VIV of structural members in unsteady winds has been proposed. The transient vibrations are predicted as the result of time domain convolution between the excitation force which is derived from the time trace of the windspeed and the impulse response function of the single degree of freedom oscillator which has the resonant properties of the target structural member. The predicted transient vibrations by the time domain model have shown remarkable accuracy as compared to the wind tunnel measurements.
- A probabilistic model has been proposed for predicting fatigue damage of a flexible cylinder excited by natural winds directly from the relevant wind statistics. These wind statistics include the mean windspeed, the turbulence intensity level, the standard deviation of the wind acceleration, and the scatter diagram of the mean windspeed. After analyzing the wind statistics and structural parameters, this model identifies three fatigue damage discount factors to account for the fluctuations of the natural winds, the expected duration of a visit by the windspeed to the critical velocity interval of the structural member and the finite structural response rise time, and the error caused by discretizing

the PDF of the mean windspeed into finite velocity bins. The probabilistic model is verified against the time domain model using high sampling rate real windspeed data. The results from the probabilistic model are consistently more conservative than those from the time domain model, but still show a factor of 10 increase in fatigue life as compared to conventional estimates based on steady state vibrations when the mean windspeed equals the critical velocity of a structural member.

- Required wind statistics which determine the duration of a visit by the windspeed to the critical velocity interval have been extracted from high sampling rate raw windspeed data which were measured in a typical maritime environment. The observed turbulence intensity ( $T_u$ ) depends on the mean windspeed, the elevation and the stability of the atmosphere. Difference in temperature gradients causes poor correlation between the turbulence and the mean windspeed. The observed values of the standard deviation of the wind acceleration ( $\sigma_{\dot{V}}$ ) show high correlation with the mean windspeed. It increases with the mean windspeed at a given elevation, and decreases as elevation increases.
- A design methodology for fatigue resistant structural members excited by natural winds has been proposed. This design methodology is based on the probabilistic model and the wind statistics derived from high sampling rate maritime wind data. It can be implemented conveniently through series of figures.

## 8.2 Recommendations

The proposed design methodology for fatigue resistant structural members excited by natural winds relates certain wind statistics to the structural fatigue damage rate. Since there was no relevant literature providing data on  $\sigma_{\dot{V}}$ , estimates were made based on high sampling rate raw windspeed data measured at one maritime site. Statistics such as  $\sigma_V$ ,  $\sigma_{\dot{V}}$ , mean windspeed and direction need to be acquired for a variety of environments.

### 8.2.1 Wind directionality

In evaluating the wind statistics for input to the probabilistic model, the direction of the wind has been always assumed to be normal to any structural member, so that only the magnitude of the windspeed was considered. This assumption greatly simplified the description of the wind statistics. Instead of decomposing the windspeed into different normal directions which depended on the orientation of each member, only the statistics of the windspeed magnitude were studied. However, this simplified description of wind statistics was achieved at a certain price. Since the information

of the wind directionality was ignored, its effect on fatigue damage rate remains to be determined.

### 8.2.2 Dependence of $\sigma_{\bar{V}}$ on $\bar{V}$

$\sigma_{\bar{V}}$  is an important parameter which determines the upcrossing statistics of the wind-speed, which in turn determine the expected duration of a visit by the windspeed to the critical velocity interval of any structural member. Based on the raw windspeed data measured at one maritime site,  $\sigma_{\bar{V}}$  was found to be highly correlated with the mean windspeed. Furthermore, the relationship between  $\sigma_{\bar{V}}$  and the mean windspeed  $\bar{V}$  can be described by the following empirical formula:

$$\sigma_{\bar{V}} = \begin{cases} 0.0649\bar{V} - 0.2648 & z = 5 \text{ [m]} \\ 0.0608\bar{V} - 0.3725 & z = 10 \text{ [m]} \\ 0.0347\bar{V} - 0.2206 & z = 46 \text{ [m]} \end{cases}$$

Readers should be aware that the above formula is based on the maritime wind data with the mean windspeeds between 10 [m·s<sup>-1</sup>] and 30 [m·s<sup>-1</sup>] and the elevations between 5 [m] to 46 [m]. It may not be applicable to land-based wind environments, and may not be appropriate to use when the windspeed or the elevation is outside of the ranges specified above. In order to obtain a reliable estimate of real fatigue damage of structural members in a wind environment where the assumptions underlying the above empirical formula for  $\sigma_{\bar{V}}$  are violated, high sampling rate raw windspeed data should be measured in that particular wind environment. Statistics of  $\sigma_{\bar{V}}$  with wind conditions different from the maritime environment should be compiled.

# Appendix A

## State Equations and Input-Output Models for a Linear System

In this Chapter, state equations will be introduced to describe a generic linear system which is governed by linear differential equations. Analytical solutions to state equations are derived and implemented by an equivalent linear difference equation. The whole solution procedure will be illustrated through an example.

### A.1 State equations and analytical solutions

Consider a generic continuous-time system shown in Figure A-1. This system is associated with a set of input variables  $u_1, u_2, \dots, u_r$  and a set of output variables  $y_1, y_2, \dots, y_p$ . For convenience, we let the input variables  $u_1, u_2, \dots, u_r$  be represented by an input vector

$$u = \begin{bmatrix} u_1 & u_2 & \dots & u_r \end{bmatrix}^T \quad (\text{A.1})$$

The output vector  $y$  is likewise defined as an  $p \times 1$  column vector

$$y = \begin{bmatrix} y_1 & y_2 & \dots & y_p \end{bmatrix}^T \quad (\text{A.2})$$

The input and the output vectors are assumed to be functions of time  $t$ . To indicate this explicitly, we write  $u(t)$  and  $y(t)$ , denoting, respectively, the value of  $u$  and  $y$  at time  $t$ .

The system itself is assumed to be linear and time-invariant, and can be described by an  $n$ th-order linear differential equation. A minimum number of  $n$  variables which contain sufficient information about the history of the system are required to allow computation of future behavior. These variables are called state variables, which can be represented by an  $n \times 1$  column vector

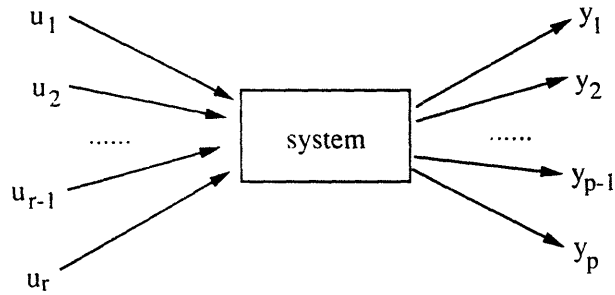


Figure A-1: A generic continuous time system

$$x = [x_1 \ x_2 \ \dots \ x_n]^T \quad (\text{A.3})$$

This vector is defined as state vector [37], and is assumed to be a function of time  $t$ , or explicitly,  $x(t)$ .

Then, instead of linear differential equations, this linear and time-invariant system can also be described by the following state equations

$$\dot{x} = Ax(t) + Bu(t) \quad (\text{A.4})$$

$$y(t) = Cx(t) + Du(t) \quad (\text{A.5})$$

where  $A, B, C, D$  are  $n \times n, n \times r, p \times n, p \times r$  matrices respectively.  $u(t)$  and  $y(t)$  are, once again, the input and the output vectors of the system.

Suppose the continuous-time system is sampled at a sampling period of  $h$ : then the input signal  $u(t)$  can be represented by a discrete sequence  $\{u(t_k) : t_k = k \times h, k = 0, 1, 2, \dots\}$ . From Åström and Wittenmark [3],  $x$  and  $y$  at the sampling instants can be solved analytically by the following set of linear difference equations:

$$x(t_{k+1}) = \Phi(t_{k+1}, t_k)x(t_k) + \Gamma(t_{k+1}, t_k)u(t_k) \quad (\text{A.6})$$

$$y(t_k) = Cx(t_k) + Du(t_k) \quad (\text{A.7})$$

where

$$\Phi(t_{k+1}, t_k) = e^{A(t_{k+1}-t_k)} \quad (\text{A.8})$$

$$\Gamma(t_{k+1}, t_k) = \int_0^{t_{k+1}-t_k} e^{As} ds B \quad (\text{A.9})$$

It is worth noticing that Equations A.6 and A.7 do not involve any approximations. They give the exact values of the state variables and the output variables at the sampling instants [3].

Since  $t_k = k \times h$ , the aforementioned difference equations A.6 and A.7 can be further simplified by replacing the continuous-time series of the input vector, the state vector and the output vector at the sampling instants by their equivalent discrete sequences

$$x[k+1] = \Phi x[k] + \Gamma u[k] \quad (\text{A.10})$$

$$y[k] = Cx[k] + Du[k] \quad (\text{A.11})$$

where

$$\Phi = e^{Ah} \quad (\text{A.12})$$

$$\Gamma = \int_0^h e^{As} ds B \quad (\text{A.13})$$

The derived analytic solutions of state equations require to evaluate matrix exponential and integration of a matrix exponential. One way of evaluating a matrix exponential is to utilize the Laplace transform [3]:

$$\begin{aligned} \mathcal{L}(e^{At}) &= \int_0^\infty e^{-st} e^{At} dt \\ &= (sI - A)^{-1} \end{aligned}$$

and the inverse Laplace transform:



$$\begin{aligned}\mathcal{L}^{-1}((sI - A)^{-1}) &= \frac{1}{2\pi i} \int_{\sigma-i\infty}^{\sigma+i\infty} (sI - A)^{-1} e^{st} ds \\ &= e^{At}\end{aligned}$$

Therefore,  $\Phi$  and  $\Gamma$  can be evaluated as

$$\begin{aligned}\Phi &= e^{Ah} \\ &= \mathcal{L}^{-1}(sI - A)^{-1}|_{t=h}\end{aligned}\tag{A.14}$$

$$\begin{aligned}\Gamma &= \int_0^h e^{Av} dv B \\ &= \int_0^h \mathcal{L}^{-1}((sI - A)^{-1})|_{t=v} dv B\end{aligned}\tag{A.15}$$

## A.2 Input-output relationship for a linear system

The relationship between the input and the output sequences of a sampled linear system can be determined by applying operator calculus on the solutions of state equations. Define  $q$  as the forward-shift operator. From equation A.10, we have

$$\begin{aligned}x[k+1] &= qx[k] \\ &= \Phi x[k] + \Gamma u[k]\end{aligned}\tag{A.16}$$

Hence

$$(qI - \Phi)x[k] = \Gamma u[k]\tag{A.17}$$

or

$$x[k] = (qI - \Phi)^{-1} \Gamma u[k]\tag{A.18}$$

From Equation A.11 and A.18

$$\begin{aligned}y[k] &= Cx[k] + Du[k] \\ &= \{C(qI - \Phi)^{-1} \Gamma + D\}u[k] \\ &= H(q)u[k]\end{aligned}\tag{A.19}$$

where

$$H(q) = C(qI - \Phi)^{-1}\Gamma + D \quad (\text{A.20})$$

Equation A.19 defines the relationship between the output and the input sequences of a linear system through a properly defined transfer function  $H(q)$ . For the given input sequence of a linear system, the output sequence can be determined by Equation A.19. The transfer function involves forward shift operators in both the numerator and the denominator, so Equation A.19 is often a difference equation.

In the following section, an example will be given to illustrate the step by step procedure of how to derive the corresponding difference equation that relates the input and the output of the given continuous-time system. The system that we are going to study is an SDOF oscillator. It is a second order continuous-time system with a single scalar input (excitation force) and a single scalar output (amplitude response).

### A.3 An example

Consider the response of the following SDOF oscillator excited by a general forcing term  $\omega_n^2 u(t)$ :

$$\ddot{y} + 2\zeta\omega_n\dot{y} + \omega_n^2 y(t) = \omega_n^2 u(t) \quad (\text{A.21})$$

Our goal is to derive the equivalent difference equation to solve for the response.

#### Step one: state equations and analytical solutions

The state vector that corresponds to Equation A.21 is

$$x = \begin{bmatrix} y(t) & \dot{y}(t) \end{bmatrix}^T \quad (\text{A.22})$$

The state equations are

$$\begin{aligned} \dot{x} &= \begin{bmatrix} 0 & 1 \\ -\omega_n^2 & -2\zeta\omega_n \end{bmatrix} x + \begin{bmatrix} 0 & \omega_n^2 \end{bmatrix} u \\ y &= \begin{bmatrix} 1 & 0 \end{bmatrix} x \end{aligned}$$

The Laplace transform method gives

$$\begin{aligned}
(sI - A)^{-1} &= \begin{bmatrix} s & -1 \\ \omega_n^2 & s + 2\zeta\omega_n \end{bmatrix}^{-1} \\
&= \frac{1}{s^2 + 2\zeta\omega_n s + \omega_n^2} \begin{bmatrix} s + 2\zeta\omega_n & 1 \\ -\omega_n^2 & s \end{bmatrix} \\
&= \begin{bmatrix} \left( \frac{-s_2}{s_1 - s_2} \right) \frac{1}{s - s_1} - \left( \frac{s_1}{s_1 - s_2} \right) \frac{1}{s - s_2} & \left( \frac{1}{s_1 - s_2} \right) \frac{1}{s - s_1} - \left( \frac{1}{s_1 - s_2} \right) \frac{1}{s - s_2} \\ \left( -\frac{\omega_n^2}{s_1 - s_2} \right) \frac{1}{s - s_1} - \left( \frac{\omega_n^2}{s_1 - s_2} \right) \frac{1}{s - s_2} & \left( \frac{s_1}{s_1 - s_2} \right) \frac{1}{s - s_2} + \left( -\frac{s_2}{s_1 - s_2} \right) \frac{1}{s - s_2} \end{bmatrix}
\end{aligned}$$

where

$$\begin{aligned}
s_1 &= -\zeta\omega_n + i\omega_n\sqrt{1 - \zeta^2} \\
s_2 &= -\zeta\omega_n - i\omega_n\sqrt{1 - \zeta^2}
\end{aligned}$$

Hence from Equations A.14 and A.15

$$\begin{aligned}
\Phi &= e^{Ah} \\
&= \begin{bmatrix} \left( \frac{-s_2}{s_1 - s_2} \right) e^{s_1 h} + \left( \frac{s_1}{s_1 - s_2} \right) e^{s_2 h} & \left( \frac{1}{s_1 - s_2} \right) e^{s_1 h} - \left( \frac{1}{s_1 - s_2} \right) e^{s_2 h} \\ \left( -\frac{\omega_n^2}{s_1 - s_2} \right) e^{s_1 h} + \left( \frac{\omega_n^2}{s_1 - s_2} \right) e^{s_2 h} & \left( \frac{s_1}{s_1 - s_2} \right) e^{s_1 h} + \left( -\frac{s_2}{s_1 - s_2} \right) e^{s_2 h} \end{bmatrix} \quad (\text{A.23})
\end{aligned}$$

$$\begin{aligned}
\Gamma &= \int_0^h e^{At} dt B \\
&= \int_0^h \begin{bmatrix} \left( \frac{\omega_n^2}{s_1 - s_2} \right) e^{s_1 t} + \left( -\frac{\omega_n^2}{s_1 - s_2} \right) e^{s_2 t} \\ \left( \frac{\omega_n^2 s_1}{s_1 - s_2} \right) e^{s_1 t} + \left( -\frac{\omega_n^2 s_2}{s_1 - s_2} \right) e^{s_2 t} \end{bmatrix} dt \\
&= \begin{bmatrix} 1 + \frac{s_2}{s_1 - s_2} e^{s_1 h} - \frac{s_1}{s_1 - s_2} e^{s_2 h} \\ \frac{\omega_n^2}{s_1 - s_2} (e^{s_1 h} - e^{s_2 h}) \end{bmatrix} \quad (\text{A.24})
\end{aligned}$$

## Step two: input-output relationship

From Equation A.23:

$$\begin{aligned}
(qI - \Phi)^{-1} &= \begin{bmatrix} q + \frac{s_2}{s_1 - s_2} e^{s_1 h} - \frac{s_1}{s_1 - s_2} e^{s_2 h} & -\frac{1}{s_1 - s_2} e^{s_1 h} + \frac{1}{s_1 - s_2} e^{s_2 h} \\ \frac{\omega_n^2}{s_1 - s_2} e^{s_1 h} - \frac{\omega_n^2}{s_1 - s_2} e^{s_2 h} & q - \frac{s_1}{s_1 - s_2} e^{s_1 h} + \frac{s_2}{s_1 - s_2} e^{s_2 h} \end{bmatrix}^{-1} \\
&= \frac{1}{q^2 + a_1 q + a_2} \begin{bmatrix} q - \frac{s_1}{s_1 - s_2} e^{s_1 h} + \frac{s_2}{s_1 - s_2} e^{s_2 h} & \frac{1}{s_1 - s_2} e^{s_1 h} - \frac{1}{s_1 - s_2} e^{s_2 h} \\ -\frac{\omega_n^2}{s_1 - s_2} e^{s_1 h} + \frac{\omega_n^2}{s_1 - s_2} e^{s_2 h} & q + \frac{s_2}{s_1 - s_2} e^{s_1 h} - \frac{s_1}{s_1 - s_2} e^{s_2 h} \end{bmatrix} \quad (\text{A.25})
\end{aligned}$$

where

$$\begin{aligned}
a_1 &= -e^{s_1 h} - e^{s_2 h} \\
&= -2e^{-\zeta\omega_n h} \cos(\omega_d h)
\end{aligned} \tag{A.26}$$

$$\begin{aligned}
a_2 &= -\frac{s_1 s_2}{(s_1 - s_2)^2} e^{2s_1 h} - \frac{s_1 s_2}{(s_1 - s_2)^2} e^{2s_2 h} + \frac{s_1^2 + s_2^2}{(s_1 - s_2)^2} e^{(s_1 + s_2)h} \\
&= e^{-2\zeta\omega_n h} + \mathcal{O}(h^2)
\end{aligned} \tag{A.27}$$

$$\omega_d = \omega_n \sqrt{1 - \zeta^2}$$

Plugging Equations A.25 and A.26 into Equation A.20, we obtain the expression of the transfer function  $H(q)$  which relates the input and the output sequences as follows:

$$\begin{aligned}
H(q) &= C(qI - \Phi)^{-1} \Gamma \\
&= \begin{bmatrix} 1 & 0 \end{bmatrix} \frac{1}{q^2 + a_1 q + a_2} \begin{bmatrix} q - \frac{s_1}{s_1 - s_2} e^{s_1 h} + \frac{s_2}{s_1 - s_2} e^{s_2 h} & \frac{1}{s_1 - s_2} e^{s_1 h} - \frac{1}{s_1 - s_2} e^{s_2 h} \\ -\frac{\omega_n^2}{s_1 - s_2} e^{s_1 h} + \frac{\omega_n^2}{s_1 - s_2} e^{s_2 h} & q + \frac{s_2}{s_1 - s_2} e^{s_1 h} - \frac{s_1}{s_1 - s_2} e^{s_2 h} \end{bmatrix} \\
&\quad \times \begin{bmatrix} 1 + \frac{s_2}{s_1 - s_2} e^{s_1 h} - \frac{s_1}{s_1 - s_2} e^{s_2 h} \\ \frac{\omega_n^2}{s_1 - s_2} (e^{s_1 h} - e^{s_2 h}) \end{bmatrix}
\end{aligned} \tag{A.28}$$

$$\begin{aligned}
&= \frac{1}{q^2 + a_1 q + a_2} \begin{bmatrix} q - \frac{s_1}{s_1 - s_2} e^{s_1 h} + \frac{s_2}{s_1 - s_2} e^{s_2 h} & \frac{1}{s_1 - s_2} e^{s_1 h} - \frac{1}{s_1 - s_2} e^{s_2 h} \end{bmatrix} \\
&\quad \times \begin{bmatrix} 1 + \frac{s_2}{s_1 - s_2} e^{s_1 h} - \frac{s_1}{s_1 - s_2} e^{s_2 h} \\ \frac{\omega_n^2}{s_1 - s_2} (e^{s_1 h} - e^{s_2 h}) \end{bmatrix}
\end{aligned} \tag{A.29}$$

$$= \frac{b_1 q + b_2}{q^2 + a_1 q + a_2} \tag{A.30}$$

where

$$\begin{aligned}
b_1 &= 1 + \frac{s_2}{s_1 - s_2} e^{s_1 h} - \frac{s_1}{s_1 - s_2} e^{s_2 h} \\
&= 1 - e^{-\zeta\omega_n h} \left( \cos \omega_d h + \frac{\zeta\omega_n}{\omega_d} \sin \omega_d h \right)
\end{aligned} \tag{A.31}$$

$$\begin{aligned}
b_2 &= b_1 \left( -\frac{s_1}{s_1 - s_2} e^{s_1 h} + \frac{s_2}{s_1 - s_2} e^{s_2 h} \right) + \frac{\omega_n^2}{(s_1 - s_2)} (e^{s_1 h} - e^{s_2 h}) \left( \frac{1}{s_1 - s_2} e^{s_1 h} - \frac{1}{s_1 - s_2} e^{s_2 h} \right) \\
&= e^{-2\zeta\omega_n h} + e^{-\zeta\omega_n h} \left( \frac{\zeta\omega_n}{\omega_d} \sin \omega_d h - \cos \omega_d h \right)
\end{aligned} \tag{A.32}$$

Following Equation A.19, the relationship between the input sequence  $u[k]$  and

the output sequence  $y[k]$  can be expressed as follows:

$$y[k] = \frac{b_1q + b_2}{q^2 + a_1q + a_2}u[k] \quad (\text{A.33})$$

or equivalently.

$$(q^2 + a_1q + a_2)y[k] = (b_1q + b_2)u[k] \quad (\text{A.34})$$

By the definition of shift-forward operator, we arrive at the following linear difference equation that relates the input and the output sequences of the sampled SDOF oscillator:

$$y[k + 2] + a_1y[k + 1] + a_2y[k] = b_1u[k + 1] + b_2u[k] \quad (\text{A.35})$$

where  $u[k]$  is the input sequence representing the excitation force.  $y[k]$  is the corresponding output sequence representing the vibration response of the SDOF oscillator.  $a_1$ ,  $a_2$ ,  $b_1$  and  $b_2$  are coefficients of the difference equation and they were defined in Equations A.26, A.27, A.31 and A.32 respectively.

# Bibliography

- [1] American Petroleum Institute. *API Recommended Practice 2A(RP 2A)*. April 1987.
- [2] Odd Jan Andersen and Jorgen Lovseth. The frøya database for gale force maritime wind. In *Eurodyn*. 1993.
- [3] K. J. Åström and B. Wittenmark. *Computer Controlled Systems*. Prentice-Hall, 1984.
- [4] W. D. Baines and E. G. Peterson. An investigation of flow through screens. *Transactions of ASME*. pages 467–480. July 1951.
- [5] Robert D. Blevins. *Flow-Induced Vibration*. Van Nostrand Rienhold, 2<sup>nd</sup> edition, 1990.
- [6] British Standards Institution. *BS8100:Parts 1 and 2:1986*.
- [7] R. B. Campbell. Personal communication. February 1992.
- [8] C.K.Cheung and W.H.Melbourne. Turbulence effects on some aerodynamic parameters of a circular cylinder at supercritical reynolds numbers. *Journal of Wind Engineering and Industrial Aerodynamics*, 14:399–410. 1983.
- [9] Det Norske Veritas. *Classification Note No. 30.5, Environmental Conditions and Environmental Loads (March,1991)*.
- [10] Det Norske Veritas. *Rules for Submarine Pipeline Systems (1981)*.
- [11] Ove Ditlevsen. Duration of visit to critical set by gaussian process. *Probabilistic Engineering Mechanics*. 1(2), 1986.
- [12] ESDU International Plc. *ESDU: Item numbers 85038/39: Circular-cylindrical Structures: Dynamic Response to Vortex Shedding*, December 1985. Amendments A to C, March 1990.
- [13] Chen-Yang Fei and J. Kim Vandiver. Vortex-induced vibrations of structural members in unsteady winds. In *International Conference on Hydro-elasticity*, 1994.

- [14] Owen M. Griffin. Vortex-induced vibrations of marine cables and structures. NRL Memorandum Report 5600, Naval Research Laboratory, June 19 1985.
- [15] M. Grigoriu. Crossings of non-gaussian translation processes. *Journal of Engineering Mechanics*, 110(4). April 1982.
- [16] B. L. Grundmeier, R. B. Campbell, and B. D. Wesselink. OTC 6174: A Solution for Wind-Induced Vortex-Shedding Vibration of the Heritage and Harmony Platforms During Transpacific Tow. In *Offshore Technology Conference*, 1989.
- [17] J.F.Howell and M.Novak. Vortex shedding from circular cylinders in turbulent flow. In *Wind Engineering*, volume 1, 1979.
- [18] Ashan Kareem. Wind-induced response analysis of tension leg platforms. *Journal of Structural Engineering*, 111(1), January 1985.
- [19] T. V. Lawson. *Wind Effects on Buildings*. Applied Science Publishers LTD, 1980.
- [20] Drahomir Lazar and Frank H. Durgin. Some measurements of pressure fluctuations on two and three dimensional bodies due to longitudinal and lateral velocity fluctuations. Technical report. MIT Wright Brothers Wind Tunnel. December 1979. WBWT-TR-1119.
- [21] Y. K. Lin. *Probabilistic Theory of Structural Dynamics*. McGraw-Hill, 1967.
- [22] Henry Liu. *Wind Engineering*. Prentice Hall, 1991.
- [23] J. L. Lumley and H. A. Panofsky. *The Structure of Atmospheric Turbulence*. John Wiley & Sons, Inc., 1964.
- [24] The Mathworks, Inc. *Pro-Matlab User's Guide, Version 3.5*.
- [25] M.Novak and H.Tanaka. Pressure correlations on a vibrating cylinder. In *Proc. 4th International Conference on Wind Effects on Buildings and Structures*, 1975.
- [26] S. Nicholls. Measuring the effects of turbulence on the vortex shedding and dynamic response of a circular cylinder. Master's thesis, Massachusetts Institute of Technology, January 1993.
- [27] Norwegian Potroleum Directorate. *Acts, Regulations and Provisions for the Petroleum Activity. Volumn 2. Guidelines concerning loads and load effects*, 1994.
- [28] M. G. Rivero. Random wave simulation using a.r.m.a. models. Master's thesis. Massachusetts Institute of Technology, February 1987.
- [29] R. W. Robinson and J. Hamilton. *A Revised Criterion for Assessing Wind Induced Vortex Vibrations in Wind Sensitive Structures*. Brown and Root Limited, August 1991. Revision of Report Number: OT0 88021.

- [30] D. Rudge and C. Fei. Response of structural members to wind-induced vortex shedding. Master's thesis. Massachusetts Institute of Technology, September 1991.
- [31] D. Rudge, C. Fei, S. Nicholls, and J. K. Vandiver. OTC 6902: The Design of Fatigue-Resistant Structural Members. In *Offshore Technology Conference*. May 1992.
- [32] Peter Sachs. *Wind Forces in Engineering*. Pergamon Press, 2<sup>nd</sup> edition, 1978.
- [33] Turgut Sarpkaya. Vortex-induced vibrations - a selective review. *Journal of Applied Mechanics*, 46:241-258, June 1979.
- [34] A. Simiu and R. Scanlan. *Wind Effects on Structures*. Wiley, 1986.
- [35] David Surry. The effect of high intensity turbulence on the aerodynamics of a rigid circular cylinder at subcritical reynolds number. Technical report, Institute for Aerospace Studies, University of Toronto, October 1969. UTIAS Report No. 142.
- [36] David Surry. Some effects of intense turbulence on the aerodynamics of a circular cylinder at subcritical reynolds number. *Journal of Fluid Mechanics*, 52:543-563, 1972.
- [37] L. K. Timothy and B. E. Bona. *State Space Analysis: An Introduction*. McGraw-Hill, 1968.
- [38] U.K. Department of Energy. *Offshore Installations: Guidance on design, construction and certification*. fourth edition, 1990.
- [39] Erik Vanmarcke. *Random Fields*. The MIT Press, 1983.